

# **Synthesis and Characterization of Organic Luminescent Materials (Zn(II) and Ru(III)) and Fabrication of Energy-Efficient Organic Light Emitting Diodes Using Alq<sub>3</sub>**

**THESIS**

Submitted in partial fulfilment  
of the requirements for the degree of  
**DOCTOR OF PHILOSOPHY**

by

**L. RAJA**

Under the Supervision of  
**Prof. S. SINDHU**



**BIRLA INSTITUTE OF TECHNOLOGY AND SCIENCE, PILANI**

**2017**

# BIRLA INSTITUTE OF TECHNOLOGY AND SCIENCE, PILANI

## CERTIFICATE

This is to certify that the thesis entitled “Synthesis and Characterization of Organic Luminescent Materials (Zn(II) and Ru(III)) and Fabrication of Energy-Efficient Organic Light Emitting Diodes Using Alq<sub>3</sub>” submitted by L. Raja ID No 2011PHXF049P for the award of Ph.D. of the Institute embodies original work done by him under my supervision.

Signature of the Supervisor :

Name in capital letters : Prof. S. Sindhu

Designation : Associate Professor

Date:

## ***ACKNOWLEDGEMENTS***

I am deeply grateful to my thesis supervisor Prof. S. Sindhu, Department of Physics, BITS Pilani, Pilani Campus for her confidence in me and my work and for giving me the opportunity to complete my dissertation as part of her research group. I am indebted to her for her mentorship, her intellectual support and for giving me the freedom to explore on my own, while providing guidance when I faltered. Her patience and support helped me overcome many difficult situations and to finish this dissertation.

I am grateful to Prof. Souvik Bhattacharyya (Vice-Chancellor), Prof. S. C. Sivasubramanian (Acting Registrar), Prof. Ashoke Kumar Sarkar (Director, Pilani) of BITS Pilani, Rajasthan, for giving me the opportunity to pursue the doctoral degree and for providing necessary facilities and support during the research.

I wish to express my gratitude to Prof. Sanjay Kumar Verma (Academic Research (Dean, Ph.D. Programme), Prof. S. Gurunaryanan (Dean, Admissions), Prof. Sunil Bhand (Dean, SRC), Prof. Hemant Ramanlal Jadhav (Assoc. Dean, SRC/ARD), Dr. P. Srinivasan (Assoc. Dean, Practice School), Prof. Hari Om Bansal (Assoc. Dean, Admissions), Prof. Bijay Kumar Rout (Assoc. Dean, ARC) and Prof. Kumar Neeraj Sachdev (Assoc. Dean, SWD).

I am also grateful to Prof. Anshuman Dalvi, HOD of Physics, Prof. D.D. Pant, Dept. of Physics, and all faculty and staff of the Physics Department.

I wish to express my sincere thanks to DAC members Prof. Raj Kumar Gupta and Prof. Manjula Devi, Dept. of Physics, BITS Plani, for moral support and for suggestions to complete the dissertation.

I sincerely thank Dr. Navin Singh (Convener, DRC) for his moral support and suggestions.

I would like to express my sincere thanks to Dr. N. C. Shivaprakash, Dr. K. R. Gunasekhar, Department of IAP, IISc, Bangalore for providing me their lab infrastructure, necessary facilities, constant support, guidance and motivation. I am also grateful to Dr. K. Narasimha Rao, late Prof. J. Nagaraju and Mr. Krishnan from Dept. of IAP, IISc. I also sincerely thank IISc, Bangalore, for allowing me to use its characterization facility whenever required.

I wish to express my gratitude to Prof. P. S. Anil Kumar, Dept. of Physics, IISc, Bangalore for providing lab facility, constant support and motivation. I sincerely acknowledge Prof. E. S. Rajagopal (Emeritus Professor), Dr. R. Ganesan, Dept. of Physics, IISc, Bangalore.

I sincerely thank my elementary school teacher Mr. Panchavarnam and mathematics teachers Mr. A. Ramesh and Mr. Govindhan, of S.M.Hr. Sec. School, Tharamangalam for their constant encouragement in my studies during my school days. I also sincerely thank Mr. Munusamy, Mr. Ranganathan, Dr. P. Sellamuthu, for encouragement and motivation to do research.

I heartily thank my post-graduate (M. Sc.) faculty Mr. L. G. Gobinath, Mr. Suresh, Ms. Parveen Banu, Mrs. Sridevi, Mr. Saravanakumr, Mrs. Nithya from S.S. College, Salem for those motivation lectures.

My heartfelt thanks to Prof. M. Shivakumar, Prof. K. Jothivenkatachalam, Dr. V. R. Sarma Dulipala and Prof. Brahadeeswaran, BIT-Campus, Anna University Tiruchirappalli, Tamil Nadu for constant encouragement and motivational lectures

My heartfelt thank to former labmates Dr. Siju C. R, and Mr. P. P. Raja for their constant help, fruitful discussions and for providing a friendly atmosphere to study and conduct research.

I would also like to acknowledge the faculty and office staff at PDC, Bangalore BITS Pilani for moral support and cooperation.

I wish to express my gratitude to Dr. Eswaramoorthy K. V., and Mr. S. Ganapathy who helped me during my research career in characterization studies, for personal discussions, constant encouragement and for their helping nature.

I sincerely thank IISc friends Mr. Rajesh Srinivasan, Mrs. Malarmathi, Dr. G. Venkatesh, Dr. Kaushik Rajaram, Dr. Suresh Perumal, Dr. Naga Boopathy, Mr. R. Venkatesh, Mr. Praveen Managutti, Dr. Debakanta Samal, Dr. S. N. Karthik, Dr. Murugan, Dr. T. R. Sharavanan, Mr. Vadivel, Dr. Balachandar, Dr. Kiruba Daniel, Dr. T. K Bera, Mr. Buddha Deka Boruah, Mr. Sukanta Nandi, Dr. Sripan C., Mr. Virendra Parab, Mr. Sreekar Guddeti, Dr. S. Tamilarasan, Mr. Venkat Subba Rao, Mr. Srinivas, Dr. KavithaVenkatesan, and all IISc friends who have helped me during my research for personal discussions and helpful attitude. My special hearty thanks to Dr. Marutheswaran for successfully carrying out computational studies.

My hearty thanks to Dr. Justin Jesuraj, Dr. R. Ramachandran, Dr. C. Sathiskumar, Mr. R. Rajesh Kumar, Mr. K. Ravikumar, Mr. N. Venkatesan, Mr. S. Selvan, Mr. Selvaraj, and Mr. Chinnamuththu Ellappan for research and personal discussions and for their helping nature.

There are no words to thank all my family members: my father Mr. Lakshmanan Venkatachalam, who is my first hero, my dearest and lovely mother Mrs. Manikkammal Lakshmanan, my dearest brother as well as my role model Mr. L. Thangamani and my sister-in-law Mrs. T. Rajampal, and my lovely sisters Mrs. Makeshwari Cinnagoundar and Mrs. Vennila Selvaraj for consistent moral support, without whose help I would not have been able reach this level in my academic career. Their dedication and prayers brought me to this level. I am privileged to say that I am the first person in my whole family to get degrees and hopefully the doctor of philosophy award.

My hearty thanks to my lovely aunt Mrs. Selvamani and my uncle Mr. V. Ealumalai and all my family members and relatives who have supported and helped me while doing my research.

My heartfelt and deepest thank to my lovely wife Mrs. Priyatharshini for her continuous support, sacrifice, unending encouragement, patience and understanding, which made my work easier.

My thanks are due to my dearest son R. Mouli, who, though too young to understand more than “daddy is going to work”, has been a constant source of joy and motivation. I sincerely acknowledge my dearest nephew Mr. T. R. Sanjay Devan, and lovely nieces Ms. T. Menaka, Ms. T. Lalitha Kumari, and Ms. T. Krishnamathi for their friendly and supportive attitude.

My hearty thanks to Dr. L. R. Shobin, Dr. Sebastian Ananth, Mr. Dhayanantha Prabhu, Dr. S. K. Thiagarajan, Dr. P. Kowsalya, Mr. Gyanan, Mr. Lakshmi Narayanan, Mr. Swaminathan and all my M. Tech classmates for their friendly support to me in all my endeavors.

I also express my sincere gratitude to one and all, and all those who have helped me directly or indirectly. Though many have not been mentioned, none is forgotten.

July 2017

L. Raja

## ABSTRACT

Organic light-emitting devices (OLEDs) are emerging technology for both lighting and flat-panel display appliances because of their distinctive advantages, such as ultra-thin thickness, low power consumption, high brightness, and wide viewing angle. The successful fabrication of OLEDs with maximum light efficiency and more fascinating properties inspired the scientific community and it is expected to replace conventional lighting sources and flat-panel displays in the near future. The efficiency of OLEDs mainly depends on the charge balance after charge carrier injection from the electrodes. Varieties of inorganic and organic materials have been employed to realize high-efficiency OLEDs. White-emitting OLED (WOLED) is of particular importance as lighting source for developing efficient solid-state lighting applications. The most important WOLED development is establishing a set of red, green and blue emissions or of equal mixing of orange and green emitters with colour purity, high efficiency, and stability. In this context, it is important to understand the photophysical, electrochemical, thermal, and morphological characteristics of luminescent molecules. The versatility of OLEDs is still being explored to further improve the technology to next level and requires improvements in both performance and environmental stability of OLEDs. The synthesis of novel light-emitting organic molecules that can emit primary colours of blue and orange with high purity.

This thesis focuses on the discovery of metal complexes for OLED applications. The research work presented here focuses mainly on, the synthesis of three 2,2':6',2''-terpyridine (terpy) ligands and investigates their photophysical, and electrochemical properties. Followed by design, synthesis and characterization of terpy-based metal complexes such as Zn(II) and Ru(III) have been investigated. Additionally, the material was prepared and characterised the highly transparent PEDOT:PSS with AgNWs hybrid-composite based transparent conductive thin film (TCF) electrode with good conduction. Finally, a fluorescent green OLED using tris-(8-hydroxyquinoline) aluminum ( $\text{Alq}_3$ ) was fabricated based on PEDOT:PSS/AgNWs hybrid-composite anode and ITO anode and compared their performance.

Chapter 1 reviews the significance of organic semiconductors and their lighting applications with survey of the current literature. The second part of Chapter1 describes the device structure, operating mechanism, materials selection, and energy level alignment of OLEDs to enhance their performance.

Chapter 2 deals with thin-film fabrication methods used in this work, such as thermal evaporation technique and spin-coating process to prepare uniform thin films. The second part of this chapter describes materials characterization techniques used in the present work, including UV-Visible absorbance spectroscopy, photoluminescence spectroscopy, time-resolved fluorescence spectroscopy, atomic force microscopy, and field emission scanning electron microscope. Electroluminescence and electrical behaviour of OLED were also examined.

Chapter 3 discusses the synthesis and characterization of three 4'-aryl substituted terpy derivatives in a single pot reaction. The photophysical behaviour of these complexes exhibits charge transition due to intra-ligand charge transition (ILCT) process. The measured fluorescence lifetime is between 0.29 and 1.55 ns. The 3,4,5-trimethoxy-phenyl-substituted terpyridine derivative shows high red-shift with respect to 4-methyl-phenyl and 2-furyl substituted terpy derivatives. This may be due to smaller reorganization energy associated with charge-transfer transition of trimethoxy phenyl substituent on terpy. These derivatives are thermally very stable. Highest occupied molecular orbital (HOMO) and lowest unoccupied molecular orbital (LUMO) energy values suggest that these terpy derivatives are good choice for electron transporting with blue fluorescent emitter as the design for fluorescent OLEDs.

Synthesis, photophysical, thermal and electrochemical behaviour of three Zn(II)-based terpy complexes (**Zn(L<sub>1</sub>-L<sub>3</sub>)**) are described in Chapter 4. The density functional theory (DFT) outlines the geometric optimization and electronic charge transition of these complexes. Dual characteristics of the optical behaviour have been observed, such as Zn(II) complexes exhibiting a deep blue-to-green fluorescence in crystalline form, while it is sky-to-deep blue in dimethylsulfoxide (DMSO). The photophysical behaviour revealed the potential charge transfer to  $\pi-\pi^*$  and  $n-\pi^*$  states due to ILCT. Hence, appropriately substituted ligands on Zn(II) ions, the result of the Zn(II)-based terpy complexes, can generate long-lived fluorescence at room temperature.

Novel orange-fluorescent Ru(III)-based terpy complexes (**Ru(L<sub>1</sub>-L<sub>3</sub>)**) have been synthesised and their characteristics studied in Chapter 5. Photophysical studies describe that the luminescence of Ru(III) complexes is due to electronic transition between the energy levels of singly unoccupied molecular orbitals (SUMO) and singly occupied molecular orbitals (SOMO). In addition, DFT calculations also show that charge transition takes places due to electron transfer between SUMO and SOMO energy levels. All complexes exhibit orange emissions with broad emission spectra

in the range of 591–620 nm in a DMSO, especially, **Ru(L<sub>2</sub>)** complex has broadened orange emission. It is very interesting to note that the electronic transition of the Ru(III) complexes is due to the ILCT and metal-to-ligand charge transfer (MLCT) process. Their radiative decay occurs by doublet exciton process. The bands centered at 591 and 620 nm demonstrate that these emissions originated from the transition of SOMO and SUMO.

Chapter 6 describes the synthesis of silver nanowires (AgNWs) of around 20  $\mu\text{m}$  length and 70 nm diameter by adapting polyol process and reports their performance. Further, PEDOT:PSS/AgNWs hybrid composite-based transparent conducting thin film (TCF) was prepared. The green fluorescent OLEDs were fabricated on PEDOT:PSS/AgNWs hybrid-composite TCF as anode and ITO anode then compared their performance. The measured current densities were 370 and 293  $\text{mA}/\text{cm}^2$  for OLEDs fabricated on PEDOT:PSS/AgNWs hybrid-composite TCF anode and ITO anode, respectively. The maximum luminous intensities were 1610 and 1260  $\text{counts}\cdot\text{s}^{-1}$  for OLEDs fabricated on PEDOT:PSS/AgNWs hybrid-composite TCF and ITO anode, respectively. Hence, the current density together with the brightness of OLED fabricated on PEDOT:PSS/AgNWs hybrid-composite TCF is significantly improved; it could be due to the enhancement of the work function (WF) of PEDOT:PSS/AgNWs hybrid-composite.

Important findings drawn from our investigations are summarised in Chapter 7. Conclusions and suggestions for future work are also made towards end of Chapter 7.



## Table of Contents

<b>Chapter 1 : Introduction</b> .....	1
1.1 Organic semiconductors .....	1
1.1.1 Conjugated materials .....	2
1.1.2 Electronic structure of conducting polymers.....	3
1.1.3 HOMO and LUMO in organic semiconductors .....	4
1.1.4 Fluorescence and phosphorescence in organic molecules .....	5
1.1.5 Singlet and triplet states .....	6
1.1.6 Charge transition in organic semiconductors .....	8
1.2 Organic light emitting materials and devices.....	8
1.2.1 OLED materials .....	8
1.2.1.1 Polymeric LED .....	9
1.2.1.2 Organic small molecule materials .....	10
1.2.1.3 Oligopyridines .....	11
1.2.2 OLED device structure.....	14
1.2.2.1 OLED operation mechanism .....	15
1.2.2.2 Energy level alignment and interfacial structure in OLEDs .....	16
1.2.2.3 Interface engineering for OLED improvement .....	18
1.2.2.4 Charge balancing .....	19
1.2.2.5 Carrier transport and recombination in OLEDs .....	20
1.2.3 Transparent conducting thin film anode .....	21

1.3	Gap in the existing research.....	23
1.4	Objective.....	24
1.5	Thesis outline.....	25
1.6	References.....	26
<b>Chapter 2 : Experimental Methods.....</b>		<b>34</b>
2.1	Chemicals and materials.....	34
2.2	Thin film growth technique.....	34
2.2.1	Spin coating.....	35
2.2.2	Chemical vapour deposition.....	36
2.2.3	Spray pyrolysis.....	37
2.2.4	Thermal evaporation.....	38
2.2.5	Sputtering deposition.....	40
2.3	Characterization tools.....	41
2.3.1	Structural characterization.....	41
2.3.1.1	Nuclear magnetic resonance spectroscopy.....	41
2.3.1.2	Mass spectrometry.....	41
2.3.1.3	FT-IR spectroscopy.....	42
2.3.2	Morphological analysis.....	42
2.3.2.1	Scanning electron microscopy.....	42
2.3.2.2	Atomic force microscopy.....	44
2.3.3	Thermal analysis.....	45
2.3.3.1	Differential scanning calorimetry.....	45

2.3.3.2	Thermogravimetric analysis .....	46
2.3.4	Photophysical studies .....	46
2.3.4.1	UV-Vis absorbance spectroscopy .....	47
2.3.4.2	Photoluminescence spectroscopy .....	49
2.3.4.3	Time-resolved fluorescence spectroscopy .....	50
2.3.5	Electrochemical analysis .....	50
2.4	Fabrication and characterization of OLED device .....	51
2.4.1	ITO substrate cleaning .....	51
2.4.2	Oxygen-plasma treatment .....	51
2.4.3	OLED device structure .....	52
2.4.4	Electroluminescent measurement .....	53
2.5	References .....	54
<b>Chapter 3 : Synthesis, photophysical, thermal and electrochemical properties of 4'-aryl substituted 2,2':6',2''-terpyridine derivatives .....</b>		<b>56</b>
3.1	Introduction .....	56
3.2	Experimental .....	58
3.2.1	Procedure for the synthesis of 4'-aryl substituted 2,2':6',2''-terpyridines .....	58
3.2.2	4'-(4-methylphenyl)- 2,2':6',2''-terpyridine: C-1 .....	59
3.2.3	4'-(2-furyl)-2,2':6',2''-terpyridine: C-2 .....	59
3.2.4	4'-(3,4,5-trimethoxyphenyl)-2,2':6',2''-terpyridine: C-3 .....	59
3.3	Results and discussion .....	60
3.3.1	UV-Vis absorbance spectra .....	60

3.3.2	Photoluminescence studies.....	62
3.3.3	Fluorescence lifetime characterizations .....	63
3.3.4	Differential scanning calorimetry analysis.....	64
3.3.5	Electrochemical analysis .....	65
3.3.6	Scanning electron microscopy.....	66
3.4	Summary.....	67
3.5	References.....	68
<b>Chapter 4 : The transition from sky blue to deep-green fluorescent Zn(II)-based 4'-aryl substituted 2,2':6',2''-terpyridine complexes for organic light emitting diodes.....</b>		<b>72</b>
4.1	Introduction.....	72
4.2	Experimental .....	74
4.2.1	Syntheses of Zn(II) complexes (L <sub>1</sub> -L <sub>3</sub> ).....	74
4.2.2	[Zn(L <sub>1</sub> ) <sub>2</sub> ].NO <sub>3</sub> : [Zn(L <sub>1</sub> )] .....	74
4.2.3	[Zn(L <sub>2</sub> ) <sub>2</sub> ].NO <sub>3</sub> : [Zn(L <sub>2</sub> )] .....	74
4.2.4	Zn(L <sub>3</sub> ) <sub>2</sub> ].NO <sub>3</sub> : [Zn(L <sub>3</sub> )] .....	76
4.3	Quantum calculation of Zn(L <sub>1</sub> -L <sub>3</sub> ) complexes.....	76
4.4	Results and discussion .....	77
4.4.1	Photophysical properties .....	77
4.4.2	Photoluminescence studies.....	79
4.4.3	Thermal properties .....	82
4.4.4	Fluorescence life time measurements .....	84
4.4.5	Electrochemical analysis .....	86

4.4.6	Scanning electron microscopy.....	88
4.5	Summary.....	89
4.6	References.....	90
<b>Chapter 5 : Orange fluorescent Ru(III) complexes based on 4'-aryl substituted 2,2':6'2"-terpyridine for OLEDs application .....</b>		
<b>95</b>		
5.1	Introduction.....	95
5.2	Experimental .....	97
5.2.1	Syntheses of Ru(III) complexes (RuL <sub>1</sub> -L <sub>3</sub> ).....	97
5.2.2	[Ru(4-Mephtpy) <sub>2</sub> ]Cl <sub>3</sub> : [Ru(L <sub>1</sub> )] .....	97
5.2.3	[Ru(3,4,5-tmphtpy) <sub>2</sub> ]Cl <sub>3</sub> : [Ru(L <sub>2</sub> )] .....	97
5.2.4	[Ru(4-thtpty) <sub>2</sub> ]Cl <sub>3</sub> : [Ru(L <sub>3</sub> )] .....	99
5.3	Quantum calculation of Ru(L <sub>1</sub> -L <sub>3</sub> ) complexes.....	99
5.4	Results and Discussion .....	101
5.4.1	UV-Vis absorbance spectra .....	101
5.4.2	Photoluminescence spectra.....	103
5.4.3	Cyclic voltammetry.....	104
5.4.4	Thermal properties .....	105
5.4.5	Fluorescence lifetime measurements .....	108
5.4.6	Scanning electron microscope .....	109
5.5	Summary.....	110
5.6	References.....	111

<b>Chapter 6 : Fabrication of fluorescent green OLEDs based on PEDOT:PSS/AgNWs hybrid-composite anode and their performance .....</b>	<b>117</b>
6.1 Introduction.....	117
6.2 Experimental methods .....	120
6.2.1 Preparation of AgNWs.....	120
6.2.2 Preparation of PEDOT:PSS/AgNWs anode.....	120
6.2.3 Fabrication of green OLEDs .....	121
6.3 Results and discussion .....	123
6.3.1 Transmittance spectra .....	124
6.3.2 Morphological studies.....	125
6.3.2.1 AFM analysis.....	125
6.3.2.2 SEM analysis .....	126
6.4 Device characterization .....	127
6.4.1 Current density-voltage (J–V) characteristics .....	128
6.4.2 Electroluminescence studies.....	129
6.5 Summary.....	130
6.6 References.....	130
<b>Chapter 7 : Conclusion and Future Scopes .....</b>	<b>137</b>
7.1 Conclusion .....	137
7.2 Future scopes.....	139
<b>APPENDIX A .....</b>	<b>141</b>
<b>APPENDIX B.....</b>	<b>147</b>

List of publications in international journals .....	158
Papers presented in national and international conferences.....	162
Brief biography of the supervisor .....	164
Brief biography of the candidate.....	165

## List of Schemes

Scheme 3.1: Synthetic procedure for the preparation of 4'-aryl substituted terpy derivatives.....	58
Scheme 4.1: Synthetic route of Zn(L <sub>1</sub> -L <sub>3</sub> ) complexes .....	75
Scheme 5.1: Synthetic route of Ru(L <sub>1</sub> -L <sub>3</sub> ) complexes .....	98



## List of Figures

Figure 1.1: Molecular and electronic structures of (a) polyethylene and (b) polyacetylene .....	3
Figure 1.2: Scheme of HOMO and LUMO of organic molecules.....	4
Figure 1.3: Jablonski energy level diagram. ....	6
Figure 1.4: Schematic illustrations of singlet and triplet states (a) and four types of electronic transitions (b). ....	7
Figure 1.5: Molecular structures of light emitting polymers including PPV, PF and PT .....	10
Figure 1.6: Chemical structure of tris-(8-hydroxyquinoline) aluminum, 2,2'-bipyridine and 2,2':6',2''-terpyridine .....	11
Figure 1.7: A typical stack layout of multilayered OLED consisting of a HTL, ETL and EML. ....	15
Figure 1.8: Operation mechanism of two layered OLEDs structure. ....	16
Figure 1.9: Energy level diagrams of organic semiconductors at interfaces: (a) Organic semiconductor interface with HIB and EIB, (b) Multi-hetero layer stack of OLED containing HTL, ETL and EML with electron-blocking barrier (EBB) and hole-block .....	17
Figure 1.10: Chemical structure of PEDOT:PSS.....	22
Figure 2.1: (a) Digital image of spin coater and (b) graphical representation of spin coating chamber .....	36
Figure 2.2: Schematic diagram of spray pyrolysis setup.....	38
Figure 2.3: (a) Scheme of thermal evaporation chamber and (b) digital image of thermal evaporation unit. ....	39
Figure 2.4: Schematic diagram of sputtering mechanism .....	40
Figure 2.5: Schematic illustration of scanning electron microscope .....	43
Figure 2.6: working principle of atomic force microscopy .....	45

Figure 2.7: Electronic energy levels and transition states .....	47
Figure 2.8: Thermal vapour deposition chamber inside: (a) before creating plasma, (b) when plasma occurs. ....	51
Figure 2.9: OLEDs device structure.....	52
Figure 2.10: Digital image of electroluminescent set-up consisting of regulated DC power supply and HR4000 spectroradiometer .....	53
Figure 3.1: UV–Vis absorbance spectra of terpy derivatives (C1–C3) in DCM .....	60
Figure 3.2: Photoluminescence spectra of terpy derivatives recorded at an excitation wavelength of 308 nm .....	62
Figure 3.3: Fluorescence lifetime decay curves for (a) C-1, (b) C-2 and (c) C-3. The excitation wavelength was 406 nm for C-1 and C-2; and 468 nm for C-3.....	63
Figure 3.4: DSC plots of terpy derivatives with the scanning rate of 10 °C min <sup>-1</sup> .....	64
Figure 3.5: Cyclic voltammogram of terpy derivatives at the potential between –2.0 V to +2.0 V in 0.1 M TBAP/DCM solution at scan rate of 100 mVs <sup>-1</sup> .....	65
Figure 3.6: SEM images of (a) C-1, (b) C-2 and (c) C-3. Inset: High magnification of C-3 .....	67
Figure 4.1: Optimized geometry and electronic distribution of the frontier orbitals for Zn(L <sub>1</sub> -L <sub>3</sub> ) complexes .....	77
Figure 4.2: UV-Vis absorbance spectra of Zn(II) complexes in DMSO solution. Inset: digital photographs of the quartz cuvette showing fluorescence of (a) Zn(L <sub>1</sub> ), (b) Zn(L <sub>2</sub> ) and (c) Zn(L <sub>3</sub> ) in DMSO solution after exposing the solution to UV radiation.....	78
Figure 4.3: PL spectra of Zn(L <sub>1</sub> -L <sub>3</sub> ) complexes recorded at excitation wavelength of 310 nm for Zn(L <sub>1</sub> ) and Zn(L <sub>3</sub> ) complexes, whereas 287 nm used for Zn(L <sub>2</sub> ) complex.....	81

Figure 4.4: PL spectra of Zn(L <sub>1</sub> -L <sub>3</sub> ) complexes; comparison of PL spectra for as prepared complexes with DMSO solution .....	82
Figure 4.5: DSC plots of Zn(L <sub>1</sub> -L <sub>3</sub> ) complexes with the scanning rate of 10 °C min <sup>-1</sup> under nitrogen atmosphere.....	83
Figure 4.6: Thermogravimetric analysis of Zn(L <sub>1</sub> -L <sub>3</sub> ) complexes under nitrogen atmosphere .....	84
Figure 4.7: Fluorescence decay spectra of Zn(L <sub>1</sub> ) (a), Zn(L <sub>2</sub> ) (b) and Zn(L <sub>3</sub> ) (c) complexes at the excitation wavelength of 402 nm with one-exponential fit residuals, $\chi^2 = 1.003$ .....	85
Figure 4.8: Cyclic voltammogram of Zn(L <sub>1</sub> -L <sub>3</sub> ) complexes in the potential between -2.2 to + 1.0 V in 0.1 M TBAP/DMF solution at scan rate of 100 mV s <sup>-1</sup> .....	87
Figure 4.9: SEM images of (a) Zn(L <sub>1</sub> ), (b) Zn(L <sub>2</sub> ) and (c) Zn(L <sub>3</sub> ) .....	89
Figure 5.1: Optimized geometry and electronic distribution of the frontier orbitals for Ru(III) terpyridine complexes (RuL <sub>1</sub> -L <sub>3</sub> ). .....	100
Figure 5.2: UV-Vis absorbance spectra of Ru(L <sub>1</sub> -L <sub>3</sub> ) complexes in DMSO.....	101
Figure 5.3: PL spectra of Ru(L <sub>1</sub> -L <sub>3</sub> ) complexes recorded at excitation wavelength of 310 nm for Ru(L <sub>1</sub> ) and Ru(L <sub>2</sub> ) complexes, whereas 290 nm for Ru(L <sub>3</sub> ) complex in DMSO.....	103
Figure 5.4: Cyclic voltammogram of Ru(L <sub>1</sub> ) complex in acetonitrile (vs.SCE). The process at about 0.25 V is due to ferrocene, added as a reference .....	105
Figure 5.5: DSC plots of the Ru(L <sub>1</sub> -L <sub>3</sub> ) complexes. ....	106
Figure 5.6: TGA thermogram of Ru(L <sub>1</sub> -L <sub>3</sub> ) complexes .....	107
Figure 5.7: Fluorescence decay spectra of Ru(L <sub>1</sub> ) (a), Ru(L <sub>2</sub> ) (b) and Ru (L <sub>3</sub> ) (c) complexes at the excitation wavelength of 310 nm with one-exponential fit residuals, $\chi^2 = 1.002$ .....	108
Figure 5.8: SEM images of (a) Ru(L <sub>1</sub> ), (b) Ru(L <sub>2</sub> ) and (c) Ru(L <sub>3</sub> ) complexes .....	109

Figure 6.1: Schematic illustration of fabricating PEDOT:PSS/AgNWs thin film.....	121
Figure 6.2: Schematic illustration of drive device (a) and AgNWs blends with PEDOT:PSS composite based OLED (b). .....	122
Figure 6.3: UV-Vis transmittance spectra of PEDOT:PSS and PEDOT:PSS/AgNWs composite TCF fabricating on corning microscope slide .....	124
Figure 6.4: AFM images of TCF-based on PEDOT:PSS and PEDOT:PSS/AgNWs hybrid-composite fabricated on corning microscope slides.....	126
Figure 6.5: SEM image of PEDOT:PSS/AgNWs composite on corning microscope slide .....	127
Figure 6.6: Current density-voltage characteristics of the fluorescent green OLEDs based on PEDOT:PSS/AgNWs and ITO anode.....	128
Figure 6.7: Plot of luminous intensity vs. wavelength of fluorescent green OLEDs based on PEDOT:PSS/AgNWs hybrid- composite and ITO anode.....	129

## List of Tables

Table 3.1: Photophysical and thermal data of terpy derivatives.....	61
Table 3.2: Electrochemical data of terpy derivatives.....	66
Table 4.1: Photophysical and fluorescence lifetime data of Zn(II) complexes at room temperature.....	79
Table 4.2: Electrochemical and thermal properties of Zn(L <sub>1</sub> -L <sub>3</sub> ) complexes.....	88
Table 5.1: Photophysical, fluorescence lifetime and thermal properties (RuL <sub>1</sub> -L <sub>3</sub> ) complexes.....	102

## List of Symbols and Abbreviations

amu	atomic mass unit
ACN	acetonitrile
a. u.	arbitrary unit
AFM	atomic force microscopy
Alq <sub>3</sub>	tris-(8-hydroxyquinoline) aluminum (III)
BCP	bathocuproine
BPhen	bathophenanthroline
bpy	2,2'-bipyridine
C	carbon
CuPc	copper phthalocyanine
LCD	liquid crystal display
CDCl <sub>3</sub>	chloroform-d
CNTs	carbon nanotubes
CPs	conducting polymers
CV	cyclic voltammetry
Calcd	calculated
DCM	dichloromethane
DFT	density functional theory
DMF	N,N-Dimethylformamide
DMSO	dimethylsulfoxide

DSC	differential scanning calorimetry
$E_f$	fermi level
FMO	frontier molecular orbital
fs	femtosecond
EL	electroluminescence
ES	electrospray ionization
ETL	electron transport layer
$^1\text{H-NMR}$	proton nuclear magnetic resonance spectroscopy
$^{13}\text{C-NMR}$	carbon nuclear magnetic resonance spectroscopy
Fc	ferrocene
H	hydrogen
HJ	heterojunction
HOMO	highest occupied molecular orbital
HTL	hole transport layer
ITO	indium tin oxide
J	coupling constant in Hz
LUMO	lowest unoccupied molecular orbital
LC	ligand centered
MLCT	metal-to-ligand charge transfer
MS	mass spectrometry
m/z	mass to charge ratio
N	nitrogen

NPB	N, N'-diphenyl-N, N'-bis(1-naphthyl)-(1,1'-biphenyl)-4,4'-diamine
NMR	nuclear magnetic resonance
ns	nanosecond
OLEDs	organic light emitting diodes
OPVC	organic photovoltaic cells
OTFT	organic thin film transistor
PF	polyfluorene
PL	photoluminescence
PEDOT	poly(3,4-ethylenedioxythiophene)
PPV	poly(p-phenylene vinylene)
ps	picosecond
PSS	poly(4-styrenesulfonic acid)
PT	polythiophene
PVCs	photovoltaic cells
ppm	parts per million
QE	quantum efficiency
RT	room temperature
s	second
SEM	scanning electron microscopy
SOMO	singly occupied molecular orbital
SUMO	singly unoccupied molecular orbital
TBAP	tetrabutylammonium perchlorate



TCF	transparent conducting thin film
T <sub>c</sub>	crystalline temperature
T <sub>d</sub>	thermal decomposition
T <sub>g</sub>	glass transition temperature
T <sub>m</sub>	melting temperature
TPD	N,N'-Bis(3-methylphenyl)-N,N'-diphenylbenzidine
TCSPC	time-correlated single-photon counting
terpy	2,2':6',2''-terpyridine
TGA	thermogravimetric analysis
TMS	tetramethylsilane
UV-Vis	ultraviolet-visible
VL	vacuum level
δ	chemical shift
λ	wavelength
λ <sub>max</sub>	wavelength at which maximum absorption occurs in nm
eV	electron volt
τ	lifetime
WF	work function
WOLEDs	white-emitting organic light emitting diodes
Wt.	weight

# CHAPTER 1

## Introduction

The fundamentals of organic semiconductors, organic light emitting materials and devices have been briefly reviewed in this chapter. Further, the mechanism and device structure of organic light emitting diodes are also discussed. The motivation and objectives of the work are discussed at the end of the chapter.

### 1.1 Organic semiconductors

Traditionally, inorganic materials and their compounds were popular for their semiconducting properties [1]. The late 1960s saw the breakthrough discovery of conducting polymers by Nobel laureates Alan J. Heeger, Alan G. MacDiarmid and Hideki Shirakawa, who proposed electrical conductivity in polyacetylene due to its specific electronic properties [2]. Following this crucial finding, organic materials have been explored for the replacement of inorganic semiconductors in optoelectronic applications [3]. The superiority of polymers over inorganic compounds lies mainly in the ease of processability [4]. The world of synthetic polymers was born and they found their way into many applications due to low cost [5]. Since the early 1980s, the field of optoelectronics has developed rapidly [6–9]. Nowadays optoelectronics is extensively used in a wide range of applications in various fields such as field effect transistors, organic light emitting diodes (OLED), solar cells, capacitors and sensors [10–14].

Organic semiconductors have unique optical and electrochemical band structures, which give them superior electrical and optical properties that are highly desirable for electronic and optoelectronic applications [15, 16]. Further research is being undertaken to enhance the properties of organic semiconductors such as good mechanical resistance, high solubility and simple synthesizing process [17–19]. These semiconductors have a unique material chemistry of  $\pi$ -conjugated molecules, which is highly preferable for the desired optoelectronic applications. They have an energy gap between the highest occupied molecular orbital (HOMO) and lowest unoccupied molecular orbital (LUMO) typically in the range of 1.5–3.5 eV, which is desirable when compared to inorganic semiconductors that have a typical band gap between 1–3 eV [20]. The advantages in using organic materials in the development of optoelectronic devices are the

use of inexpensive, simple material-processing techniques like solution process and a high-throughput device assembly, predominantly through printing methods. Among the various organic materials available, organic polymer semiconductors play a vital role in fabricating optoelectronic devices. Polymers are usually classified into two types based on their electrical conductivity: conjugated polymers and saturated or non-conjugated polymers [21].

### **1.1.1 Conjugated materials**

Conjugated polymers are organic molecules that are characterised by a backbone chain of alternating double and single bonds. They possess conjugated  $\pi$ -electrons that can be easily delocalized rather than being part of one valence bond. Currently, conjugated polymers are the most important class of organic semiconductors used to fabricate OLEDs and optoelectronic devices due to their unique optical, electrical and mechanical properties [22]. Optoelectronic devices can be made of conducting or semiconducting  $\pi$ -conjugated materials. These organic electronic devices are different from conventional inorganic electronic devices. During the current scientific and technological revolution, the study of high-performance materials such as conjugated conducting materials has steadily increased for optoelectronic applications [23, 24]. The need for smaller, thinner and flexible electronic devices has led to the development of new materials like conducting polymers (CPs), which have novel features and simplified manufacturing methods [25]. They possess the electrical, electronic and optical properties of metals while retaining mechanical flexibility [26]. These polymers are called as intrinsically conducting polymers (ICPs) and are commonly known as synthetic metals [7]. The electrical conductivity of ICPs is more than that of insulators and extends into the range of common metals. Due to the feasibility of charge transportation, mechanical stability and processability of conjugated conducting polymers, they are the most preferred materials to fabricate OLEDs [27]. The study of the electronic structure of organic semiconductors is imperative for an understanding of the conduction mechanism, which is an important phenomenon in optoelectronic device applications.

### 1.1.2 Electronic structure of conducting polymers

Conducting polymers are normally insulators in the neutral form. Nevertheless, their electrical conductivity can be improved from the insulating to the conducting state using oxidation (p-doping) or reduction (n-doping) processes [28].

The principle behind the conduction mechanism of conjugated CPs is different from that of inorganic semiconductors. The molecular and electronic structures of non-conjugated (polyethylene) and conjugated (polyacetylene) polymers are shown in Figure 1.1.

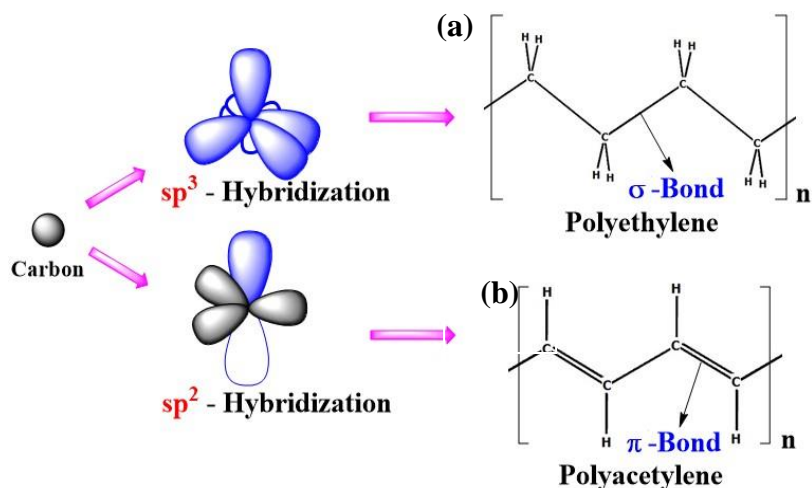


Figure 1.1: Molecular and electronic structures of (a) polyethylene and (b) polyacetylene

In the former case, valence electrons of the carbon atom in the main chain are hybridized with  $sp^3$  configuration and each carbon atom is attached to four other atoms [29]. Hence the atomic orbitals of non-conjugated polymers are completely saturated, making them insulators in nature. In conjugated polymers, the electrons in the carbon orbitals are hybridized with  $sp^2$ - $p_z$  configuration [30], which results in one unpaired electron ( $\pi$ -electron) per carbon atom. Each carbon atom is covalently bonded to three other carbon atoms; the unhybridized  $p_z$  orbitals of adjacent carbon atoms along the backbone overlap to increase the delocalized  $\pi$  bands. Conjugated polymers manifest metallic or semiconducting properties depending on whether the bands are filled completely or partially. The configuration of  $sp^2$  hybridization forms three sigma-bonds and one  $\pi$ -bond per carbon atom [5]. The energy values of the LUMOs and

HOMOs of organic materials are the deciding factor in the fabrication of optoelectronic devices [31].

### 1.1.3 HOMO and LUMO in organic semiconductors

The commonly used practical model for describing the mechanisms of chemical reactivity is the frontier molecular orbital (FMO) theory, which was developed by the Nobel laureate Kenichi Fukui in 1950 [32]. The chemical reaction of a molecule is dominated by two frontier orbitals, namely the HOMO and LUMO. The FMO theory governs the interaction of each organic molecule with others. The HOMO is the highest-energy molecular orbital that has electrons in it and the LUMO is the next energy orbital level close to HOMO, which always has states that are empty of electrons. Generally, the energy levels of the HOMO and LUMO in organic semiconductor molecules are mainly based on  $\pi$ -orbitals. Thus, the HOMO represents a  $\pi$ -bonding orbital while the LUMO corresponds to a  $\pi^*$ -antibonding orbital [33].

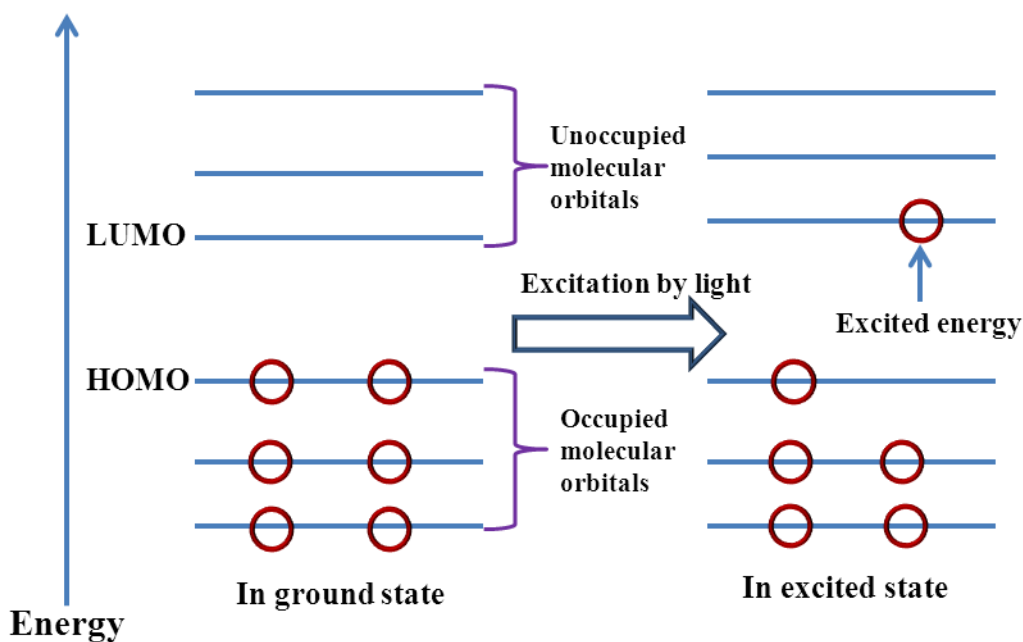


Figure 1.2: Scheme of HOMO and LUMO of organic molecules [34]

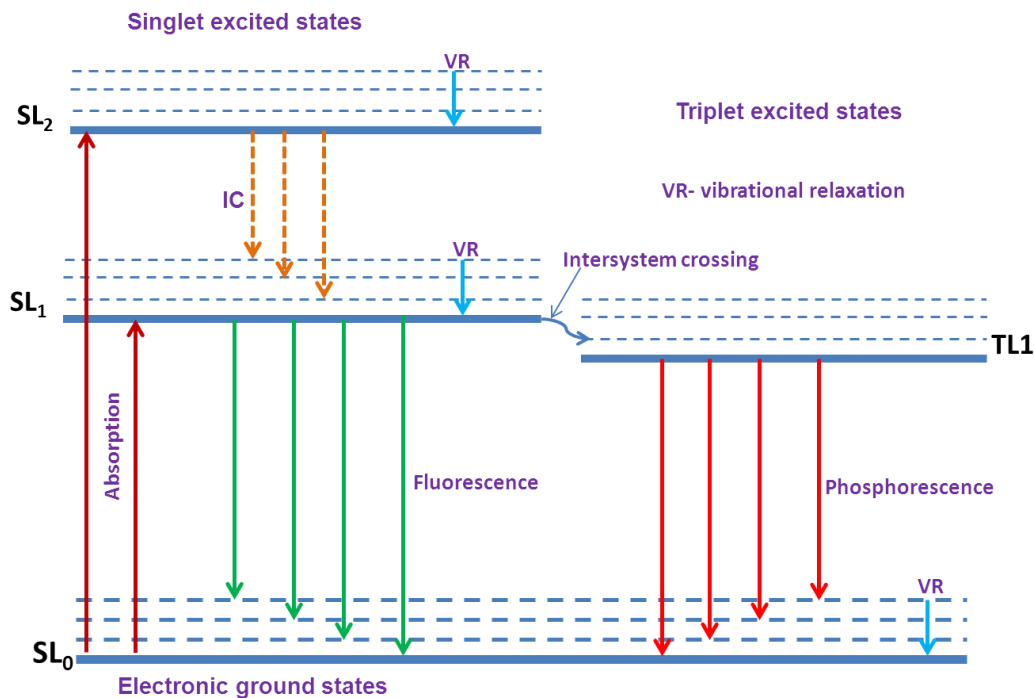
The energy gap between the HOMO and LUMO demonstrates the maximum wavelength that can be absorbed by organic molecules. Figure 1.2 shows the schematic representation of energy

levels in the HOMO and LUMO. The circle represents an electron in an orbital; when light of high frequency is absorbed by an electron in the HOMO energy level, it moves into the LUMO energy level. The structures of organic semiconductors are typically like the conjugated architecture of an alternating single ( $\sigma$ ) and double ( $\pi$ ) bonds network. The weak  $\pi$ -bonding and  $\pi^*$ -antibonding atomic orbitals of the molecules are overlapped with neighboring atomic orbitals to form new molecular orbitals. In addition the  $\pi$ -bonds in the molecule interact with each other freely, leading to a localized  $\pi$  structure in the new molecular orbitals. The electrons involved in the  $\pi$ -bonds are loosely bound, which enables relatively easy delocalization [35]. These delocalized  $\pi$ -electrons are the conduction electrons in conjugated organic semiconductors; they can be extended over the whole molecule for charge transition. The luminescent molecules are typically classified into two types as fluorescent and phosphorescent emitters.

#### **1.1.4 Fluorescence and phosphorescence in organic molecules**

The excitation and emission of electrons in organic luminescent molecules are described by the Jablonski energy level diagram. Figure 1.3 shows the schematic diagram of the singlet ground state  $SL_0$ , the excited singlet states  $SL_1$  and  $SL_2$  and the excited triplet state  $TL_1$ .  $SL_0$  represents the electronic energy of the molecule in the ground state. At room temperature, most of the molecules are in the ground state; their energy state corresponds to the electronic, rotational and vibrational degrees of freedom. In general, the vibrational energy level decreases with increase in the energy whereas, the density of the state increases with increase in the vibrational energy [36]. The transition in energy is depicted by considering only the electronic states of the energy levels, excluding the rotational and vibrational energy levels.

The electrons in the outermost orbital in organic molecules absorb a photon and move into the first excited state ( $SL_1$ ). The Franck-Condon factor decides the relative intensities of the vibronic transitions in this manifold [32]. The typical life of this state ( $SL_1$ ) is in the range of 1–10 fs. Depending on the nature of the material, the  $SL_1$  excited state leads to a rapid transition back to the  $SL_0$  state either by fluorescence or non-radiative transition.



**Figure 1.3: Jablonski energy level diagram**

There is a small probability of transition from the excited singlet state to the excited triplet state through an intersystem-crossing of the excitons [37]. This is a weak process and utilizes about 10 ps for the transition. From the excited triplet state, the exciton energy can be released either through phosphorescence or non-radiative process. In general, there are two types of electronic processes that occur when a luminescent molecule is hit by external energy; they result in a singlet or triplet state, which is discussed in the following section.

### 1.1.5 Singlet and triplet states

The difference between spins of the ground singlet, excited singlet and excited triplet states of unpaired electrons are schematically illustrated in Figure 1.4. When a molecule is hit by an optical or electrical energy, an electron in the ground state ( $SL_0$ ) is promoted to an excited state resulting in two unpaired electrons with one electron in the LUMO and the other remaining in the HOMO level, with each electron bearing a spin of  $1/2$ . Hence, an electron can have a spin quantum number of either  $+1/2$  or  $-1/2$ .

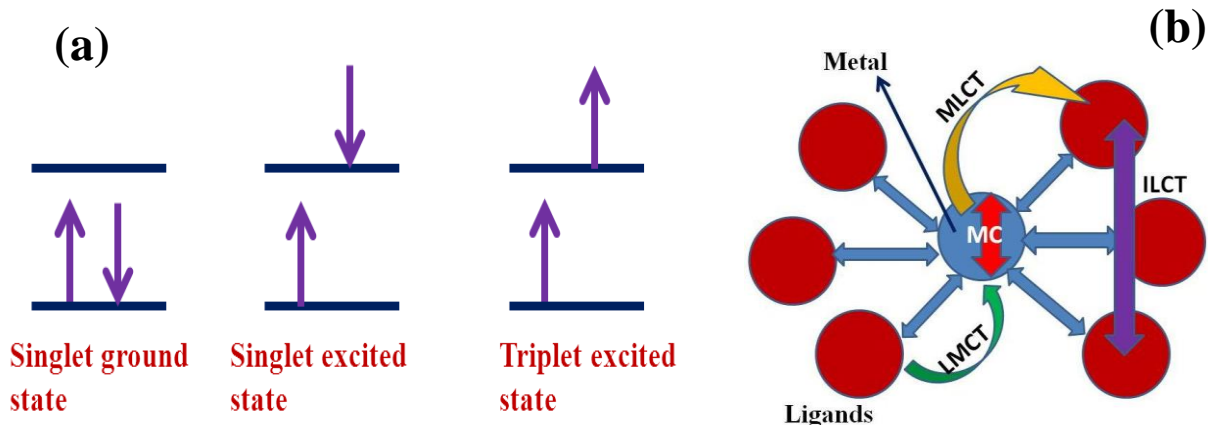


Figure 1.4: Schematic illustrations of singlet and triplet states (a) and four type of electronic transitions (b).

The total spin ( $S$ ) value of these two unpaired electrons can be either  $S=1$  or  $S=0$  according to quantum mechanical selection rules. The  $S=0$  state is called as singlet state, where the spin is antisymmetric during the exchange of electrons. The spin state is defined by:

$$\sigma_- = \frac{1}{\sqrt{2}} \{ \uparrow\downarrow - \downarrow\uparrow \} \text{ ----- (1.1)}$$

The  $S=1$  state is called as triplet state, which has a spin that is symmetric during the exchange of particles. The three possible spin states are:

$$\sigma_+ = \frac{1}{\sqrt{2}} \{ \uparrow\downarrow + \downarrow\uparrow \} \text{ ----- (1.2)}$$

$$\sigma_+ = \uparrow\uparrow \text{ ----- (1.3)}$$

$$\sigma_+ = \downarrow\downarrow \text{ ----- (1.4)}$$

where the symbols  $\uparrow$  and  $\downarrow$  denote the possible spin states of each electron [38].

To achieve highly-efficient electroluminescent devices, some factors are crucial such as the photophysical properties of active materials, electrochemical band gap and energy level alignment to adjacent layers [39]. The photophysical properties of luminescent materials can be described by the process of charge transfer.



### 1.1.6 Charge transition in organic semiconductors

The study of charge transition in luminescent materials is very important to design a new luminescent material for an OLED emitting a specific colour. Four types of electronic transitions or electronic states are commonly possible in organometallic complexes (Figure 1.4 (b)), as described below:

i) Metal-centered (MC) transition: The d orbitals of a metal are split upon ligand coordination. The excited d-d states arise from the promotion of electrons in the d orbitals, which are basically confined to the metal centre.

ii) Metal-to-ligand charge transfer (MLCT): An electron is promoted from the d orbital of a metal to a vacant  $\pi^*$  orbital in the ligand system.

iii) Intraligand charge transition (ILCT): An electron is promoted from a  $\pi$ -bonding or n-bonding orbital to a higher energy  $\pi^*$ -antibonding orbital.

(iv) Ligand-to-metal charge transfer (LMCT): An electronic charge is transferred from the ligand  $\pi$ -system to a metal d-centered orbital.

These transitions provide extensive photophysical properties to design new luminescent metal complexes with predetermined luminescent features.

## 1.2 Organic light emitting materials and devices

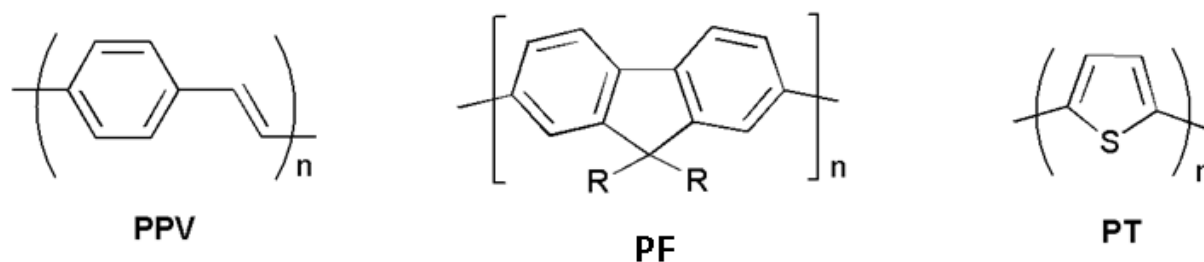
### 1.2.1 OLED materials

Organic light emitting materials have a crucial role in deciding the performance of OLEDs in terms of luminescent colour, external potential and lifetime of the device [40, 42]. A good electroluminescent material should have two significant properties: it should efficiently transport charge carriers (electrons and holes) and have a good emissive layer (EML). OLEDs are typically classified into two types based on the nature of the EML, namely polymeric light emitting diode (PLED) and small-molecule OLED (SMOLED). The EML of a PLED is made of electroluminescent conjugated conducting polymers; the polymer consists of a chain of repeating

structural units and the size of the polymer is determined by an average of the molecular weights of monomer units. In the case of SMOLED, the small molecules are composed of a fixed number of atoms; they have a molecular weight less than 1000 amu with a well-defined structure. The EML of SMOLED is governed by either fluorescent or phosphorescent organic small molecules [43, 44]. The main difference between PLED and SMOLED is that the PLED is prepared by solution processing whereas the SMOLED is fabricated by vacuum deposition process.

#### **1.2.1.1 Polymeric LED**

The solution processing method is a simple technique to synthesize lighting and display devices (with large area) at a low cost [45, 46]. On the laboratory scale, polymer films are prepared by simple wet chemical methods such as spin coating and dip coating. However, for fabricating films with large area, either the Langmuir-Blodgett or inkjet printing process is required. The solution process-based PLED is fabricated with a very thin layer of semiconducting polymer material sandwiched between two charge injection electrodes, wherein the polymer is used as an emissive material. The typical PLED is fabricated using a glass substrate partially coated with a transparent electrode that is used as the anode and holes are inserted into the EML [47, 48]. A semiconducting thin luminescent polymer film with thickness typically in the range of 30–100 nm is coated over the anode. Eventually, the PLED is completed by depositing a low-work function (WF) metal cathode. The conjugated polymer-based efficient PLED was reported by R. H. Friend and co-workers in 1990, in which poly(p-phenylene vinylene) (PPV) was used as an emissive material [49]. PPV is a highly-stable conjugated CP and is a reasonable donor of electrons. It can be easily chemical-doped with a strong acid or oxidizing agent. The measured conductivity of p-doped PPV is up to  $10^4$  S/cm [50]. PPV and its derivatives emit yellow colour because their absorption band is centered in the range of 400–420 nm.



**Figure 1.5: Molecular structures of light emitting polymers including PPV, PF and PT**

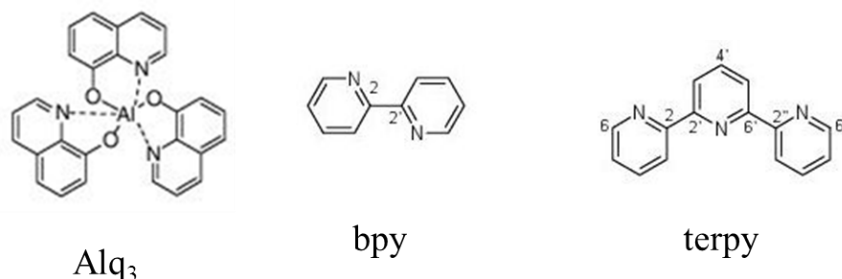
Polyfluorene (PF) is another type of strong violet fluorescent aromatic compound. It is well known for its extremely conjugated planar  $\pi$ -electron structure. Nowadays, polythiophene (PT) and its derivatives are employed as the most important classes of linear conjugated conducting polymers for preparing PLEDs. Figure 1.5 shows the molecular structures of some important light emitting polymers such as PPV, PF and PT. Over the past two decades, significant work has been done to demonstrate the commercial applications of PLEDs in solid state lighting and display.

### 1.2.1.2 Organic small molecule materials

Electroluminescence (EL) of organic semiconductors was first reported by Pope in 1963 [51]. They observed an emission from a single crystal of anthracene about a few tens of micrometers in thickness. Subsequent to the first report of efficient OLEDs by Tang and Van Slyke in 1987 [52], much work has been done to develop OLEDs. They used tris-(8-hydroxyquinoline) aluminum ( $\text{Alq}_3$ ) as an electron-transporting and electroluminescent (EL) material; it is widely employed as an electron-transporting material (ETM) and EL material in SMOLEDs. It is a fluorescent dye ( $\lambda_{\text{max}} = 519 \text{ nm}$ ) emitting green colour and can be used as an ETM or host for other bluish-green–red fluorescent dyes in OLEDs. Due to the ease in its preparation and formation of uniform thin films through vacuum deposition, it is the most-preferred electroluminescent material till date. It also has good thermal stability with a glass transition temperature ( $T_g$ ) of about  $170 \text{ }^\circ\text{C}$ . However, it has an electron mobility ( $10^{-6}$ – $10^{-7} \text{ cm}^2/\text{V}\cdot\text{s}$ ) that is one–two orders lower than that of the most-commonly used hole-transporting small molecules such as N,N'-Bis(3-methylphenyl)-N,N'-diphenylbenzidine (TPD) and N,N'-Di(1-naphthyl)-

N,N'-diphenyl-(1,1'-biphenyl)-4,4'-diamine (NPB). TPD and NPB have a hole mobility in the range of  $1 \times 10^{-3} \text{ cm}^2/\text{V}\cdot\text{s}$  [53, 54]. Alq<sub>3</sub> has the limitation of fluorescence quenches and traps for charges as well. Eventually, the long-term performance of the device gradually deteriorated.

Several researchers tested and reported alternative materials to Alq<sub>3</sub> including metal quinolates, oxazoles, oxadiazoles, pyridyl compounds, thiazoles, imidazoles, oligophenylenes and phenanthrolines [55–60]. Among these, the phenanthroline derivatives, bathophenanthroline (BPhen) and bathocuproine (BCP) have been extensively studied due to their high mobility and deep HOMO levels compared to that of Alq<sub>3</sub>, which make them excellent hole blockers in OLED applications [61, 62]. Xu-Hui Zhu *et al.* reported that phenanthroline derivatives give higher performance in terms of their device-structure compared to Alq<sub>3</sub>; devices based on phenanthroline derivatives give a reduction in the operating voltage and increase in power efficiency compared to Alq<sub>3</sub>-based devices [63–65].



**Figure 1.6: Chemical structure of Alq<sub>3</sub>, bpy and terpy**

### 1.2.1.3 Oligopyridines

Oligopyridines gained a special interest in coordination chemistry due to their attractive photophysical and electrochemical properties for fluorescence-based applications. Figure 1.6 illustrates the chemical structure of the oligopyridines having nitrogen ligands. The widely used bidentate pyridine ligand was the 2,2'-bipyridine (bpy). However, due to its photophysical and thermal properties limitation, tridentate pyridine ligands such as 2,2':6',2''-terpyridine (terpy) are used more in coordination chemistry. The synthesis of terpy was first reported by Burstall and Morgan in 1932 [66, 67]. It is widely used with various metals, as a suitable ligand to prepare complexes. The 2,2':6',2''-terpyridine and its derivatives are extensively studied as outstanding

complex agents for a wide range of transition metal ions. Moreover, the kinetics and mechanisms of metal complexes and their stability have been studied by various research groups. The multitude of potential applications is the result of tremendous advances in the design of terpy derivatives. The crucial characteristic features of terpy-based metal complexes, such as good reversible redox process and photophysical properties, depend on the electronic influence of the substituents. Terpy-based complexes are widely used as luminescent materials, in photochemistry and as sensitizers in light-to-electricity conversion.

#### **1.2.1.3.1 Metal complexes**

Terpy ligands-based transition complexes are interesting for fluorescence- and solar cell-applications due to the high oxidation state and attractive photophysical properties of transition metals such as Ru(II and III), Os(II), Ir (III), Pt(II) and Zn(II). The derivatives of terpy ligands have been prepared and applied in enantioselective reactions with transition metals [68]. Moreover, the insertion of one substituent at the 4'-position of the terpy does not create any enantiomeric complexes. Hence, the functionalization of terpy at 4'-position is of particular importance. Terpy can easily form many stable complexes with a variety of transition metal ions, which are useful in catalysis, molecular electronics and supramolecular chemistry. Among the N-heterocyclic ligands, the 2,2':6',2''-terpyridines have very high binding affinity towards transition metal ions because of their chelate effect [69, 70]. The complexation of one or two terpy ligands leads to a stable metal complex; it can form bis-complexes as well. Metal complexes have octahedral coordination geometries and possess distinct electrochemical, photophysical, magnetic and thermal properties.

#### **1.2.1.3.2 Zn(II) metal complexes**

Small organic molecules, including coordination compounds, are widely employed to fabricate OLEDs either by spin-coating or vacuum deposition methods. Due to their reasonable flexibility and high stability in design structure and modification, rare-earth and luminescent transition metal complexes have gained more attention for application in OLEDs [71]. Pyridyl compounds have nitrogen atoms that serve as manifold interaction to form stable coordination complexes with several metals. Among the well-studied materials composed of bpy and transition metals,

$\text{Ru}(\text{bpy})_3^{2+}$  is a popular for luminescent applications. Nowadays, with the rapid growth of supramolecular chemistry, the focus is on terpy ligand offers more synthetic and structural advantages than the bpy.

A novel Zn(II)-based terpy complex was synthesised by Accorsi *et al.* and studied for applications in OLEDs [72]. Zn(II) belongs to the group 12 metal (II) containing a  $d^{10}$  closed-shell electronic configuration. Because of the high ionization potential of closed-shell metal (38 eV for Cd(II) and 40 eV for Zn(II)), any state involving excitation of the d electron should have high energy. Therefore, d–d transitions are usually absent in group 12 metal-based complexes. Thus, the lowest-energy excited states in the group 12 metal complexes are predominantly composed of ILCT states alone [73]. For terpy-based Zn(II) metal complexes, the Zn (II)–terpyridine MLCT can be omitted and the observed behaviour should rise from an ILCT state [74–76].

#### **1.2.1.3.3 Ru(III) metal complexes**

During the search for new materials, it was found that novel inorganic–organic hybrid structures based on metal complexes, which have garnered much interest over the last two decades. Now, there is a strong focus on terpy and octahedral bis-terpy metal complexes that offer the advantage of increased symmetry; in the case of Ru(II) or Ru(III) complexation, there is an arrival to a directed complexation process.

There is great complexity in the different oxidation states of ruthenium ions, including Ru(II), Ru(III), and Ru(IV) states as ruthenium complexes undergo reversible redox process. Recently, Ru(II) and Ru(III) complexes with pyridine-based ligands, such as bpy, phenanthroline, and terpy, have attracted attention for their role in enhancing the efficiency of OLED. Zhu *et al.* have designed and synthesised a novel phosphorescent Ru(II) based-organometallic complexes with peripheral carbazole substituents and found enhanced luminescence efficiency of the devices [77]. Ru complexes usually exhibit both MLCT and ILCT band transition. Terpy has been known for its wide range of applications in supramolecular chemistry, which leads to the formation of racks, grids, knots and dendrimers. Due to the good electrochemical and photophysical properties of Ru-based metal complexes, these systems have been extensively

studied for optoelectronic applications. Particularly, the photophysical and electrochemical behaviours of  $[\text{Ru}(\text{bpy})_3]^{2+}$  metal complexes have been widely studied and have attracted interest for further development.

As discussed in the earlier section (1.1.3), small molecules are classified into two types as fluorescent and phosphorescent emitters. Among fluorescent molecules, the most studied fluorescent emitter is  $\text{Alq}_3$  because of the ease in its synthesis and processing. It has been a good green fluorescent emitter till date. But the quantum efficiency (QE) of such a fluorescent molecule-based SMOLED is limited by spin statistics to just about 25%, which is certainly not sufficient to meet commercial standards. Therefore, new fluorescent materials with high QE are needed. In general, the establishment of singlet and triplet excitons through electrical excitation has the statistical ratio of about 1:3. Therefore, fluorescence through electrical excitation is an ineffective transition since it uses a maximum of 25% of the electrically-generated excited states. However in triplet transition, 75% of the excitons are involved in the EL process through phosphorescence; here, the transition occurs through spin-orbit coupling. Typically, the spin-orbit coupling of organic molecules is very weak. Nevertheless, the spin-orbit coupling can be significantly enhanced by introducing heavy metal atoms (such as Platinum (Pt), Osmium (Os) and Iridium (Ir)) into the molecule. The highly-efficient green-colour emitter belongs to a class of phosphorescent materials that are based on Ir organometallic complexes.

### **1.2.2 OLED device structure**

The light-emitting active layer is based on a luminescent material, typically a polymer or fluorescent/phosphorescent molecules. Nowadays, both polymers and small molecules are employed to fabricate OLEDs. These devices are expected to take over flat panel displays and solid state lighting applications in the near future. An OLED structure generally consists of multiple layers, with each layer having its distinct function. Figure 1.7 shows the schematic diagram of an OLED structure: it starts with indium tin oxide (ITO) followed by a hole transport layer (HTL), emission layer (EML), electron transport layer (ETL) and metal cathode.

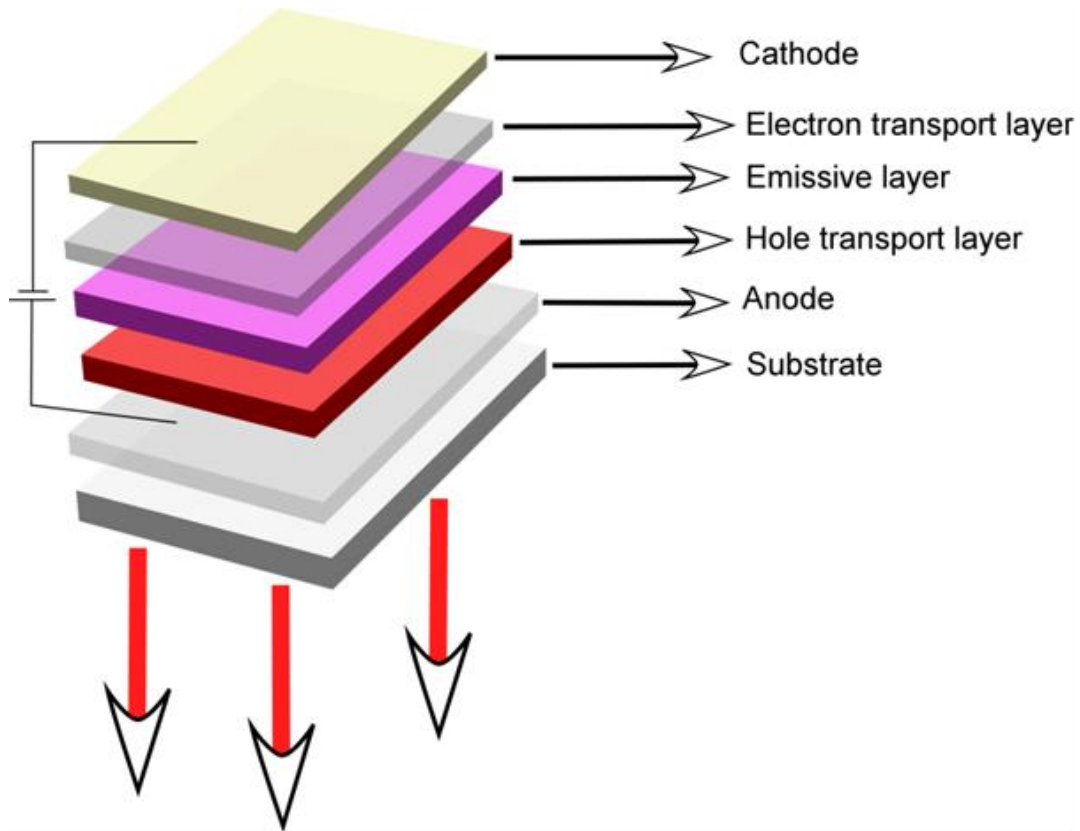


Figure 1.7: A typical stack layout of multilayered OLED consisting of a HTL, ETL and EML

### 1.2.2.1 OLED operation mechanism

The principle behind the operation of a simple bi-layered OLED structure is shown in Figure 1.8. When a forward bias is applied, charge carriers (holes and electrons) are injected from the anode and cathode respectively. These charge carriers drift under the influence of the external field. They meet at the emissive layer and recombine to form excitons. The radiative relaxation of these excitons generates photons, which exit from the transparent electrode side of the OLEDs. Organic light emitting diodes are usually classified into three types according to the direction of light extraction: (i) top-emitting OLEDs, in which light exits from the semi-transparent cathode side; (ii) bottom-emitting OLEDs, in which light exits from the transparent conducting thin film (TCF) electrode of the device (here, the metal cathode is made with an opaque material to enhance the light out coupling efficiency); (iii) OLEDs made with transparent or semi-



transparent electrodes, which are being developed for specific applications such as head-up displays and smart windows.

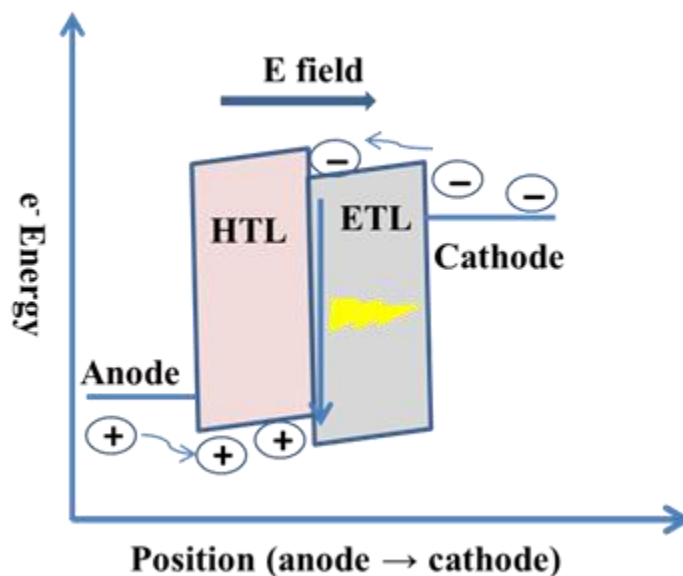
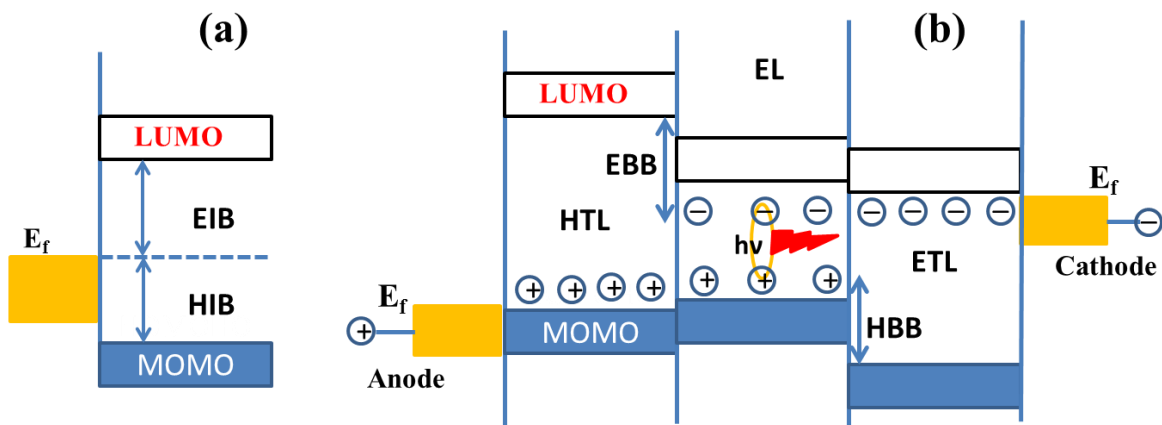


Figure 1.8: Operation mechanism of two layered OLEDs structure.

### 1.2.2.2 Energy level alignment and interfacial structure in OLEDs

The functions and efficiency of organic electronic devices such as OLEDs, organic photovoltaic cells (OPVCs) and organic thin film transistors (OTFTs) mainly depend on the electronic structure of interfaces. During the operation, a forward bias is applied to OTFTs and OLEDs such that the cathode has a negative charge with respect to the anode. Hence, the charge carriers are injected from the electrode into the organic semiconductor layers. To attain a low operational voltage, the energy barriers between consecutive layers should be minimal to enable ease of charge injection and transportation. The change in potential well and electronic states at the interfaces between metals and organic solids are discussed below.



**Figure 1.9: Energy level diagrams of organic semiconductors at interfaces: (a) Organic semiconductor interface with HIB and EIB, (b) Multi-hetero layer stack of OLED containing HTL, ETL and EML with electron-blocking barrier (EBB) and hole-block**

When a metal and an organic solid are far from each other, their energy levels are associated to their vacuum levels (VL) because an electron is at rest for the infinite distance. However, when they come into contact, the organic layer is now in the potential of the surface dipole of the metal electrode. Hence, the energy levels are elevated so that they have a common VL in an extremely narrow interfacial gap. Therefore, multiple layers are used in OLEDs to separate the region of charge injection and transportation from the region of exciton formation and recombination. The proper adjustment of energy levels among the interfaces of organic heterojunction is a very important parameter that is necessary to ease the transport of a hole (electron) across the interface while simultaneously blocking an electron (hole). Figure 1.9 reveals the various electronic energy levels and energy parameters of organic solid–metal interfaces. In general, the relative energy positions of the electrode fermi level ( $E_f$ ), HOMO and LUMO energy levels are used to characterize interface energetics. They predominantly govern the transport of charges and formation of excitons. The HOMO and LUMO are the frontier molecular orbitals (FMOs) of organic conjugated fragments. The hole injection barrier (HIB) and electron injection barrier (EIB) are typically measured by inverse photoelectron spectroscopy (IPES) and ultraviolet photoelectron spectroscopy (UPS), which are the most common methods used to study the electronic properties of interfaces in semiconductor devices.

### 1.2.2.3 Interface engineering for OLED improvement

Of late, OLEDs have become increasingly popular as new display technology, but there is still a need to improve their stability and efficiency. The important features of OLEDs are charge carrier injection, transportation and charge carrier balancing on consecutive layers. This behaviour of OLED plays a vital role in the optimisation of device efficiency as it has great influence on the charge carriers (electron or hole) balance in the device. In general, an ohmic contact is chosen at the electrode/organic interface for easy carrier injection. Energy barriers exist at the organic/electrode interfaces, as a result of low power efficiencies and require high operating voltages. Hence, an electron injection layer requires enhancing the electron injection from cathode to ETL. The electron injection has been extensively studied for a variety of electron transport materials and metallic electrodes [78–80]. Shaheen *et al.* studied the insertion of thin layer of LiF between Al cathode and ETL to enhance the electron injection [81]. The enhanced injection was attributed to band-bending process, and eventually matches the interface layers by lowering the energy barrier. LiF, Al<sub>2</sub>O<sub>3</sub> and MgO are commonly used as electron injection layer material in OLEDs [82].

Like electron injection layer, the hole injection layer also enhances the hole injection from anode to HTL. At the anode/organic interface, inserting a thin film of copper phthalocyanine (CuPc) was found to improve the efficiency and life-times of the devices [83–84]. The HOMO of CuPc was found suitable for the WF of ITO and organic HTL. The typically used HTL are PEDOT:PSS and NPB in OLEDs. WO<sub>3</sub>, MoO<sub>3</sub> and surface treatments, such as UV-Ozone, and oxygen-plasma enhance hole injection owing to reduced energy barrier. Therefore, there is a VL shift and an intermediate energy level is rendered by the additional layer [85].

There are three consecutive processes to determine the light emission in an OLED.

i) Interfacial process:

The performance and lifetime of OLEDs are critically dependent on the properties of both interface and active materials. In OLEDs, metal electrodes are utilised to inject charge into organic semiconductor layers. Thus, control over the interface between inorganic electrode and organic semiconductor is essential. The study of energy barriers at the interface of

organic layers and electrodes is important phenomenon to enhance charge transportation. Understanding of this process at the interface is necessary for efficient injection of electrons and holes from cathode and anode, respectively. Effective electrons and hole injection enable achieve significant progress in the performance of OLEDs.

ii) Electrical process:

The electrical process of OLED is determined by the mobility of charge carriers, such as electrons and holes. In general, the mobility of the hole is higher than that of the electron. Therefore, the transportation properties of charge carriers are very important at heterojunction. Efficient OLED requires balancing charge injection and transportation. The adjustment of the interface between the electrodes and organic semiconductor is vital to improve charge-injection, transport, and recombination in OLED performances.

iii) Optical process:

The injected holes and electrons drift under the influence of the external electric field. They meet at the recombination region, where excitons are formed. These excitons generate the photons. Light output and efficiency of OLED are mainly dependent on the balanced injection of charge carriers, which can be achieved by either charge injection facility or charge confinement for the bipolar recombination process. Balanced charge injection needs the anode and cathode WF to match with the HOMO and LUMO energy levels of the HTL and ETL/light-emitting layers, respectively. Hence, one can conclude that optimising three electronic processes, (i) charge injection, (ii) transport, and (iii) recombination will improve the OLED performance.

#### **1.2.2.4 Charge balancing**

To achieve charge balance, the following three consecutive steps are necessary in OLEDs.

i) Injection of charge carriers

ii) Transportation of charge carriers

### iii) Radiative recombination process

The injection of charge carriers helps tunnel the barrier easily at the interface of electrodes and organic layers for optoelectronic devices to enhance the performance of devices. In carrier injection process, high light emission efficiency can be achieved through reducing the interfacial energy barriers between organic thin film layers and metal electrodes. It may also be controlling the electron and hole injection. Electrons are injected from low WF metal cathode into LUMO of the consecutive organic layer. While holes are injected from high WF of TCF electrode into HOMO of the consecutive organic layer, generally, low-work function metals including Al and Ca are often used as cathode materials [86–88], which have better energy matches with consecutive layers. However, such materials are very sensitive to environmental conditions, and degrade easily on exposure to air. To overcome such a situation, the devices are encapsulated prior to use [89].

The injection of charges is required to tunnel the barrier at the interface of electrodes and organic layers. Holes and electrons are injected from the anode and cathode into organic layer via HOMO and LUMO, respectively. Anodes usually have the WF of 4.5 to 5 eV, whereas the cathodes have it at 2.7 to 3 eV. For easy injection of holes it would be advantageous if the HOMO energy level matches with the work function of the anode and for electron injection the LUMO energy level should match with the WF of the cathode.

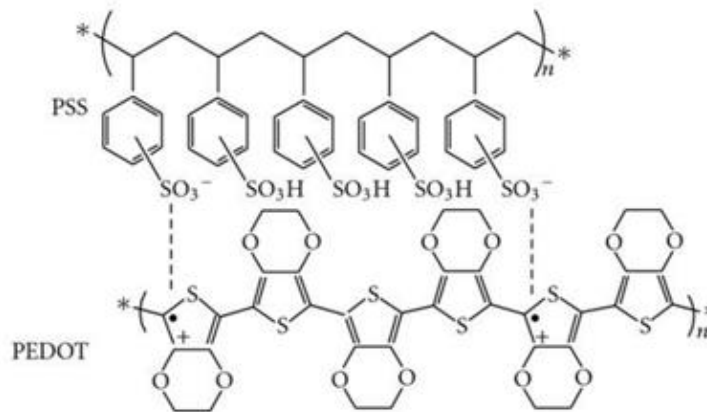
#### **1.2.2.5 Carrier transport and recombination in OLEDs**

The injected charge carriers are transported into the recombination zone as follows: The recombination zone always needs to be away from the electrodes to avoid non-radiative decay owing to quenching near the electrodes. Thus, it usually should be near the centre from the electrodes in OLED devices. The exact position of the recombination zone can be identified by charge carriers through drift diffusion. The charge balance can be bothered by differences in charge mobilities and privileged charge injection of one charge carrier over the other because the hole mobility is greater than that of electron mobility. Therefore, in typical hetero-junction OLEDs, hole injection barrier is slightly lower than that of electron injection barrier. Hence, there is a need to improve electron injection efficiency transportability [90]. Efficient OLEDs

require the effective recombination of equal number of electrons and hole mobility [91]. When two different charge carriers, such as electrons and holes are separated by a potential barrier, one can move to the other through tunneling barrier or it moved over the barrier via an activated state. This process is called hopping [92]. The energy state is involved in the hopping transport of holes and electrons from narrow bands around the HOMO and LUMO energy levels, respectively. When two charge carriers, such as electrons and holes are in the proximity of ETL and HTL interfaces they recombine to form exciton states, eventually emitting light due to decay of energy as radiate recombination [93].

### **1.2.3 Transparent conducting thin film anode**

The transparent conducting material, which serves as an anode in optoelectronic devices, should be optically transparent and electrically conducting. The material used for the anode is typically a high WF material. It is one of the significant components in optoelectronic devices including OLEDs, photovoltaic cells (PVCs), liquid crystal displays (LCDs) and sensors. The commonly used material for TCFs is Sn-doped ITO ( $\text{In}_2\text{O}_3$ ) because of its prominent properties such as high conductivity and more transparency on glass or plastic substrates. Nevertheless, indium is expensive due to its scarcity and ITO is prone to conductivity failure on account of crack generation when subjected to tensile or compressive bending [94, 95]. To overcome these problems, extensive research is being carried out on materials as alternatives to ITO. The commonly used alternative materials include conducting polymers (CPs), transparent conductive oxides (TCOs), carbon nanotubes (CNTs), and graphene and metal nanowires [96, 97]. Among these, a class of CPs called poly (3,4-ethyldioxythiophene) (PEDOT) doped with poly (styrenesulfonic acid) (PSS) has gained more attention due to its distinguishable advantages such as high transparency, high conductivity, environmental friendliness and ability to be processed by wet chemical methods.



**Figure 1.10: Chemical structure of PEDOT:PSS.**

Figure 1.10 shows the chemical structure of PEDOT:PSS; the top structure is PEDOT and the lower structure is PSS. In general, PEDOT is hydrophobic in nature; hence, it cannot be processed in water. In comparison, PEDOT:PSS contains the hydrophilic PSS. Therefore, it can be easily processed through diverse preparation methods such as spin coating, spray coating, drop coating and ink-printing techniques. It has a conductivity ranging from 400–600 S/cm while retaining a transparency of about 80% of the visible light [98]. To enhance the conductivity of TCFs based on PEDOT:PSS, organic solvents such as salts, surfactants, zwitterions and acids can be used (polar solvent vapour annealing methods); they increase the conductivity to around 1000 S/cm. An addition of ionic liquids to PEDOT:PSS can further increase the conductivity value to over 2500 S/cm. The conductivity can be extended to over 4000 S/cm by post-solvent treatment with sulfuric acid ( $\text{H}_2\text{SO}_4$ ) solution and it is comparable to that of commercial ITOs.

The origin and mechanism of the conductivity enhancement of PEDOT:PSS is still unclear. Two mechanisms are believed to be involved: one is the elimination of insulating PSS materials from PEDOT, which leads to an exposure of the conducting PEDOT layer; the other is the change in the conformation and morphology of PEDOT:PSS. Efforts to discover the exact mechanism are required; this will serve as a guide for future research on further conductivity enhancement and more practical applications of PEDOT:PSS.

### 1.3 Gap in the existing research

OLEDs are an emerging technology for both lighting and flat-panel display appliances owing to their distinctive advantages, which include low power consumption, ultra-thin thickness, high brightness, and wide-viewing angle. Considerable work is going on both in academic institutions and research laboratories on the synthesis and performance of electroluminescent materials for OLEDs. There are many reports on the development of full-colour white-emitting organic light emitting diodes (WOLEDs) flat-panel displays using organic and inorganic materials [99–101]. Efforts are on to develop flat-panel display technology. However, they have not yielded the desired results for the current requirement. So, further efforts are to be made to develop economically affordable and potentially applicable devices for various optoelectronic applications.

Considerable research work on WOLEDs is being carried out by all developed countries like the European countries, USA, China, Japan, and South Korea [102–105]. Center for Wafer Technology and Smart Systems, and Imec works on flexible electronics and OLED displays have developed AMOLED display on flexible substrates [106]. WOLEDs have also been widely investigated as the next-generation solid-state lighting and flat-panel display applications. The most important development in WOLED is establishing a set of red, green and blue emissions or equal mixing of orange and green emitters with colour purity, high efficiency, and stability. The versatility of OLEDs is being explored to take the technology to the next level and requires improvements in both performance and environmental stability. Blue-emitting organic materials are important for solid-state lighting applications. However, their availability is still scarce compared to that of green- and red-emitting materials because of their intrinsic wide band gap, and hence the difficulty in preparing them. Therefore, the synthesis and characterization of deep green and orange fluorescent materials are some of the challenges faced by researchers. In general, OLEDs are made of TCF anode. ITO is the most commonly used TCF anode for OLEDs as it has high transparency, high work function, and ease of processability. However, it has some limitation, such as high cost due to it being rare on the earth and consequent scarcity. Nevertheless, it is not an ideal choice for flexible optoelectronic devices. Thus, a great deal of interest has been devoted to find replacement for ITO. Moreover, of the total cost of the



optoelectronic devices, large amount is spent on the preparation of TCF electrode. The fabrication of high-performance TCF with good conductivity and high transparency is the other challenge for the researchers. Hence, TCF enjoys a unique position in opto-electronic applications. This research field has great significance and is promising technology for academic institutions and for industrial applications.

#### 1.4 Objective

The fabrication of full-colour flat panel displays is mainly linked to the commercialization of highly-efficient emitters in the red, green and blue regions. Since 1987, numerous reports are available related to the fabrication of red- and green-based OLEDs. However, the efficiency of blue OLEDs requires further improvement. Low power consuming optoelectronic devices including OLEDs will be the thriving technologies in the near future for solid state lighting and display applications. Many OLED devices are currently available in the market but they are very expensive for the users. The motivation for this research work is making the devices inexpensive. The two possible ways to achieve a reduction in cost are: preparation of materials with low cost and utilization of prepared TCF instead of commercial (costly) ITO electrodes. Based on the overall research objective, the specific targets are:

- (i) To synthesis and study the photophysical and electrochemical properties of 4'-ary substituted 2,2':6',2''-terpyridine derivatives as deep blue fluorescent materials.
- (ii) To study the geometrical optimization and the photophysical, electrochemical and thermal properties of 4'-aryl substituted 2,2':2'',6'-terpyridine based Zn(II) metal complexes needed for blue fluorescent OLEDs; to address the aggregation-induced emission enhancement of these materials.
- (iii) To study the photophysical, electrochemical and thermal properties of orange emitters based on Ru(III) complexes. Many reports are available on 2,2':2'',6'-terpyridine substituted Ru(II) metal complexes and it has been observed that the life time of the fluorophore is in the range of a few microseconds. However, the 4'-aryl substituted 2,2':2'',6'-terpyridine based Ru(III) metal complexes exhibit a life time of a fraction of nano seconds. Systematic studies on these derivatives are required.

- (iv) To fabricate low-cost TCFs for application in optoelectronic devices such as OPVCs, OLEDs and sensors.
- (v) To fabricate bilayer OLEDs using the prepared TCFs and study the performance of these devices.

## 1.5 Thesis outline

*Chapter 1* summarizes the significance of organic semiconductors and their solid-state lighting and flat-panel display applications and also provides a review of the current literature. Further, the mechanism and device structure of organic light-emitting diodes are also discussed. The motivation, gaps in the existing research, and objectives of the work are also discussed at the end of the chapter.

*Chapter 2* provides an overview of the experimental methods and concepts of characterization techniques, which are used to analyse the structural, photophysical, electrochemical and thermal properties of the materials. The preparation and characterization of TCF for optoelectronic devices have also been described. In addition, the choice of materials and fabrication process of OLEDs are also covered. Electroluminescence and electrical properties of OLED are also analysed.

*Chapter 3* discusses the synthesis and characterization of three 4'-aryl substituted 2,2':6',2''-terpyridine derivatives in a single pot reaction. The photophysical, electrochemical, thermal and morphological properties of the synthesised material have also been studied and discussed in detail.

*Chapter 4* explores the synthesis, photophysical, thermal and electrochemical properties of three novel blue-to-green fluorescent Zn(II)-based terpy complexes ( $Zn(L_1-L_3)$ ). The charge transition has been investigated as the potential charge transfer to the  $n-\pi^*$  and  $\pi-\pi^*$  states of the ILCT in the complexes are analysed. The geometry, optimization and electronic structure of these complexes were assessed by density functional theory (DFT). Dual characteristics of the optical behaviour have been observed, such as Zn(II) complexes exhibiting a deep blue-to-green fluorescence in crystalline form, while it is sky-to-deep blue in dimethylsulfoxide (DMSO). The photophysical properties revealed the potential charge transfer to  $\pi-\pi^*$  and  $n-\pi^*$  states due to ILCT.

*Chapter 5* addresses another interesting and noteworthy class of metal complexes as a series of three novel 4'-aryl substituted orange-fluorescent Ru(III)-based terpy complexes. Photophysical studies describe that the luminescence of these complexes is due to electronic transition between the energy levels of singly unoccupied molecular orbitals (SUMO) and singly occupied molecular orbitals (SOMO). In addition, DFT calculations were carried out to study the electron transfer between SUMO and SOMO energy levels. The heavy metal effect of Ru(III) ions and the photophysical characteristics in the presence of MLCT have also been studied.

*Chapter 6* covers the preparation and characterization of silver nanowires (AgNWs) for the fabrication of TCF anode for OLEDs. In addition, I discuss the preparation, optical and morphological studies of TCF based on AgNWs and PEDOT:PSS hybrid-composite. Fluorescent green OLEDs with PEDOT:PSS and Alq<sub>3</sub> as the hole transport-layer and electroluminescent-layer, respectively, were fabricated and characterised. Two types of green fluorescent OLEDs were prepared: (i) OLED made up of commercial ITO as an anode, and (ii) ITO-free OLED as AgNWs and PEDOT:PSS hybrid-composite thin film-based anode. Their luminescence intensity–wavelength and current density–voltage measurements were systematically studied and compared.

In *Chapter 7*, the complete work has been summarised and novel investigations reported. In this chapter, the conclusion of the work is presented as also the future scope of the work.

## **1.6 References**

- [1] Wagner R.S., Treuting R.G., *J. Appl. Phys.*, 1961, 32: 2490–2491.
- [2] Chiang C.K., Fincher C.R., Park Y.W., Heeger A.J., Shirakawa H., Louis E.J., Gau S.C., MacDiarmid A.G., *Phys. Rev. Lett.*, 1977, 39: 1098–1101.
- [3] Holmes A.B., Bradley D.D.C., Brown A.R., Burn P.L., Burroughes J.H., Friendt R.H., Greenham N.C., Gymer R.W., Halliday D.A., Jackson R.W., Kraft A., Martens J.H.F., Pichler K., Samuel I.D.W., *Synth. Met.*, 1993, 55: 4031–4040.
- [4] Spanggaard H., Krebs F.C., *Sol. Energy Mater. Sol. Cells.*, 2004, 83: 125–146.
- [5] Xian Y.D., *Int. J. Mol. Sci.*, 2011, 12: 1575–1594.

- [6] Nagai Y., Sasabe H., Takahashi J., Onuma N., Ito T., Ohisa S., Kido J., *J. Mater. Chem. C.*, 2017, 5: 527–530.
- [7] Ma H., Yip H-L., Huang F., Jen A.K.-Y., *Adv. Funct. Mater.*, 2010, 20: 1371–1388.
- [8] Crone B.K., Campbell I.H., Davids P.S., Smith D.L., Neef C.J., Ferraris J.P., *J. Appl. Phys.* 1999, 86: 5768–5774.
- [9] D’Andrade B.W., Forrest S.R., *Adv. Mater.*, 2004, 16: 1585–1595.
- [10] Ishii H., Sugiyama K., Ito E., Seki K., *Adv. Mater.*, 1999, 11: 605–625.
- [11] Tang F., Liu L., Alva L., Jia Y., Fang G., *Sol. Energ. Mat. Sol. Cells.*, 2017, 160: 1–6.
- [12] Reineke S., Lindner F., Schwartz G., Seidler N., Walzer K., Lussem B., Leo K., *Nature.*, 2009, 459: 234–238.
- [13] Jesuraj P.J., Jeganathan K., Navaneethan M., Hayakawa Y., *Synth. Met.*, 2016, 211: 155–160.
- [14] Clarke T.M., Durrant J.R., *Chem. Rev.*, 2010, 110: 6736–6767.
- [15] Zhang Y., Jiang H., Liu Y., Zhou K., Wang Y., Tan H., Su S., Zhu W., *Dalton Trans.*, 2016, 45: 14131–14140.
- [16] Aizawa N., Pu Y.-J., Watanabe M., Chiba T., Ideta K., Toyota N., Igarashi M., Suzuri Y., Sasabe H., Kido J., *Nat. Commun.*, 2014, 5: 5756. DOI: 10.1038/ncomms6756.
- [17] Aitken B.S., Wieruszewski P.M., Graham K.R., Reynolds J.R., Wagener K.B., *Macromolecules.*, 2012, 45: 705–712.
- [18] Jang J., Chang M., Yoon H., *Adv. Mater.*, 2005, 17: 1616–1620.
- [19] Skotheim T.A., Reynolds J.R., *Handbook of conducting polymers*. 3<sup>rd</sup> Ed. CRC Press: New York, 2007.

- [20] Pope M., Swenberg C.E., *Electronic Processes in Organic Crystals and Polymers.*, 2<sup>nd</sup> Ed., Oxford University Press, New York, 1999.
- [21] Freund M.S., Deore B.A., *Self-Doped Conducting Polymers*, John Wiley and Sons, Ltd, 2007.
- [22] Wang J., Liu K., Ma L., Zhan X., *Chem. Rev.*, 2016, 116: 14675–14725.
- [23] Gsanger M., Bialas D., Huang L., Stolte M., Würthner F., *Adv. Mater.*, 2016, 28: 3615–3645
- [24] Ostroverkhova O., *Chem. Rev. 2016*, 116: 13279–13412.
- [25] Lin Y., Fan H., Li Y., Zhan X., *Adv. Mater.*, 2012, 24: 3087–3106.
- [26] Sekine C., Tsubata Y., Yamada T., Kitano M., Doi S., *Sci. Technol. Adv. Mater*, 2014, 15: 034203, Doi:10.1088/1468-6996/15/3/034203.
- [27] Vohra V., Anzai T., *J. Nanomater.*, 2017, 2017: 1–18.
- [28] Salzmann I., Heimel G., Oehzelt M., Winkler S., Koch N., *Acc. Chem. Res.*, 2016, 49: 370–378.
- [29] Liu Z., Zhao X., Zhang X., Yan X., Wu Y., Chen Y., Tian J., *J. Phys. Chem. Lett.*, 2011, 2: 1972–1977.
- [30] Mann G., Baranano D., Hartwig J.F., Rheingold A.L., Guzei I.A., *J. Am. Chem. Soc.*, 1998, 120: 9205-9219.
- [31] Zhang P., Dou W., Ju Z., Yang L., Tang X., Liu W., Wu Y., *Org. Electron.*, 2013, 14: 915–925.
- [32] Fukui K., Yonezawa T., Shingu H., *J. Chem. Phys.*, 1952, 20: 722–725.
- [33] Du X., Qi J., Zhang Z., Ma D., Wang Z.Y., *Chem. Mater.*, 2012, 24: 2178–2185.

- [34] [https://www.iapp.de/organische-elektronik.de/en/?Basics\\_\\_\\_Doping](https://www.iapp.de/organische-elektronik.de/en/?Basics___Doping) (accessed on 1<sup>st</sup> February, 2017).
- [35] Krygowski T.M., Stepien B.T., *Chem. Rev.*, 2005, 105: 3482–3512.
- [36] Bajpai M., Srivastava R., Dhar R., R.S. Tiwari., *Indian J. Matet. Sci.*, 2016, 2016: 1–8.
- [37] Opitz A., *J. Phys. Condens. Matter.*, 2017, 29: 133001-133016.
- [38] Brutting W., *Physics of organic semiconductors*, Wiley-VCH, Berlin, 2005.
- [39] Kulkarni A.P., Tonzola C.J., Babel A., Jenekhe S.A., *Chem. Mater.*, 2004,16: 4556–4573.
- [40] Ho P.K.H., Kim J.S., Burroughes J.H., Becker H., Li S.F.Y., Brown T.M., Cacialli F., Friend R.H., *Nature*, 2000, 404: 481–484.
- [41] Akatsuka T., Roldán-Carmona C., Ortí E., Bolink H.J., *Adv. Mater.*, 2014, 26: 770–774.
- [42] White R.T., Thibau E.S., Lu Z.H., *Sci. Rep.*, 2016, 6: 21109.
- [43] Duan L., Qiao J., Sun Y., Qiu Y., *Adv.Mater.*, 2011, 23: 1137–1144.
- [44] Yu T., Liu L., Xie Z., Ma Y., *Sci. China Chem. June.*, 2015, 58: 907–915.
- [45] Aizawa N., Pu Y.J., Watanabe M., Chiba T., Ideta K., Toyota N., Igarashi M., Suzuri Y., Sasabe H., Kido J., *Nat. commun.*, 2014, 5: 5756.
- [46] Zhang M., Hofle S., Czolk J., Mertens A., Colsmann A., *Nanoscale*, 2015, 7: 20009–20014.
- [47] Hofle S., Bernhard C., Bruns M., Kubel C., Scherer T., Lemmer U., Colsmann A., *Appl. Mater. Interfaces*, 2015, 7: 8132–8137.
- [48] Chiba T., Pu Y.-J., Kido J., *Adv. Mater.*, 2015, 27: 4681–4687.
- [49] Burroughes J.H., Bradley D.D.C., Brown A.R., Marks R.N., Mackay K., Friend R.H., Burns P.L., Holmes A.B., *Nature*, 1990, 347: 539–541.

- [50] Friend R.H., Bradley D.D.C., Townsend P.D, *J. Phys. D: Appl. Phys.*, 1987, 20: 1367–1384.
- [51] Pope M., Kallmann H., Magnante P., *J. Chem. Phys.*, 1963, 38: 2042–2043.
- [52] Tang C.W., VanSlyke S.A., *Appl. Phys. Lett.*, 1987, 51: 913–915.
- [53] Lee T.H., Lai K.M., Leung L.M., *Polymer*, 2009, 50: 4602–4611.
- [54] Kathirgamanathan P., Surendrakumar S., Vanga R.R., Ravichandran S., Lara J.A., Ganeshamurugan S., Kumaravel M., Paramaswara G., Arkley V., *Org. Electron.*, 2011, 12: 666–676.
- [55] Tanaka D., Takeda T., Chiba T., Watanabe S., Kido J., *Chem. Lett.*, 2007, 36: 262–263.
- [56] Sasabe H., Chiba T., Su S.J, Pu Y.-J., Naayama K., Kido J., *Chem. Commun.*, 2008, 5821–5823.
- [57] Reinke S., Lindner F., Schwartz G., Seidler N., Walzer K., Lussem B., Leo K., *Nature*, 2009, 459: 234–238.
- [58] Ichikawa M., Hiramatsu N., Yokoyama N., Miki T., Narita S., Koyama T., Taniguchi Y., *Phys. Status Solidi RRL*, 2006, 1: 37–48.
- [59] Chen H.F., Yang S.J., Tsai Z.H., Hung W.Y., Wang T.C., Wong K.T., *J. Mater. Chem.*, 2009, 19: 8112–8118.
- [60] Li Y.-J., Sasabe H., Su S.-J, Tanaka D., Takeda T., Pu Y.-J., Kido J., *Chem. Lett.*, 2009, 38: 712–715.
- [61] Zeng L., Chen Y., Liu J., Huang H., Guan R., Ji L., Chao H., *Sci. Rep.*, 2016, 6: 19449.
- [62] Zhuang T., Su Z., Liu y., Chu B., Li W., Wang J, Jin F., Yan X., Zhao B., Zhang F., Fan D., *Appl. Phys. Lett.*, 2012, 100: 243902.
- [63] Wei X.-F., Tan W.-Y., Zou J.-H., Guo Q.-X., Gao D.-Y., Ma D.-G., Peng J., Cao Y., Zhu X.-H., *J. Mat. Chem. C.*, 2017, 5: 2329–2336.

- [64] Xiao L.X., Chen Z.J., Qu B., Luo J.X., Kong S., Gong Q.H., Kido J., *Adv. Mater.*, 2011, 23, 926–952.
- [65] Brauchli S.Y., Bozic-Weber B., Constable E.C., Hostettler N., Housecroft C.E., Zampese J., *RSC Adv.*, 2014, 4: 34801–34815.
- [66] Morgan G.T., Burstall F.H., *J. Chem. Soc.* 1932, 20–30.
- [67] Burstall F.H., *J. Chem. Soc.*, 1934, 1498–1500.
- [68] Chi Y., Chou P-T., *Chem. Soc. Rev.*, 2010, 39: 638–655.
- [69] Lehn J-M., *Supramolecular Chemistry, Concepts and Perspectives*, VCH, Weinheim, 1995.
- [70] Vogtle F., *Supramolecular Chemistry: An Introduction*, J. Wiley and Sons, 1993.
- [71] Slinker J., Bernards D., Houston P.L., Abruna H.D., Bernhard S., Malliaras G.G., *Chem. Commun.*, 2003, 19: 2392–2399.
- [72] Wang D., Xu Q-L, Zhang S., Li H-Y., Wang C-C., Li T-Y, Jing Y-M, Huang W., Zheng Y.X., Accorsi G., *Dalton Trans.*, 2013, 42: 2716–2723.
- [73] Kimachi S., Ikeda S., Miki H., Azumi T., Crosby G.A., *Coord. Chem. Rev.*, 1994, 132: 43–54.
- [74] Leroy S., Soujanya T., Fages F., *Tetrahedron Lett.*, 2001, 42: 1665–1672.
- [75] Ghedini M., Deda M.L., Aiello I., Grisolia A., *J. Chem. Soc., Dalton Trans.*, 2002, 17: 3406–3409.
- [76] Reichardt C., *Chem. Rev.*, 1994, 94: 2319–2358.
- [77] Zhu Y., Gu C., Tang S., Fei T., Gu X., Wang H, Wang Z., Wang F., Lu D., Ma Y., *J. Mater. Chem.*, 2009, 19: 3941–3949.



- [78] Burroughes J.H., Bradley D.D.C., Brown A.R., Marks R.N., Mackay K., Friend R.H., Burn P.L., Holmes A.B., *Nature*, 1990, 347: 539–541.
- [79] Chan M.Y., Lai S.L., Fung M.K., Lee C.S., Lee S.T., *J. Appl. Phys.*, 2004, 95: 5397.
- [80] Li Y., Fung M.K., Xie Z., Lee S., Hung L.S., Shi J., *Adv. Mater.*, 2002, 14: 1317–1321.
- [81] Shaheen S.E., Jabbour G.E., Morrell M.M., Kippelen K.Y., Peyghambarian N., Nabor M.-F., Schlaf R., Mash E.A., Armstrong N.R., *J. Appl. Phys.*, 1998, 84: 2324–2327.
- [82]. Tang H., Li F., Shinar J., *Appl. Phys. Lett.*, 1997, 71 : 2560.
- [83] Tadayyon S.M., Grandin H.M., Griffiths K., Norton P.R., Aziz H., Popvic Z.D., *Org. Electron.*, 2004, 5: 157–163.
- [84] Van Slyke S.A., Chen C.H., Tang C.W., *Appl. Phys. Lett.*, 1996, 69: 2160.
- [85] You H., Dai Y., Zhang Z., Ma D., *J. Appl. Phys.*, 2007, 101: 026105–026108.
- [86] Kawahara J., Ersman P.A., *Org. Electron.*, 2012, 3: 469–474.
- [87] Sanchez J.C., DiPasquale A.G., *Chem. Mater.*, 2007, 19: 6459–6470.
- [88] Liu J., Chen Y., *Semicond. Sci. technol.*, 2011, 26: 095011.
- [89] Campbell I.H., Smith D.L., *Appl. Phys. Lett.*, 1999, 74: 561.
- [90] Liu J., Wu X., Shi X., Wang J., Min Z., Wang Y., Yang M., He G., *Appl. Mater. Interfaces*, 2015, 7: 6438–6443.
- [91] Konezny S.J., Smith D.L., *J. Appl. Phys.* 2006, 99: 064509.
- [92] Davids P.S., Campbell I.H., *J. Appl. Phys.*, 2007, 82: 6319.
- [93] Diouf B.B., Jeon W.S., *Synth. Met.*, 2011, 161: 2087– 2091.
- [94] Yu H.H., Hwang S.-J., Hwang K.-C., *Opt. Commun.*, 2005, 248: 51–57.

- [95] Paetzold R., Heuser K., Henseler D., Roeger S., Wittmann G., Winnacker A., *Appl. Phys. Lett.*, 2003, 82: 3342.
- [96] Martínez-Sarti L., Pertegas A., Monrabal-Capilla M., Gilshteyn E., Varjos I., Kauppinen Esko I., Nasibulin A.G., Sessolo M., Bolink H.J., *Org. Electron.*, 2016, 30: 36–39.
- [97] Yun D.-J., Hong K., Kim S., Yun W.-M., Jang J.-Y., Kwon W.-S., Park C.-E., Rhee S.-W., *Appl. Mater. Interfaces.*, 2011, 3: 43–49.
- [98] Louwet F., Groenendaal L., Dhaen J., Manca J., Van Luppen J., Verdonck E., Leenders L., *Synth. Met.*, 2003, 135: 115–117.
- [99] Chang Y.-L., Song Y., Wang Z., Helander M.G., Qiu J., Chai L., Liu Z., Scholes G.D., Lu Z., *Adv. Func. Mater.*, 2013, 23: 705–712.
- [100] Wu Z., Luo J., Sun N., Zhu L., Sun H., Yu L., Yang D., Qiao X., Chen J., Yang C., Ma D., *Adv. Funct. Mater.*, 2016, 26: 3306–3313.
- [101] Chang Y.-L., Lu Z.-H., *Display Technol. J.*, 2013, 9: 459–468.
- [102] Jung S.H., Kwon K.-Y., Jung J.H., *Chem. Commun.*, 2015, 51: 952–955.
- [103] Yang X., Xu X., Dang J.-S., Zhou G., Ho C.-L., Wong W.-Y., *Inorg.Chem.*, 2016, 55: 1720–1727
- [104] Cheng G., So G.K.-M., To W.-P., Chen Y., Kwok C.-C., Ma C., Guan X., Chang C., *Chem. Sci.*, 2015, 6: 4623–4635.
- [105] Yang J., Huang J., Li Q., Li Z., *J. Mater. Chem. C.*, 2016, 4: 2663–2684.
- [106] Ying L., Ho C.-L., Wu H., Cao Y., Wong W.-Y., *Adv. Mater.*, 2014, 26: 2459–2473.

## CHAPTER 2

### Experimental Methods

This chapter provides an overview of the experimental methods and the basic concepts of characterization techniques used to analyse the structural, photophysical, electrochemical and thermal properties of the materials, thin films and devices presented in this work. The second part describes materials characterization techniques used in the present work including UV-Vis absorbance spectroscopy, photoluminescence, time-resolved fluorescence spectroscopy, atomic force microscopy, and field emission scanning electron microscope. The preparation and characterization of TCF for optoelectronic devices are also described. In addition, the materials synthesis and fabrication process of OLEDs have also been covered. Electroluminescence and electrical behaviour of OLEDs were also studied.

#### 2.1 Chemicals and materials

(3,4-ethyldioxythiophene) (PEDOT) doped with polystyrene sulfonic acid (PSS)-25 wt % of water (molecular weight,  $M_w=10,00,000$ ), tris-(8-hydroxyquinoline) aluminum ( $Alq_3$ ), dichloromethane (DCM), dimethylsulfoxide (DMSO), N,N-Dimethylformamide (DMF), indium tin oxide (ITO) coated glass plates (sheet resistivity of 8–12  $\Omega/Sq$ ) were purchased from Sigma-Aldrich. 2-acetylpyridine, 4-methylbenzaldehyde, 2-furaldehyde and 3,4,5-trimethoxybenzaldehyde derivatives were purchased from Sigma-Aldrich. All the chemical and solvents were research grade and used as received.

#### 2.2 Thin film growth technique

Nowadays, a wide variety of methods are available for deposition of thin films. The process differs to a great degree in their chemical and physical principles of operation. Each method in the preparation of thin films has been developed because of its unique advantages over others, while each process also has its own limitations. In order to optimize desired film characteristics, it is essential to understand the advantages and limits of the preparation methods for device applications. The desired film thicknesses are closely related to the deposition and the formation conditions. In general, thin films have the thickness in the range of a few angstroms to several

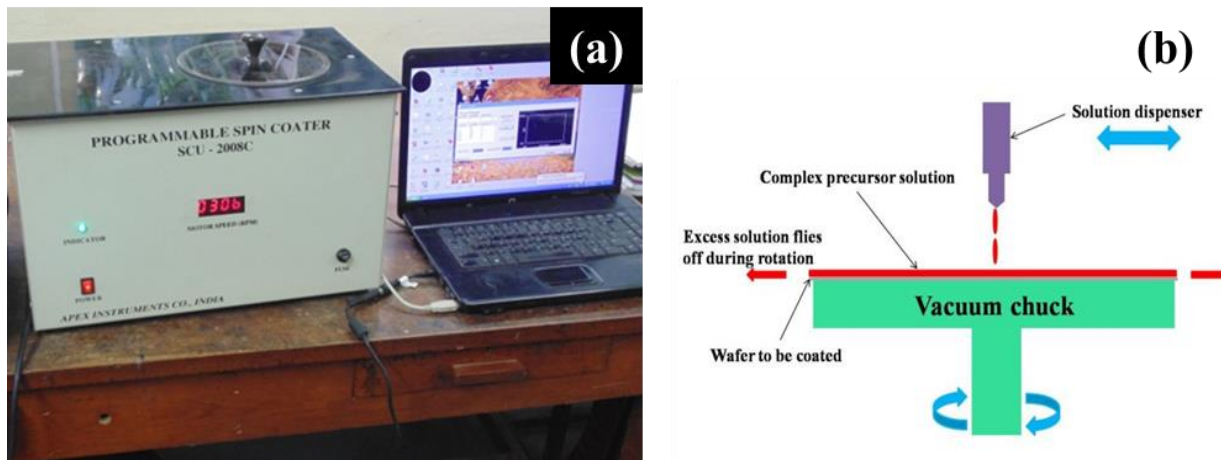
microns. The repeatability of the processes is significant for the manufacturing of semiconductor devices. The uniformity in composition and thickness are of great concern for most of the deposition methods [1]. The three sequential steps involved in thin film deposition process are listed as follows:

- i. Transformation of the condensed phase such as, solid or liquid into the gaseous.
- ii. Transportation of these vapours from the source to substrate through a medium.
- iii. Condensation of the vapours onto the substrate.

Thin film deposition methods are widely classified into two types-Physical and Chemical depositions [2]. Various chemical and physical deposition methods are available for preparation of thin film of CPs and small organic materials. Some of the chemical methods include dip-coating [3], chemical vapor deposition (CVD) [4], solvent evaporation epitaxial method [5], electrophoresis [6], sol-gel synthesis [7–8] and spray pyrolysis [9]. Thermal evaporation, electron beam evaporation, pulsed ion beam evaporation [10], RF sputtering; Pulsed Laser Deposition (PLD) and Atomic Layer Epitaxial (ALE) are example of physical deposition methods. The following sections give a brief outline of the various thin film deposition route.

### **2.2.1 Spin coating**

Spin coating is one of the most commonly used techniques in preparation of films of desired thickness on a suitable substrate. It is currently being used as the leading technique to prepare uniform thin films of organic and inorganic materials with thickness of the order of a few nanometers to some microns. Advantages of the spin coating process are speedy preparation of uniform films and ease. The precursor solution is dropped onto the substrate, which is placed on a vacuum chuck. It is then set to a desired rotation speed, so that the solution spreads over the substrate by centrifugal force and excess solution drains out from the substrate. The digital image and graphical representation of the spin coating unit are shown in Figure 2.1.



**Figure 2.1: (a) Digital image of spin coater and (b) graphical representation of spin coating chamber**

A characteristic spin process consists of a dispense step in which the precursor solution is deposited onto the surface of the substrate, whereas a high speed spinning and drying step is used to eliminate the excess solvents. In general, there are two methods used to dispense the precursor solution- static and dynamic process. In Static Dispense Process; the precursor solution is simply dropped onto the centre of the substrate. The amount of solution to be dropped depends on the size of the substrate and the viscosity of the solution to be coated. On the other hand, in Dynamic Dispense Process, the solution is dispensed when the substrate is rotating at a low speed (in terms of RPM-Rotations per minutes). This helps to spread the solution over the substrate and can result in less waste of materials. This is an advantageous method, particularly when the solution or substrate itself has meager wetting abilities. The vacuum chuck is used to hold the substrate during the spinning of the solution. The combination of spin speed and time selection for these steps will generally be decided by the required thickness of the thin film.

### **2.2.2 Chemical vapour deposition**

Chemical vapour deposition (CVD) is a process of condensation of atomistic species formed via chemical reaction of the precursors. This gives highly pure materials with great structural control at monolayer level. It is also used to grow single and multilayer nanostructures and composition with controlled dimension with good precision and high structural selection. The distinctive features of CVD techniques include free-standing film and enable the fabrication of nano-device

ceramic matrix composite, and carbon–carbon nano composites. The flexibility of CVD leads to high growth rate and is a leading technique for the preparation of thin films for various applications including optoelectronics, microelectronics, dielectrics for microelectronics, refractory ceramic materials used for hard coatings, metallic films, fibre production and coating. CVD involves homogeneous reactions of gas phases, and heterogeneous chemical reactions on substrate, which happen on heated surface substrate. It leads to the growth of fine powders and thin films. Furthermore, it has the capability of controllably creating chemical hetero structures. Varieties of CVD-processing techniques are available in recent years, such as plasma-enhanced (PECVD), low-pressure (LPCVD), laser-enhanced (LECVD), and metal-organic (MOCVD) chemical vapor deposition.

### **2.2.3 Spray pyrolysis**

Spray pyrolysis is a processing technique being considered to prepare thin and thick films of ceramic coatings and powders. It is a thermally activated reaction between clusters of liquid or vapour atoms of different chemical species. Unlike many other thin-film deposition techniques, spray pyrolysis is a simple and relatively cost-effective processing method, mainly due to its simple equipment. Spray pyrolysis does not require high-quality substrates and reagents. Its main advantages are good reproducibility, easy addition of doping materials, high film growth rates, materials homogeneity in thin-film product and the potential for deposition over a large area. The composition of the thin film can be controlled with reagents and precursor solution. Spray pyrolysis is a technique through which porous or dense thin films and powders can be obtained by controlling the deposition parameters. This technique necessitates the atomization of a precursor solution that is thrown directly over the substrate where the thin film is formed. Even multilayered thin films can also be prepared using this technique. In this process, the reagents are dissolved in the carrier liquid which is sprayed onto an unheated or heated substrate to form the minute droplets. In the case of heated substrate, the substrate is maintained at a high temperature of about 400 °C.

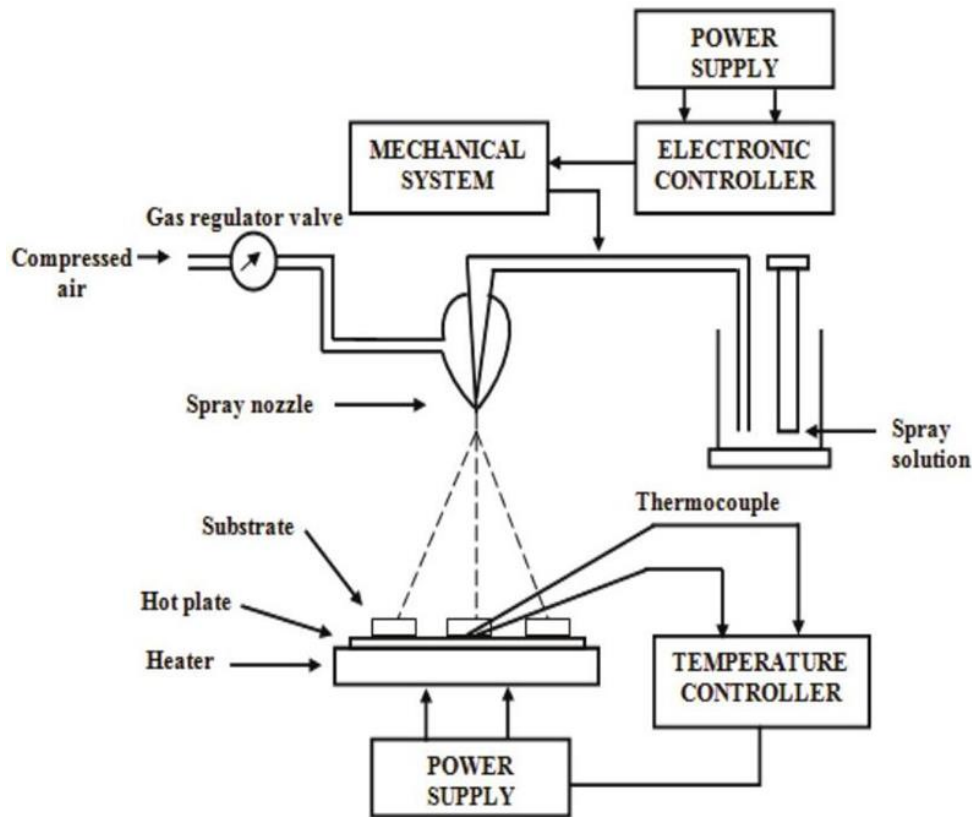


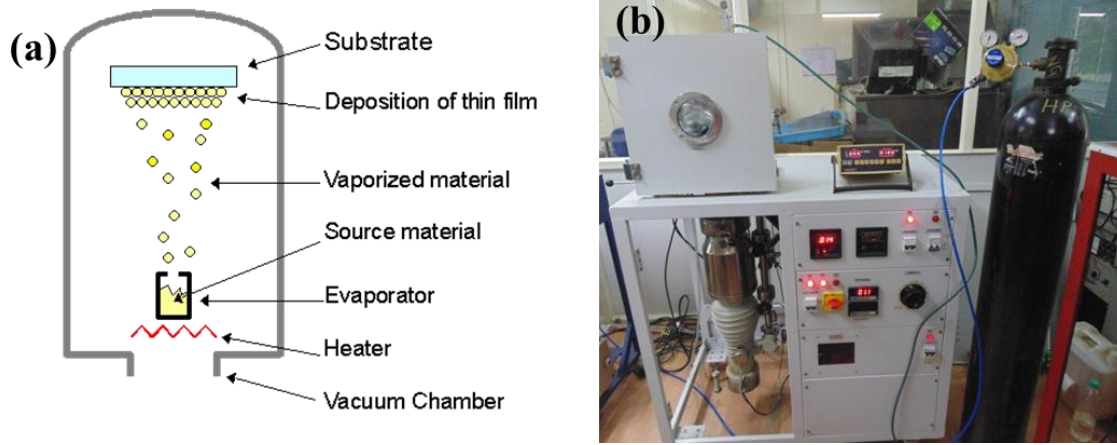
Figure 2.2: Schematic diagram of spray pyrolysis setup [11]

The sprayed droplets undergo pyrolytic decomposition to form a cluster or single crystal of the desired product in which the excess solvent and volatile by-products escape as vapour. The hot substrate renders the thermal energy needed for decomposition and the eventual recombination of the species, sintering and crystallization of the crystallites suitable to form a uniform thin film. Nowadays, automated spray pyrolysis equipment is also available to synthesis uniform thin film as shown in Figure 2.2.

#### 2.2.4 Thermal evaporation

Thermal evaporation is a commonly used technique to prepare the thin film of inorganic materials, such as metals and their alloys. However, this technique is being used to prepare the thin film of low molecular weight organic compounds. The process involves heating up of a source material until it evaporates and condenses onto the substrate. Solid materials vaporise when heated to sufficiently high temperatures. Moreover, the formation of oxides and

incorporation of impurities in the growing thin film can be avoided when the chamber is maintained in high vacuum.



**Figure 2.3: (a) Scheme of thermal evaporation chamber (Reproduced from Ref. [12]) and (b) digital image of thermal evaporation unit**

The mean free paths of vapour atoms are of the same order as the vacuum chamber dimension when the chamber pressures as low as  $10^{-5}$  or  $10^{-6}$  mbar. Commonly, there are two types of vacuum pump operating in serial: Rotary and Diffusion pump. Therefore, the vapour particles can travel in a straight line from the evaporation source to the substrate without being considerably scattered as shown in the Figure 2.3 (a) [13]. In this technique, average energy of the vapour atom is in the range of a few tenths of electron volts when it reaches the surface of the substrate.

In this method, the source material, evaporated as filament evaporation process, is a simple electrical resistive heat element or filament. A wide variety of physical configurations are available for the filaments, depending on the nature of the materials and coating of the film needed. In many coating applications, crucibles offer unique advantages to other types of sources. Filaments are heated directly by attaching the ends to a low voltage, high current supply to evaporate the material. The characteristics and quality of the deposited thin film depends on various parameters including substrate temperature, substrate to target distance, rate of deposition and base pressure. The homogeneity of the thin films depends on the geometry of the evaporation source and the distance from the source material to the substrate. In the present



work, the deposition of the organic complexes and metal electrode were prepared using thermal evaporation (see Figure 2.3 (b)) via resistive heating technique (VEC, Vacuum Solutions Technologies, Bangalore, India). A quartz crystal thickness monitor is placed near the evaporation zone, which is used to measure the deposition rate and thickness of thermally evaporated thin films (Thickness monitor, Model: DTM-501).

### 2.2.5 Sputtering deposition

The main concept in sputtering process is the ejection of surface atoms from the surface of target material by momentum transfer of the bombarding ions. It is basically a momentum transfer phenomenon in which the momentum of the incident atom is transferred to the target material atoms. It's a class of physical vapour deposition technique and finds a significant place in thin-film deposition. The main advantage of sputtering is that it is a non-thermal physical process. One of its main advantages is its utility in the etching process as well as deposition depending on the ion energy.

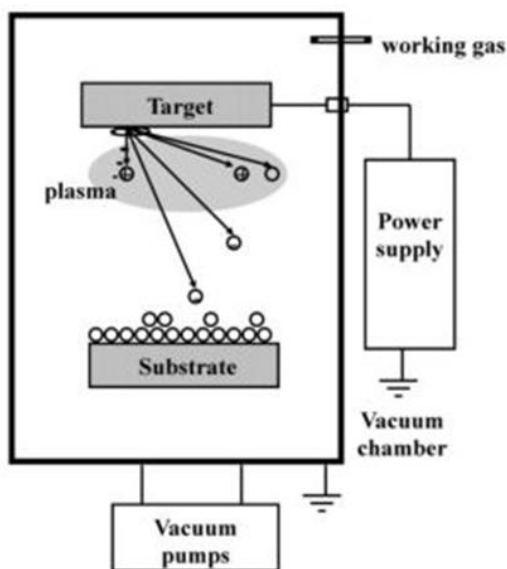


Figure 2.4: Schematic diagram of sputtering mechanism [14]

The incident energy of the bombarding species determines the nature of the particular phenomenon. The sputtering mechanism is shown in Figure 2.4. When a high voltage is applied across a pair of electrodes in a low-pressure gas, the gas gets ionised and a plasma or glow

discharge is formed. The ions in the plasma are very energetic and being positively charged are attracted towards the cathode and on striking cause the ejection of the cathode material [15]. An Argon gas is commonly used in sputtering process because it provides large ions for sputtering and being an inert gas it does not react chemically with the target. The sputtering process is used in this work to prepare the Al cathode of about 100 nm at a vacuum of  $10^{-6}$  mbar.

## **2.3 Characterization tools**

### **2.3.1 Structural characterization**

The structural characterizations of prepared materials in this dissertation were studied by  $^1\text{H}$  NMR,  $^{13}\text{C}$  NMR, mass spectrometry and FTIR-spectrometry.

#### **2.3.1.1 Nuclear magnetic resonance spectroscopy**

Nuclear magnetic resonance spectroscopy, commonly referred as NMR spectroscopy, has become the preeminent technique for determining the physical and chemical properties of atoms or molecules in which they are contained. It relies on the phenomenon of nuclear magnetic resonance and can provide elaborate information about the reaction states, dynamics and chemical structure of molecules. The intramolecular magnetic field around the atom in the molecules changes the resonance frequency, consequently, giving access to details of the electronic structure of a molecule and its functional groups.  $^1\text{H}$  (300 and 400 MHz) and  $^{13}\text{C}$  (100 MHz) spectra were taken in  $\text{CDCl}_3$  solution at room temperature with a Bruker AV400 instrument with chemical shifts relative to tetramethylsilane (TMS).

#### **2.3.1.2 Mass spectrometry**

Mass spectrometry (MS) is an exceedingly sensitive and specific analytical technique that can precisely determine the identities and quantities of compounds within a sample. It ionises chemical species and sorts the ions based on their mass-to-charge ratio. In simpler terms, a mass spectrum measures the masses within a sample; the mass spectrum is a plot of the ion signal as a function of the mass-to-charge ratio. Mass spectra are used to determine the isotopic-signature or elemental composition of a sample. The masses of particles or molecules present in the spectrum

help to elucidate the chemical structures of molecules. MS is used in various fields and is applied to pure samples as well as complex mixtures. In this study, mass spectra of the prepared ligands and metal complexes were recorded on a LC–MS Q–ToF micro analyzer (Shimadzu), using electrospray ionization (ESI) mode.

### **2.3.1.3 FT-IR spectroscopy**

Fourier transform infrared (FT-IR) spectroscopy is a commonly used technique in industry and laboratory for the several decades as a non-destructive method to identify chemical compositions in liquids, powders, gases and thin films. In FT-IR spectrometry, the IR radiation is passed to the sample. Some of the IR radiation is absorbed by the sample and some of it is passed through out (transmitted). FT-IR spectra can be observed when the materials absorb the electromagnetic radiation in the wavelength range of 400 to 4000  $\text{cm}^{-1}$ . The resulting spectrum represents the molecular absorption and transmission, creating molecular finger prints of the sample. Functional groups present in the molecule absorb radiation at characteristic wavelengths in the IR region. Like finger prints, no two unique molecular structures produce the same infrared spectrum. This makes FT-IR spectroscopy very useful for several types of analyses including the vibration and rotation properties of the samples. Thus, IR spectroscopy can provide information about the functional groups, qualitative and quantitative analysis. FT-IR spectra of the prepared materials were recorded in the range of 4000–400  $\text{cm}^{-1}$  using Bruker-Alpha FT-IR spectrophotometer. The C, H, N, and S analyses were performed on a Vario EL III Elemental analyzer.

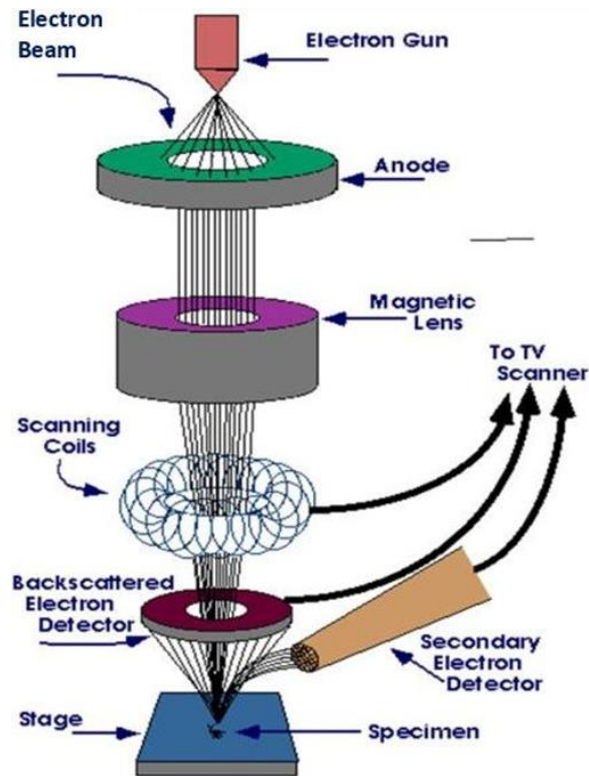
## **2.3.2 Morphological analysis**

Surface morphology of the synthesised ligands and terpy compounds were analysed by field emission scanning electron microscope (FE-SEM) and atomic force microscopy (AFM).

### **2.3.2.1 Scanning electron microscope**

Scanning electron microscope (SEM) is a widely used method for high resolution imaging of surfaces. It is the most commonly used instrument for obtaining micro structural and surface features of thin films and powder. The SEM uses electrons for imaging, whereas an optical microscope uses visible light for imaging the sample. The advantages of SEM over optical

microscope include much higher magnification ( $>100,000\times$ ) and depth of field upto 100 times that of light microscopy. Figure 2.5 shows the schematic illustration of SEM.



**Figure 2.5: Schematic illustration of scanning electron microscope**

In SEM, the focused electron beam scans across the sample surface in a raster fashion, generates secondary and backscattered electrons, which are detected by the detectors to generate the topography of surface of the sample. The elastic scattering produces backscattered electrons (energy  $> 50$  eV) and inelastic scattering produces secondary electrons (energy  $< 50$  eV), X-rays and also Auger electrons. Since secondary electrons come from the surface layer, the picture obtained is a faithful reproduction of the surface features. Secondary electron imaging can provide high-resolution imaging of fine surface morphology.

These signals are obtained from specific emission volumes within the sample and can be used to examine many characteristics of the sample. X-rays emitted are characteristic of the elements present in the sample, which can be used to study the chemical composition and is called energy dispersive X-ray spectroscopy. The auger electrons can be used to map the local chemical

composition of nanostructures with a good spatial resolution called as a scanning auger microscopy and spectroscopy [16]. Before scanning the samples in SEM, the samples were coated using gold sputtering of about 10 nm. Imaging was performed at electronic high tension (EHT) values between 2.0 and 20 kV, depending upon the required magnification and quality of the micrograph. The surface morphology of the materials was studied using FEI ESEM Quanta 200.

### **2.3.2.2 Atomic force microscopy**

Atomic force microscopy (AFM) is a scanning probe force microscopic technique invented by Binnig *et al.* [17] that helps measure the morphology of the surface at nanometer resolution. Figure 2.6 shows the working principle of AFM. It is one of the widely used non-destructive methods to investigate the surface of the nanomaterials. Here, a small sharp tip mounted on the cantilever scans the sample to obtain its morphology. The AFM tip usually has an edge in nanometers and oscillates with its resonant frequency. The interaction of the tip with surface features contributes to the variation in the tip oscillation frequency.

In general, two types of forces are encountered in AFM—they are repulsive and attractive to van der Waals forces. Mostly, repulsive forces are active in non-contact AFM operations. The nature of the sample surface makes the tip bend or lean as compared to natural oscillation frequency. Meanwhile, a laser diode is placed exactly at the tip and the reflection is received on position-sensitive photo detector setup. Due to the variation experienced at the tip, the reflection of the laser spot changes, which when fed into the software, generate topographic images. A feedback unit is attached to the piezo-electric setup to maintain the frequency of the probe tip. The cantilevers can be designed with specific spring constants as per the mode of operation.

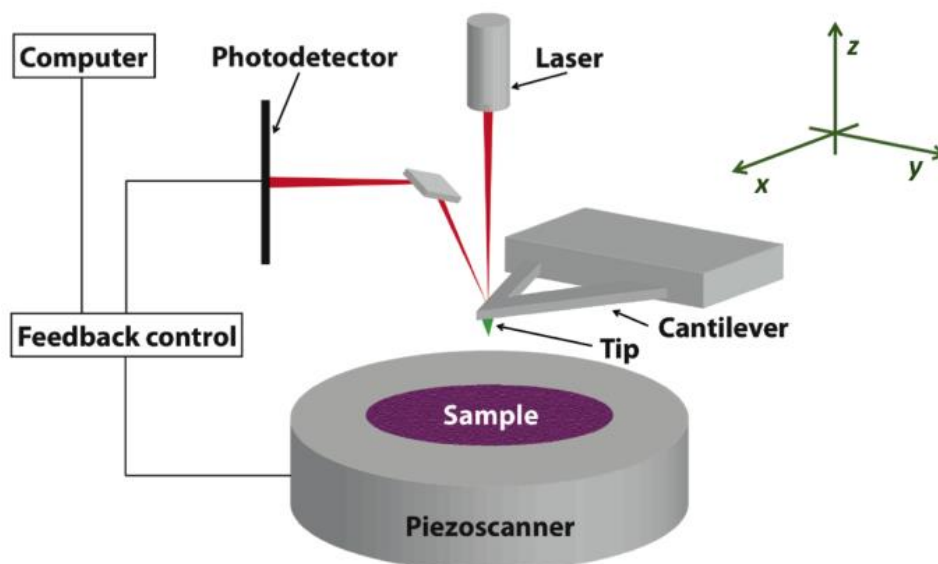


Figure 2.6: working principle of atomic force microscopy [Reproduced from ref. 18]

In general, two types of forces are encountered during the operation of AFM- Repulsive and Attractive Van der Waals forces depending on the position of the tip from the sample surface. It can scan the areas in the sample as small as 100 nm and as large as 100 microns. The morphology of the sample was studied using the AFM analyser (Model: A100-SGS AFM) at the AFM Facility (A.P.E. Research, Italy), Materials Research Centre, Indian Institute of Science, Bangalore, India.

### 2.3.3 Thermal analysis

The thermal behaviours of the synthesised ligands and terpy metal complexes were studied by differential scanning calorimeter and thermo gravimetric analysis.

#### 2.3.3.1 Differential scanning calorimetry

The differential scanning calorimeter (DSC) is widely used technique to investigate the thermal behaviour of the material. It works as comparison of the heat capacity ( $C_p$ ) of material with the function of a temperature. A sample of known mass is heated or cooled, consequently, the changes in its  $C_p$  is tracked as changes in its heat flow. This allows the detection of transitions like melts, phase changes, glass transitions and curing of the sample. It is used to study the

crucial thermal properties such as crystalline and amorphous behaviour, polymorph and eutectic transitions, curing and degree of cure. In order to measure the glass transition temperature ( $T_g$ ), melting temperature ( $T_m$ ) and crystalline temperature ( $T_c$ ) of the materials were carried out by DSC. A Netzsch DSC-200PC instrument was used to study the thermal properties of the synthesised material. In DSC, the differences in the amount of heat required for increasing the temperature of the sample and the reference is measured as a function of temperature. The temperature scale of the DSC is calibrated from the melting point of Indium, and empty aluminum pans were used as reference. The sample placed in an aluminum pan and the dynamic heating was carried out at a rate of 5 or 10 °C/min from room temperature to beyond the  $T_m$  of the sample in a nitrogen atmosphere.

### **2.3.3.2 Thermogravimetric analysis**

Thermogravimetric analysis (TGA) is performed to determine change in weight of a sample in relation to change in temperature. It is commonly employed to determine characteristics of materials such as polymers, degradation temperatures and absorbed moisture content of materials, the level of organic and inorganic components in materials, decomposition points of explosives and solvent residues. A high precision balance with a pan (generally platinum) loaded with the sample is placed in a small electrically heated oven with a thermocouple to accurately measure the temperature. Sample and reference are heated by a single source and the temperatures are measured by thermo couples embedded in the sample and reference, and attached to their pans. The weight loss corresponding to various temperatures is measured [19]. The inner atmosphere of the oven purged with an inert gas to prevent oxidation or other undesired reactions. The temperature is then raised gradually and weight loss is plotted against the temperature. The TGA of the samples were characterised in a nitrogen atmosphere at heating rate of 5 and 10 °C/min using TGAQ50, TA Instruments.

### **2.3.4 Photophysical studies**

The study of photophysical properties including electronic excitation and emission of the material is of great interest for optoelectronic applications. In order to investigate the excitation

and emission behaviour of the material is carried out here by UV-Visible (UV-Vis) absorbance and photoluminescence (PL) spectra respectively, which is described in the following sections.

### 2.3.4.1 UV-Vis absorbance spectroscopy

UV-Vis absorption spectroscopy is the measurement of light when it is passed through a sample. The principle of UV-Vis spectrometer is based on the ability of molecule to absorb ultraviolet and visible light. In this technique, the absorption of light in the visible and its adjacent regions (near UV and IR) of the sample is measured. The absorption of light corresponds to the excitation of outer electrons in the molecules. In this region the atoms and molecules have the electronic transitions. The outer most electrons of the molecules get excited from the HOMO to LUMO energy levels when the molecules absorb the external energy. This UV-Vis absorption spectrometer deals that the electronic transition of materials from the ground state to excited state [21].

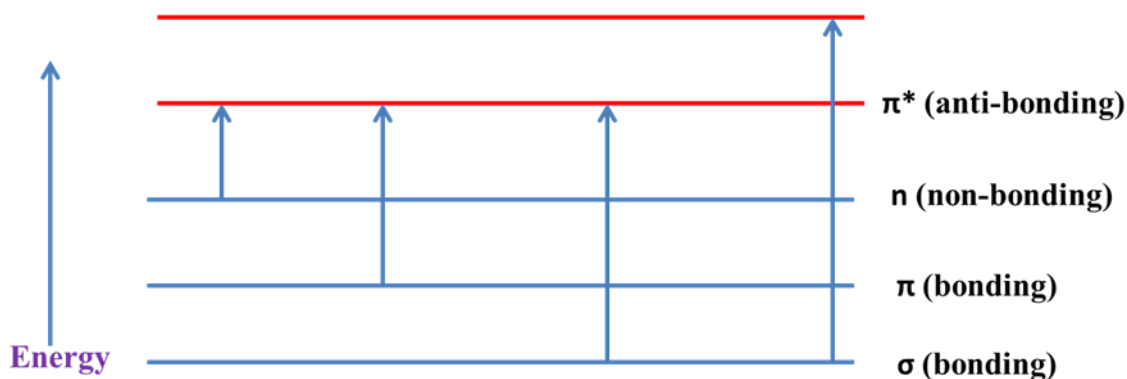


Figure 2.7: Electronic energy levels and transition states [20]

When a sample is exposed to UV-Vis-NIR light that matches the energy difference between possible electronic transitions within the molecule, a part of the light energy would be absorbed by the molecule and the electrons can be promoted from lower energy level to the higher energy level. This UV-Vis absorption spectrometer records the degree of absorption by the sample at different wavelengths and the resulting plot of absorbance against wavelength is called as absorption spectrum.



The electronic states of the molecule in the ground state contain two electrons of equal and opposite spin with each filled molecular orbital. One of these electrons in the highest filled  $\pi$  molecular orbital absorbs light, consequently, rise to the lowest unfilled  $\pi^*$  molecular orbital energy level. Hence, the ground state bonding molecular orbitals can be excited into anti-bonding molecular orbitals (see Figure 2.7). There are four types of transitions possible, such as,  $\pi\text{-}\pi^*$ ,  $n\text{-}\pi^*$ ,  $\sigma\text{-}\sigma^*$  and  $n\text{-}\sigma^*$  transitions. The energy required for various transitions are in the following order:  $\sigma\text{-}\sigma^* > n\text{-}\sigma^* > \pi\text{-}\pi^* > n\text{-}\pi^*$ .

i)  $\sigma\text{-}\sigma^*$  transition

In this transition, an electron in the bonding  $\sigma$  orbital is excited to the corresponding anti-bonding  $\sigma^*$  orbital by absorption of electromagnetic radiation. Since  $\sigma$  bond is very strong, this type of transition is high energy processes.

ii)  $n\text{-}\sigma^*$  transition

The  $n\text{-}\sigma^*$  transition is observed in the saturated compounds having one heteroatom with unshared electron pairs. This transition requires lesser energy than that of  $\sigma\text{-}\sigma^*$  transitions

iii)  $\pi\text{-}\pi^*$  and  $n\text{-}\pi^*$  transitions

Most of the organic compounds undergo  $\pi\text{-}\pi^*$  and  $n\text{-}\pi^*$  type of transitions. These transitions require the presence of an unsaturated functional group to  $\pi$  orbitals.

In UV-Vis spectroscopy, a detector measures the intensity of light ( $I$ ) after it has passed through a sample, and compares it with the initial intensity of light ( $I_0$ ) before it passed through the sample. The ratio  $I/I_0$  are known as the optical transmittance of the sample, and are typically presented as %T. The method is often used in a quantitative way to determine the concentrations of absorbing species in solution by using the Beer-Lambert Law as given Equation 2.1:

$$A = \log_{10} (I_0/I) = \epsilon cl \text{ ----- (2.1)}$$

where,  $A$  is the absorbance,  $\epsilon$ - the molar absorptivity ( $L \text{ mol}^{-1}\text{cm}^{-1}$ ),  $c$ - the concentration of the sample ( $\text{mol L}^{-1}$ ), and  $l$  is the length of cell (cm). UV-Vis absorption spectra of the samples were

recorded by UV-Vis optical spectrophotometer of ocean optics, model: DH-2000-BAL. The experiments were carried out with 1M concentration of the solution. The standard quartz cuvette of 10 mm optical path was used for spectroscopic studies.

#### **2.3.4.2 Photoluminescence spectroscopy**

Photoluminescence (PL) spectroscopy is widely used nondestructive analytical method to investigate the emission behaviour of luminescent materials. Two simultaneous processes occur during PL measurements. In the first process, the light source is directed onto a sample, where it is absorbed by the sample, and the electronic transition takes place into the high energy levels, called as photo-excitation; meanwhile they will release energy in the form of photons as it relaxes and returns to lower energy level. The emission of light through this process is known as photoluminescence.

Excitation by absorbance of a photon in luminescent material leads to a major class of technically important luminescent species, which can be either fluorescence or phosphorescence. The pair of electrons occupies the same electronic ground state with opposite spins and said to be in a singlet spin state. When the sample absorbs UV or visible light, one of the valence electrons moves from the ground state to an excited state with a conservation of the spin of electrons. Following this process, emission takes place and the emission of photon from the singlet excited state to the singlet ground state is called as fluorescence. Thus, the fluorescence decays rapidly once the source of excitation is removed. In some cases, an electron in a singlet excited state is transformed into a triplet excited state, in which its spin is no longer paired with the ground state. The emission between a triplet excited state and a singlet ground state is called as phosphorescence. Therefore, the phosphorescence may continue for some time after eradicating the excitation source. The PL spectra are recorded by measuring the intensity of emitted radiation as a function of emission wavelength. It is used to characterize a given luminescent material by recording its excitation and emission wavelength. Therefore, the quantity of PL emitted from a material is related to the relative amount of radiative and non-radiative recombination rates. The PL spectra of the materials were recorded with a Shimadzu RF-5301PC fluorescence spectrophotometer.

### **2.3.4.3 Time-resolved fluorescence spectroscopy**

Time-resolved fluorescence (TRF) spectroscopy is an important study for the characterization of fluorescence lifetime measurements. In this technique, the fluorescence of a sample is monitored as a function of time after excitation by a flash of light. The time resolution can be obtained in a number of ways, depending on the required sensitivity and time resolution. It is able to resolve the important physical actions in real time scales, including shorter detection time with better resolution. Luminescence lifetime plays a key role in determining the performance of luminescence of material. Fluorescence lifetime is the time spent by a fluorophore in the excited state before returning to the ground state by emitting a photon. Luminescence lifetime of the material is studied by an Edinburgh FL920 time-correlated pulsed single-photon-counting instrument. Moreover, the repetition rate of pulse was 1 MHz and excitation pulse width was less than 200 ps using diode LASER for all experiments. The instrumental response function (IRF) was used as 200 ps for the lifetime measurements characteristics.

### **2.3.5 Electrochemical analysis**

Cyclic voltammetry (CV) is a dynamic electrochemical method to investigate the electrochemical behaviour as well as to estimate the energy values. Electrochemical properties of materials were analysed using CV, while electrochemical behaviours of materials were investigated in three electrode cell systems. Platinum wire and platinum foil were used as working and counter electrode, respectively. Non-aqueous Ag/Ag<sup>+</sup> electrode was used as reference electrode. A 0.1M of tetrabutylammonium perchlorate (TBAP) dissolved into dimethylformamide (DMF) at a scan rate of 0.1 Vs<sup>-1</sup>, which was used as an electrolyte solution and ferrocene (Fc) as an internal standard. Current is measured and a plot of current density as a function of potential is obtained. The characteristic peaks in the CV are caused by the presence of the diffusion layer near the electrode surface. A typical CV analysis generally starts at low potentials where no redox reactions occur in anodic direction. The current flowing at the solution interface/working electrode is monitored as a function of the applied potential. Both quantitative and qualitative data may be obtained and the technique finds particular use in preliminary studies of new systems. The cyclic voltammogram shows the potentials at which oxidation and reduction

processes occur, the potential range over which the solvent is stable, and the degree of reversibility of the electrode reactions. Furthermore, repeated cycling reveals the electrochemical stability of electroactive species. The electrochemical behaviour of the prepared ligands and metal complexes were performed using CH Instrument electrochemical analyzer: Model CHI6005D.

## 2.4 Fabrication and characterization of OLED device

### 2.4.1 ITO substrate cleaning

The ITO substrates were cut as per the requirement of the device fabrication, then ultrasonically cleaned with the deionized water, followed by washing in acetone and methanol for 10 minutes respectively. The ITO substrates were then oven dried for 20 minutes to remove residual water vapor and volatile contaminants at around 80–90 °C. These cleaned ITO substrates were either stored under vacuum in a desiccator or moved to vacuum evaporation system for the deposition.

### 2.4.2 Oxygen-plasma treatment

Work function (WF) of the ITO substrate is very important for OLED fabrication as it determines the energy barrier between the anode and HTL. The energy barrier between the ITO and HTL should be minimal to allow hole injection, which means that the ITO work function must be as large as possible. The WF of ITO can be easily controlled by plasma treatment process.

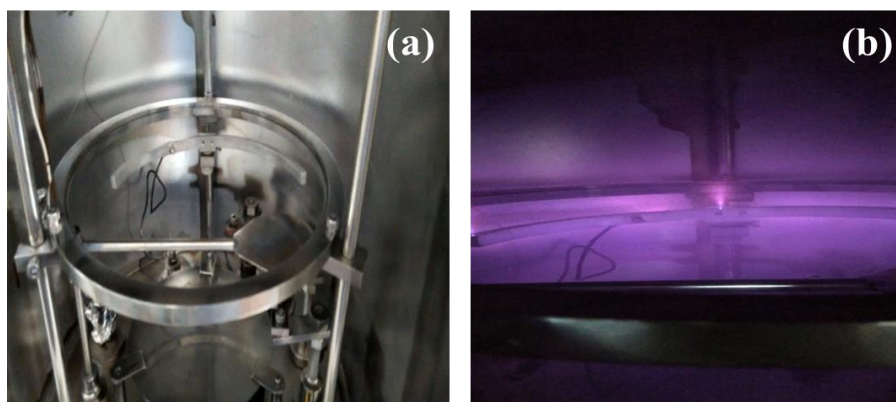


Figure 2.8: Thermal vapour deposition chamber inside: (a) before creating plasma, (b) when plasma occurs

This plasma treatment removes the hydrocarbons that lower the ITO work function. In this present work, oxygen plasma is used for the ITO substrate treatment. The oxygen plasma cleans organic and some inorganic contaminants from the ITO film and induce surface dipoles that increase the work function. Figure 2.8(a) shows the digital image of inside the thermal vapour deposition chamber. Plasma is created inside the vacuum chamber when it maintains the critical pressure of oxygen of 0.050 to 0.080 mbar with a current of 35 A (see Figure 2.8 (b)). Plasma intensity is increased while increasing the applied current. This plasma is very useful in treating the surface of the TCO coating and eventually, the work function of the TCO can be modified. The work function of ITO substrate can be increased from 4.7 eV to 5.0 eV so that it reduces the energy barrier for hole injection at the interface between ITO and HTL and improves the device driving voltage, efficiency and lifetime.

### 2.4.3 OLED device structure

For OLED fabrication, a conducting film of poly(3,4-ethylenedioxythiophene) doped with poly(styrenesulfonate) (PEDOT:PSS) was spin coated at 2000 rpm after oxygen plasma exposure of cleaned ITO-coated substrate, followed by annealing at 120 °C for 5 minutes. The active layer of electroluminescent material was deposited by thermal evaporation.

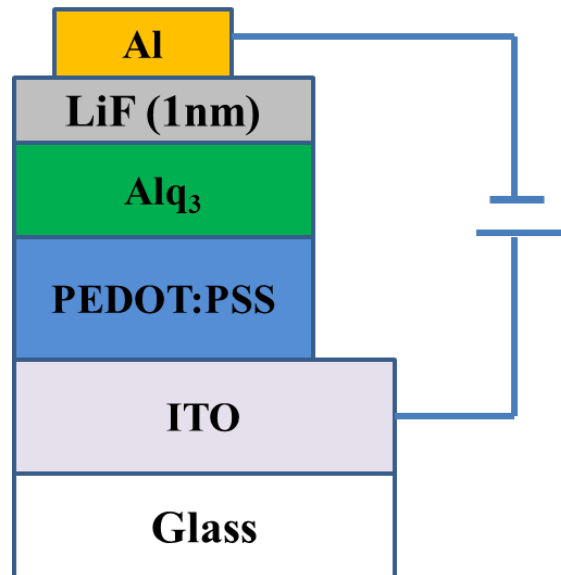
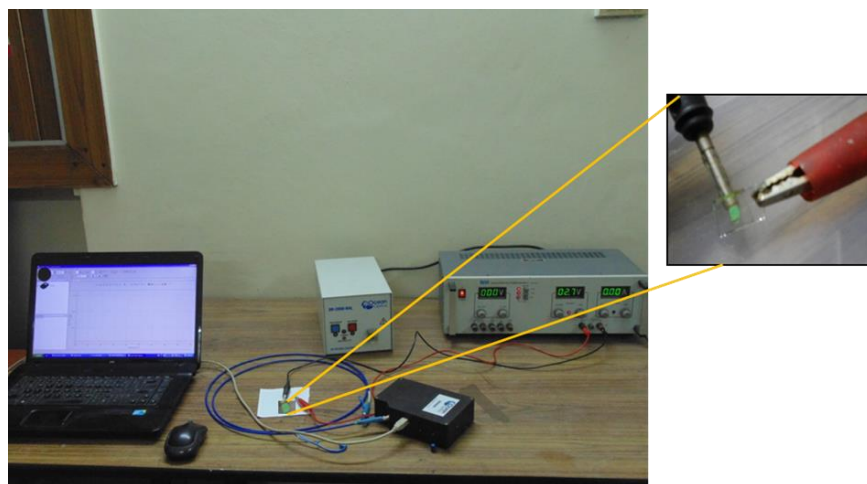


Figure 2.9: OLEDs device structure

This device has taken from the chamber and mask to choose the active area for luminescence, where the device emits the light. The cathode aluminum was thermally evaporated through a shadow mask. Al (100 nm) electrode was deposited by thermal evaporation on top of this active layer. The ITO and Al were used as anode and cathode respectively, for all devices. The thickness of lithium fluoride (LiF) of 1 nm was inserted between electroluminescent active layer and Al cathode, so as to act as an electron buffer layer. In the present work the small molecules are normally prepared by thermal evaporation of the thin film layers in a high vacuum chamber ( $<10^{-6}$  mbar). The thickness of layers can be accurately controlled by a thickness monitor placed in the vicinity of the substrate. Figure 2.9 shows the bilayer structure of OLEDs. Triaxial probe station electrical measurements were performed on Keithley 2636 source measure unit with a current compliance setting at 100 mA.

#### 2.4.4 Electroluminescent measurement

Electroluminescence studies are used to quantify the wavelength and intensity of luminescence emitted from a material or a device as a result of applied potential. The photon emission was measured using HR4000 spectroradiometer (Ocean optics Pvt. Ltd) as shown in Figure 2.10.



**Figure 2.10: Digital image of electroluminescent set-up consisting of regulated DC power supply (Aplab Pvt. Ltd) and HR4000 spectroradiometer**

The measurement of photons with integrating sphere, the standard light sources of Deuterium and Halogen has been used to evaluate the device emission. In general, spectroradiometer is used

to monitor the spectral power distribution from a source. The spectral data can be used to calculate various parameters such as colour temperature, CIE (International commission on illumination) coordinates, irradiance and absorbance. It encompasses various components, first collection of light (by cosine corrector or fiber optics); usually it is achieved by employing a diffusing material on the top of the instrument. Then, it is delivered to monochromator, where light is spectrally resolved to their wavelength and intensity. After the dispersion, the light corresponds to particular wavelength is passed to photo detector where radiation is converted into electric signals. An important role of spectroradiometric measurement is the calibration of measured intensity with standard irradiance. Therefore, it gives a way to quantify the output of the spectroradiometer in terms of physical unit either Lumen or Candela.

## 2.5 References

- [1] Seshan K., *Handbook of thin-film deposition processes and techniques principles, methods, equipment and applications*, 2nd Edition, Noyes publications, William Andrew publishing, Norwich, New York, U.S.A, 2001.
- [2] George J., *Preparation of Thin Films*, Marcel Dekker Inc., New York, 1992.
- [3] Miyata T., Nakatani T., Minami T., *Thin Solid Films*, 2000, 373: 145–149.
- [4] Minami T., Kuroi Y., Dakata S., *J. Vac. Sci. Technol. A*, 1996, 14: 1736–1740.
- [5] Yan Z., Koike M., Takei H., *J. Cryst. Growth*, 1996, 165: 183–186.
- [6] Yang S. H., *J. Electrochem. Soc.*, 2003, 150: H250–H253.
- [7] Sei T., Nomura Y., Tsuchiya T., *J. Non-Cryst. Solids.*, 1997, 218: 135–138.
- [8] Ji Z., Kun L., Yongliang S., Zhizhen Y., *J. Cryst. Growth*, 2003, 255: 353–356.
- [9] Lou Z., Hao J., *Appl. Phys. A*, 2005, 80: 151–154.
- [10] Honda N., Suzuki T., Yunogami T., Suematsu H., Jiang W., Yatsui K., *Jpn. J. Appl. Phys.*, 2005, 44: 695–697.

- [11] Udayakumar R., Khanaa V., Saravanan T., *Indian J. Sci. Technol.*, 2013, 6: 4754–4757.
- [12] <http://hivatec.ca/consulting-design/thin-film-deposition/> (Accessed on 02 March, 2017)
- [13] Maissel L.I., Glang R., *Handbook of Thin Film Technology*, McGraw-Hill, New York, 1970.
- [14] [http://www.sneresearch.com/eng/info/column.php?pg=6&device2=&s\\_type=&sub\\_cat=&s\\_word=](http://www.sneresearch.com/eng/info/column.php?pg=6&device2=&s_type=&sub_cat=&s_word=) (Accessed on 03 March, 2017)
- [15] Chopra, Kasturi L., *Thin film phenomena*, McGraw-Hill, New York, 1969.
- [16] Goldstein J., Newbury D., Joy D., Lyman C., Echlin D., *Scanning Electron Microscopy and X-ray Microanalysis*, 3<sup>rd</sup> Edition, Springer Science and Business Media, Inc., USA, 2003.
- [17] Binnig G., Quate C., Gerber C., Atomic force microscope, *Phys. Rev. Lett.*, 1986, 56: 930–933.
- [18] <https://amyhallr.wordpress.com/2013/03/15/atomic-force-microscopy/>. (Accessed on 02 April, 2017)
- [19] Bower D.I., *An introduction to polymer physics*, Cambridge University Press, Cambridge, UK, 2002.
- [20] Pavia D.L., Lampman G.M., Kriz G.S., *Introduction to Spectroscopy*, Saunders Golden Sunburst Series, 2<sup>nd</sup> edition., USA, 1997.
- [21] Skoog D.A., Holler F.J., Crouch S.R., *Principles of Instrumental Analysis*, 6th Rd., Belmont, CA, Thomson Brooks, 2007.



## CHAPTER 3

### **Synthesis, photophysical, thermal and electrochemical properties of 4'-aryl substituted 2,2':6',2''-terpyridine derivatives**

This chapter discusses the design, synthesis and characterization of the three 4'-aryl substituted terpy derivatives (**C-1–C-3**) in a single pot reaction. Structural, photophysical, electrochemical and thermal properties of the materials have also been investigated. In addition, the thermal stability, morphological analysis and fluorescence lifetime of all the three derivatives were also discussed. This chapter also describes the significant emission in the blue region (380–440 nm) and fast fluorescence lifetimes of the derivatives. The 3,4,5-trimethoxy-phenyl-substituted terpyridine derivative shows a high red shift with respect to 4-methylphenyl and 2-furyl-substituted terpy derivative. The calculated HOMO and LUMO values suggest that the synthesised three terpy derivatives favour electron-transporting and fluorescent emitter to design blue fluorescent OLEDs

#### **3.1 Introduction**

Fluorescent organic light-emitting diode is a type of OLED, in which the electroluminescence (EL) originates from the fluorescence of organic materials [1–3]. Solid-state device applications require a novel emissive material, especially in the blue wavelength range [4–5]. Several families of luminescent materials have been screened for this purpose [6–8]. In comparison to analogous systems, such as 2,2'-bipyridine (bpy) and 1,10-phenanthroline (phen), which captured early on the attention in coordination chemistry, 2,2':2'',6'-terpyridine (terpy) derivatives gained significance in coordination and supramolecular chemistry due to their technical merits over the last few decades [9–11]. The terpy is a molecule with three pyridine rings connected together through  $\alpha$ -positions of the nitrogen ring. Morgan et al. first reported its synthesis in 1932 [12]. The terpy acts as a tridentate nitrogen donor ligand and seldom as bi- or mono-dentate nitrogen donor. The presence of nearly coplanar three-nitrogen donor atoms in the molecule dramatically increases its metal-binding capacity in comparison to bi- and mono-nitrogen aromatic ligands [13].

The blue-emitting organic materials are important in preparing the solid-state lighting applications. However, their availability is still scarce compared to that of green- and red-emitting materials because of their intrinsic wide band gap, and hence the difficulty to prepare them [14]. Li et al. studied the phosphorescent-host mixed blue emission to improve the efficiency and lifetime of blue-emitting devices [15]. Nevertheless, the design of blue phosphorescent materials is still under way. On the other hand, blue-emitting OLEDs based on fluorescent materials are among the easiest to design [16]. Wang and others report that arylimidazol-fused phenanthroline derivatives exhibited fast electron transport and injection in blue light-emitting devices. However, the strong aggregation tendency of the materials not only leads to the red shifting of their emission spectra, but also to deterioration in the performance of the device [17–19]. Nevertheless, a few reports suggest the application of terpy and its derivatives as efficient and stable organic fluorescent blue emitters [20–23]. Hence, it is necessary to study and understand the thermal stability, photophysical properties and electrochemical activity of the aryl substituted terpyridine ligands to fabricate blue fluorescent OLEDs. Therefore, the design and synthesis of novel luminescent materials and understanding of their photophysical properties are very important in designing the blue fluorescent OLEDs [24–28]. Thus, intensive efforts, especially on blue fluorescent materials, are under way to further improve the OLEDs technology.

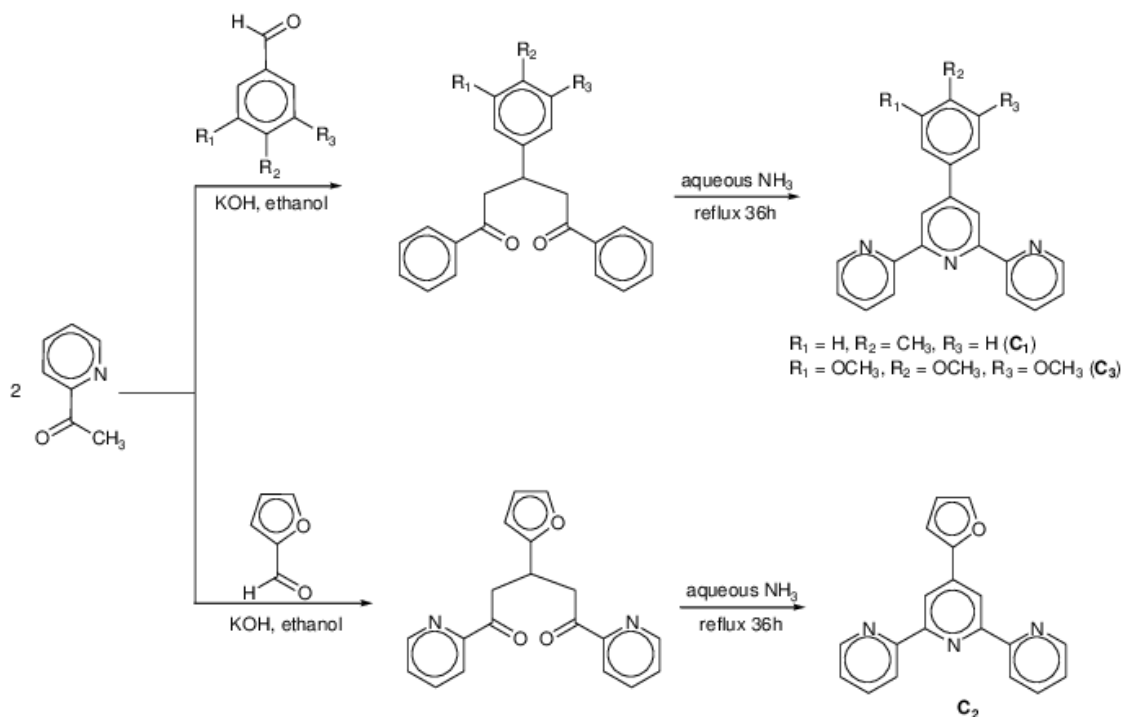
In this chapter, various aryl substituted terpy derivatives for blue fluorescent OLED applications are discussed. In this context, synthesis of three terpy derivatives were carried out, namely, (i) 4'-(4-methylphenyl)-2,2':6',2''-terpyridine, (ii) 4'-(2-furyl)-2,2':6',2''-terpyridine, and (iii) 4'-(3,4,5-trimethoxyphenyl)-2,2':6',2''-terpyridine in a single pot reaction through the formation of an intermediate and studied their photophysical, electrochemical and thermal behaviour for fluorescent application. To the best of our knowledge, there has been no clear understanding of electronic excitation, emission and thermal properties of terpyridine and its functional groups. The direct attachment of the 2-furyl and 3,4,5-trimethoxy phenyl groups to the 4'-position of terpy causes the red-shift compared to 4-methyl substituted terpy. This is due to the smaller reorganization of energy associated with the charge transfer (CT) transition in the derivatives. This study indicates that terpy derivatives are not only electron-transporting material, but are also

an excellent choice for blue fluorescent emitter to design blue fluorescent OLEDs applications. In subsequent sections, their synthesis and characterization are discussed.

## 3.2 Experimental

### 3.2.1 Procedure for the synthesis of 4'-aryl substituted 2,2':6',2''-terpyridines

2-acetylpyridine (1.4 mL, 5 mmol), aqueous solution of KOH (2 mL, 15%), and aqueous NH<sub>3</sub> solution (20 mL, conc.) were added to a mixture of aldehyde (4-methylbenzaldehyde (0.29 mL, 2.5 mmol), 2-furaldehyde (0.20 mL, 2.5 mmol)) and 3, 4, 5-methylbenzaldehyde (0.3924 g, 2.5 mmol) and ethanol (100 mL) in turn. The resulting mixture was reflux for 36 hours, and then cooled to room temperature. The off-white solid was collected by filtration and washed with ice-cold ethanol (10 mL). Pure white solids were obtained after recrystallization. Scheme 3.1 shows the synthesis of terpy derivatives in a single pot reaction.



Scheme 3.1: Synthetic procedure for the preparation of 4'-aryl substituted terpy derivatives

### 3.2.2 4'-(4-methylphenyl)-2,2':6',2''-terpyridine: C-1

Yield: 50%, T<sub>m</sub>. 167 °C, Anal. Calcd for C<sub>22</sub>H<sub>17</sub>N<sub>3</sub>: C, 81.71; H, 5.30; N, 12.99. Found: C, 81.69; H, 5.37; N, 12.87. IR:  $\nu$  = 3048 (w), 3013 (w), 2968 (w), 1602 (w), 1583 (s), 1565 (m), 1465 (m), 1385 (m), 1111 (w), 1073 (w), 1038 (w), 821 (m), 789 (s), 742 (w), 732 (s), 682 (m), 658 (m), 620 (m) cm<sup>-1</sup>. <sup>1</sup>H NMR (300 MHz, CDCl<sub>3</sub>):  $\delta$  = 2.44 (s, 3 H), 7.33 (d, J=7.8 Hz, 2 H), 7.35-7.38 (m, 2 H), 7.84 (d, J=7.8 Hz, 2H), 7.89 (m, J=1.8 Hz, 2 H), 8.68 (d, J= 7.8 Hz, 2 H), 8.75 (d, J=3.6Hz, 4 H) ppm. <sup>13</sup>C NMR (CDCl<sub>3</sub>, 100 MHz):  $\delta$  = 21.29, 118.71, 121.45, 123.81, 127.16, 129.67, 135.41, 136.99, 139.13, 149.00, 150.20, 155.73, 156.23 ppm. MS (ESI, *m/z*): 323.21 [M]<sup>+</sup>.

### 3.2.3 4'-(2-furyl)-2,2':6',2''-terpyridine: C-2

Yield: 50%, T<sub>m</sub>. 224 °C, Anal. Calcd for C<sub>19</sub>H<sub>13</sub>N<sub>3</sub>O: C, 76.24; H, 4.38; N, 14.04. Found: C, 76.62; H, 4.58; N, 14.24. IR:  $\nu$  = 3042 (w), 3021 (w), 2931 (m), 1577 (w), 1512 (s), 1461 (m), 1383 (m), 1312 (m), 1118 (w), 1009 (w), 1038 (w), 821 (m), 719 (s), 647 (w), 615 cm<sup>-1</sup>. <sup>1</sup>H NMR (300 MHz, CDCl<sub>3</sub>):  $\delta$  = 7.07 (s, 2 H), 7.34-7.38 (m, 2 H), 7.85-7.91 (m, 2H), 8.66 (d, 4H), 8.73 (d, 3H) ppm. <sup>13</sup>C NMR (CDCl<sub>3</sub>, 100 MHz):  $\delta$  = 56.48, 61.01, 104.70, 118.67, 121.47, 123.89, 134.49, 136.94, 149.10, 150.57, 153.64, 155.89, 156.23 ppm. MS (ESI, *m/z*): 299.34 [M]<sup>+</sup>.

### 3.2.4 4'-(3,4,5-trimethoxyphenyl)-2,2':6',2''-terpyridine: C-3

Yield: 61%, T<sub>m</sub>. 187 °C, Anal. Calcd for C<sub>24</sub>H<sub>21</sub>N<sub>3</sub>O<sub>3</sub>: C, 72.16; H, 5.30; N, 9.69. Found: C, 72.69; H, 5.37; N, 9.67. IR:  $\nu$  = 3080 (w), 2950 (w), 1686 (m), 1577 (s), 1544 (w), 1505 (m), 1461 (w), 1370 (m), 1106 (w), 1009 (m), 912 (w), 796 (m), 726 (s) cm<sup>-1</sup>. <sup>1</sup>H NMR (400 MHz, CDCl<sub>3</sub>)  $\delta$ : = 3.92 (s, 3 H), 3.99 (s, 6 H), 7.06 (s, 1H), 7.26 (s, 1H), 7.34-7.37 (m, 4H), 7.84-7.90 (m, 3H), 8.67 (d, 7.8 Hz, 2 H), 8.72 (d, 2 H) ppm. <sup>13</sup>C NMR (CDCl<sub>3</sub>, 100 MHz):  $\delta$  = 56.49, 60.99, 104.78, 118.89, 121.44, 123.84, 134.57, 136.88, 139.06, 149.10, 150.57, 153.65, 155.91, 156.26 ppm. MS (ESI, *m/z*): 399.72 [M]<sup>+</sup>.

### 3.3 Results and discussion

Terpy derivatives were synthesised according to modified literature procedure as shown in scheme 3.1 [29]. In this study, potassium hydroxide was used as the base. A diketone intermediate was obtained during this reaction, which was added with 28–30% ammonia solution and refluxing for 36 h, resulting in crude terpyridines (crude yield 57–65%). After crystallization of the impure terpyridines from  $\text{CHCl}_3:\text{Et}_2\text{O}$  (1:1), pure terpyridine was obtained in 50–61% yields. These compounds are stable in air, they were obtained in good yields and characterised by analytical and spectroscopic methods (FTIR,  $^1\text{H}$ ,  $^{13}\text{C}$ -NMR and ESI-MS) (Figure A1.1–A1.6, Appendix A). The analytical data of the complexes agreed well with the proposed molecular formulae.

#### 3.3.1 UV–Vis absorbance spectra

The UV–Vis absorbance spectra of the synthesised terpy derivatives were studied in dichloromethane (DCM) and are shown in Figure 3.1. The absorption spectra of all terpy derivatives exhibit broad absorption bands between 240 and 330 nm.

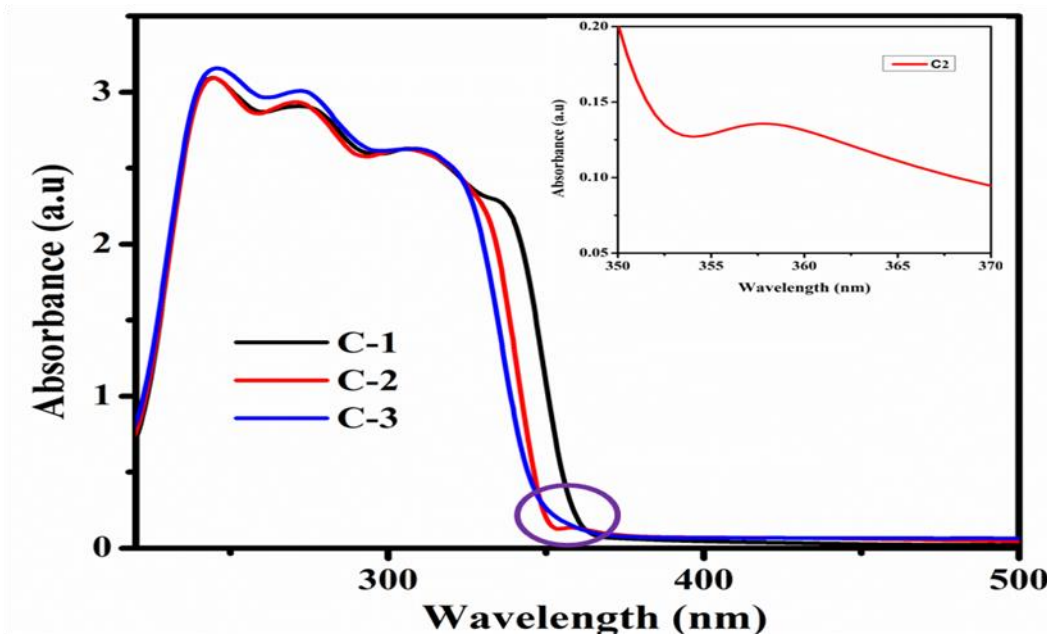


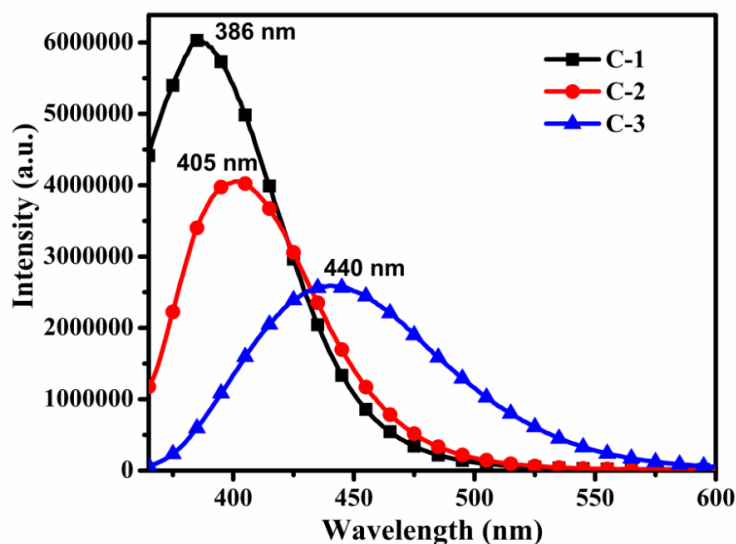
Figure 3.1: UV–Vis absorbance spectra of terpy derivatives (C1–C3) in DCM. Inset: enlarged the absorbance spectrum of C-2.

These absorption bands were due to strong  $\pi-\pi^*$  transitions of delocalized  $\pi$  electrons in the terpy derivatives [30–31]. These are the vibronic bands transitions. All terpy derivatives show three absorption peaks, where absorption peaks of **C-1** and **C-2** occurs in same wavelength region as 244, 270, and 308 nm. However, compared to **C-1** and **C-2**, the maximum absorption peaks of **C-3** shifted towards longer wavelength (red-shift) and noticed at 246, 272 and 309 nm. This is because of  $\pi-\pi^*$  transitions dominate in compound **C-3** [32–34]. An additional peak for **C-2** has also been observed at 358 nm. Compound **C-3** exhibits a modest red-shift due to presence of more electron donating methoxy groups that increase the amount of delocalization, and hence low energy absorption. Photophysical properties of the synthesised terpy derivatives in DCM were characterised by UV-Vis absorbance spectra, PL spectra and fluorescence lifetime characterization at room temperature as summarized in Table 3.1.

**Table 3.1: Photophysical and thermal data of terpy derivatives**

Compounds	Absorption $\lambda_{\max}$ (nm)	Emission	Emission	Fluorescence Lifetime (ns)	$T_m$ (°C)
		(PL) $\lambda_{\max}$ (nm)	(Fluorescence) $\lambda_{\max}$ (nm)		
C-1	244, 270, 308	386	406	0.35	167
C-2	244, 270, 308	405	415	1.55	224
C-3	246, 272, 309	440	471	0.29	187

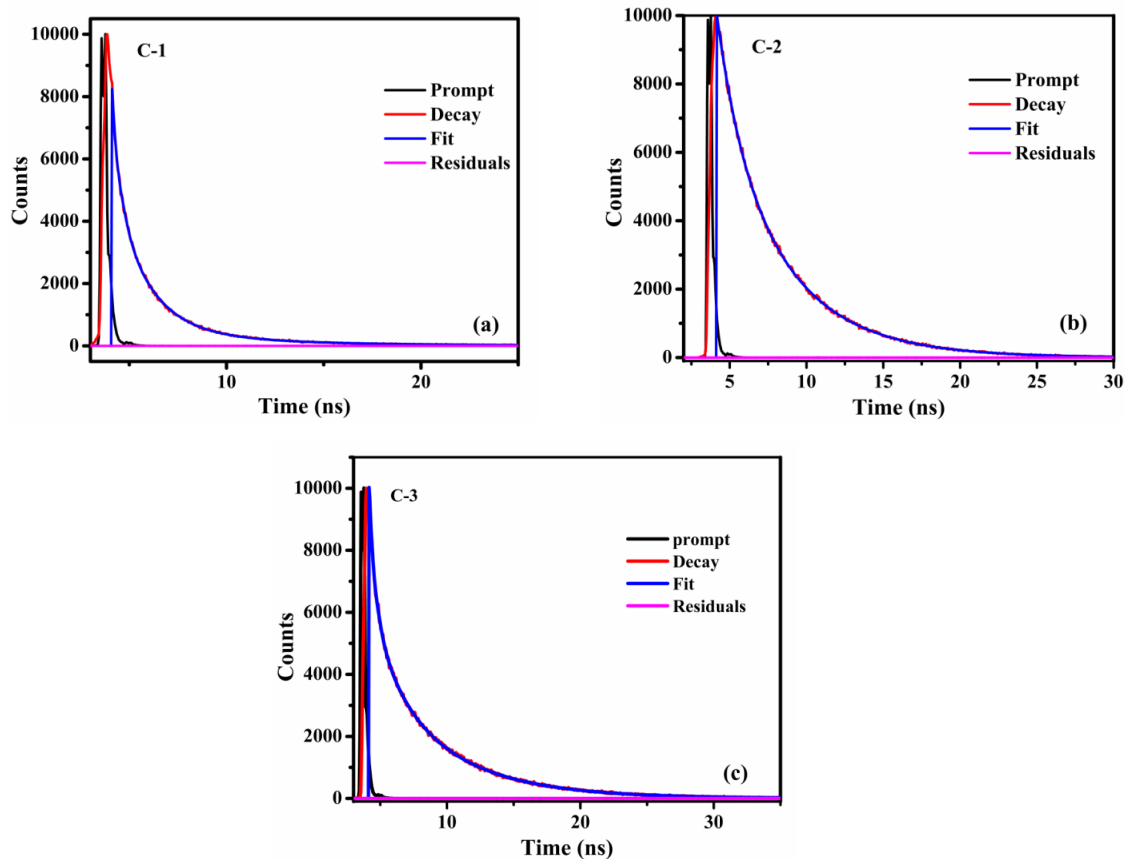
### 3.3.2 Photoluminescence studies



**Figure 3.2:** Photoluminescence spectra of terpy derivatives at solution (a) state and thin film (b) recorded at an excitation wavelength of 308 nm.

Figure 3.2 shows the PL spectra of the terpy derivatives studied at the excitation wavelength of 308 nm. 1 M concentration was used for the emission study with the 10 ms integration time and standard excitation powers for all terpy derivatives. It depicts the emission band that occurs in the visible region of the electromagnetic spectrum. The maximum emission peaks were observed at 386, 405 and 440 nm for **C-1**, **C-2** and **C-3**, respectively. Trimethoxyphenyl substituent on terpyridine has wide broadened emission spectrum (365–600 nm) compared to that of methylphenyl and 2-furyl substituent on terpyridine (365–525 nm). The presence of stronger electron donor group has resulted to the bathochromic shift in the blue region as confirmed by UV–Vis absorption spectra [35–37]. Among all the three compounds, **C-3** exhibits a longest emission observed at 440 nm. From the above results, it can be concluded that terpy derivatives are good photoluminescent materials with red-shifted emission when adding the electron-donating functional groups at the 4'-position of the terpy.

### 3.3.3 Fluorescence lifetime characterizations



**Figure 3.3: Fluorescence lifetime decay curves for (a) C-1, (b) C-2 and (c) C-3. The emission wavelength was 406 nm for C-1 and C-2; and 468 nm for C-3**

Luminescence lifetime plays a key role in determining the performance of luminescent materials. Fluorescence lifetime is the time spent by a fluorophore in the excited state before returning to the ground state by emitting a photon [38]. The luminescence decay curves of terpy derivatives are shown in Figure 3.3. The luminescent lifetime is measured by  $1/e$  point of the decay curve with the exponential decay:  $I = I_0e^{-t/\tau}$ , where  $I_0$  is the intensity (when  $t = 0$ ),  $t$  is time after the absorption, and  $\tau$  is lifetime of the fluorophores. The measured life times of **C-1** and **C-2** at the emission wavelength of 406 nm were 0.35 and 1.55 ns respectively, whereas **C-3** showed the fast life time of 0.29 ns at the emission wavelength of 468 nm. The excitation wavelength was 308 nm for the three terpy derivatives.



### 3.3.4 Differential scanning calorimetry analysis

Thermal stability of terpy derivatives were examined using DSC under nitrogen atmosphere as shown in Figure 3.4. The samples were heated up from room temperature to beyond the melting temperature at the scanning rate of  $10\text{ }^{\circ}\text{C min}^{-1}$ . DSC thermogram of all three terpy derivatives showed an endothermic peak, which indicates the  $T_m$  of the samples. The observed melting temperatures were 167, 224 and  $187\text{ }^{\circ}\text{C}$  for **C-1**, **C-2** and **C-3**, respectively, as listed in Table 3.1. It was observed that **C-2** is more stable than that of **C-1** and **C-3**, which can be due to the strong aromatic interaction between 2-furyl and terpyridine. The sharp melting points indicate that the synthesised terpy powders were of high purity [39, 40]. In DSC, no obvious  $T_g$  were observed for any of the three terpy derivatives, indicating non-amorphous nature of the compounds.

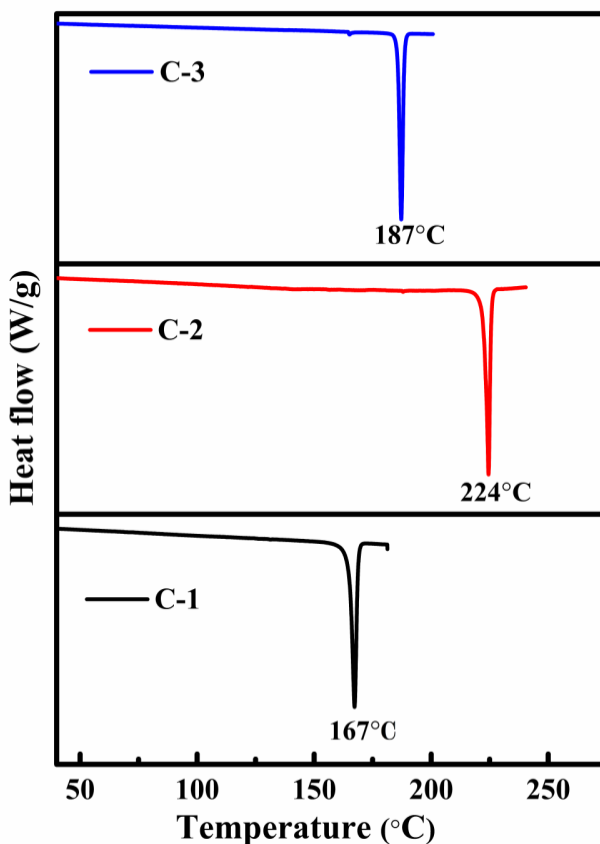
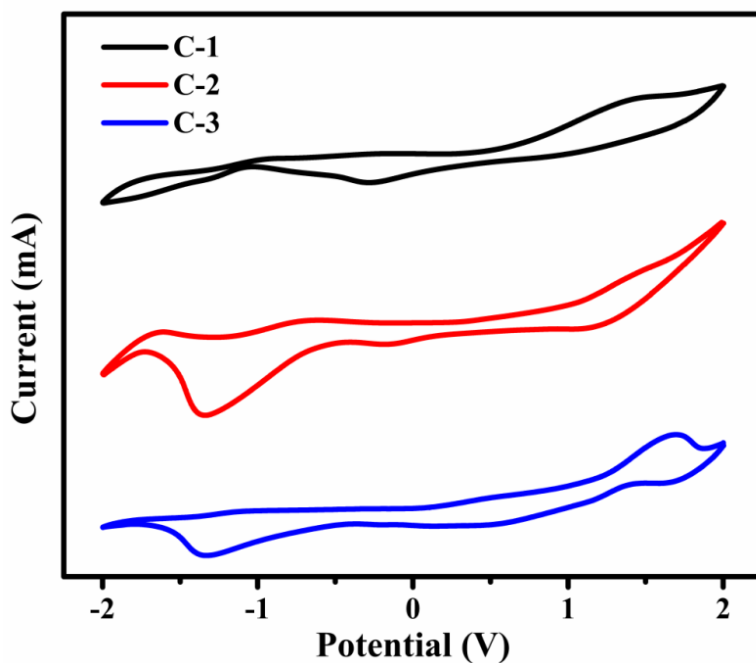


Figure 3.4: DSC plots of terpy derivatives with the scanning rate of  $10\text{ }^{\circ}\text{C min}^{-1}$

### 3.3.5 Electrochemical analysis

Cyclic voltammetry (CV) is a dynamic electrochemical method to investigate the electrochemical behaviour as well as to estimate the HOMO and LUMO energy levels. The electrochemical properties of terpy derivatives were analysed using CV in the potential range of  $-2.0$  to  $+2.0$  V in  $0.1$  M tetrabutylammonium perchlorate (TBAP)/ dichloromethane solution at a scan rate of  $0.1 \text{ Vs}^{-1}$  as shown in Figure 3.5. All terpy derivatives showed reversible redox process, indicating that the derivatives are electrochemically active [41]. The values of HOMO and LUMO levels of three compounds were calculated according to the empirical formula and its corresponding electrochemical data are listed in Table 3.2.  $E_{\text{HOMO}} = -(E_{\text{ox}} + 4.40) \text{ eV}$  and  $E_{\text{LUMO}} = -(E_{\text{red}} + 4.40) \text{ eV}$  respectively, where  $E_{\text{ox}}$  and  $E_{\text{red}}$  are oxidation and reduction peak potential, respectively.



**Figure 3.5:** Cyclic voltammogram of terpy derivatives at the potential between  $-2.0$  V to  $+2.0$  V in  $0.1$  M TBAP/DCM solution at scan rate of  $100 \text{ mVs}^{-1}$

Electrochemical band gap ( $E_g$ ) of the material was calculated by determining the difference between  $E_{\text{HOMO}}$  and  $E_{\text{LUMO}}$  [42]. HOMO energy levels of **C-1**, **C-2** and **C-3** were calculated as  $5.96$ ,  $5.86$  and  $6.08$  eV respectively, measured from the oxidation peaks of the compounds.

LUMO energy levels of **C-1**, **C-2** and **C-3** were evaluated to be -3.01, -3.04 and -3.06 eV, respectively. The  $E_g$  of the materials were estimated to be 2.95, 2.82 and 3.02 eV for **C-1**, **C-2** and **C-3** respectively. It was observed that HOMO energy levels increased from 5.96 eV to 6.08 eV and the LUMO energy values are in the range of 3.01 eV to 3.06 eV. These modulations of HOMO levels are confirming that the terpy derivatives are electron rich in nature. The calculated band gap values of the terpy compounds have reasonable agreement with recently reported by Wan *et al.* for fluorenyl anthracene [43]. From the  $E_g$  and HOMO-LUMO values, it is noteworthy to propose that synthesised terpy derivatives can be effectively used as blue emitters in fluorescent OLED applications [44, 45].

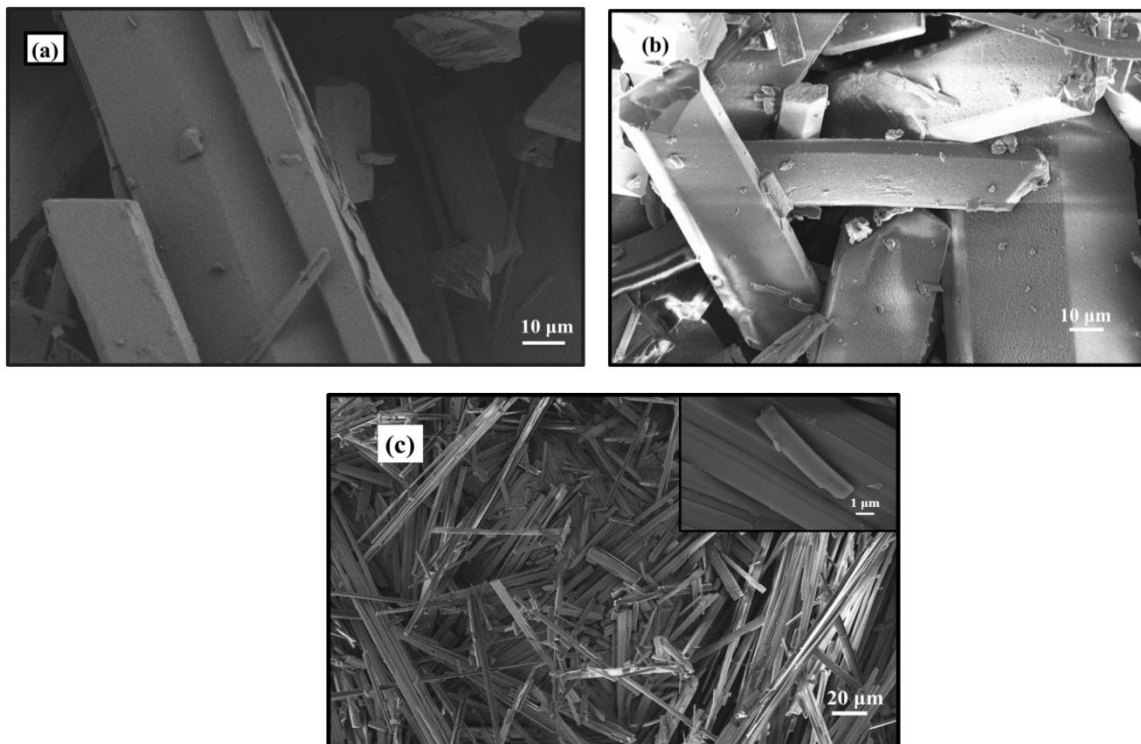
**Table 3.2: Electrochemical data of terpy derivatives**

Compounds	$E_{ox}$ (V)	$E_{red}$ (V)	HOMO (eV)	LUMO (eV)	Electrochemical band gap ( $E_g$ ) (eV)
C-1	1.57	-1.38	5.96	3.01	2.95
C-2	1.47	-1.35	5.86	3.04	2.82
C-3	1.69	-1.33	6.08	3.06	3.02

### 3.3.6 Scanning electron microscopy

Surface morphology of the synthesised terpy compounds were analysed by field emission scanning electron microscopy (FE-SEM), as shown in Figure 3.6. Before scanning the samples in SEM, the samples were coated with gold sputtering coating of about 10 nm to avoid the discharge. Imaging was performed at electronic high tension (EHT) values between 2.0 and 5.0 kV. SEM micrograph of **C-1** as shown in Figure 3.6 (a), exhibits smooth and hexagonal morphology. The powder has hexa symmetry at the edges around 80-100  $\mu\text{m}$  in length (see Figure 3.6 (b)). The homogeneous distribution of **C-3** derivative powder about 200  $\mu\text{m}$  in length and less than 1  $\mu\text{m}$  diameter sized rods are shown in Figure 3.6 (c); it shows that three terpy compounds have smooth morphology along their length, confirming consistency of the rods

reported in literature that good crystalline nature materials give high luminescence quantum yield. Chen *et al.* suggested that luminescence of the materials increase with crystalline nature [46]. Further, it can be inferred from the SEM micrographs that the rods are well distributed without exhibiting formation like cluttering, and distortion.



**Figure 3.6: SEM images of (a) C-1, (b) C-2 and (c) C-3. Inset: High magnification of C-3**

### 3.4 Summary

This chapter reports the synthesis and characterization of 4'-substituted 2,2':6',2''-terpyridine derivatives for blue fluorescent emitter OLEDs application. Their photophysical and electrochemical properties were investigated. The derivatives showed good thermal stability, significant emission in the blue region (380–440 nm) and fast fluorescence lifetime (0.35, 1.55 and 0.29 ns for **C-1**, **C-2** and **C-3**, respectively). The methoxy-substituted terpyridine derivative showed high red-shift with respect to methyl phenyl and 2-furyl substituted terpy derivatives in the blue region of electromagnetic spectrum. This may be due to a smaller reorganization energy associated with the charge transfer transition of trimethoxyphenyl, which is more applicable for

blue fluorescent emitters. The calculated HOMO and LUMO values of these derivatives can be used for electron-transporting and electroluminescent materials.

### 3.5 References

- [1] Chou C.H., Chen F.C, *Nanoscale*, 2014, 6: 8444–8458.
- [2] Koldemir U., Graham K.R., Salazar D.H., McCarley T.D., Reynolds J.R., *J. Mater. Chem.*, 2011, 21: 6480–6482.
- [3] Schmidbauer S., Hohenleutner A., Konig B., *Adv. Mater.*, 2013, 25: 2114–2129.
- [4] Stolz S., Scherer M., Mankel E., Lovrincic R., Schinke J., Kowalsky W., *Appl. Mater. Interfaces*, 2014, 6: 6616–6622.
- [5] White M.S., Kaltenbrunner M., Glowacki E.D., Gutnichenko K., Kettlgruber G., Graz I., Aazou S., *Nat. Photonics*, 2013, 7: 811–816.
- [6] Sekitani T., Nakajima H., Maeda H., Fukushima T., Aida T., Hata K., Someya T., *Nat. Mater.*, 2009, 8: 494–499.
- [7] Krasnov A.N., *Appl. Phys. Lett.*, 2002, 80: 3853.
- [8] Reineke S., Lindner F., Schwartz G., Seidler N., Walzer K., Lussem B., Leo K., *Nature*, 2009, 459: 234–239.
- [9] Ikawa S., Yagin S., Maeda T., Nakazumi H., Sakurai Y., *J. Lumin.*, 2014, 155: 368–373.
- [10] Velmurugan G., Venuvanalingam P., *Dalton Trans.*, 2015, 44: 8529–8542.
- [11] Bolink H.J., Cappelli L., Coronado E., Gavina P., *Inorg. Chem.*, 2005, 44: 5966–5968.
- [12] Morgan G.T., Burstall F.H., *J. Chem. Soc.*, 1932, 20–30.
- [13] Storrier G.D., Colbran S.B., Craig D.C., *J. Chem. Soc., Dalton Trans.*, 1997: 3011–3028.
- [14]. Xu R.-P., Li Y.-Q., Tang J.X., *J. Mater. Chem. C.*, 2016, 4: 9116–9142.

- [15] Chen P., Zhao L., Duan Y., Zhao Y., Xie W., Xie G., Liu S., Zhang L., Li B., *J. Lumin.*, 2011, 131: 2144–2149.
- [16] Yue S., Zhang S., Zhang Z., Wu Y., Wang P., Guo R., Chen Y., Qu D., Wu Q., Zhao Y., Liu S., *J. Lumin.*, 2013, 143: 619–622.
- [17] Wang M., Jin Y., Yang H., Fu H., Hu L., *RSC Adv.*, 2013, 3: 8211–8214.
- [18] Li B., Qin X., You J., Cong X., Lan J., *Org. Biomol. Chem.*, 2013, 11: 1290–1293.
- [19] He A., Zhong C., Huang H., Zhou Y., He Y., *J. Lumin.*, 2008, 128: 1291–1296.
- [20] Ji Z., Li S., Li Y., Sun W., *Inorg. Chem.*, 2010, 49: 1337–1346.
- [21] Schluetter F., Wild A., Winter A., Hager M.D., Baumgartel A., Frirbe C., Schubert U.S., *Macromolecules*, 2010, 43: 2759–2771.
- [22] Liu C.-L., Zheng C.-J., Liu X.-K., Chen Z., Yang J.-P., Li F., Ou X.-M., Zhang X.-H., *J. Mater. Chem. C*, 2015, 3: 1068–1076
- [23] Zhang B.-H., Tan G.-P., Lam C.-S., Yao B., Ho C.-L., Liu L.-H., Xie Z.-Y., Wong W.-Y., W.-Y. Ding W.-Y., Wang L.-X., *Adv. Mater.*, 2012, 24: 1873–1877.
- [24] Qureshi M., Sundar Manoharan S., Singh S.P., Mahapatra Y.N., *Solid State Commun.*, 2005, 133: 305–309.
- [25] Reineke., Lindner F., Schwartz G., Seidler N., Walzer K., Lussem B., Leo K., *Nature*, 2009, 459: 234–238.
- [26] Brown D.G., Sanguantrakun N., Schulze B., Schubert U.S., Berlinguett C.P., *J. Am. Chem. Soc.*, 2012, 134: 12354–12357.
- [27] Ardo S., Meyer G. *J. Chem. Soc. Rev.*, 2009, 38: 115–164.
- [28] Bomben P.G., Robson K.C.D., Berlinguette C.P., *Coord. Chem. Rev.*, 2012, 256: 1438–1450.

- [29] Naseri Z., Kharat A.N., Banavand A., Bakhoda A, Foroutannejad S., *Polyhedron.*, 2012, 33: 396–403.
- [30] Hobert S.E., Carney J.T., Cummings S.D., *Inorg. Chim. Acta*, 2001, 318: 89–96.
- [31] Yu T., Su W., Lia W., Hong Z., Hua R., Li M., Chu B., Li B., Zhang Z., Hu Z.Z., *Inorg. Chim. Acta.*, 2006, 359: 2246–2251.
- [32] Wang D., Xu Q-L, Zhang S., Li H-Y., Wang C.C., Li T.-Y., Jing Y.-M., Huang W., Zheng Y-X., Accorsi G., *Dalton Trans.*, 2013, 42: 2716–2723.
- [33] Constable E., *Chem. Soc. Rev.*, 2007, 36: 246–253.
- [34] Juris A., Campagna S., Bidd I., Lehn J.-M., Ziessel R., *Inorg. Chem.*, 1988, 27: 4007–4011.
- [35] He A., Zhong C., Huang H., Zhou Y., He Y., Zhang H., *J. Lumin.*, 2008, 128: 1291–1296.
- [36] Striplin D.R., Crossby G.A., *Coord. Chem. Rev.*, 2001, 211: 163–175.
- [37] Shaw J.R., Schmehl R.H., *J. Am. Chem. Soc.*, 1991, 113: 1046–1047.
- [38] Su S-J., Cai C., Takamatsu J., Kido J., *Org. Electron.*, 2012, 13: 1937–1947.
- [39] Kambe H., Horie K., Suzuki T., Therm T., *Anal. Calorim.*, 1972, 4: 461–469.
- [40] Chiu C-W., Chow T.J., Chuen C-H, Lin H-M, Tao Y-T., *Chem. Mater.*, 2003, 15: 4527–4532.
- [41] Scholz., Fritz., *Electroanalytical Methods. Guide to Experiments and Applications*, Springer-Verlag, Berlin, 2002.
- [42] Misra A., Kumar P., Srivastava R., Dhawan S.K., Kamalasanan M.N., Chandra S., *Indian J. Pure Appl. Phys.*, 2005, 43: 921–925.
- [43] Wan W., Du H., Wang J., Le Y., Jiang H., Chen H., Zhu S., Hao J., *Dyes Pigment*, 2013, 96: 642–652.

- [44] Maestri M., Armaroli N., Balzani V., Constable E.C., Thompson A.M.W.C., *Inorg. Chem.*, 1995, 34: 2159–2161.
- [45] Feng X., Hu J-Y., Tomiyasu H., Seto N., Redshaw C., Elsegoodd M.R.J., Yamato T., *Org. Biomol. Chem.*, 2013, 11, 8366–8374.
- [46] Chen W., Peng Q., Li Y., *Adv. Mater.*, 2008, 20: 2747–2750.



## CHAPTER 4

### **The transition from sky blue to deep-green fluorescent Zn(II)-based 4'-aryl substituted 2,2':6',2''-terpyridine complexes for OLEDs**

In this chapter, the design, synthesis and characterization of three novel 4'-aryl substituted blue-to-green fluorescent Zn(II)-based terpy complexes ( $\text{Zn}(\text{L}_1\text{-L}_3)$ ) have been described. The photophysical, thermal and electrochemical properties of these complexes have been thoroughly studied. In addition, the geometric optimisation and electronic structure of the complexes have been assessed by DFT. Dual characteristics of optical behaviour have also been observed, such as Zn(II) complexes exhibiting a deep blue-to-green fluorescence in crystalline form, while it is sky-to-deep blue in DMSO. The photophysical behaviour reveals the potential charge transfer to  $\pi\text{-}\pi^*$  and  $n\text{-}\pi^*$  states due to ILCT.

#### **4.1 Introduction**

In recent years, several types of organic and polymeric luminescent materials have been explored extensively for the fabrication of OLEDs as hole transport layers, electron injection-transport layers, dopants and hosts [1–4]. New luminescent materials are being explored for their attractive custom-tailored designs and versatility of synthesis [5–11]. To fabricate efficient white OLEDs requires the composition of three primary colours that include red, green, and blue emitters with equal stability, colour purity and high efficiency [12, 13]. Though red and green light emitters have been studied widely, the blue light emitters are relatively less studied because of their low highest-occupied molecular orbital (HOMO) energy levels and intrinsic wide band gaps, which hinder the charge transport between the adjacent layers in OLEDs [14, 15].

To realize true solid-state OLEDs, research is being focused on developing new blue-emitting fluorescent materials. In previous chapter it was discussed about the photophysical, thermal and electrochemical properties of terpy ligands with various electron-donating substituents at 4'-aryl position in terpyridine [16–20]. However, such properties of these pristine organic luminescent materials need to be improved further to achieve better and more efficient fluorescent OLEDs. These issues can be overcome by integrating a metal with organic materials to form metal-ligand

coordination complexes, which enhance the performance of the OLEDs [21–23]. This can provide high stability and flexibility in the structural design of OLED applications and also unique optical and electronic properties [24]. Their unique properties, make these heavy metal ions, such as Pt(II), Os(II), Ir(III) and Pd(II), as suitable ligands to develop new electroluminescent materials [25–27]. Considering their abundance, cost-effectiveness, toxicity as well as easily tunable band gap, Zn(II) ions have been found to have more potential applications in OLEDs [28, 29]. In addition, the terpy derivatives of suitable substituents in the 4'-position feature interesting photophysical and electrochemical properties, which can help in the formation of stable metal-organic coordination complexes. Further, metal orbitals in the excited state induce new photophysical behaviour [30]. The terpy is well known for its high binding affinity towards di- and trivalent metal ions to form octahedral coordination complexes [31]. Moreover, the photophysical properties of Zn(II) bis-terpy complexes can easily be altered by simply changing the substituent at the 4'-position of the ligand [32]. There are many reports on the synthesis and characterization of Zn(II)-based terpy complexes for luminescent applications [33]. Schlutter *et al.* studied the electro-optical properties of self-assembled metallo-polymers containing electron-donating and electron-withdrawing Zn(II)-based bis-terpy derivatives. They observed emissions ranging from bright blue to orange, which are strongly dependent on the nature of the  $\pi$ -conjugated bis-terpy system [34]. Recently, Fu Tang *et al.* studied small molecules of tetraphenylethene for sky blue fluorescent OLED applications [35]. To the best of our knowledge, there has been no clear report of photophysical, thermal, and electrochemical properties of Zn(II)-based terpy and its functional groups given. Hence, recent research demonstrates that the synthesis of deep blue and green fluorescent materials for OLED applications with easy colour tunability and detailed studies of photophysical, thermal and electrochemical properties is still a challenge [36, 37].

This chapter details about the synthesis and investigation of three novel blue-to-green fluorescent Zn(II)-based terpy complexes for fluorescent OLED applications and their photophysical, thermal and electrochemical properties. Finally, a complex of a sky-to-deep blue fluorescence in DMSO and a deep blue-to-green luminescence in the crystalline states were synthesised

successfully. Therefore, these complexes can be utilized as electron transport and EL materials for both blue and green fluorescent OLED applications.

## 4.2 Experimental

### 4.2.1 Syntheses of Zn(II) complexes: Zn(L<sub>1</sub>-L<sub>3</sub>)

The synthesis route of terpyridine ligands **C**<sub>1</sub> and **C**<sub>2</sub> was carried out in the early chapter and published elsewhere [20]. Ligand **C**<sub>3</sub> was also synthesised using a procedure similar to that performed for ligands **C**<sub>1</sub> and **C**<sub>2</sub>. The following section deals that the preparation of metal complexes.

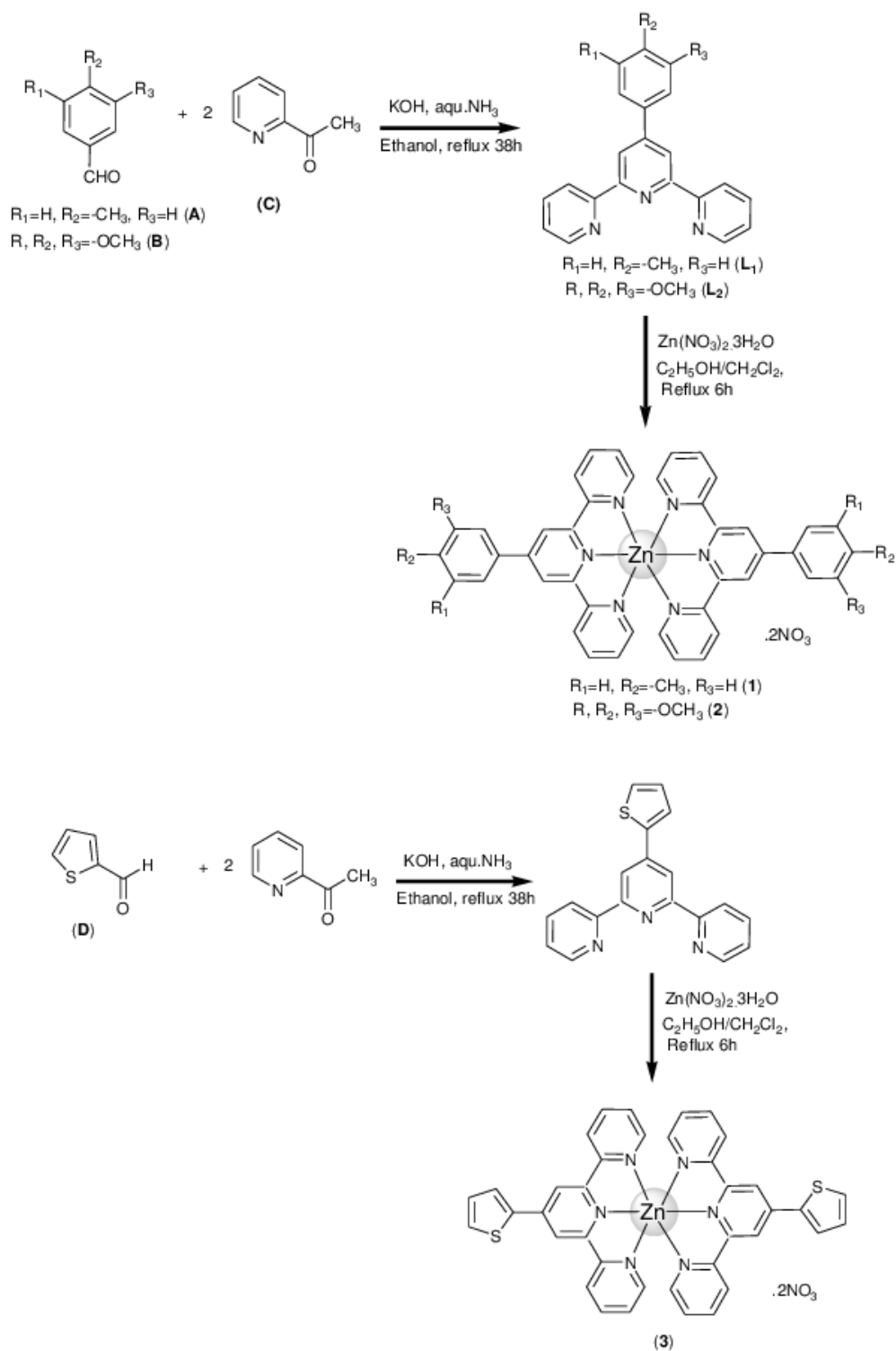
The complexes were prepared by the following method, an ethanolic solution (15 ml) of Zn(NO<sub>3</sub>)<sub>2</sub>·3H<sub>2</sub>O (0.24 g, 1.0 mmol) was added dropwise to a DCM solution (15 ml) of the terpyridine ligand (4-mephtpy, 0.32 g; 3,4,5-tmphtpy, 0.35 g; 1.0 mmol, 4-thtpty, 0.28 g; 1.0 mmol) under vigorous stirring. The reaction mixture was refluxed for 6 hours to obtain a crystalline solid of the precursor complex and washed with ice-cold ethanol followed by diethyl ether and finally dried in a vacuum. Scheme 4.1 shows the synthetic route of Zn(L<sub>1</sub>-L<sub>3</sub>) complexes.

### 4.2.2 [Zn(L<sub>1</sub>)<sub>2</sub>].NO<sub>3</sub>: [Zn(L<sub>1</sub>)]

Yield: 79%, T<sub>m</sub>. 384 °C, Anal. Calcd for C<sub>44</sub>H<sub>34</sub>N<sub>8</sub>O<sub>6</sub>Zn: C, 63.20; H, 4.10; N, 13.40. Found: C, 63.31; H, 4.23; N, 13.52. IR (KBr):  $\nu = 3102$  (w), 2943 (w), 1602 (m), 1548 (w), 1471 (s), 1403 (w), 1362 (m), 1281 (s), 1123 (m), 1007 (m), 886 (m), 832 (m), 787 (s), 719 (w), 672 (w), 653 (m), 698 (m) cm<sup>-1</sup>. MS (ESI, *m/z*): 656.12 [M-2NO<sub>3</sub>]<sup>+</sup>.

### 4.2.3 [Zn(L<sub>2</sub>)<sub>2</sub>].NO<sub>3</sub>: [Zn(L<sub>2</sub>)]

Yield: 81%. T<sub>m</sub>. 313 °C, Anal. Calcd for C<sub>48</sub>H<sub>42</sub>N<sub>8</sub>O<sub>12</sub>Zn: C, 58.33; H, 4.28; N, 11.34. Found: C, 58.42; H, 4.23; N, 11.37. IR (KBr):  $\nu = 3103$  (w), 2943 (w), 2838 (m), 1602 (m), 1548 (w), 1471 (s), 1402 (w), 1364 (m), 1271 (s), 1123 (m), 1007 (m), 886 (m), 832 (m), 787 (s), 719 (w), 677 (w), 654 (m), 692 (m) cm<sup>-1</sup>. MS (ESI, *m/z*): 864.27 [M-2NO<sub>3</sub>]<sup>+</sup>.



Scheme 4.1: Synthetic route of Zn(L<sub>1</sub>-L<sub>3</sub>) complexes

#### 4.2.4 Zn(L<sub>3</sub>)<sub>2</sub>·NO<sub>3</sub>: [Zn(L<sub>3</sub>)]

Yield: 76%, T<sub>m</sub>. 370 °C, Anal. Calcd for C<sub>38</sub>H<sub>26</sub>N<sub>8</sub>O<sub>6</sub>SRu: C, 57.91; H, 3.33; N, 14.22; S, 4.12. Found: C, 57.98; H, 3.38; N, 14.34; S, 4.12. IR (KBr):  $\nu = 3748$  (w), 3567 (w), 3077 (w), 1605 (m), 1553 (m), 1465 (m), 1419 (m), 1419 (m), 1218 (w), 1010 (s), 848 (w), 776 (s), 717 (s), 684 (m) cm<sup>-1</sup>. MS (ESI, *m/z*): 664.11 [M-2NO<sub>3</sub>]<sup>+</sup>.

### 4.3 Quantum calculation of Zn(L<sub>1</sub>-L<sub>3</sub>) complexes

The geometry optimization and electronic structure of the Zn(L<sub>1</sub>-L<sub>3</sub>) complexes were performed by the DFT using a B3LYP/def2-TZvP basis set with a Gaussian-09 program [37]. The frontier molecular orbitals (FMOs) along with the individual contributions of the Zn(II) complexes with fully optimized is shown in Figure 4.1. In FMOs, there is no charge contribution from Zn(II) to terpy ligands or vice-versa due to the filled d<sup>10</sup> electronic configuration. Hence, the involvement of charge transfer is mainly due to intraligand ( $\pi-\pi^*$ ) charge transition (ILCT) states [38].

In all the complexes, the HOMO energy level is mostly localized on the 4'- aryl substituent ring, whereas the LUMO energy is localized on the terpy ring. Therefore, the electronic excitations and emission processes of the Zn(II) complexes are mainly attributed to the  $\pi-\pi^*$  transitions of the phenyl substituted terpyridine chromophores [39]. It has been observed that the molecular orbitals of Zn(II) are more stable as they are located on lower energy levels. In addition, the LUMO+1 and HOMO-1 orbitals of the three complexes are given in the appendix B information which further confirms the charge transfer processes in the complexes ( see Appendix B, B21.1–B2.3).

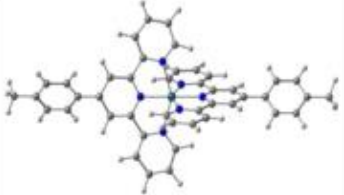
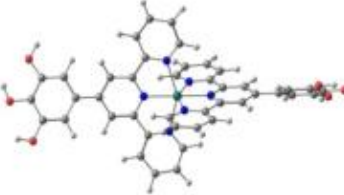

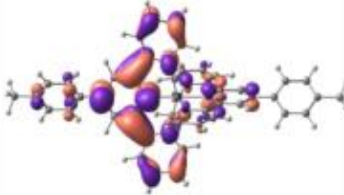
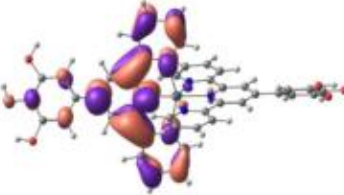
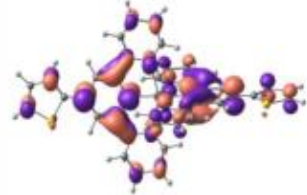
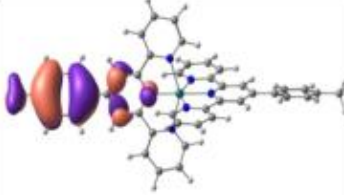
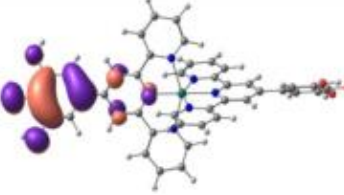
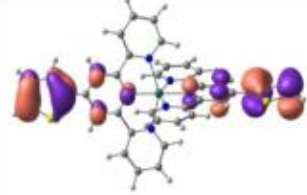
Complex	Zn(L <sub>1</sub> )	Zn(L <sub>2</sub> )	Zn(L <sub>3</sub> )
Geometry			
LUMO			
HOMO			

Figure 4.1: Optimized geometry and electronic distribution of the frontier orbitals for Zn(L<sub>1</sub>-L<sub>3</sub>) complexes

## 4.4 Results and discussion

### 4.4.1 Photophysical properties

The absorption spectra of the Zn(II) complexes in a DMSO solution are shown in Figure 4.2. The intense absorption bands of the three complexes were observed in the UV range between 240 and 380 nm, and are due to the spin-allowed ILCT states with the absorption bands of the free ligands (see Table 4.1). Furthermore, in complexes **Zn(L<sub>1</sub>)** and **Zn(L<sub>3</sub>)** there were observed three maximum absorption peaks in the UV region; among them two absorption peaks at 273, and 310 nm come under the same wavelength region and the third peak appeared in different wavelength regions as 343 and 351 nm for **Zn(L<sub>1</sub>)** and **Zn(L<sub>3</sub>)** complexes, respectively.

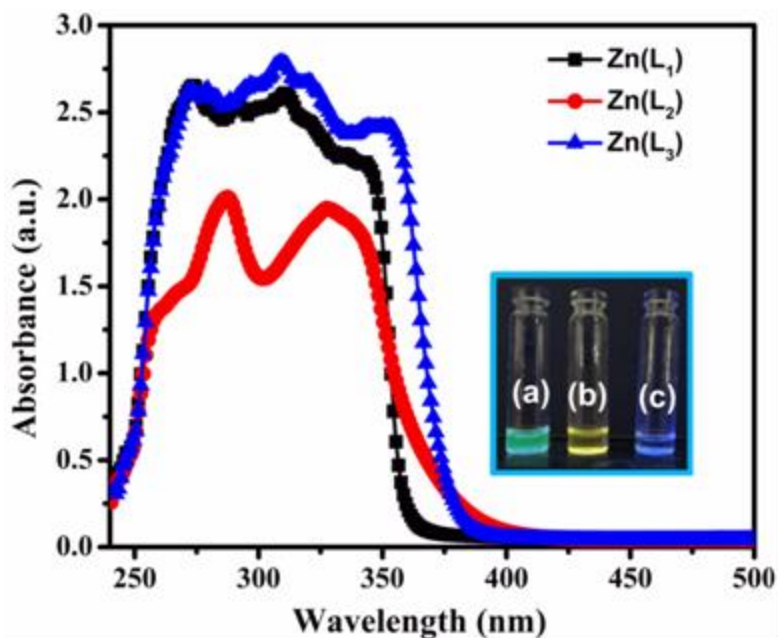


Figure 4.2: UV-Vis absorbance spectra of Zn(II) complexes in DMSO solution. Inset: digital photographs of the quartz cuvette showing fluorescence of (a) Zn(L<sub>1</sub>), (b) Zn(L<sub>2</sub>) and (c) Zn(L<sub>3</sub>) in DMSO solution after exposing the solution to UV radiation

These absorption peaks are mainly due to the ILCT of the  $\pi-\pi^*$  and  $n-\pi^*$  transitions. As expected, the electron-donating group of 2-thiophenyl at the 4'-position of the terpy ring in the **Zn(L<sub>3</sub>)** complex shifts towards the longer wavelength compared to the **Zn(L<sub>1</sub>)** complex, resulting in an 8 nm bathochromic-shift in the absorption spectrum. The absorption spectra of the **Zn(L<sub>1</sub>)** and **Zn(L<sub>3</sub>)** complexes are almost identical, which suggests that the same transitions take place in these complexes. However, the maximum absorption peaks of the **Zn(L<sub>2</sub>)** complex were observed at 287 and 327 nm due to the  $\pi-\pi^*$  and the  $n-\pi^*$  of the ILCT. Furthermore, an additional shoulder band was observed around 253 nm, and this is due to the  $n-\pi^*$  transition of the terpy ligands. The absence of a third peak around 345 nm in the **Zn(L<sub>2</sub>)** complex could be accounted for by a forbidden energy transition between Zn(II) and a 3,4,5-trimethoxyphenyl substituent. The **Zn(L<sub>2</sub>)** complex shows a bathochromic shift that confirms its electron-donating nature when compared to the **Zn(L<sub>1</sub>)** and **Zn(L<sub>3</sub>)** complexes, which can be further verified through the highest-occupied molecular orbital (HOMO) and the lowest-unoccupied molecular orbital (LUMO) energy levels of the complexes. Son *et al.* have studied a series of electron-donating substituents in the 4'-position of the oxazolylphenolate ligand into the Zn(II) complexes

and reported that the electron-donating groups can induce a large red-shift in the emission spectrum [40]. This red shift of the absorption bands could be attributed to a decrease in the LUMO energy values of the complexes [41]. As reported in the literature, the contribution of  $Zn^{2+}$  ions appears to be distinctly negligible [42–44]. The charge transfer from Zn(II) to terpyridine MLCT can be excluded and hence it mainly originates due to the ILCT states. The variation of the first derivative of the optical absorption intensity with respect to the illuminated photon energy of the complexes rises to the optical band gap [see Appendix B, B2.4–B2.6]. The maximum derivatives of **Zn(L<sub>1</sub>)**, **Zn(L<sub>2</sub>)** and **Zn(L<sub>3</sub>)** appear at 3.51, 3.54 and 3.40 eV, respectively (see Table 4.1).

**Table 4.1: Photophysical and fluorescence lifetime data of Zn(II) complexes at room temperature**

Complexes	Absorption $\lambda_{\max}$ (nm)	Emission $\lambda_{\max}$ (nm)		Lifetime (ns)	Optical band gap ( $E_g$ ) (eV)
		Solution	Crystalline		
Zn(L <sub>1</sub> )	273, 310, 343	386	473	6.23	3.51
Zn(L <sub>2</sub> )	287, 327	450	535	3.98	3.54
Zn(L <sub>3</sub> )	273, 310, 351	417	470	5.82	3.40

#### 4.4.2 Photoluminescence studies

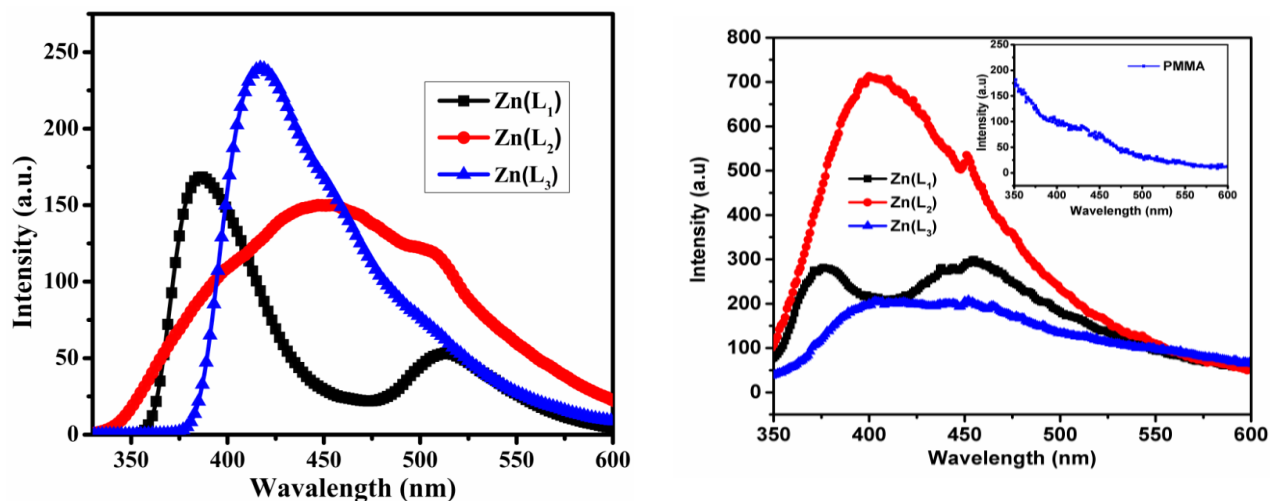
Figure 4.3 shows the PL spectra of the **Zn(L<sub>1</sub>-L<sub>3</sub>)** complexes in a DMSO solution recorded at room temperature with an excitation wavelength of 310 nm for the **Zn(L<sub>1</sub>)** and **Zn(L<sub>3</sub>)** complexes, whereas an excitation wavelength of 287 nm is used for the **Zn(L<sub>2</sub>)** complex. All the complexes show emission bands in the visible region of the electromagnetic spectrum. The maximum emission peaks were observed at 386, 450 and 417 nm for the **Zn(L<sub>1</sub>)**, **Zn(L<sub>2</sub>)** and **Zn(L<sub>3</sub>)** complexes, respectively, as summarized in Table 4.1. The fine fitting plots of the PL spectra for the three complexes are shown in the Appendix B (Figure B2.7-B2.9). The 3,4,5-trimethoxyphenyl substituent on terpy in the Zn(II) complex has a broader emission spectrum (365–600 nm) than the other Zn(II) complexes. This may be due to the more electron-donating



nature of the 3,4,5-trimethoxyphenyl substituent on Zn(II) of the **Zn(L<sub>2</sub>)** complex. Hence the **Zn(L<sub>2</sub>)** complex has a comparatively higher electronic transition than the **Zn(L<sub>1</sub>)** and **Zn(L<sub>3</sub>)** complexes. Furthermore, it is to be noticed that the shoulder peaks observed at 508 nm for the **Zn(L<sub>1</sub>)** and **Zn(L<sub>2</sub>)** complexes are absent for the **Zn(L<sub>3</sub>)** complex. This non-appearance of the shoulder peak around 508 nm in the **Zn(L<sub>3</sub>)** complex may be attributed to the forbidden charge transition between the thiophenyl ring and the Zn(II) ion. These shoulder band emissions are the traces of electron delocalization that arise due to the presence of heavy metal ions in the complexes and are not contributed by the MLCT process. It is noticed that the addition of electron donor group to the Zn(II) complex increases the wavelength shift towards the higher end with a shift of 24 and 64 nm for the **Zn(L<sub>3</sub>)** and **Zn(L<sub>2</sub>)** complexes, respectively, with respect to the **Zn(L<sub>1</sub>)** complex.

As already confirmed by the UV-Vis absorption spectra, the presence of the more electron-donating nature of 3,4,5-trimethoxyphenyl in the **Zn(L<sub>2</sub>)** complex contributed more to a bathochromic shift. The electronic transitions of both the absorption and emission states persist by the ILCT process. It is confirmed that the MLCT process neglect and the observed transition should arise from the ILCT state only because Zn(II) is a closed-shell d<sup>10</sup> ion, so that the interactions among the metal d orbitals can be ignored [45-46]. It can be concluded that the three Zn(II) complexes are excellent fluorescent emitters.

For a further understanding of the emission properties of these complexes, experiments were carried out with the solid-state PL spectra which are compared with the solution state PL spectra as shown in Fig. 4.3 For the solid state PL spectra, the prepared **Zn(II)** complexes were recorded at room temperature with an excitation wavelength of 350 nm for the **Zn(L<sub>1</sub>)** and **Zn(L<sub>3</sub>)** complexes, whereas the excitation wavelength was 327 nm for the **Zn(L<sub>2</sub>)** complex. The observed maximum emission



**Figure 4.3:** PL spectra of Zn(L<sub>1</sub>-L<sub>3</sub>) complexes in solution state (a) and thin film (b) recorded at excitation wavelength of 310 nm for Zn(L<sub>1</sub>) and Zn(L<sub>3</sub>) complexes, whereas 287 nm used for Zn(L<sub>2</sub>) complex

bands were at 473, 535 and 470 nm for the **Zn(L<sub>1</sub>)**, **Zn(L<sub>2</sub>)** and **Zn(L<sub>3</sub>)** complexes, respectively (see Table 4.1). When the solid state PL spectra are compared with the solution PL spectra, the maximum emission bands of the solid state PL of the **Zn(L<sub>1</sub>-L<sub>3</sub>)** complexes is obviously red-shifted by 87, 85, and 53 nm respectively with respect to the **Zn(L<sub>1</sub>-L<sub>3</sub>)** complexes in the DMSO solution. These significant red-shifted emissions depend on varying parameters like the planarity of a molecule (irregular arrangement in the crystalline state) and intermolecular forces such as  $\pi$ - $\pi^*$  stacking and excimers [47].

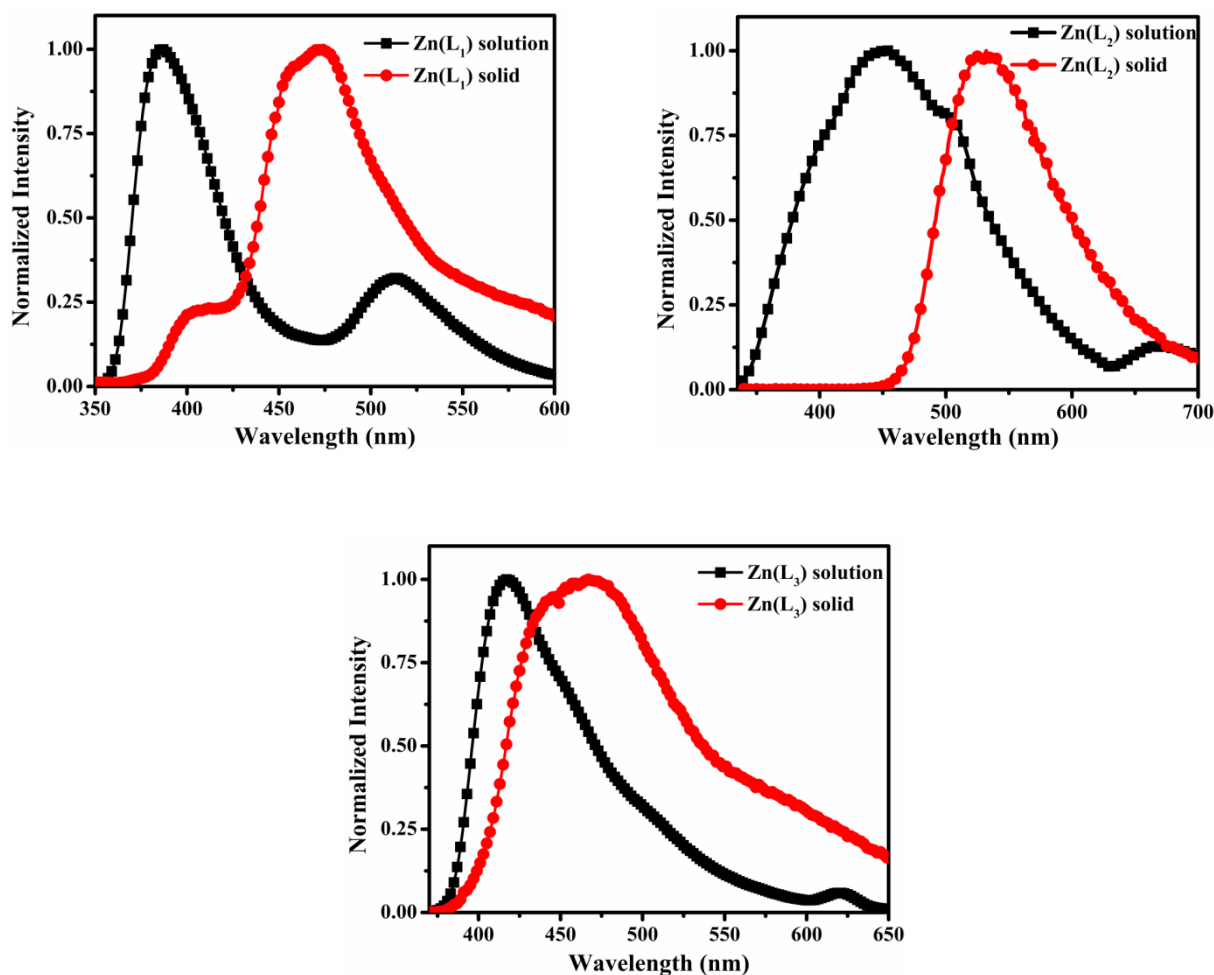
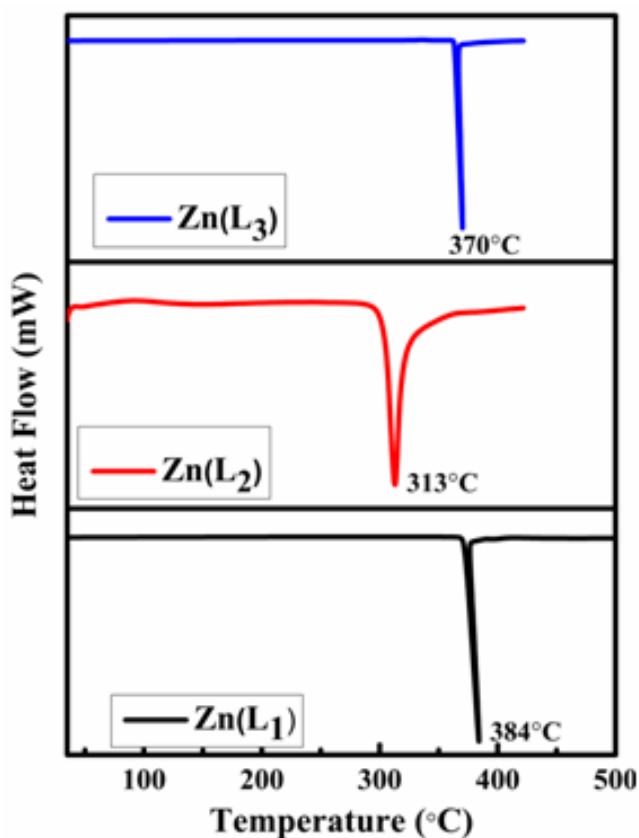


Figure 4.4: PL spectra of Zn(L<sub>1</sub>-L<sub>3</sub>) complexes; comparison of PL spectra for as prepared complexes with DMSO solution

#### 4.4.3 Thermal properties

The thermal stability of a material is essential for optoelectronic applications, which are directly related to device performance such as efficiency, lifetime, etc. To study the thermal behaviour, the TGA and DSC measurements were carried out for the three Zn(II) complexes. The thermal decomposition ( $T_d$ ), melting temperatures ( $T_m$ ), and glass transition temperatures ( $T_g$ ) of these complexes were systematically studied. Figure 4.5 shows the DSC plots of the **Zn(L<sub>1</sub>-L<sub>3</sub>)** complexes under a nitrogen atmosphere where the samples were heated up from room temperature to slightly above their melting point at a scanning rate of  $10\text{ }^\circ\text{C min}^{-1}$ . It is clear that

all the Zn(II) complexes show an endothermic peak, which depicts the melting point ( $T_m$ ) of the complexes. The observed melting temperatures were 384, 313 and 370 °C for **Zn(L<sub>1</sub>)**, **Zn(L<sub>2</sub>)** and **Zn(L<sub>3</sub>)**, respectively [see Table 4.2]. The melting of the **Zn(L<sub>1</sub>)** and **Zn(L<sub>3</sub>)** complexes exhibits sharp endothermic peaks, whereas a broad endothermic peak images for the **Zn(L<sub>2</sub>)** complex. Among the three complexes, **Zn(L<sub>1</sub>)** has a higher  $T_m$  than the other two Zn(II) complexes. This high  $T_m$  can be due to the strong interaction of a 4-methylphenyl terpy with Zn(II) to form a thermally more stable **Zn(L<sub>1</sub>)** complex.



**Figure 4.5:** DSC plots of Zn(L<sub>1</sub>-L<sub>3</sub>) complexes with the scanning rate of 10 °C min<sup>-1</sup> under nitrogen atmosphere

In the DSC thermograms, **Zn(L<sub>1</sub>)** and **Zn(L<sub>3</sub>)** show no signature of  $T_g$  and crystalline temperature ( $T_c$ ). However, the thermogram of the **Zn(L<sub>2</sub>)** complex shows a small inflection (exothermic peak) at a low temperature of around 50 °C, which might be due to the presence of volatile substrate elimination. To clarify the traces of  $T_g$  in the **Zn(L<sub>2</sub>)** complex, experiment were

repeated at a slow scan rate of 5 °C min<sup>-1</sup> and the same pattern was noticed as at 10 °C min<sup>-1</sup> (see Appendix B, Figure B2.10). In conclusion, all the three complexes are thermally very stable as well as crystalline.

Likewise, the TGA analyses of the three complexes are shown in Figure 4.6. It is noticed that no significant weight loss occurs at a low temperature and these complexes exhibit a good thermal stability with T<sub>d</sub> (thermal-decomposition temperature at a wt. % of 95 %) in the range of 287–370 °C. The observed weight losses of 5% were 370, 287 and 350 °C for the **Zn(L<sub>1</sub>)**, **Zn(L<sub>2</sub>)** and **Zn(L<sub>3</sub>)** complexes, respectively. The maximum rate of weight loss T<sub>d</sub> (thermal-decomposition temperature at a wt. % of 37%) occurs at 588 °C for **Zn(L<sub>1</sub>)** and **Zn(L<sub>3</sub>)**, whereas the maximum rate of weight loss T<sub>d</sub> (thermal-decomposition at a wt. % of 55%) takes place at 588 °C for the **Zn(L<sub>2</sub>)** complex. Furthermore, 38 wt. % of the residue composed of zinc ash remained above 590 °C for the **Zn(L<sub>1</sub>)** and **Zn(L<sub>3</sub>)** complexes. In conclusion, these Zn(II) complexes are greatly stable upon exposure to air and depicted high thermal stability in a nitrogen atmosphere.

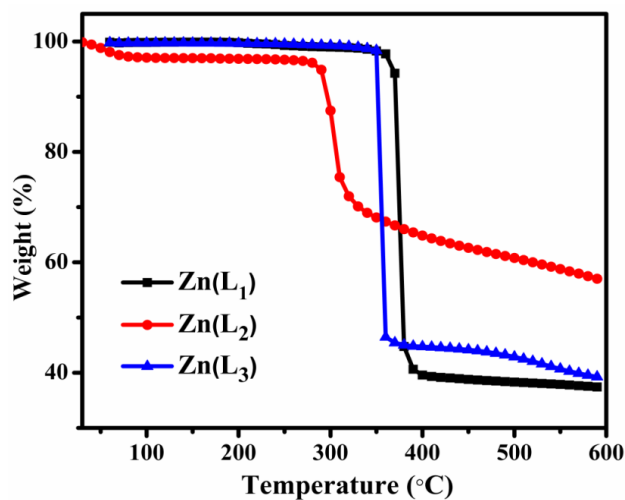
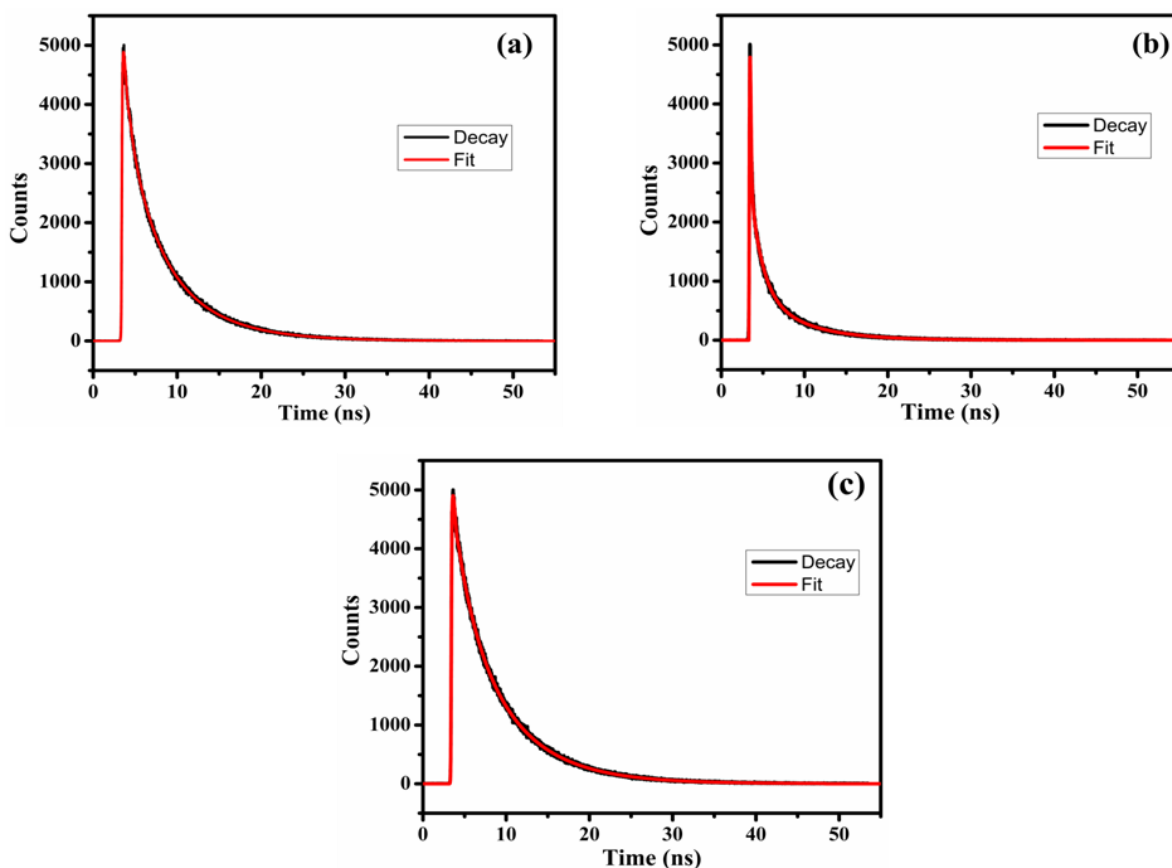


Figure 4.6: Thermogravimetric analysis of Zn(L<sub>1</sub>-L<sub>3</sub>) complexes under nitrogen atmosphere

#### 4.4.4 Fluorescence life time measurements

The lifetime of luminescence is an important parameter because the luminescent property of a material depends upon the luminescence lifetime. Figure 4.7 shows the fitted decay curve of **Zn(L<sub>1</sub>-L<sub>3</sub>)** complexes in DMSO by using the time-correlated single photon counting (TCSPC)

method under laser excitation at 402 nm with a 96.8 ps pulse width. The luminescence decay spectra of the three complexes were fitted by a single exponential decay function. The observed lifetimes are 6.23, 3.98 and 5.82 ns for **Zn(L<sub>1</sub>)**, **Zn(L<sub>2</sub>)** and **Zn(L<sub>3</sub>)**, respectively. The measured lifetime of the **Zn(L<sub>1</sub>)** complex is significantly longer than the other two Zn(II) complexes. It has been reported that the longer conjugation length in the ligand leads to a longer lifetime [48]. The short-lived fluorescence of **Zn(L<sub>2</sub>)** might be assigned to the strong intramolecular coupling interaction of trimethoxy fluorphores which lead to the fast charge transfer process. The lifetime on the nanoseconds time scale indicates that the three complexes have the fluorescent character of the luminescence.



**Figure 4.7: Fluorescence decay spectra of Zn(L<sub>1</sub>) (a), Zn(L<sub>2</sub>) (b) and Zn(L<sub>3</sub>) (c) complexes at the excitation wavelength of 402 nm with one-exponential fit residuals,  $\chi^2 = 1.003$**

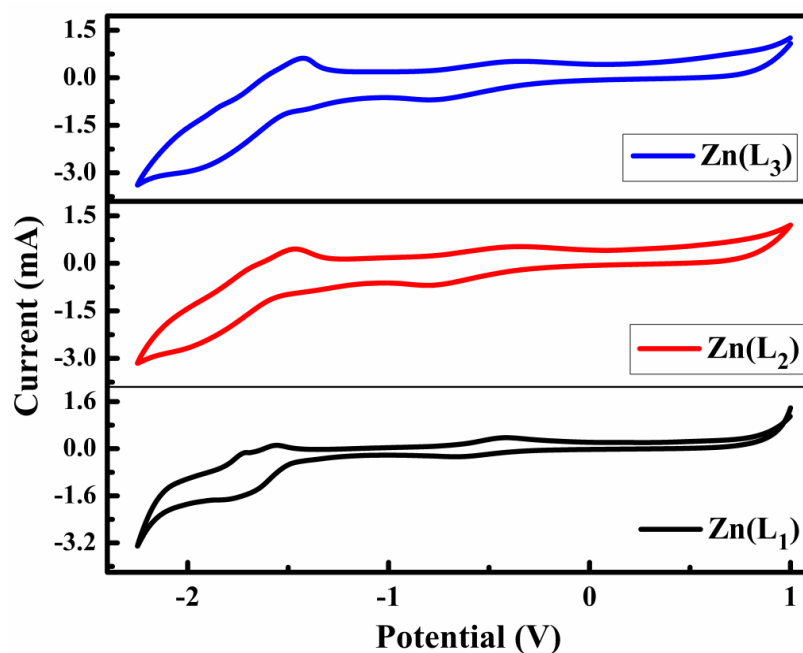
#### 4.4.5 Electrochemical analysis

The electrochemical behaviour of the three **Zn(L<sub>1</sub>-L<sub>3</sub>)** complexes were studied by cyclic voltammetry (CV) measurement in a three-electrode cell system. Platinum wire and platinum foil were used as the working and counter electrodes, respectively. A non-aqueous Ag/Ag<sup>+</sup> electrode was used as the reference electrode. 0.1 M of tetrabutylammonium perchlorate (TBAP) was dissolved in dimethylformamide (DMF) which was used as an electrolyte solution, and ferrocene (Fc) as an internal standard. Figure 4.8 shows the cyclic voltammogram of the **Zn(L<sub>1</sub>-L<sub>3</sub>)** complexes in the potential range of -2.2 to +1.0 V at a scan rate of 100 mV s<sup>-1</sup>. The detailed electrochemical properties of the three Zn(II) complexes are listed in Table 4.2. All the complexes show quasi-reversible reduction peaks and an onset reduction potential was observed in the range of -1.08 to -1.19 V. These reduction peaks are mainly attributed to the reduction of the terpy ligands within the complexes [49]. Owing to their electron-donating phenyl rings in the 4'-position of the terpy ligand in the Zn(II) complexes, a featured distinct reduction potential is observed towards the negative potential side. As expected, no significant oxidation processes were observed in the anodic scans upto +1.0 V. In an account of the stable d<sup>10</sup> electron configuration of the Zn(II) metal centers, it is difficult to observe the oxidation peak [50-51]. Hence, the estimation of the highest-occupied molecular orbital (HOMO) energy values and the electrochemical band gap for this material cannot be calculated directly from the electrochemical data. Therefore, the HOMO energy values are calculated by their optical band gaps (see Table 4.1) and reduction potentials [52]. The LUMO energy levels are calculated from the onset reduction potentials with the reference energy level of ferrocene (4.8 eV below the vacuum level) as given by equation (4.1) [53]:

$$E^{LUMO} = [-(E^{onset} - E^{onset}(Fc/Fc^+)) - 4.8] eV \text{ ----- (4.1)}$$

Where,  $E^{onset}$  is the onset potential of reduction, and  $E^{onset}(Fc/Fc^+)$  is the onset potential of ferrocene. The estimated LUMO energy levels are -3.13, -3.03 and -3.07 eV whereas the observed HOMO energy levels start from -6.47 to -6.64 eV for **Zn(L<sub>1</sub>)**, **Zn(L<sub>2</sub>)** and **Zn(L<sub>3</sub>)**, respectively. On the other hand, all the Zn(II) complexes show a central-ion structure such as two terpy ligands coordinated to a Zn(II) core, and the estimated HOMO energy levels are found

to have small variations as listed in Table 4.2. Therefore, the nature of the electron-donating 4'-aryl substituent plays an important role in determining the electrochemical transition of the Zn(II) bis-terpy complexes. Moreover, the position of HOMO and LUMO energy levels for these Zn(II) complexes reveals the expected reasonable mobility of the electrons [54]. Furthermore, the observed significant red shift in the absorption bands (see Figure 4.1) of the complexes mainly originates due to the decrease of LUMO energy levels. Since the LUMO energy levels are related to the red shift in the UV-Vis absorption spectrum and the same are found in the Zn(II) complexes; this confirms the change in the LUMO levels. This assumption is further supported by the results of the density functional analysis.



**Figure 4.8:** Cyclic voltammogram of Zn(L<sub>1</sub>-L<sub>3</sub>) complexes in the potential between -2.2 to + 1.0 V in 0.1 M TBAP/DMF solution at scan rate of 100 mV s<sup>-1</sup>



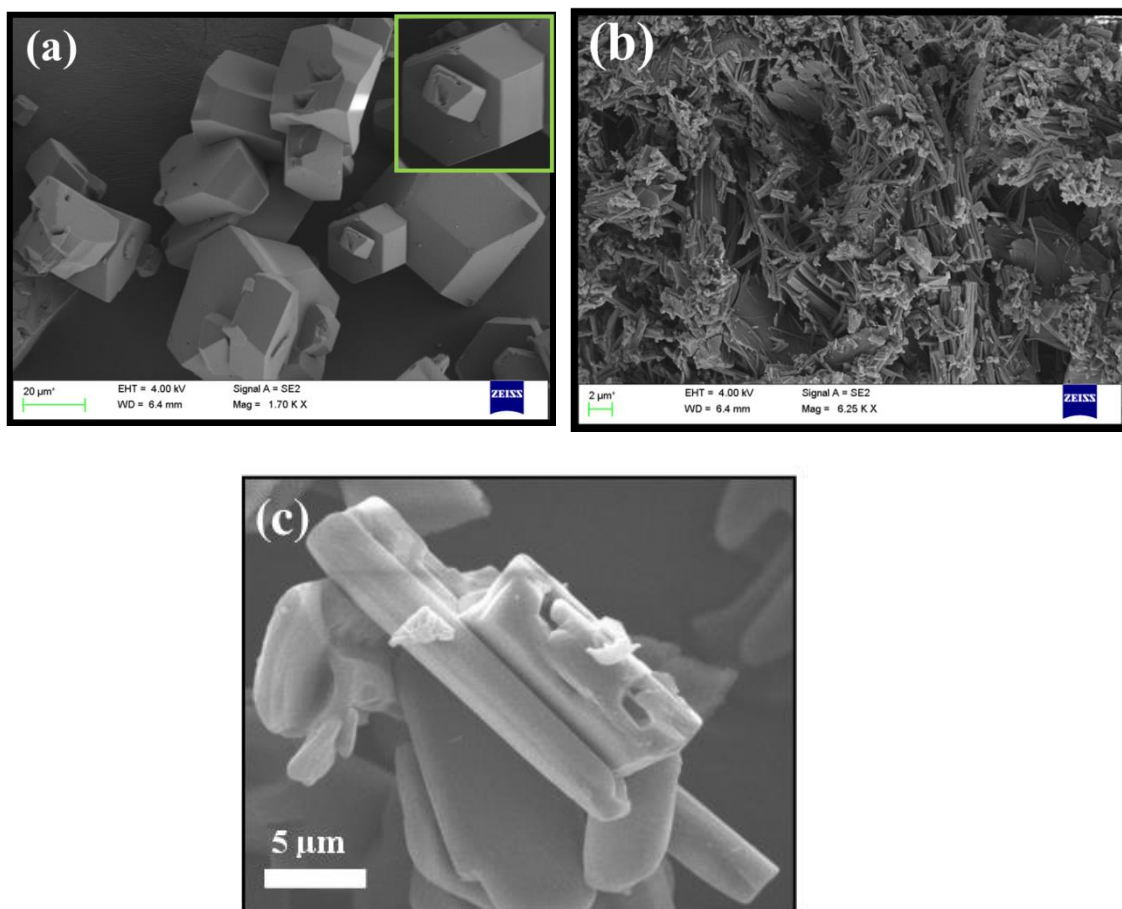
**Table 4.2: Electrochemical and thermal properties of Zn(L<sub>1</sub>-L<sub>3</sub>) complexes**

Complexes	E <sub>onset</sub> <sup>red</sup> (V)	LUMO (eV)	HOMO (eV)	T <sub>m</sub> (°C)	T <sub>d</sub> (°C)
Zn(L <sub>1</sub> )	-1.08	-3.13	6.64	384	370
Zn(L <sub>2</sub> )	-1.11	-3.03	6.58	313	287
Zn(L <sub>3</sub> )	-1.19	-3.07	6.47	370	350

Where, LUMO was measured from the onset of reduction potential. HOMO was calculated using LUMO and optical band gap energy. T<sub>m</sub> - Melting temperature, T<sub>d</sub> - Thermal-decomposition temperature at a wt. % of 5%. The potential of Fc/Fc<sup>+</sup> vs Ag/Ag<sup>+</sup> electrode was measured to be 0.20 V.

#### 4.4.6 Scanning electron microscope

The surface morphology of the as-prepared Zn(II) complexes were analysed by SEM as depicted in Figure 4.9. Figure 4.9(a) shows a SEM micrograph of the **Zn(L<sub>1</sub>)** complex, where hexagonal structural-like particles are observed. The size of the particles ranges from 5 to 50 μm and the inset shows a clear hexagonal particle of **Zn(L<sub>1</sub>)**. Figure 4.9(b) depicts the one-dimensional nano rod like structure of the **Zn(L<sub>2</sub>)** complex with the diameter ranging from 30 to 50 nm and the length being about a few micrometers. Moreover, an SEM image of the **Zn(L<sub>3</sub>)** complex as shown in Figure 4.9(c) and one-dimensional micro-rod structures with diameters of around 3 μm and about 25 μm length were noticed. The SEM images of the complexes reveal that the **Zn(L<sub>2</sub>)** complex has more surface area which could enhance the luminescent properties [55].



**Figure 4.9: SEM images of (a) Zn(L<sub>1</sub>), (b) Zn(L<sub>2</sub>) and (c) Zn(L<sub>3</sub>)**

## 4.5 Summary

In summary, a comprehensive investigation of the photophysical properties of the Zn(II) complexes were studied by varying electron-donating R substituents at the 4'-position of the 2,2':6',2''-terpyridine ring. These complexes exhibit high thermal stability without any significant weight loss below 300 °C. All the complexes show good PL emissions in a DMSO the L<sub>2</sub> substituent on the Zn(II) complex, especially, has a broadened emission spectrum ca. 365–600 nm. The observed maximum emission wavelengths are 473 and 535 nm in solid state PL spectra for the Zn(L<sub>1</sub>) and Zn(L<sub>2</sub>) complex, respectively. The measurements of the excited state lifetime confirm that the potential charge transfer to the  $\pi$ - $\pi^*$  state of the ILCT state in the complexes is efficient. These observations imply that simply changing the terminal substituent

can lead to different optical properties such as a deep blue emission in **Zn(L<sub>1</sub>)** complex whereas **Zn(L<sub>2</sub>)** complex emits a deep green fluorescence. Although the devices using these complexes have not been demonstrated in this article and are beyond the scope of the current discussion, it is believed that the OLEDs based on them would exhibit a promising performance according to the current results and have potential electron-transporting properties from the terpyridine derivatives. The current work illustrates that with appropriately substituted ligands, Zn(II) complexes can generate long-lived fluorescence at room temperature, which is quite rare. Such molecules are of fundamental interest, yet are also poised for potential applications in optoelectronics and luminescence-based technologies.

#### 4.6 References

- [1] Matthew J.J., Mayr C., Schmidt T.D., Lampe T., Djurovich P.I., Brütting W., Thompson M.E., *Nat. Mater.*, 15, 2016: 85–91.
- [2] Kim J.Y., Joo C.W., Lee J., Woo J.-C., Oh J.Y., Baek N.S., Chu H.Y., Lee J.-I., *RSC Adv.*, 2015, 5: 8415–8421.
- [3] Yang J., Huang J., Li Q., Li Z., *J. Mater. Chem. C.*, 2016, 4: 2663–2684.
- [4] Cho G., Lee H., Woo S., Nam S., Kim H., Kim Y., *Nanoscale*, 2011, 3: 1073–1077.
- [5] Reineke S., Lindner F., Schwartz G., Seidler N., Walzer K., Lussem B., Leo K., *Nature*, 2009, 459: 234–238.
- [6] Gather M.C., Köhnen A., Meerholz K., *Adv. Mater.*, 2011, 23: 233–248.
- [7] Han T.-H., Lee Y., Choi M., Woo S.-H., Bae S.-H., Hong B.H., Ahn J.-H., Lee T.-W., *Nat. Photonics.*, 2012, 6: 105–110.
- [8] Zhou L., Xiang H.-Y., Shen S., Li Y.-Q., Chen J.-D., Xie H.-J., Goldthorpe I.A., Chen Y.-Q., Lee S.-T., Tang J.-X., *ACS Nano*, 2014: 8, 12796–12805
- [9] Chen P., Chen B., Zuo L., Duan Y., Han G., Sheng R., Xue k., Zhao Y., *Org. Electron.*, 2016, 31: 136–141.

- [10] Cheng G., So G.K-M., To W.-P., Chen Y., Kwok C.-C., Ma C., Guan X., Chang X., Kwok W.-M., Che C.-M., *Chem. Sci.*, 2015, 6: 4623–4635.
- [11] Farinola G.M., Ragni R., *Chem. Soc. Rev.*, 2011, 40: 3467–3482.
- [12] Kim Y.H., Shin D.C, Kim S.-H., Ko C.-H., Yu H.-S., Chae Y.-S., Kwon S. K, *Adv. Mater.*, 2001, 13: 1690–1693.
- [13] Chen D., Han L., Liu D., Ye K., Liu Y., Zhang J., Wang Y., *RSC Adv.*, 2015, 5: 18328–18334.
- [14] Yang X., Xu X., Zhou G., *J. Mater. Chem. C.*, 2015, 3: 913–944.
- [15] Jesuraj J.P., Jeganathan K., *RSC Adv.*, 2015, 5: 684–689.
- [16] Wang S., Wang X., Yao B., Zhang B., Ding J., Xie Z., Wang L., *Sci Rep.*, 2015, 5: 12487.
- [17] Zhang Y., Lai S.-L., Tong Q.-X., Lo M.F., Ng T.-W., Chan M.Y., Wen Z.-C., He J., Jeff K.S., Tang X.L., Liu W.-M., Ko C.-C., Wang P.F., Lee C.-S., *Chem. Mater.*, 2012, 24: 61–70.
- [18] Zhao Y., Duan L., Zhang X., Zhang D., Qiao J., Dong G., Wang L., Qiu Y., *RSC Adv.*, 2013, 3: 21453–21460.
- [19] Zhang P., Dou W., Ju Z., Yang L., Tang X., Liu W., Wu Y., *Org. Electron.*, 2013, 14: 915–925.
- [20] Lakshmanan R., Shivaprakash N.C., Sindhu S., *J. Lumin.*, 2015, 168: 145–150.
- [21] Son H.-J., Han W.-S., Chun J.-Y., Kang B.-K., Kwon S.-N., Ko J., Han S.J., Lee C., Kim S.J., Kang S.O., *Inorg. Chem.*, 2008, 47: 5666–5676.
- [22] Andres P.R., Schubert U.S., *Adv. Mater.*, 2004, 16: 1043–1068.
- [23] Xu H., Chen R., Sun Q., Lai W., Su Q., Huang W., Liu X., *Chem. Soc. Rev.*, 2014, 43: 3259–3302.

- [24] Jung S.H., Kwon K.-Y., Jung J.H., *Chem. Commun.*, 2015, 51: 952–955.
- [25] Yersin H., Rausch A.F., Czerwieniec R., Hofbeck T., Fischer T., *Coord. Chem. Rev.*, 2011, 255: 2622–2652
- [26] Yang X., Xu X., Dang J.-S., Zhou G., Ho C.-L., Wong W.-Y., *Inorg.Chem.*, 2016, 55: 1720–1727.
- [27] Liu J., Liu A., Chen M., Qian D.-J., *RSC Adv.*, 2012, 2: 241–249.
- [28] Hong Y., Chen S., Leung C.W.T., Lam J.W.Y., Liu J., Tseng N.-W., Kwok R.T.K., Yu Y., Wang Z., Tang B.Z., *Appl. Mater. Interfaces*, 2011, 3: 3411–3418.
- [29] Cheng G., So G.K.-M., To W.-P., Chen Y., Kwok C.-C., Ma C., Guan X., Chang X., Kwok W.-M., Che C.-M., *Chem. Sci.*, 2015, 6: 4623–4635.
- [30] Winter A., Friebe C., Chipper M., Schubert U.S., Presselt M., Dietzek B., Schmitt M., Popp J., *ChemPhysChem.*, 2009, 10: 787–798.
- [31] Schubert U.S., Eschbaumer C., *Angew. Chem. Int. Ed.* 2002, 41: 2892–2926.
- [32] Heller M., Schubert U.S., *Eur. J. Org. Chem.*, 2003, 2003: 947–961.
- [33] Holyer R.H., Hubbard C.D., Kettle S.F.A., Wilkiss R.G., *Inorg. Chem.*, 1966, 5: 622–625.
- [34] Schlütter F., Wild A., Winter A., Hager M.D., Baumgaertel A., Friebe C., Schubert U.S., *Macromolecules*, 2010, 43: 2759–2771.
- [35] Tang F., Peng J., Liu R., Yao C., Xu X., Li L., *RSC Adv.*, 2015, 5: 71419–71424.
- [36] Vogel A. I., *Textbook of Practical Organic Chemistry*, 5th edn, Longman, London, 1989, pp. 264.
- [37] Frisch M. J., et al., *Gaussian 09, Revision A.02*, Gaussian, Inc., Wallingford, CT, 2009
- [38] Walters K.A., Kim Y.-J., Hupp J.T., *J.Electroanal. Chem.*, 2003, 554-555: 449–458.

- [39] Mallesham G., Swetha C., Niveditha S., Mohanty M.E., Babu N.J., Kumar A., Bhanuprakash K., Rao V.J., *J. mater. Chem. C*, 2015, 3: 1208–1224.
- [40] Son H.-J., Han W.-S., Chun J.-Y., Kang B.-K., Kwon S.-N., Ko J., Han S.J., Lee C., Kim S.J., Kang S.O., *Inorg. Chem.*, 2008, 47: 5666–5676.
- [41] Das P., Ghosh A., Kesharwani M.K., Ramu V., Ganguly B., Das A., *Eur. J. Inorg. Chem.*, 2011, 2011: 3050–3058.
- [42] Qureshi M., Manoharan S.S., Singh S.P., Mahapatra Y.N., *Solid State Commun.*, 2005, 133: 305–309.
- [43] Leroy S., Soujanya T., Fages F., *Tetrahedron Letters.*, 2001, 42: 1665–1667.
- [44] Pabitra k Nayak, Neeraj Agarwal, N Periasamy, *J. Chem. Sci.*, 2010, 122, 119–124.
- [45] Walters K.A., Kim Y.-J., Hupp J.T., *J. Electroanal. Chem.*, 2003, 554-555: 449-458.
- [46] Wang X.-Y., Guerso A.D., Schmehl R.H., *Chem. Commun.*, 2002, 2344–2345.
- [47] Yang M., Xu D., Xi W., Wang L., Zheng J., Huang J., Zhang J., Zhou H., Wu J., Tian Y., *J. Org. Chem.*, 2013, 78: 10344–10359.
- [48] McCusker C.E., Chakraborty A., Castellano F.N., *J. Phys. Chem. A*, 2014, 118: 10391–10399.
- [49] Yu S.-C., Kwok C.-C., Chan W.-K., Che C.-M., *Adv. Mater.*, 2003, 15: 1643–1647.
- [50] Chen Y.-Y., Tao Y.T., Lin H.-C., *Macromolecules*, 2006, 39: 8559–8566.
- [51] Chen Y.Y., Lin H. C.J., *Polym. Sci., Part A: Polym. Chem.*, 2007, 45: 3243–3255.
- [52] Tang F., Peng J., Liu R., Yao C., Xu X., Li L., *RSC Adv.*, 2015, 5: 71419–71424.
- [53] Janietz S., Bradley D.D.C., Grell M., Giebeler C., Inbasekaran M., Woo E.P., *Appl. Phys. Lett.*, 1998, 73: 2453–2455.

- [54] Lee J-F., Chen Y-.C., Lin J.T-.S., Wu C-.C., Chen C-.Y., Dai C-.A., Chao C-.Y., Chen H-.L., Liao W.B., *Tetrahedron.*, 2011, 67: 1696–1702.
- [55] Hu J-.S., Ji H-.X., Cao A-.M., Huang Z.X., Zhang Y., Wan L.J., Xia A.D., Yu D.P., Meng X-.M., Lee S-.T, *Chem. Commun.*, 2007, 3083–3085.

## CHAPTER 5

### Orange fluorescent Ru(III) complexes based on 4'-aryl substituted 2.2':6'2'' terpyridine for OLEDs application

This chapter explores the design, synthesis and characterization of a class of organometallic complexes as a series of three novel 4'-aryl substituted orange-fluorescent **Ru(L<sub>1</sub>-L<sub>3</sub>)** complexes. Moreover, DFT outlines the geometric optimisation and electronic charge transition of these complexes. Photophysical studies describe that the luminescence of Ru(III) complexes is due to electronic transition between the energy levels of singly unoccupied molecular orbitals (SUMO) and singly occupied molecular orbitals (SOMO). It also exhibits the potential charge transfer to  $\pi-\pi^*$  and  $n-\pi^*$  states due to MLCT and ILCT processes of the complexes. The observed bands centered at 591 and 620 nm demonstrate that these emissions originated from the transition of SUMO to SOMO energy levels, that is, from the radiative decay from the doublet exciton. Due to the heavy metal effect of Ru(III) ions the photophysical behaviour depends on the MLCT process. This chapter concludes that the all three **Ru(L<sub>1</sub>-L<sub>3</sub>)** complexes are fallen orange emission.

#### 5.1 Introduction

Currently, organometallic complexes are used widely to synthesize optoelectronic devices, such as organic solar cells and for OLEDs [1–5]. Transition metal-based organometallic complexes are of interest due to their versatile nature like ease of tuning the photophysical, electrochemical and magnetic properties [6–8]. These properties strongly depend on the oxidation states of the transition metal used in the complex. Among the various transition metals, ruthenium has gained interest in the preparation of organometallic complexes for OLED applications [9, 10]. Barthelmes *et al.* synthesised ruthenium-based terpy metal complexes and studied their photophysical and electrochemical properties [11]. Other research groups studied these and the thermal properties of Ru(II)-based pyridine complexes [12–14]. Many studies have been conducted on the synthesis and characterization of Ru(II)-based terpy complexes for luminescent applications [15–19]. Kelch *et al.* studied the spectroscopic and electrochemical behaviour of rod-like ruthenium (II) coordination polymers [20] and observed deep orange emissions, strongly



dependent on the nature of  $\pi$ -conjugated bis-terpy ligands. The spectroscopic and electrochemical properties of self-assembled metallo-polymers containing electron-donating and electron-withdrawing Ru(III)-based bis-terpy derivatives are still not clear [21, 22].

The luminescence and redox properties of Ru(III) complexes are of great interest among the researchers for their range of fundamental and practical applications [23–27]. Ru (III)-based terpy complexes exhibit a strong orange emission with a suitable solvent. These emission bands could be due to the MLCT process of the complexes [28–32]. The white light can be generated by mixing orange and blue emitters [33–35]. Heteroleptic ruthenium complexes have more advantages as functions of different groups can be integrated into one molecule. Such complexes usually consist of two ligands with easily substituting functional groups. It has been observed that the functional groups in the ligand introduce interesting photophysical and electrochemical properties to the complexes [36–39]. Researchers found that fluorine substitutions into the ligand can lower the HOMO energy level [40].

Phosphorescence is frequently detected in Ru(III) complexes at room temperature, which is attributed to the low-lying MLCT excited states. It has both ligand-centered (LC) and MLCT charge transition process [41–43]. Extensive work has been carried out on dinuclear Ru(II) homo- and hetero-metallic complexes. In these complexes, the two metal centers are connected by an organic wire type bridge. The Ru(II)-based terpy complexes exhibit phosphorescence behaviour in a few microseconds, whereas Ru(III)-based terpy complexes exhibit similar characteristics in about a few nanoseconds [44–46]. Hence, the photophysical and electrochemical behaviour of Ru ion depend on the oxidation states; it's interesting to study the oxidation states of Ru ion-based organometallic complexes [47–49]. A lack of interest in the photochemical behaviour of Ru(III) derivatives arises from observations that although their lowest excited states are luminescent in glasses at low temperatures, they are essentially non-emissive and short-lived in solution at ambient temperature. It is necessary to introduce cyclo-metallated ligands to complexes for luminescence in solution [50].

In this chapter, the synthesis of a series of three new orange-fluorescent Ru(III)-based terpyridine complexes and their characteristics like photophysical, thermal and electrochemical for

fluorescent OLED applications are discussed. The introduction of electron-donor substituents onto a terpy ligand results in fluorescent emission at room temperature in Ru(III) complexes. These are reflected in the electrochemical properties with the electron-releasing substituents stabilizing the Ru(III) state and lowering the potential of the Ru(II)/Ru(III) couples.

## 5.2 Experimental

### 5.2.1 Syntheses of Ru(III) complexes (RuL<sub>1</sub>-L<sub>3</sub>)

The synthesis of terpyridine ligands, such as **C<sub>1</sub>** and **C<sub>2</sub>**, was discussed in Chapter 3 and published elsewhere [51]. Ligand **C<sub>3</sub>** was also synthesised using a procedure similar to that performed for ligands **C<sub>1</sub>** and **C<sub>2</sub>**. The following sections provide the details of preparation of metal complexes.

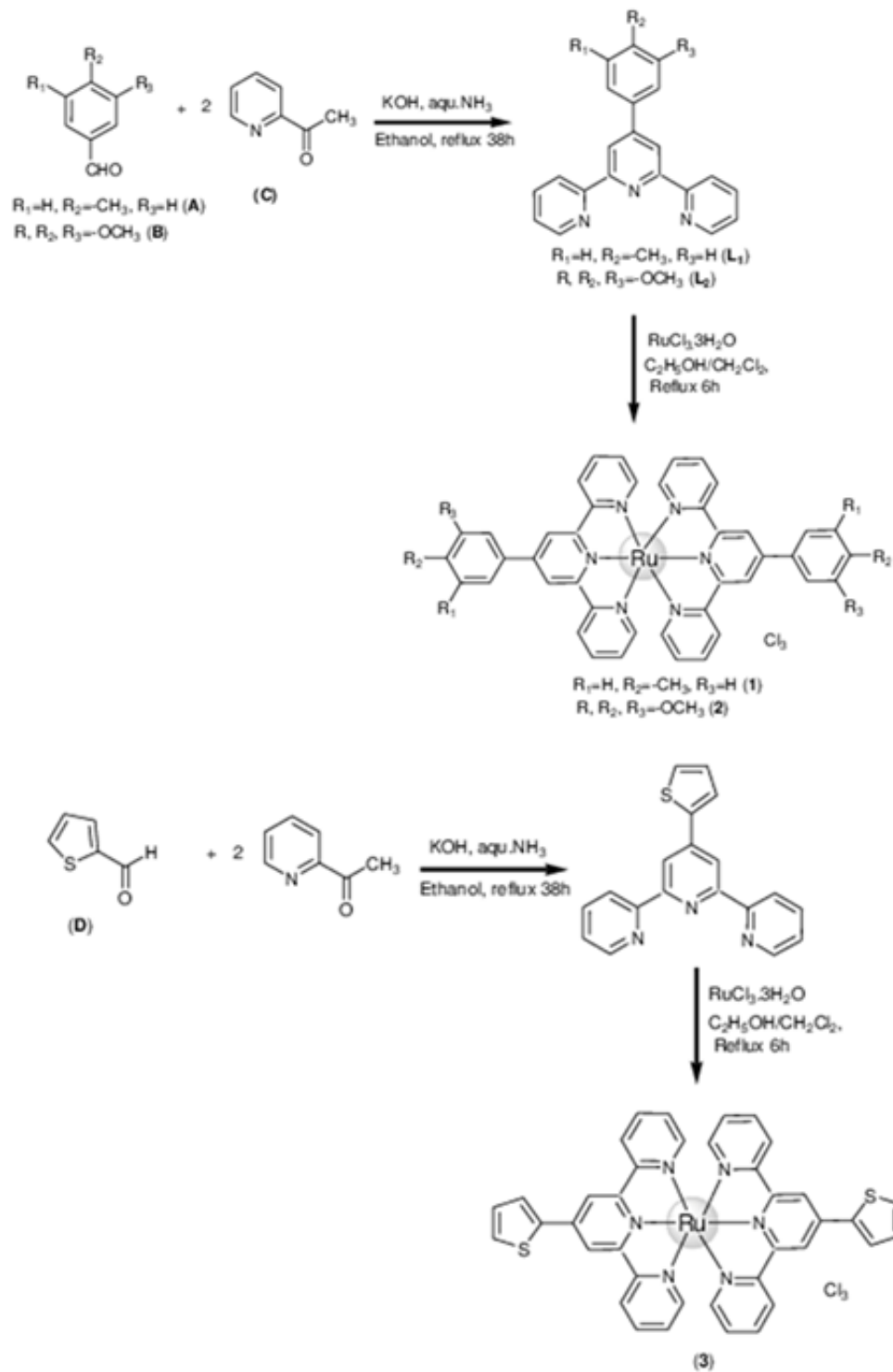
The complexes were prepared following a general synthetic route. An ethanolic solution (15 ml) of RuCl<sub>3</sub>·3H<sub>2</sub>O (0.26 g, 1.0 mmol) was added dropwise to a dichloromethane solution (15 ml) of the terpyridine ligand (4-Mephtpy, 0.32 g; 3,4,5-tmphtpy, 0.35 g; 1.0 mmol, 4-thtpy, 0.28 g; 1.0 mmol) with stirring. The reaction mixture was refluxed for 6 hours to obtain a crystalline solid of the precursor complex, which was filtered, washed with ice-cold ethanol followed by diethyl ether and finally dried in a vacuum. Scheme 5.1 shows synthetic route of (**RuL<sub>1</sub>-L<sub>3</sub>**) complexes.

#### 5.2.2 [Ru(4-Mephtpy)<sub>2</sub>]Cl<sub>3</sub>: [Ru(L<sub>1</sub>)]

Yield: 67%, T<sub>m</sub>. 425 °C, Anal. Calcd for C<sub>44</sub>H<sub>34</sub>Cl<sub>3</sub>N<sub>6</sub>Ru: C, 61.87; H, 4.01; N, 9.84. Found: C, 61.69; H, 4.07; N, 9.87. IR (KBr):  $\nu = 3379$  (w), 3308 (w), 3075 (w), 1586 (m), 1508 (m), 1461 (m), 1397 (m), 1306 (m), 1124 (w), 984 (s), 833 (m), 786 (m), 715 (s), 742 (w), 732 (s), 682 (m), 658 (m), 620 (m) cm<sup>-1</sup>. MS (ESI, *m/z*): 784.18 [M-3Cl]<sup>+</sup>.

#### 5.2.3 [Ru(3,4,5-tmphtpy)<sub>2</sub>]Cl<sub>3</sub>: [Ru(L<sub>2</sub>)]

Yield: 74%, T<sub>m</sub>. 429 °C, Anal. Calcd for C<sub>48</sub>H<sub>42</sub>Cl<sub>3</sub>N<sub>6</sub>O<sub>6</sub>Ru: C, 57.29; H, 4.21; N, 8.35. Found: C, 57.31; H, 4.23; N, 8.37. IR (KBr):  $\nu = 3379$  (w), 3307 (w), 1586 (m), 1508 (m), 1397 (m), 1351 (m), 1308 (w), 1162 (s), 1124 (m), 884 (m), 833 (s), 786 (w), 715 (s), 647 (m) cm<sup>-1</sup>. MS (ESI, *m/z*): 899.94 [M-3Cl]<sup>+</sup>



Scheme 5.1: Synthetic route of Ru(III) terpyridine complexes (RuL<sub>1</sub>-L<sub>3</sub>)

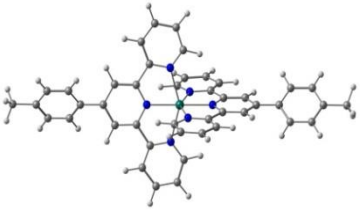
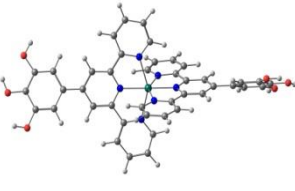
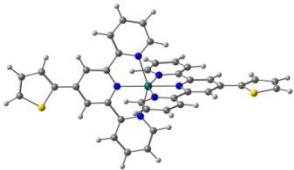
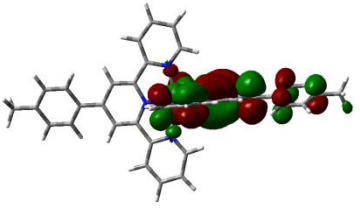
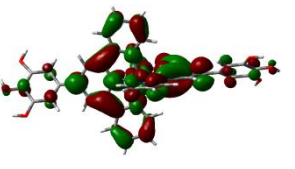
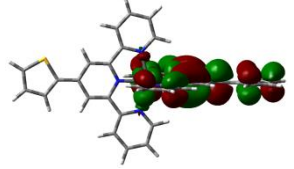
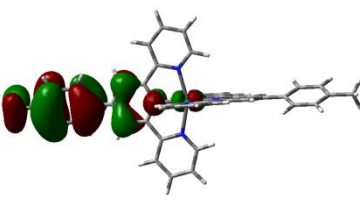
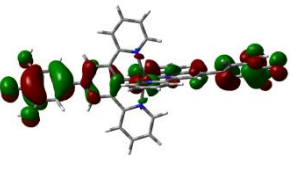
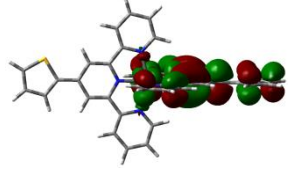
#### 5.2.4 [Ru(4-thtpy)<sub>2</sub>]Cl<sub>3</sub>: [Ru(L<sub>3</sub>)]

Yield: 68%, T<sub>m</sub>. 471 °C, Anal. Calcd for C<sub>38</sub>H<sub>26</sub>Cl<sub>3</sub>N<sub>6</sub>SRu: C, 56.62; H, 3.25; N, 10.42; S, 3.98. Found: C, 56.69; H, 3.28; N, 10.47; S, 3.97. IR (KBr):  $\nu = 3467$  (w), 3056 (w), 3075 (w), 1595 (m), 1527 (m), 1414 (m), 1419 (m), 1359 (m), 1237 (w), 838 (s), 780 (s), 716 (s), 626 (m), 658 (m) cm<sup>-1</sup>. MS (ESI, *m/z*): 699.81 [M-3Cl]<sup>+</sup>.

### 5.3 Quantum calculation of Ru(L<sub>1</sub>-L<sub>3</sub>) complexes

Geometric optimization and electronic structure of the **Ru(L<sub>1</sub>-L<sub>3</sub>)** complexes were achieved by DFT using a B3LYP/def2-TZvP basis set employing Gaussian-09 program [52]. In addition, energy levels of the frontier molecular orbitals (i.e., HOMO, SOMO, SUMO, and LUMO) of three Ru(III) complexes were also obtained. The FMOs along with individual contributions of Ru(III) complexes were fully optimized as shown in Figure 5.1. FMOs have two types of charge transitions in the complexes MLCT and ILCT. MLCT can be attributed to charge transition between SOMO and SUMO energy levels of Ru ion. In ILCT, the charge transition takes place between SOMO/HOMO and the higher energy orbitals. This is mainly attributed to  $\pi-\pi^*$  and  $n-\pi^*$  of terpyridine ligands [53–55].

In all the complexes, the SOMO energy level is mostly localized on the 4'-aryl substituent ring, whereas the SUMO energy is localized between Ru ion and the terpy ring. Therefore, the electronic emission processes of all complexes are mainly attributed to the Ru(III) ions, such as transition from SUMO to SOMO, that is, the radiative decay takes place from the doublet excitons. The orange emission of the complexes is confirmed by PL spectra; the molecular orbitals of Ru(III) are more stable as they are located at lower energy levels.

Complex	Ru(L <sub>1</sub> )	Ru(L <sub>2</sub> )	Ru(L <sub>3</sub> )
Geometry			
SUMO			
SOMO			

**Figure 5.1: Optimized geometry and electronic distribution of the frontier orbitals for Ru(III) terpy complexes (RuL<sub>1</sub>-L<sub>3</sub>)**

## 5.4 Results and Discussion

### 5.4.1 UV-Vis absorbance spectra

The study of photophysical properties of Ru(III)-based terpy complex is of great interest to researchers because of their potential in optoelectronic applications. To investigate the influence of the electron-donating substituent on terpy of Ru(III) complex, its photophysical properties, such as UV-Vis absorption and PL spectra were evaluated. The UV-Vis absorption spectra of **Ru(L<sub>1</sub>-L<sub>3</sub>)** complexes in DMSO solution at room temperature are shown in Figure 5.2. All complexes exhibit high intense absorption bands (250–350 nm) in UV region and less intense absorption bands in the visible region (495–505 nm).

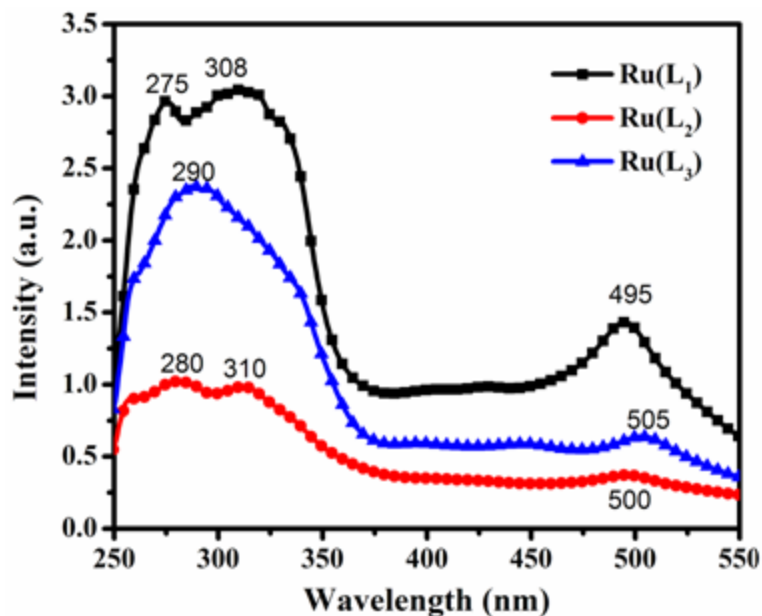


Figure 5.2: UV-Vis absorbance spectra of Ru(L<sub>1</sub>-L<sub>3</sub>) complexes in DMSO

The former are due to  $\pi-\pi^*$  and  $n-\pi^*$  of LC charge transition of terpyridine ligands and the latter to spin-allowed  $d-\pi^*$  of MLCT transition process [56–58]. The shorter wavelength bands of the spectra are attributed to transitions from SOMO/HOMO to higher energy orbitals. Two maximum absorption bands were observed for **Ru(L<sub>1</sub>)** and **Ru(L<sub>2</sub>)** complexes, while one was observed for **Ru(L<sub>3</sub>)** complex in the UV region of electromagnetic radiation. The maximum

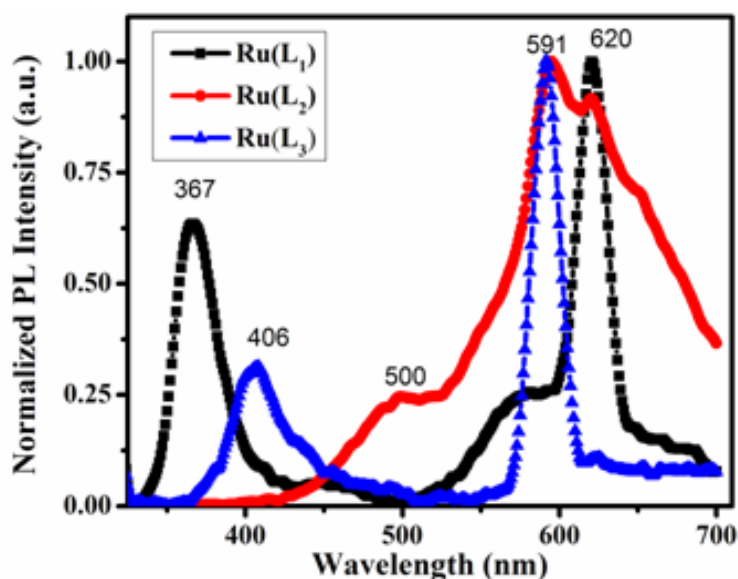
absorption peaks were observed at 275 and 308 nm for **Ru(L<sub>1</sub>)**, 280 and 310 nm for **Ru(L<sub>2</sub>)** and 290 nm for **Ru(L<sub>3</sub>)** complexes (Table 5.1). The bathochromic shifts of the maximum absorbance of 5 and 10 nm are seen for **Ru(L<sub>2</sub>)** and **Ru(L<sub>3</sub>)** complexes, respectively. The absence of second peak as expected around 310 nm in **Ru(L<sub>3</sub>)** complex could be due to the forbidden energy transition between Ru(III) and **L<sub>3</sub>** ligand. In the absorption spectra, some bands are centered at approximately 495, 500 and 505 nm for **Ru(L<sub>1</sub>)**, **Ru(L<sub>2</sub>)** and **Ru(L<sub>3</sub>)** complexes corresponding to the energy gap of 2.50, 2.48 and 2.46 eV, respectively, which are assigned to the electronic transition from SOMO to SUMO. The less intense and narrow absorption bands about 500 nm caused orange emission of these complexes. These bands could be due to d-d transition, which has been observed for similar ruthenium (IV) complexes [45, 59, 60]. These charge transition bands also depict the 5 and 10 nm bathochromic shift for **Ru(L<sub>2</sub>)** and **Ru(L<sub>3</sub>)** complexes, respectively. Hence, the electron-donating substituents of 3,4,5-trimethoxyphenyl and 4-thiophenyl group on terpy would have caused the red shift of **Ru(L<sub>2</sub>)** and **Ru(L<sub>3</sub>)** complexes compared to **Ru(L<sub>1</sub>)** complex. No significant bands were observed for the metal-centered (MC) charge transition of all Ru(III) complexes.

**Table 5.1: Synthetic route of Ru(III) terpyridine complexes (RuL<sub>1</sub>-L<sub>3</sub>)**

Complexes	Absorption ( $\lambda_{\max}$ )		Emission ( $\lambda_{\max}$ )	Optical band gap (eV)	Fluorescence Lifetime (ns)	Melting point (°C)
	LC	MLCT				
Ru(L <sub>1</sub> )	275, 308	459	620	2.50	0.27	425
Ru(L <sub>2</sub> )	280, 310	500	591	2.48	0.46	429
Ru(L <sub>3</sub> )	290	505	591	2.46	0.52	471

### 5.4.2 Photoluminescence spectra

The PL spectra were recorded on excitation at 310 nm for **Ru(L<sub>1</sub>)** and **Ru(L<sub>2</sub>)** complexes, while 290 nm for **Ru(L<sub>3</sub>)** complex corresponds to the maximum absorption wavelength of the complexes. The PL spectra of **Ru(L<sub>1</sub>-L<sub>3</sub>)** complexes are shown in Figure 5.3. A summary of photophysical data of three complexes is presented in Table 5.1. The PL spectra show that the maximum emission bands are in the visible region of the electromagnetic spectrum. The dilute solution of Ru(III) complexes in DMSO shows a strong orange emission in the wavelength range starting from 591 to 620 nm. These emission bands could be due to the MLCT process of the complexes as confirmed by UV-Vis absorption spectra [61]. The absorption maximum of the spin-allowed MLCT band in the visible region for Os(terpy)<sup>2+</sup> lies at the same wavelength as that of Ru(terpy) [60, 62–64].



**Figure 5.3:** PL spectra of **Ru(L<sub>1</sub>-L<sub>3</sub>)** complexes recorded at excitation wavelength of 310 nm for **Ru(L<sub>1</sub>)** and **Ru(L<sub>2</sub>)** complexes, whereas 290 nm for **Ru(L<sub>3</sub>)** complex in DMSO

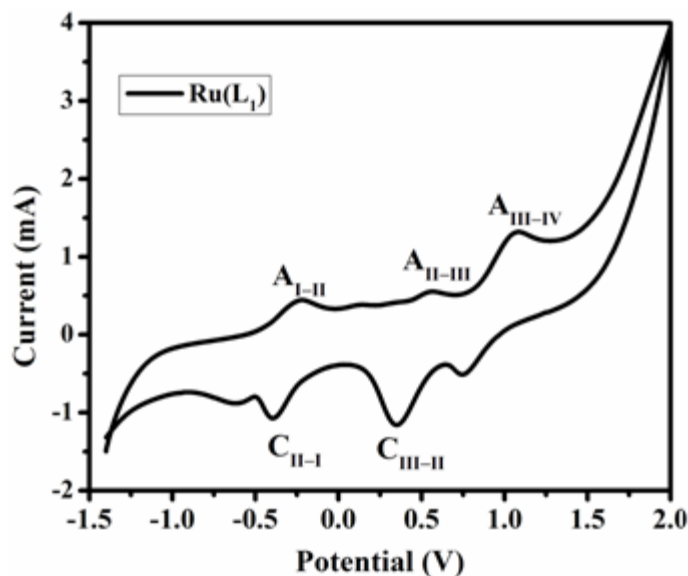
Further, the emission maximum band in the visible region for **Ru(L<sub>2</sub>)** complex lies at the same wavelength as that of **Ru(L<sub>3</sub>)** complex, but the emission maximum was observed at 591 nm. This could be due to the more covalent characteristic nature of the MLCT transition in the Ru(III) complexes [65]. Since **Ru(L<sub>2</sub>)** and **Ru(L<sub>3</sub>)** complexes have the same emission maximum bands it is believed that the same MLCT contributed for these two complexes too. The maximum



emission band was observed at 620 nm for **Ru(L<sub>1</sub>)** complex, and the shoulder peak was at 620 nm for **Ru(L<sub>2</sub>)** complex. All these transitions take place in the lower energy transition from MLCT to the ground state [66]. In addition, the **Ru(L<sub>2</sub>)** complex has the broadened emission spectrum compared to **Ru(L<sub>1</sub>)** and **Ru(L<sub>3</sub>)** complexes in the visible region. This broad emission of the **Ru(L<sub>2</sub>)** complex could be due to the more electron-donating nature of the 3,4,5-trimethoxyphenyl substituent (to terpy ligand on Ru(III)). The luminescence band of the **Ru(L<sub>2</sub>)** and **Ru(L<sub>3</sub>)** complexes was considerably shifted to the blue by 29 nm compared to **Ru(L<sub>1</sub>)** complex. Further, less-intense emission bands were observed at 367, 406 and 500 nm for **Ru(L<sub>1</sub>)**, **Ru(L<sub>2</sub>)** and **Ru(L<sub>3</sub>)** complexes, respectively, probably due to charge transition between LC transitions of terpy ligands. The red shifts are consistent with the LC charge transition of the UV-Vis absorption maximum. The bands centering at approximately 591 and 620 nm demonstrate that the emissions originated from the transition of SUMO to SOMO, that is, the radiative decay from the doublet excitons.

### 5.4.3 Cyclic voltammetry

The redox properties of the **Ru(L<sub>1</sub>-L<sub>3</sub>)** complexes were studied by measurement with CV in a three-electrode cell system. Tetrabutylammonium perchlorate (TBAP) (0.1 M) was dissolved in acetonitrile (ACN) and used as an electrolyte solution with ferrocene (Fc) as an internal standard. Figure 5.4 shows the cyclic voltammogram of the **Ru(L<sub>1</sub>)** complex in the potential range between -1.4 and +2.0 V at a scan rate of 100 mV s<sup>-1</sup>. The electrochemical properties of the Ru(III) complexes are mainly dependent on the influence of Ru(III) ions and not of terpy ligands [67, 68]. Hence, the **Ru(L<sub>1</sub>)** complex was considered to discuss the electrochemical properties of the Ru(III) complex. All three Ru(III) complexes show a similar redox behaviour. The three redox couples have been observed in the potential range of 1.1 to -0.4 V for the **Ru(L<sub>1</sub>)** complex. The electrochemical data for the three Ru(III) complexes is listed in Table 5.2. Further, it has been noticed that the all complexes show a good reversible redox process.



**Figure 5.4:** Cyclic voltammogram of Ru(L<sub>1</sub>) complex in acetonitrile (vs.SCE). The process at about 0.25 V is due to ferrocene, added as a reference

The cathodic peak C<sub>III→II</sub> at a potential of 0.35 V and the anodic peak A<sub>II→III</sub> at a potential of 0.55 V correspond to the reduction of Ru(III) to Ru(II) and the oxidation of Ru(II) to Ru(III), respectively [69]. Moreover, the second redox couple is associated with successive reduction of Ru(II) to Ru(I) (peaks C<sub>II→I</sub> at the potential of -0.40) and correspond with the oxidation of Ru(I) to Ru(II) (peaks A<sub>I→II</sub> at the potential of -0.22 V), respectively. The additional anodic peak at A<sub>III→IV</sub> observed at a potential of 1.08 V could be attributed to the oxidation of Ru(III) to Ru(IV). This peak is associated with a cathodic peak potential of 0.75 V, which can be due to the reduction of Ru(IV) to Ru(III) [70].

#### 5.4.4 Thermal properties

The thermal properties of the three **Ru(L<sub>1</sub>-L<sub>3</sub>)** complexes are characterised by TGA and DSC analysis. The T<sub>d</sub>, T<sub>g</sub> and T<sub>m</sub> of these complexes were systematically studied. Figure 5.5 shows the DSC curves of the **Ru(L<sub>1</sub>-L<sub>3</sub>)** complexes under nitrogen atmosphere, while the samples were heated up from room temperature to slightly above their melting temperature at a scanning rate of 10 °C min<sup>-1</sup>.

It is observed that all the Ru(III) complexes have an endothermic peak, which shows the melting point of the complexes. The observed melting temperatures were 425, 429 and 471 °C for **Ru(L<sub>1</sub>)**, **Ru(L<sub>2</sub>)** and **Ru(L<sub>3</sub>)** complexes, respectively. The melting point of the **Ru(L<sub>1</sub>)** and **Ru(L<sub>3</sub>)** complexes shows sharp endothermic peaks, whereas it is a broad endothermic peak for the **Ru(L<sub>2</sub>)** complex. Among the three Ru(III) complexes, **Ru(L<sub>3</sub>)** has a higher  $T_m$  than the other two Ru(III) complexes, and hence, **Ru(L<sub>3</sub>)** complex is thermally more stable [71]. The DSC thermograms of Ru(III) complexes show no signature of  $T_g$  and crystalline temperature ( $T_c$ ). However, the thermogram of the Ru(III) complexes shows a small inflection (exothermic peak) at a low temperature, which could be due to the elimination of volatile substrate. In conclusion, all the three complexes are thermally very stable as well as crystalline [72].

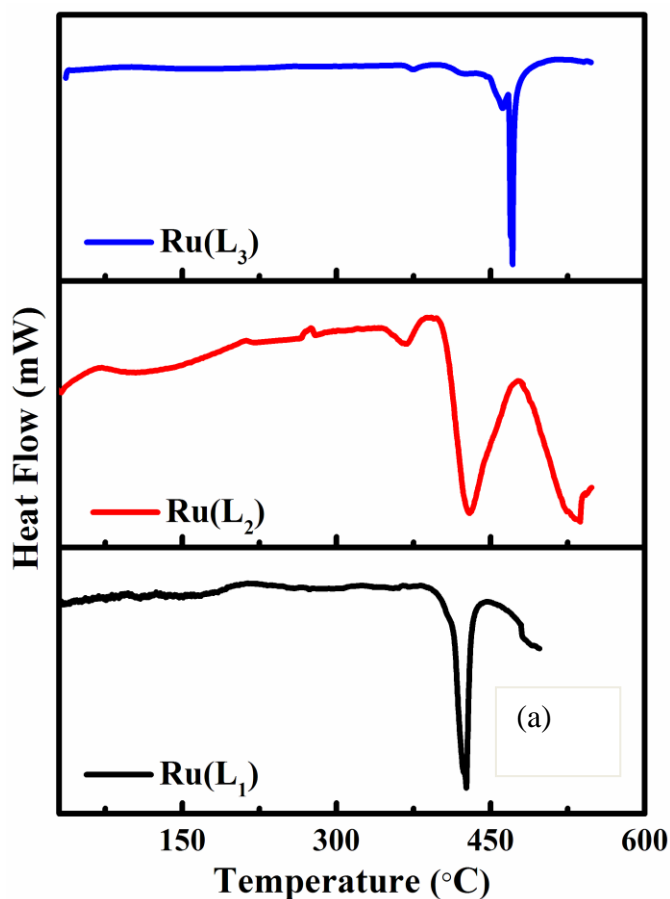


Figure 5.5: DSC plots of the Ru(L<sub>1</sub>-L<sub>3</sub>) complexes

The observed degradation temperatures are 202, 310 and 210 °C for **Ru(L<sub>1</sub>)**, **Ru(L<sub>2</sub>)** and **Ru(L<sub>3</sub>)** complexes, respectively (see Figure 5.6). **Ru(L<sub>2</sub>)** complex shows higher degradation temperature and thermal stability than the other two Ru(III) complexes [73]. It is observed that no significant weight loss takes place at low temperatures. Hence, these complexes exhibit a good thermal stability with T<sub>d</sub> (thermal-decomposition temperature at a wt.% of 95) in the range 250–313 °C. The observed weight losses of 5% were 250, 313 and 297 °C for the **Ru(L<sub>1</sub>)**, **Ru(L<sub>2</sub>)** and **Ru(L<sub>3</sub>)** complexes, respectively.

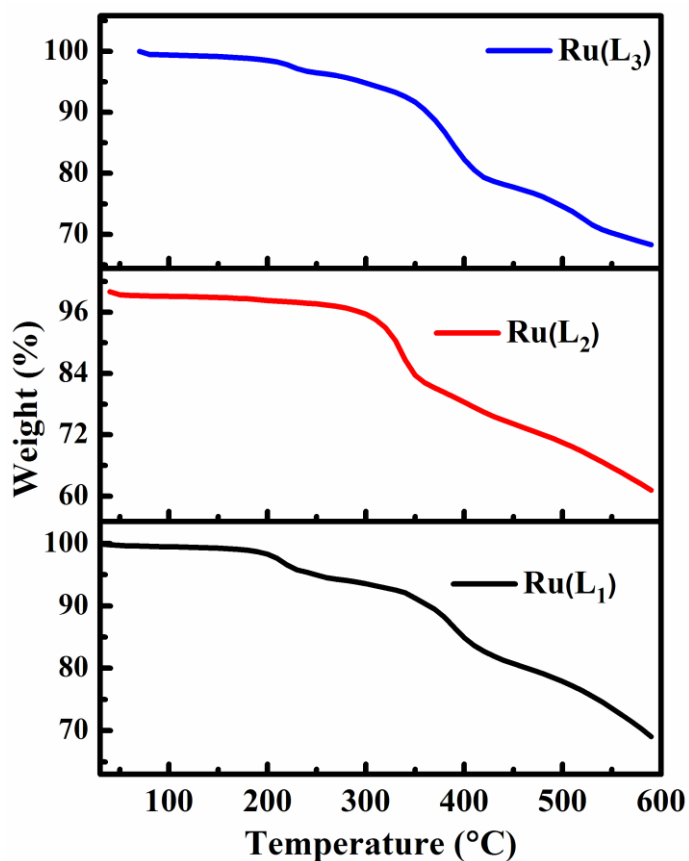


Figure 5.6: TGA thermogram of Ru(L1-L3) complexes

The maximum rate of weight loss T<sub>d</sub> (thermal-decomposition temperature at a wt. % of 39%) takes place at 590 °C for **Ru(L<sub>2</sub>)** complex. Moreover, around 70 wt. % of the residue composed of ruthenium ash and remained above 590 °C for the **Ru(L<sub>1</sub>)** and **Ru(L<sub>3</sub>)** complexes. Compared to the free ligand, the metal complexes revealed a significant increase in thermal stability, as can

be seen from the temperature onset of a 5% weight loss [74]. Hence, Ru(III) complexes are more stable on exposure to air and showed high thermal stability in nitrogen atmosphere.

#### 5.4.5 Fluorescence lifetime measurements

The lifetime of luminescence is an important parameter as the luminescence property of a material depends on it [75]. Figure 5.7 shows the fitted decay curve of **Ru(L<sub>1-3</sub>)** complexes in DMSO obtained by using the TCSPC method under laser excitation at 310 nm with a 96.8 ps pulse width. The luminescence decay spectra of the three complexes were fitted by a single exponential decay function. The observed lifetimes are 0.27, 0.46 and 0.52 ns for **Ru(L<sub>1</sub>)**, **Ru(L<sub>2</sub>)** and **Ru(L<sub>3</sub>)**, respectively. Hence, the measured lifetime of the **Ru(L<sub>3</sub>)** complex is significantly longer than the other two Ru(III) complexes.

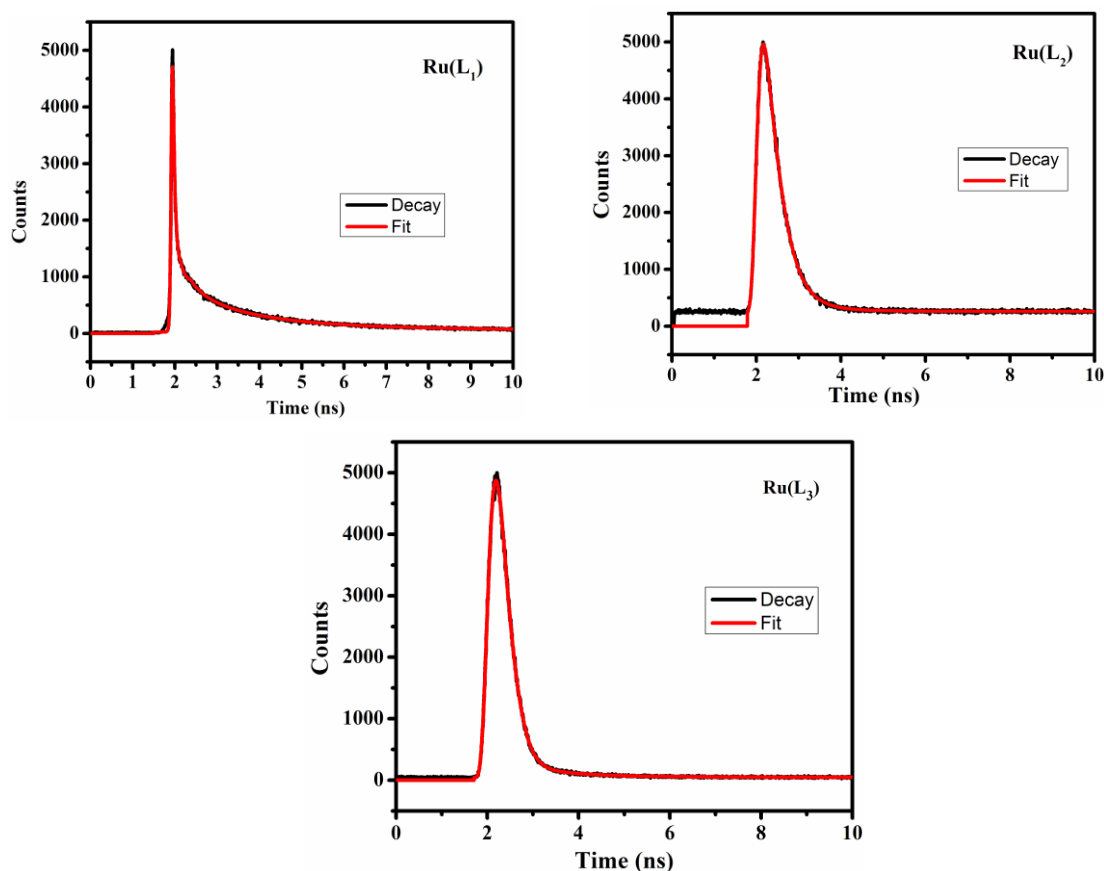
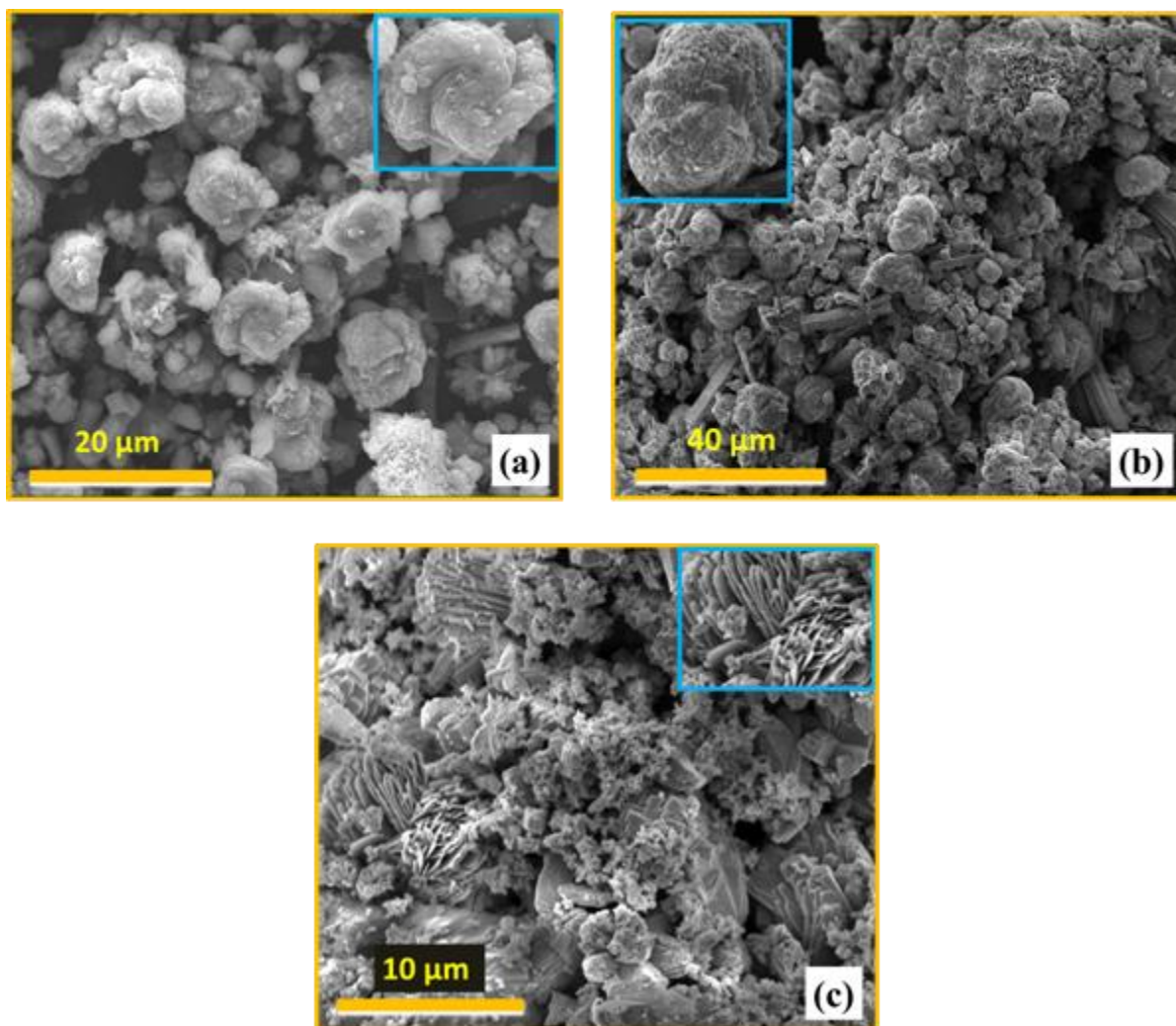


Figure 5.7: Fluorescence decay spectra of Ru(L<sub>1</sub>) (a), Ru(L<sub>2</sub>) (b) and Ru(L<sub>3</sub>) (c) complexes at the excitation wavelength of 310 nm with one-exponential fit residuals,  $\chi^2 = 1.002$

It has been reported that the longer conjugation length in the ligand leads to longer lifetime [76]. The short-lived fluorescence of **Ru(L<sub>1</sub>)** might be assigned to the strong intramolecular coupling interaction of trimethoxy fluorphores which lead to the fast charge transfer process. The lifetime on the nanosecond time scale indicates that the three Ru(III) complexes have the fluorescent character of the luminescence.

#### 5.4.6 Scanning electron microscope



**Figure 5.8:** SEM images of (a) Ru(L<sub>1</sub>), (b) Ru(L<sub>2</sub>) and (c) Ru(L<sub>3</sub>) complexes

The surface morphology of the synthesised **Ru(L<sub>1</sub>-L<sub>3</sub>)** complexes was analysed by SEM as depicted in Figure 5.8. Figure 5.8(a) shows an SEM micrograph of the **Ru(L<sub>1</sub>)** complex, where cauliflower-like structural particles have been observed. The size of the particles ranges from 5 to 10  $\mu\text{m}$  and the inset shows a clear cauliflower-like structural particle of **Ru(L<sub>1</sub>)**. Figure 5.8(b) depicts the cauliflower-like structure along with one-dimensional nano rod of the **Ru(L<sub>2</sub>)** complex with the diameter ranging from 7 to 12  $\mu\text{m}$  and the length being about a few micrometers. Moreover, the SEM image of the **Ru(L<sub>3</sub>)** complex, as shown in Figure 5.8(c) shows one-dimensional micro-rod structures with diameters of around 3  $\mu\text{m}$  and about 7  $\mu\text{m}$  length. The SEM images of the complexes reveal that the **Ru(L<sub>2</sub>)** complex has more surface area and a greater surface-to-volume ratio which could enhance the luminescence properties [77].

## 5.5 Summary

In summary, three novel Ru(III) complexes were synthesised and their photophysical, electrochemical and thermal properties were studied by varying the electron-donating substituents at the 4'-position of the 2,2':6',2''-terpyridine ring. Spectral analysis showed that electroluminescence of the OLED originated from electron transition between SUMO and SOMO. These complexes exhibit high thermal stability without any significant weight loss below 250 °C. All the complexes show good PL emissions in a DMSO solution with a broad emission spectrum ca. 591–620 nm. The **Ru(L<sub>2</sub>)** complex exhibits a broad orange emission compared to **Ru(L<sub>1</sub>)** and **Ru(L<sub>3</sub>)** complexes. The measurements of the excited state lifetime confirm that the potential charge transfer to the  $\pi$ - $\pi^*$  state of the MLCT state in the complexes is efficient. The bands centered on 591 and 620 nm demonstrate that these emissions originated from the transition of SUMO to SOMO, that is, from radiative decay from the doublet exciton. These observations imply that by simply changing the terminal the substituent can lead to various optical properties, such as deep orange emission for the three **Ru(L<sub>1</sub>-L<sub>3</sub>)** complex. Although the devices using these complexes have not been demonstrated in this work and are beyond the scope of the current discussion, it is believed that the OLEDs based on them would exhibit a promising performance according to the current results and have potential electron-transporting properties from terpyridine derivatives.

## 5.6 References

- [1] Jou J.-H., Su Y.-T., Hsiao M.-T., Yu H.-H., He Z.-K., Fu S.-C, Chiang C.-H., Chen C.-T., Chou C.-H, Shyue J.-J., *J. Phys. Chem. C*, 2016, 120: 18794–1802.
- [2] Nagai Y., Sasabe H., Takahashi J., Onuma N., Ito T., Ohisa S., Kido J., *J. Mater. Chem. C*, 2017, 5: 527–530.
- [3] Sun Y., Stephen R.F., *Nat. Photon.*, 2008, 2: 483–487
- [4] Wood S., Connor D., Jone C.W., Claverly J.D., Blakesley J.C., Giusca C., Castro F.A., *Sol. Energ. Mat. Sol. Cells*, 2017, 161: 89–95.
- [5] Reineke S., Thomschke M., Bjorn L., Leo K., *Rev. Mod. Phys.*, 2013, 85: 1245–1293.
- [6] Kim K.-H., Liao J.-L., Lee S. W., Sim B., Moon C.-K., Lee G.-H., Kim H. J., Chi Y., Kim J.-J, *Adv. Mater.*, 2016, 28: 2526–2532.
- [7] Constable E.C., Alexander M.W.C.T., Armaroli N., Balzani V., Maestri M., *Polyhedron*, 1992, 11: 2707–2709.
- [8] Seino Y., Inomata S., Sasabe H., Pu Y.-J., Kido J., *Adv. Mater.*, 2016, 28: 2638–2643.
- [9] Wang D., Xu Q-L., Zhang S., Li H-Y, Wang C-C., Li T-Y., Jing Y-M., Huang W., Zheng Y-X., Accorsi G., *Dalton Trans.*, 2013, 42: 2716–2723.
- [10] Juris A., Balzani V., Barigelletti F., Campagna S., Belser P., Zelewsky A.V., *Coord. Chem. Rev.*, 1988, 84: 85–277.
- [11] Barthelmes K., Kubel J., Winter A., Wachtler M., Friebe C., Dietzek B., Schubert U.S., *Inorg. Chem.*, 2015, 54: 3159–3171.
- [12] Medlycott E.A., Hanan, G.S., *Chem. Soc. Rev.*, 2005, 34: 133–142.
- [13] Medlycott E.A., Hanan G.S., *Coord. Chem. Rev.*, 2006, 250: 1763–1799.
- [14] Jiang H., Lee S.J., Lin W., *Org. Lett.*, 2002, 4: 2149–2152.



- [15] Chaignon F., Torroba J., Blart E., Borgstrom M., Hammarstrom L., Odobel F., *New J. Chem.*, 2005, 29: 1272–1284.
- [16] Allen B.D., Benniston A.C., Harriman A., Mallon L.J., Pariani C., *Phys. Chem. Chem. Phys.*, 2006, 8: 4112–4118.
- [17] Albinsson B., Martensson J., *J. Photochem. Photobiol. C*, 2008, 9: 138–155.
- [18] Siebert R., Hunger C., Guthmuller J., Schlutter, F., Winter A., Schubert U. S., Gonzalez L., Dietzek B., Popp J., *J. Phys. Chem. C*, 2011, 115: 12677–12680.
- [19] Mishra A., Mena-Osteritz E., Bäuerle P., Beilstein J. Org. Chem., 2013, 9: 866–876.
- [20] Kelch S., Rehahn M., *Chem. Commun.*, 1999, 1123–1124.
- [21] Wild A., Winter A., Schlutter F., Schubert U. S., *Chem. Soc. Rev.*, 2011, 40: 1459–1511.
- [22] Rudmann H., Shimada S., Rubner M.F., *J. Am. Chem. Soc.*, 2002, 124: 4918–4921.
- [23] Chmielewski P.J., Latos-Grazynski L., Pacholska E., *Inorg. Chem.*, 1994, 33: 1992–1999.
- [24] Latos-Grazynski L., Lisowski J., Olmstead M.M., Balch A. L., *Inorg. Chem.*, 1989, 28: 3328–3331.
- [25] Latos-Grazynski L., Lisowski J., Chmielewski P.J., Grzeszczuk M., Olmstead M.M., Balch A.L., *Inorg. Chem.*, 1994, 33: 192–197.
- [26] Chuang C.H., Ou C.K., Liu S.T., Kumar A., Ching W.M., Chiang P.C. Dela Rosa M.A., Hung C.H., *Inorg. Chem.*, 2011, 50: 11947–11957.
- [27] Biaek M., Biaonska A., Latos-Grazynski L., *Inorg. Chem.*, 2015, 54: 6184–6194.
- [28] Umamahesh B., Karthikeyan N.S., Sathiyarayanan K.I., Malicka J.M., Cocchi M., *J. Mater. Chem. C*, 2016, 4: 10053–10060.
- [29] Kusamoto T., Kume S., Nishihara H., *J. Am. Chem. Soc.*, 2008, 130: 13844–13845.

- [30] Gianferrara T., Bratsos I., Iengo E., Milani B., Ostric A., Spagnul C., Zangrando E., Alessio E., *Dalton Trans.*, 2009, 10742–10756.
- [31] Brothers P.J., Collman J.P., *Acc. Chem. Res.*, 1986, 19: 209–215.
- [32] Bialek M.J., Latos-Grazynski L., *Inorg. Chem.*, 2016, 55: 1758–1769.
- [33] Reineke S., Lindner F., Schwartz G., Schwartz G., Seidler N., Walzer K., Lussem B., Leo K., *Nature*, 2009, 459: 234–238.
- [34] Han T.H., Choi M.-R., Jeon C.-W., Kim Y.-H., Kwon S.-K., Lee T.-W., *Sci. Adv.* 2016 2: 1–8.
- [35] Chen J., Zhao F., Ma D., *Mater. Today*, 2014, 17 175–183.
- [36] De Silva A.P., Gunaratne H.Q.N., Gunnlaugsson T., Huxley A.J.M., McCoy C.P., Rademacher J., Rice T.E., *Chem. Rev.*, 1997, 97: 1515–1565.
- [37] Vogtle F., *Supramolecular Chemistry*, Wiley, Chichester, 1993.
- [38]. Van der Drift R.C., Bouwman E., Drent E., *J. Organomet. Chem.*, 2002, 650: 1–24.
- [39] Andres P.R., Schubert U.S., *Macromol. Rapid Commun.*, 2004, 25: 1371–1375.
- [40] Kosaka W., Itoh M., Miyasaka H., *Dalton Trans.*, 2015, 44: 8156–8168.
- [41] Mishra D., Naskar S., Butcher R.J., Chattopadhyay S.K., *Inorg. Chim. Acta.*, 2005, 358: 3115–3121.
- [42] Motokawa N., Matsunaga S., Takaishi S., Miyasaka H., Yamashita M., Dunbar K.R., *J. Am. Chem. Soc.*, 2010, 132: 11943–11951.
- [43] Tessore F., Roberto D., Ugo R., Pizzotti M., Quici S., Cavazzini M., Bruni S., Angelis F.D., *Inorg. Chem.*, 2005, 44: 8967–8978.
- [44] Vogtle F., Plevoets M., Nieger M., Azzellini G.A., Credi A., Cola L.D., Marchis V.D., Venturi M., Balzani V., *J. Am. Chem. Soc.* 1999, 121: 6290–6298.

- [45] Jablonska-Wawrzycka A., Rogala P., Michałkiewicz S., Hodorowicz M., Barszcza B., *Dalton Trans.*, 2013, 42: 6092–6101.
- [46] Allardyce S., Dyson P.J., *Platinum Metals Rev.*, 2001, 45: 62–69.
- [47] Clarke M.J., *Coord. Chem. Rev.*, 2003, 236: 209–233.
- [48] Van der Drift R.C., Bouwman E., Drent E., *J. Organomet. Chem.*, 2002: 650: 1–24.
- [49] Browne W.R., Hage R., Vos J.G., *Coord. Chem. Rev.*, 2006, 250: 1653–1668.
- [50] Chowdhury N.S., Seth D.K., Drew M. G. B., Bhattacharya S., *Inorg. Chim. Acta*, 2011, 372: 183–190.
- [51] Lakshmanan R., Shivaprakash N.C., Sindhu S., *J. Lumin.*, 2015, 168: 145–150.
- [52] Frisch M. J., et al., *Gaussian 09, Revision A.02*, Gaussian, Inc., Wallingford, CT, 2009.
- [53] Miyasaka H., Campos-Fernández C.S., Clérac R., Dunbar K.R., *Angew. Chem., Int. Ed.*, 2000, 39: 3831–3835.
- [54] Motokawa N., Oyama T., Matsunaga S., Miyasaka H., Sugimoto K., Lopez Y.M., N., Dunbar K. R., *Dalton Trans.*, 2008, 4099–4102.
- [55] Miyasaka H., Motokawa N., Atsuumi R., Kamo H., Asai Y., Yamashita M., *Dalton Trans.*, 2011, 40: 673–682.
- [56] Stone M.L., Crosby G.A., *Chem. Phys. Lett.*, 1981, 79: 169–173.
- [57] Wu K.Q., *Dalton Transactions*, 2012, 41: 11000–11008.
- [58] Priyarega S., Tamizh M.M., Karvembu R., Prabhakaran R., Natarajan K., *J. Chem. Sci.*, 2011, 123: 319–325.
- [59] Coe B.J., Thompson D.W., Culbertson C.T., Schoonover J.R., Meyer T.J., *Inorg. Chem.*, 1995, 34: 3385–3395.

- [60] Constable E.C., Housecroft C.E., Schofield E.R., Encinas S., Armaroli N., Barigelletti F., Flamigni L., Figgemeier L., Vos J.G., *Chem. Commun.*, 1999, 869–870.
- [61] Stone M.L., Crosby G.A., *Chem. Phys. Lett.*, 1981, 79: 169–173.
- [62] Winkler J. R., Netzel T. L., Creutz C., Sutin N., *J. Am. Chem. Soc.*, 1987, 109: 2381–2392.
- [63] De Silva A.P., Gunaratne H.Q.N., Gunnlaugsson T., Huxley A.J.M., McCoy C.P., Rademacher J., Rice T.E., *Chem. Rev.*, 1997, 97:1515–1566.
- [64] Hammarstrom L., Barigelletti F., Flamigni L., Indelli M. T., Armaroli N., Calogero G., Guardigli M., Sour A., Collin J.-P., Sauvage J.-P., *J. Phys. Chem. A*, 1997, 101: 9061–9069.
- [65] Hutchison K., Morris J.C., Nile T.A, Walsh J.L., *Inorg. Chem.*, 1999, 38: 2516–2523.
- [66] Sinkeldam R.W., Greco N.J., Tor Y., *Chem. Rev.*, 2010, 110: 2579–2619.
- [67] Qin J., Hu L., Lei N., Liu Y.-F., Zhang K.-K., Zuo J.-L., *Acta Chim. Slov.*, 2014, 61: 740–745.
- [68] Santoni M.-P., Medlycott E.A., Hanan G.S., Hasenknopf B., Proust A., Nastasi F., Campagna S., Chiorboli C., Argazzid R., Scandola F., *Dalton Trans.*, 2009, 3964–3970.
- [69] Breivogel A., Hempel K., Heinze K., *Inorg. Chim. Acta*, 2011, 374: 152–162.
- [70] Brown D.G., Sangantrakun N., Schulze B., Schubert U.S., Berlinguette C.P., *J. Am. Chem. Soc.*, 2012, 134: 12354–12357.
- [71] Amirnasr M., Nazeeruddin M.-K., Gratzel M., *Thermochimica Acta*, 2000, 348: 105–114.
- [72] Kavitha N., Lakshmi P.V.A., *J. Saudi Chem. Soc.*, 2017, 21: S457-S466.
- [73] Gherab K.N., Gatri R., Hank Z., Dick B., R.-J. Kutta, Winter R., Luc J., Sahraoui B., Fillaut J.-L., *J. Mater. Chem.*, 2010, 20: 2858–2864.

- [74] Nazeeruddin M.-K., Amirasr M., Comte P., Mackay J.R., McQuillan A.J., Houriet R., Gratzel M., *Langmuir*, 2000, 16: 8525–8528.
- [75] Su S.-J., Cai C., Takamatsu J., Kido J., *Org. Electron.*, 2012, 13: 1937–1947.
- [76] McCusker C.E., Chakraborty A., Castellano F.N., *J. Phys. Chem. A* 2014, 118: 10391–10399.
- [77] Hu J.-S., Ji H.-X., Cao A.-M., Huang Z.-X., Zhang Y., Wan L.-J., Xia A.-D., Yu D.-P., Meng X.-M., Lee S.-T., *Chem. Commun.*, 2007, 3083–3085.

## CHAPTER 6

### **Fabrication of fluorescent green OLEDs based on PEDOT:PSS/AgNWs hybrid-composite anode and their performance**

This chapter covers the preparation and characterization of silver nanowires (AgNWs) for the fabrication of TCF anode for OLEDs. In addition, I discuss the preparation, optical and morphological studies of TCF based on AgNWs and PEDOT:PSS hybrid-composite. Fluorescent green OLEDs with PEDOT:PSS and Alq<sub>3</sub> as the hole transport-layer and electroluminescent-layer, respectively, were fabricated and characterised. Two types of green fluorescent OLEDs were prepared: (i) OLED made up of commercial ITO as an anode, and (ii) ITO-free OLED as AgNWs and PEDOT:PSS hybrid-composite thin film-based anode. Their luminescence intensity-wavelength and current density-voltage measurements were systematically studied and compared.

#### **6.1 Introduction**

The use of organic printed electronics has been expanding to a variety of applications, which include OLEDs, OPVCs, wearable electronics, electronic papers and electrochromic devices (ECDs) [1–7]. OLEDs are likely to be used in the next-generation displays and solid-state lighting applications. The thickness of organic materials is only a few hundreds of nanometers, and hence, OLED panels can be very thin [8–12]. They can be made of flexible, ultra-thin, and light-weight devices and with cost-efficient productivity should bring innovation to our lives [13–15]. In general, OLEDs are made of TCF as one of the electrodes. ITO is the most commonly used TCF anodes for OLEDs as it has high transparency, high work function, availability, and ease of processability [16–18]. However, it has some limitation, such as high cost due to being rare on the earth and scarcity. Nevertheless, it is not an ideal choice for flexible optoelectronic devices because the devices are made up on flexible plastic substrates and the ITO breaks easily as a result of which the ITOs are bent [19]. Thus, a great deal of interest has been devoted to find replacement for ITO.

Several emerging nanomaterials, such as, CNTs, conducting polymers, metal meshes, graphene, modified oxide anodes, nanocomposite anodes have been developed as a TCF to substitute for ITO [20–24]. Among these, nanocomposite anodes play a vital role with their very promising optical, electronic and mechanical properties. One-dimensional nanostructure can provide the conventional material with new behaviour and functionality in electrical, mechanical, and thermal characteristics [25–27]. It includes wires, rods, and tubes, and is expected to play an important role in fabricating the TCF electrode. The synthesis and characterization of nanowires have gained attention over the last two decades [28]. In particular, much effort has been devoted to the controlled synthesis of one-dimensional nanostructures from metallic conductors because of their potential use as interconnects or active components in fabricating nanoscale devices. The metallic NWs provide unique properties, such as photophysical, electrical, electronic and mechanical characteristics for nano-scale devices [29–31]. Silver nanowires (AgNWs) represent a particular class of interesting nanostructures to synthesize and study their behaviour as bulk silver exhibits high thermal and electrical conductivity among all metals. Therefore, it is an essential material and has a variety of commercial applications; its performance in these applications could potentially be enhanced by processing it into one-dimension nanostructure with controllable dimensions and aspect ratios [32–34].

In general, the PEDOT:PSS is used to fabricate the TCF electrode with uniform film, but the conductivity of this film is usually very low, thus, it requires further improvement, either chemical modifications or adding some nano-fillers to achieve high-performance like good conductivity and high transparency [35–37]. The film heater fabricated on metal nanowire-based TCF electrode shows a significant optoelectronic and heating performance. Nonetheless, the poor adhesion of metal network to the substrate limits its wide applications [38]. Ou *et al.* observed that the electronic conductivity of poly (methyl methacrylate) (PMMA) filled with carbon black increased about 10 orders of magnitude [39]. Thus, the usage of these TCF electrodes was not preferred as the replacement of commercial ITO electrodes forcing researchers to address this issue. Ghosh *et al.* prepared a transparent conducting thin film comprising AgNWs in an ultrathin polyimide foil, and obtained high transmittance (of about 90 %) with strong adhesion, and low surface roughness (2.4 nm) [40].

The large surface areas of AgNWs are one of the most attractive features that facilitate the creation of a large interface into hybrid-nanocomposites. Adding conductive fillers into a polymer network is an effective way to improve their electronic conductivity. PEDOT:PSS/AgNWs hybrid composite can be prepared by various wet chemical methods including spin-coating, screen printing, spray pyrolysis and dip-coating process [41–44]. The transparent and conductive PEDOT:PSS/AgNW/PEDOT:PSS hybrid film has been prepared using the spin-coating technique with the maximum transmittance of 83 % [45]. Xin He *et al.* studied the PEDOT:PSS/AgNWs composite film prepared by screen-printed process for transparent heaters and found that the length of the AgNWs was larger than the mesh size in case of screen printing, thus, several NWs got curved and broken due to the extrusion in the printing method [46]. Spin-coating is the simplest process for the preparation of PEDOT:PSS/AgNWs composite with high transmittance and high electronic conductivity as compared to ITO anode.

An ideal OLED requires well-matched energy level alignments to the consecutive layers with high luminous efficiency, balanced injection of charge carriers, and sufficient high stability under applying bias [47–49]. The direct hole injection from ITO anode is not efficient owing to its energy disparity at the interfaces. Consequently, high operating voltages are required to overcome the injection barrier resulting in reduced efficiency in the devices. To overcome this, its anode needs to function effectively [50, 51]. Hence, the PEDOT:PSS/AgNWs hybrid composite-based electrode could solve this problem and it also replaces the conventional ITO for the fabrication of highly efficient OLEDs, as the PEDOT:PSS/AgNWs hybrid composite-based electrode has HOMO levels matching well with the HOMO level of HTL (PEDOT:PSS) [37, 52–54].

In this work, the AgNWs of around 20  $\mu\text{m}$  length and 70 nm diameters were synthesised by adapting polyol process and studied their performances for application in OLEDs as a TCF anode. The PEDOT:PSS/AgNWs hybrid composite-based electrode was prepared and studied its photophysical behaviour and analysed its morphological changes for use in OLEDs. Further, the design and performance of fluorescent green OLEDs with PEDOT:PSS and Alq<sub>3</sub> as the hole transport-layer and electroluminescent-layer, respectively, have been discussed. Two types of green fluorescent OLEDs were designed to understand the physical phenomena like current



density and electroluminescence behaviours; (i) OLEDs made of commercial ITO anode, and (ii) ITO-free OLEDs as PEDOT:PSS/AgNWs hybrid-composite thin film-based anode. Their luminescence intensity-wavelength and current density-voltage measurements were systematically studied.

## **6.2 Experimental methods**

### **6.2.1 Preparation of AgNWs**

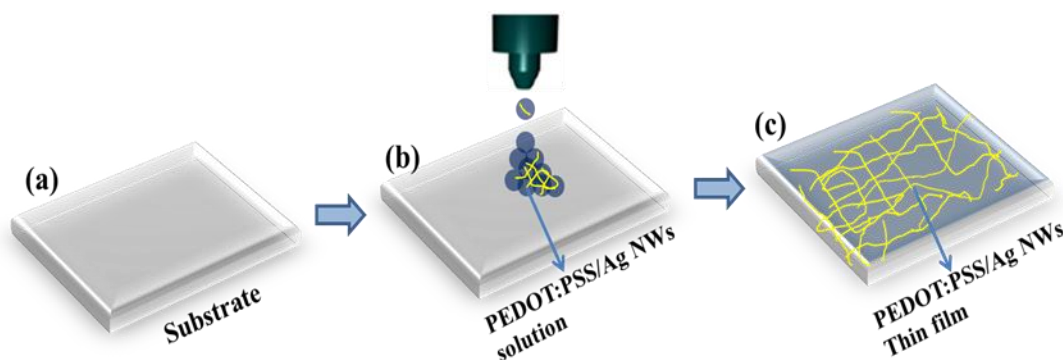
The AgNWs were prepared by modified polyol-process [55, 56]. In a typical synthesis, a solution of 50 ml glycerol containing 1.46 g of polyvinylpyrrolidone (PVP) (Sigma Aldrich, MW~55,000) and 15 mg of NaCl was made by dissolving the PVP and NaCl in glycerol in a 150-ml round-bottomed flask at 80 °C. The mixture was stirred and heated until a clear homogeneous solution emerged and the solution was allowed to cool to room temperature. At that temperature, 395 mg of AgNO<sub>3</sub> was added to it, followed by stirring for 5 min to dissolve the silver nitrate completely (in glycerol). The mixture was heated at a heating rate of 10 °C/min for 20 min. The heating was stopped when the solution turned gray–green. One hundred ml of double-distilled water was added to the final mixture, and then agitated for 2 min with an ultrasonicator. The diluted solution was then centrifuged at 8000 rpm for 10 min. The supernatant was decanted and the remaining precipitate at the bottom was washed with copious amount of water. Eventually, the purified AgNWs were separated with the assistance of a 300 nm pore size membrane using vacuum filter and preserved in ethanol at room temperature.

### **6.2.2 Preparation of PEDOT:PSS/AgNWs anode**

PEDOT:PSS/AgNWs composite thin film was fabricated on Corning® microscope slide (substrate) by spin-coating technique at room temperature. Before spinning, the substrates were cut as per requirement of device fabrication, and then ultrasonically cleaned with deionized water, followed by washing in acetone and methanol for 15 min to remove the dust, grease and other impurities on the substrate surface. These substrates were then oven-dried for 20 min to remove the residual water vapor and volatile contaminants at around 80–90 °C. After that, 0.5

mg of dried AgNWs was added as the optimized values to 1 mL of PEDOT:PSS suspension, and then the mixtures were stirred intensely to obtain a homogeneous PEDOT:PSS/AgNWs solution.

In spin-coating, the initial velocity was 500 rpm and the high speed was 3000 rpm. Figure 6.1 shows a schematic illustration of fabricating PEDOT:PSS/AgNWs composite thin film. The solution of PEDOT:PSS/AgNWs was deposited on the substrate with many cycles to form a homogeneous PEDOT:PSS/AgNWs network transparent conducting thin film. However, in our case that the AgNWs are aligned as horizontally. Moreover, the observed diameter of AgNWs was around 40–50 nm.



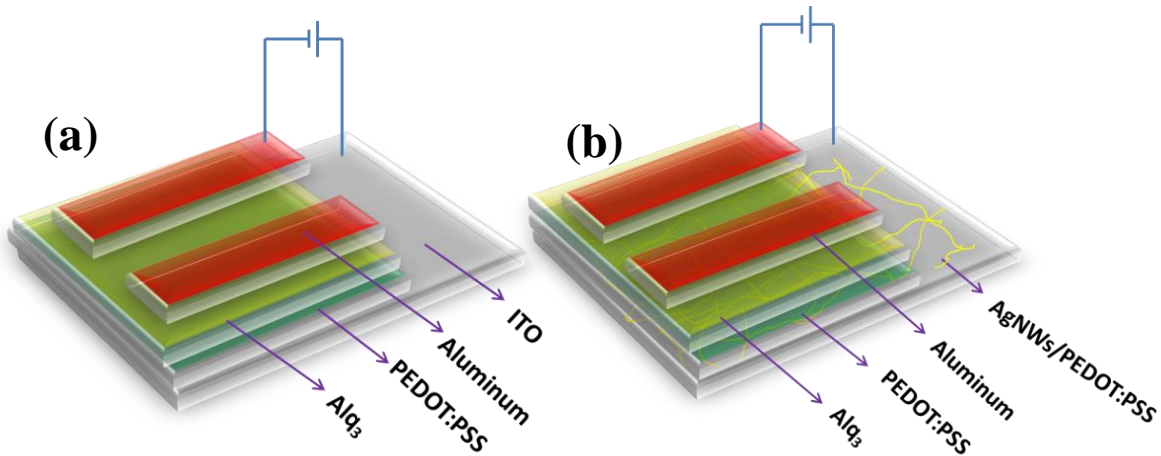
**Figure 6.1: Schematic illustration of fabricating PEDOT:PSS/AgNWs thin film**

By repeated spinning of PEDOT:PSS/AgNWs solution highly transparent and conductive hybrid composite thin films were fabricated. The dependence of the optical and electrical behaviour of the spin-coating hybrid TCF on the number of spin-coating cycles of the PEDOT:PSS/AgNWs was investigated. While increasing the spinning cycles the electrical conductivity of the prepared thin film was increased simultaneously so that the optical transmittance of the thin film decreases for more cycles. The optical transmittance of the prepared TCF was measured using an UV-Vis spectrophotometer. The sheet resistance was determined by Lucas Labs Four-Point probe methods. The surface morphologies were analysed using field emission SEM and AFM analyses.

### 6.2.3 Fabrication of green OLEDs

Alq<sub>3</sub> is a widely used green luminescent n-type organic semiconductor for fabrication of OLEDs. It possesses a high drift mobility to electrons as  $1.4 \times 10^{-6} \text{ cm}^2/\text{V.s}$ , whereas it exhibits a lower

hole mobility of  $2.0 \times 10^{-8} \text{ cm}^2/\text{V}\cdot\text{s}$  [57]. The unique photophysical, electrochemical and thermal properties of  $\text{Alq}_3$  make it attractive for the fabrication of green OLEDs. The ITO/organic interface are one of the main factors; it determines the performance of the OLEDs [58–61]. In single-layered OLEDs, the rough ITO surface of the electric shorts and the unbalanced hole-electron injection cause the oxidation of organic emitting layer by oxygen diffusing out of the ITO, limiting the lifetime of the device [62, 63]. To maintain the charge balance in  $\text{Alq}_3$ , an HTL, namely, PEDOT:PSS is inserted between the ITO and the organic emissive layers. As the ultrathin layer of PEDOT:PSS the films are more transparent to visible light; this additional layer of OLEDs does not readily diminish the light output and instead leads to a substantial improvement of the lifetime and luminous efficiency and reduces the operating voltage [64–66]. The beneficial effects of PEDOT:PSS arise from the smoothing of the ITO surface and the reduction of the hole-injection barrier due to high energy of the occupied electronic levels of PEDOT in comparison with that of ITO [61, 67]. PEDOT:PSS is a stable emulsion in water, and as a result is easy to spin-coat on ITO.



**Figure 6.2: Schematic illustration of drive device (a) and AgNWs blends with PEDOT:PSS composite based OLED (b)**

Figure 6.2 shows the schematic of heterojunction (HJ)-based OLEDs with  $\text{Alq}_3$  as the electron transport and emissive layer. An HJ is an interface that occurs between two regions or layers of dissimilar semiconductors. To elucidate the performance of the devices, two device architectures

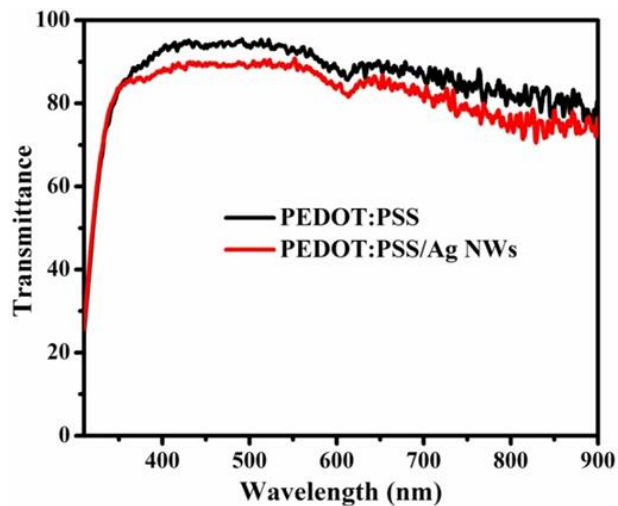
were employed, namely, drive devices and OLEDs. Figure 6.2 (a) shows the double-layered drive device consisting of HTL of PEDOT:PSS (60 nm), ETL/EML of Alq<sub>3</sub> (80 nm) and 1 nm of LiF layer followed by about 100 nm thickness of aluminum cathode. The solution of PEDOT:PSS has been spin-coated on pre-cleaned and oxygen plasma-treated ITO anode for subsequent device fabrication. After preparing the PEDOT:PSS thin film by spin-coating technique the substrate has been loaded on to thermal evaporation chamber (Figure 2.1). Alq<sub>3</sub> is thermally evaporated by maintaining the evaporation rates of 2 Å/s. Fifteen minutes after the evaporation of the organic materials, their film is deposited onto the substrate. Then the film containing the substrate is taken out of the chamber, and a custom-made mechanical mask made of steel sheet is placed on the Alq<sub>3</sub> thin film followed by 1 nm of LiF layer and thermally evaporated by maintaining the evaporation rate of 1 Å/s. Finally, a 100 nm of Al was thermally evaporated at the evaporation rate of 1 nm/s. All evaporations have been done at the chamber pressure of  $8 \times 10^{-5}$  mbar. Fluorescent green OLED (Figure 6.2 (b)) was prepared as drive device, where the anode is used as PEDOT:PSS/AgNWs composite film instead of ITO. The deposition rates are monitored using a quartz crystal monitor. The current-voltage characteristics of the devices were measured with Keithly 2636 source meter and measurements were reconfirmed by triaxial probe station. The photon emission was measured using HR4000 spectroradiometer as shown in Figure 2.8.

### **6.3 Results and discussion**

The concentration of the AgNWs is a key element in film properties, such as electronic conductivity and optical transparency for the spin-coating technique. A uniform film with good conductive and high transparence characteristics could thus be fabricated as the concentration of AgNWs in PEDOT:PSS is 0.5 mg/ml. The TCF characteristics include photophysical and morphological analysis and are discussed in the following sections. Green fluorescent OLEDs were fabricated based on commercial ITO and PEDOT:PSS/AgNWs composite film were based on TCF anode and their electric and photonic properties were compared.

### 6.3.1 Transmittance spectra

Figure 6.3 shows the transmittance spectra of PEDOT:PSS and PEDOT:PSS/AgNWs composite TCF fabricated on Corning microscope slides. The reason for choosing the Corning microscope slide is because of its high optical transparency and very smooth surface compared to conventional microscope slides. The TCF layer made of PEDOT:PSS exhibits a high transparency as PEDOT:PSS is optically more transparent when it is thin [37, 68, 69]. The observed transmittance was 92% at the wavelength of 550 nm for the TCF made of pristine PEDOT:PSS. As AgNWs have a higher absorption than the PEDOT:PSS/AgNWs hybrid-composite, which is made of a 0.5 mg of AgNWs mixed with 1 ml of PEDOT:PSS solution in the visible region of electromagnetic radiation, a slight decrease in the transmittance was noticed [70]. The observed transmittance was 88% for PEDOT:PSS/AgNWs hybrid-composite-based TCF. Nevertheless, the composite film mentioned above showed distinct visibility and uniform distribution of the NWs on the substrate. As the concentration of AgNWs increases, the crossed network in the film became more intensive, which lead to an increase in the electronic conductivity, while the transmittance of the composite film declined, which is not shown in the Figure 6.3. The measured sheet resistance was about 140 k $\Omega$ /sq and 30  $\Omega$ /sq for the TCF made on PEDOT:PSS alone and on PEDOT:PSS/AgNWs hybrid-composite-based TCF, respectively.



**Figure 6.3: UV-Vis transmittance spectra of PEDOT:PSS and PEDOT:PSS/AgNWs composite TCF fabricating on corning microscope slide**

Nevertheless, the composite film mentioned above showed distinct visibility and uniform distribution of the NWs on the substrate.

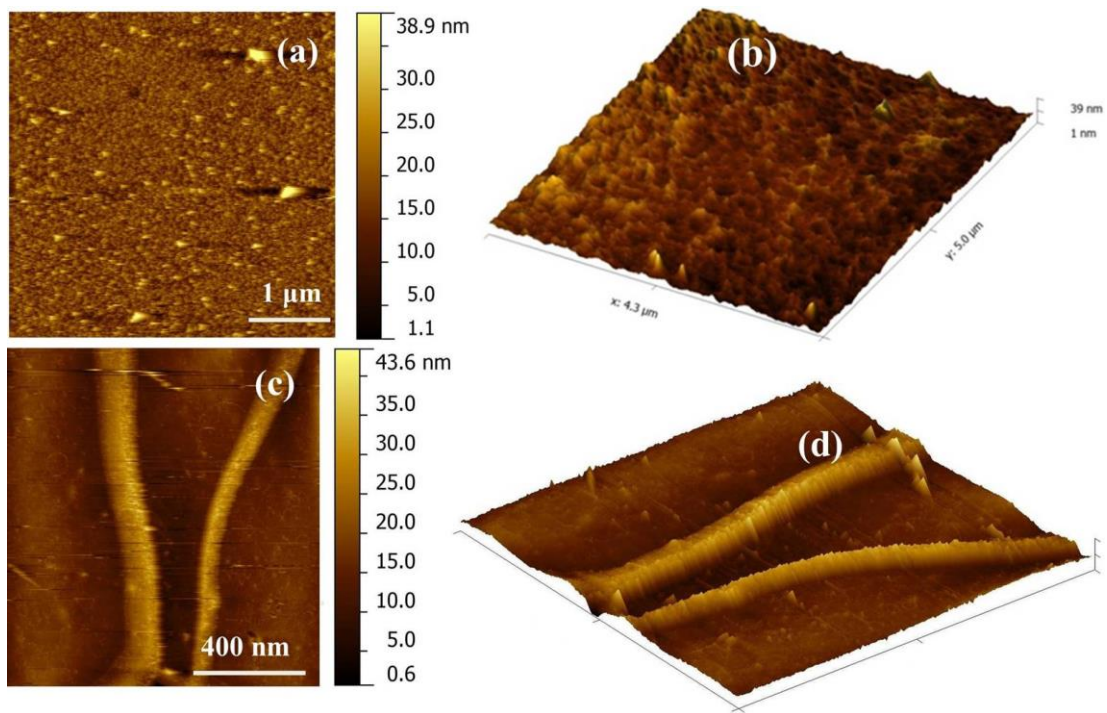
### **6.3.2 Morphological studies**

The surface morphology plays a key role in the performance of OLEDs. The surface morphology of TCF based on PEDOT:PSS and also PEDOT:PSS/AgNWs hybrid-composite was studied by SEM and AFM analysis as described below.

#### **6.3.2.1 AFM analysis**

Figure 6.4 shows the AFM images of PEDOT:PSS and PEDOT:PSS/AgNWs hybrid-composite TCF fabricated on Corning microscope slides. As can be seen in Figure 6.4(a), the concentration of 0.5 mg of AgNWs mixed with 1 ml of PEDOT:PSS hybrid-composite-based TCF fabricated on Corning microscope slide shows the extremely smoother side of the AgNWs.

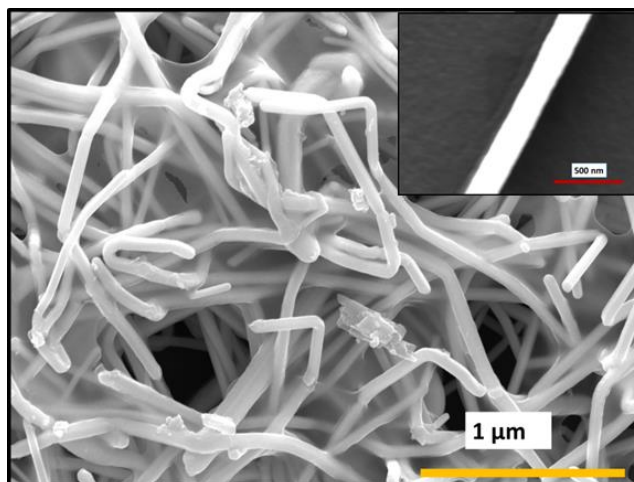
Figure 6.4(b) shows the three-dimensional image of the PEDOT:PSS/AgNWs hybrid-composite-based TCF. Figure 6.4(c) exhibits the morphology of PEDOT:PSS-based TCF fabricated on Corning microscope slide. It exhibits that the conductive PEDOT:PSS spreads over the substrate in a very uniform and smooth manner with a small roughness and granule morphology [25, 71]. The measured average roughness of the film was 1.6 nm. It shows that PEDOT:PSS has a strong adhesion on the Corning microscope slide because the substrate for the oxygen-plasma treatment before the spin-coating of PEDOT:PSS and PEDOT:PSS/AgNWs hybrid-composite enhances the adhesion of the film on the substrate. The 3D image of Figure 6.4 (d) shows that the morphology of PEDOT:PSS thin film is very small, spherical, and tiny pile shaped due to undulated premature nanostructured aggregation of particles, which may be due to limited solubility.



**Figure 6.4:** AFM images of TCF-based on PEDOT:PSS (a, b) and PEDOT:PSS/AgNWs hybrid-composite (c, d) fabricated on Corning® microscope slides

### 6.3.2.2 SEM analysis

Figure 6.5 shows the SEM image of PEDOT:PSS/AgNWs hybrid-composite TCF fabricated on the Corning microscope slide by 0.5 mg of AgNWs in 1 ml of PEDOT:PSS. The inset is a magnified SEM image of the AgNW, and depicts the NWs surfaces covered by polymer PEDOT:PSS. The AgNWs network could provide more electron pathways, and significantly enhance the electronic conductivity of the composite thin film [72]. Meanwhile, the coverage of PEDOT:PSS on AgNWs could isolate the NWs from the air, preventing the oxidation of metallic AgNWs enhancing adhesion on the substrate [73].



**Figure 6.5: SEM image of PEDOT:PSS/AgNWs composite on Corning microscope slide**

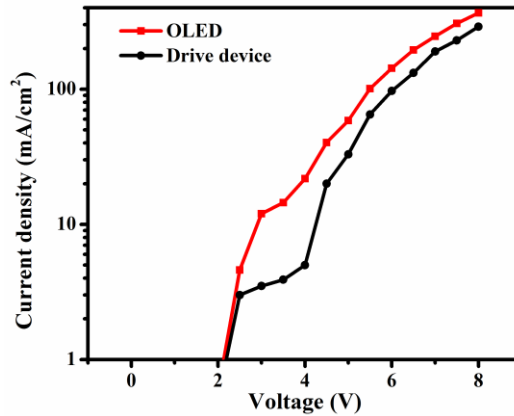
When the AgNWs concentrations increase, this makes the crossed network in the film more intensive and leads to increase in the conductivity while the transmittance declined for the composite thin films. The PEDOT:PSS/AgNWs composite consists of AgNWs densely packed together and interconnected with each other. The surface of the composite NWs was smooth and clear. The surface structure of the composite NWs is maintained even after spinning. The electronic conductivity of the NW-hybrid is mainly derived from the PEDOT:PSS, and the increase in the electronic conductivity arises from NWs-structural rearrangement of PEDOT:PSS which is interconnected on the surface of the NWs.

#### **6.4 Device characterization**

Current density-voltage and luminous intensity VS wavelength characteristics of fluorescent green OLEDs based on PEDOT:PSS/AgNWs and ITO anode are described below.



### 6.4.1 Current density-voltage (J–V) characteristics



**Figure 6.6: Current density-voltage characteristics of the fluorescent green OLEDs based on PEDOT:PSS/AgNWs and ITO anode**

The current density-voltage characteristics of the green fluorescent OLEDs fabricated on PEDOT:PSS/AgNWs and ITO anode are shown in Figure 6.6. Before preparing the HTL of PEDOT:PSS all the electrodes had undergone oxygen-plasma treatment for 2 min. It's observed that the increase in oxygen plasma exposure time on anodes beyond 2 minutes increased the WF further. However, this increment is limited to approximately 0.1 to 0.5 eV. Further, increment of WF is not possible. Moreover, the hole injection barrier between ITO/PEDOT:PSS is more than 0.7 eV. Thus, charge imbalance in Alq<sub>3</sub> layer due to high current density results in weaker luminescence in OLEDs [74]. Hence, the device characteristics further deteriorate with increase in plasma exposure time. The plasma-exposure time was optimized and maintained as 2 min for all the anodes used to fabricate the OLEDs reported here. The observed threshold voltage for the OLED fabricated on PEDOT:PSS/AgNWs hybrid-composite-based TCF anode was 2.6 V, whereas it was 3.9 V for the OLED fabricated on the ITO anode. This superior performance is attributed to the enhancement of the WF by PEDOT:PSS/AgNWs hybrid-composite. When increasing the drive voltage for both OLEDs after reaching the threshold voltage the current densities also increase rapidly. The OLED fabricated on PEDOT:PSS/AgNWs hybrid-composite TCF has more current density than the one made with the ITO anode. The observed current densities were 370 and 293 mA/cm<sup>2</sup> for OLEDs fabricated on PEDOT:PSS/AgNWs hybrid-composite TCF-based anode and ITO anode, respectively. With increasing drive voltage, higher

current density was observed in the OLEDs fabricated on PEDOT:PSS/AgNWs anodes. The higher resistance of the ITO anode may lead to a higher voltage drop on the anode, which may result in a lower current density lowering the luminous intensity compared to OLED fabricated on PEDOT:PSS/AgNWs hybrid-composite TCF anode.

#### 6.4.2 Electroluminescence studies

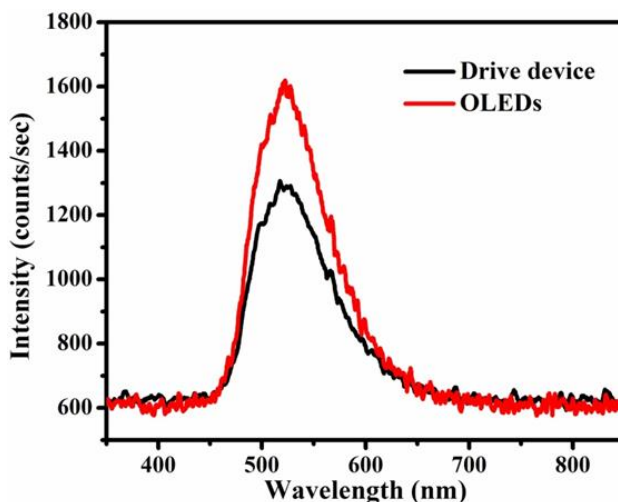


Figure 6.7: Plot of luminous intensity vs. wavelength of fluorescent green OLEDs based on PEDOT:PSS/AgNWs hybrid-composite and ITO anode

Figure 6.7 shows the luminous intensity-wavelength characteristics of fluorescent green OLEDs fabricated on PEDOT:PSS/AgNWs hybrid-composite TCF and ITO anodes. The fluorescent green OLED fabricated on PEDOT:PSS/AgNWs hybrid-composite-based TCF anode has a higher luminous intensity than the one with the ITO anode at the drive voltage of 6 V. This is due to well-matching WF of PEDOT:PSS/AgNWs hybrid-composite TCF anode with the hole transport layer of PEDOT:PSS. As the WF of PEDOT:PSS/AgNWs hybrid-composite TCF matches with HTL of PEDOT:PSS the holes can be easily injected into HTL, which should result in a lower turn-on voltage and a higher luminous intensity at a lower drive voltage in the fluorescent green OLEDs [75–76]. With increasing drive voltage, higher luminous intensity was also observed in the fluorescent green OLEDs fabricated on PEDOT:PSS/AgNWs hybrid-composite TCF anode than the one with the ITO anode. The observed maximum luminous intensities were 1610 and 1260 counts.s<sup>-1</sup> for green fluorescent OLEDs fabricated on

PEDOT:PSS/AgNWs hybrid-composite TCF and ITO anode, respectively at a wavelength of 530 nm. The current density together with the brightness of the OLED fabricated on PEDOT:PSS/AgNWs hybrid-composite TCF is significantly improved as compared to ITO anode-based OLED.

## 6.5 Summary

The synthesis of AgNWs of around 20  $\mu\text{m}$  length and 70 nm diameters were achieved by adapting polyol process and studied its performances for application in OLEDs as a TCF anode. The optimized concentration of AgNWs is 0.5 mg in 1 ml of PEDOT:PSS and was used to fabricate PEDOT:PSS/AgNWs hybrid-composite TCF electrode on Corning microscope slide using the spin-coating technique, resulting in high transparency (88%) and good conductive ( $30\Omega/\text{sq}$ ) thin film. The uniformity and optoelectronic properties of the fabricated TCF were systematically studied by AFM analysis and UV-Vis transmittance spectra, respectively. Two types of green fluorescent OLEDs were prepared; OLEDs made of commercial ITO anode and ITO-free OLEDs as AgNWs and PEDOT:PSS hybrid-composite TCF-based anode. The OLED fabricated on PEDOT:PSS/AgNWs hybrid-composite TCF has more current density than ITO anode-based OLED. The observed current densities were 370 and 293  $\text{mA}/\text{cm}^2$  for OLEDs fabricated on PEDOT:PSS/AgNWs hybrid-composite TCF-based anode and ITO anode, respectively. The observed maximum luminous intensities were 1610 and 1260  $\text{counts}\cdot\text{s}^{-1}$  for green fluorescent OLEDs fabricated on PEDOT:PSS/AgNWs hybrid-composite TCF and ITO anode, respectively, at a wavelength of 530 nm. The current density together with the brightness of the OLED fabricated on PEDOT:PSS/AgNWs hybrid-composite TCF is significantly improved; it could be due to the enhancement of WF of PEDOT:PSS/AgNWs hybrid-composite.

## 6.6 References

- [1] Choi W.-S., Kim W.J., Park S.-H., Cho S.O., Lee J.K., Park J.P., Ha J.-S., Chung T.H., Jeong T., *Solid-State Electron.*, 2017, 127: 57–60.

- [2] Kim T., McCall J.G., Jung Y.H., Huang X., Siuda E.R., Li Y., Song J., Song Y.M., Pao H.A., Kim R.-H., Lu C., Lee S.D., Song S., Shin G., Al-Hasani R., Kim S., Tan M P., Huang v, Omenetto F.G., Rogers J.A., Bruchas M.R., *Science*, 2013, 340: 211–216.
- [3] Lakshmanan R., Raja P.P., Shivaprakash N.C., Sindhu S., *J Mater Sci: Mater Electron.*, 2016, 27: 6035–6042.
- [4] Koo W H., Jeong S M., Araoka F., Ishikawa K., Nishimura S., Toyooka T., Takezoe H., *Nat. Photon.*, 2010, 4: 222–226.
- [5] Kim K. S., Zhao Y., Jang H., Lee S.Y., Kim J.M., Kim K.S., Ahn J-H., Kim P., Choi, Hong B.H., *Nature*, 2009, 457: 706–710.
- [6] Siju C.R., Raja L., Shivaprakash N.C., Sindhu S., *J. Solid. State. Electrochem.*, 2015, 19: 1393–1402.
- [7] Lakshmanan R., Prabhu P.P., Shivaprakash N.C., Sindhu S., *J. Appl. Polym. Sci.*, 2014, 131: 40717.
- [8] Ou. Q.-D., Zhou L., Li Y-Q., Shen S., Chen J-D., Li C., Wang Q-K., Lee S-T., *Adv. Funct. Mater.*, 2014, 24: 7249–7256.
- [9] Lee J., Chen H-F., Batagoda T., Coburn C., Djurovich P.I., Thompson M.E., Forres S.R., *Nat. Mater.*, 2015, 15: 92–98.
- [10] Zhao, Zhu L., Liu Y., Wang Y., Ma D., *Org. Electron.*, 2015, 27: 207-211.
- [11] Yu. P., Tsai C.-Y., Chang J.-K, Lai C.-C., Chen P.-H., Lai Y.-C., Tsai P.-T., Li M.-C., Pan H.-T., Huang Y.-Y., *ACS Nano*, 2013, 7: 10780–10787.
- [12] Reineke S., Leo W.K., *Phys. Rev. B*, 2007, 75: 125328.
- [13] Hofmann S., Rosenow T.C., Gather M.C., Lüssem B., Leo K., *Phys. Rev. B.*, 2012, 85: 245209.

- [14] Sun N., Wang Q., Zhao Y., Chen Y., Yang D., Zhao F., Chen F., Ma D., *Adv. Mater.*, 2014, 26: 1617–1621.
- [15] Zhao F., Sun N., Zhang H., Chen J., Ma D., *J. Appl. Phys.*, 2012, 112: 084504.
- [16] An B.W., Gwak E.J., Kim K., Kim Y.C., Jang J., Kim J.Y., Park J.U., *Nano Lett.* 2016, 16: 471–478.
- [17] Li J., Liang J., Jian X., Hu W., Li J., Pei Q.A., *Macromol. Mater. Eng.*, 2014, 299: 1403–1409.
- [18] Kim D., Zhu L., Jeong D.-J., Chun K., Bang Y.-Y., Kim S.-R., Kim J.-H., Oh S.-K., *Carbon.*, 2013, 63: 530–536.
- [19] Ko E.-H., Kim H.-J., Lee S.-J., Lee J.-H., Kim H.-K., *RSC Adv.*, 2016, 6: 46634–46642.
- [20] Yu X., Yu X., Zhang J., Zhang D., Ni J., Cai H., Zhang D., Zhao Y., *Mater Lett.*, 2015, 145: 219–223.
- [21] Choi K.-H., Kim J., Noh Y.-J., Na S.-I., Kim H.-K., *Sol. Energ. Mat. Sol. Cells*, 2013, 110: 147–153.
- [22] Lee J.-H., Shin H.-S., Noh Y.-J., Na S.-I., Kim H.-K., *Sol. Energ. Mate. Sol. Cells*, 2013, 114: 15–23.
- [23] Hu L., Kim H.S., Lee J.-Y., Peumans P., Cui Y., *ACS Nano*, 2010, 5: 2955–2963.
- [24] Lee H.J., Hwang J.H., Choi K.B., Jung S.-G., Kim K.N., Shim Y.S., Park C.H., Park Y.W., Ju B.-K., *Appl. Mater. Interfaces*, 2013, 5: 10397–10403.
- [25] Zhang D., Ryu K., Liu X., Polikarpov E., Ly J., Tompson M.E., Zhou C., *Nano Lett.*, 2006, 6: 1880–1886.
- [26] Wang G.-F., Tao X.-M., Wang R.-X., *Nanotechnology*, 2008, 19: 145201.
- [27] Kazaoui S., Minami N., Nalini B., Kim Y., Takada N., Hara K., *Appl. Phys. Lett.*, 2005, 87: 211914.

- [28] Celle C., Mayousse C., Moreau E., Basti H., Carella A., Simonato J.-P., *Nano Res.*, 2012, 5: 427–433.
- [29] Park B., Bae I.-G., Huh Y.H., *Sci. Rep.*, 2016, 6: 19485.
- [30] Ji S., He W., Wang K., Ran Y., Ye C., *small*, 2014, 10: 4951–4960.
- [31] Lee H., Lee K., Park J.T., Kin W.C., Lee H., *Adv. Funct. Mat.*, 2014, 24: 3276–3283.
- [32] Duan X., Huang Y., Cui Y., Wang J., Lieber C.M., *Nature*, 2001, 409: 66–69.
- [33] Xia Y., Yang P., Sun Y., Wu Y., Mayers B., Gates B., Yin Y., Kim F., Yan H., *Adv. Mater.*, 2003, 15: 353–389.
- [34] Barnes T.M., Reese M.O., Bergeson J.D., Larsen B.A., Blackburn J.L., Beard M.C., Bult J., Lagemaat J.V.D., *Adv. Energy Mater.*, 2012, 2: 353–360.
- [35] Wu Z., Chen Z., Du X., Logan J.M., Sippel J., Nikolou M., Kamaras K., Reynolds J.R., Tanner D.B., Hebard A.F., Rinzler A.G., *Science*, 2004, 305: 1273–1276.
- [36] Lee J.-Y., Connor S.T., Cui Y., Peumans P., *Nano Lett.*, 2008, 8: 689–692.
- [37] Vosgueritchian M., Lipomi D.J., Bao Z., *Adv. Funct. Mater.*, 2011, 22: 421–428.
- [38] Sui D., Huang Y., Huang L., Liang J., Ma Y., Chen Y., *Small*, 2011, 7: 3186–3192.
- [39] Ou R.Q., Gupta S., Parker C.A., Gerhardt R.A., *J. Phys. Chem. B*, 2006, 110: 22365–22373.
- [40] Ghosh D.S., Chen T.L., Mkhitarian V., Pruneri V., *Appl. Mater. Interfaces* 2014, 6: 20943–20948.
- [41] Chou C.-Y., Liu H.-S., Liou G.-S., *RSC Adv.* 2016, 6: 61386–61392.
- [42] Liu Y.-S., Feng J., Ou X.-L., Cui H.-F., Xu M., Sun H.-B., *Org. Electron.*, 2016, 31: 247–252.
- [43] Duan S., Zhang L., Wang Z., Li C., *RSC Adv.*, 2015, 5: 95280–95286.

- [44] Ghosh D.S., Chen T.L., Mkhitarian V., Pruneri V., *Appl. Mater. Interfaces*, 2014, 6, 20943–20948.
- [45] Qingqing Y., Jinliang Y., Delan M., *J. Semicond.* 2015, 36: 123005.
- [46] He X., He R., Lan Q., Wu W., Duan F., Xiao J., Zhang M., Zeng Q., Wu J., Liu J., *Materials*, 2017, 10: 220.
- [47] Hill I.G., Kahn A., *J. Appl. Phys.*, 1998, 84: 5583–5586.
- [48] Wang Z.B., Helander M.G., Qiu J., Puzzo D.P., Greiner M.T., Hudson Z.M., Wang S., Liu Z.W., Lu Z.H., *Nat. Photon.*, 2011, 5: 753–757 .
- [49] Mashford B.S., Stevenson M., Popovic Z., Hamilton C., Zhou Z., Breen C., Steckel J., Bulovic V., BawendiM., Coe-Sullivan S., Kazlas P.T., *Nat. Photon.*, 2013, 7: 407–412.
- [50] Castellani M., Winkler S., Broker B., Baumgarten M., Mullen K., Koch N., *Appl. Phys. A*, 2014, 114: 291–295.
- [51] Koldemir U., Braid J.L., Morgenstern A., Eberhart M., Collins R.T., Olson D.C., Sellinger A., *Phys. Chem. Lett.*, 2015, 6: 2269–2276.
- [52] Kang H., Jung S., Jeong S., Kim G., Lee K., *Nat. Commun.*, 2015, 6, 6503.
- [53] Yun H.J., Kim S.J., Hwang J.H., Shim Y.S., Jung S.-G., Park Y.W., Ju B.-K., *Sci Rep.*, 2016, 6: 34150.
- [54] Lee J., Lee P., Lee H., Lee D., Lee S.S., Ko S.H., *Nanoscale*, 2012, 4: 6408–6414.
- [55] Yang C., Gu H., Lin W., Yuen M.M., Wong C.P., Xiong M., Gao B., *Adv. Mater.*, 2011, 23: 3052–3056.
- [56] Shobin L.R., Sastikumar D., Manivannan S., *Sens. Actuator A-Phys.*, 2014, 214: 74–80.
- [57] Kepler R.G., Beeson P.M., Jacobs S.J, Anderson R.A., Sinclair M.B., Valencia V.S., Cahill P.A., *Appl. Phys. Lett.*, 1995, 66: 3618–3620.

- [58] Andersson P. D., Nilsson D., Svensson P.O., Chen M., Malmstrom A., Remonen T., Kugler T., Berggren M., *Adv. Mater.*, 2002, 14: 1460–1464.
- [59] Gustafsson G., Cao Y., Treacy G.M, Klavetter F., Colaneri N., Heeger A.J., *Nature*, 1992, 357: 477–479.
- [60] Wong K.W., Yip H.L., Luo Y., Yong K.Y., Lau W.M., Low K.H., Chow H.F., Gao Z.Q., Yeung W.L., Chang C.C., *Appl. Phys. Lett.*, 2002, 80: 2788–2790.
- [61] Kugler T., Andersson A., Holmes A.B., Li X., Salaneck W.R., *Synth Met.*, 1999, 100: 163–168.
- [62] Elschner A., Bruder F., Heuer W.W., Jonas F., Karbach A., Kirchmeyer S., Thurn S., Wehrmann R., *Synth. Met.*, 2000, 139: 111–112.
- [63] Karg S., Scott J.C., Salem J.R., Angelopoulos M., *Synth. Met.*, 1996, 80: 111–117.
- [64] Kim J.S., Ho P.K.H., Thomas P.D.S., Friend R.H., Cacialli F., Bao G.W., Li S.F.Y., *Chem. Phys. Lett.*, 1999, 315: 307–312.
- [65] Carter S.A., Angelopoulos M., Karg S., Brock P.J., Scott J.C., *Appl. Phys. Lett.*, 1997, 70: 2067–2069.
- [66] Carter J.C., Grizzi I., Heeks S.K., Lacey D.J., Latham S.G., May P.G., Ruiz de-los Panos O., Pichler K., Towns C.R., Wittmann H.F., *Appl. Phys. Lett.*, 1997, 71: 3436–3447.
- [67] Brown T.M., Kim J.S., Friend R.H., Cacialli F., Daik R., Feast W.J., *Appl. Phys. Lett.*, 1999, 75: 1679–1681.
- [68] Teo M.Y., Kim N., Kee S., Kim B.S., Kim G., Hong S., Jung S., Lee K., *Appl. Mater. Interfaces*, 2017, 9: 819–826.
- [69] McCarthy J.E., Hanley C.A., Brennan L.J., Lambertini V.G., Gun'ko Y.K., *J. Mater. Chem. C*, 2014, 2: 764–770.



- [70] Xu Q., Song T., Cui W., Liu Y., Xu W., Lee S.-T., Sun B., *Appl. Mater. Interfaces*, 2015, 7: 3272–3279.
- [71] Ghazy O.A., Ibrahim M.M., Elfadl F.I.A., Hosni H.M., Shehata E.M., Deghiedy N.M., Balboul M.R., *J. Rad. Res. Appl. Sci.*, 2015, 8, 166–172.
- [72] Qingqing Y., Jinliang Y., Delan M., *JoS.*, 2015, 36: 123005.
- [73] Hwang B., Lim S., *J. Nanomater.*, 2017, 2017: 1489186.
- [74] Hong Y., Yang J., Kwak J., Lee C., *J. Inf. Disp.*, 2009, 10, 111–116.
- [75] Fournet P., Coleman J.N., Lahr B., Drury A., Blau W.J., OBrien D.F., *J. Appl. Phys.*, 2001, 90: 969–975.
- [76] Koch N., Kahn A., Ghijsen J., Pireaux J.J., Scwartz J., Johnson R.L., Elschner A., *Appl. Phys. Lett.*, 2003, 82: 70–72.

## CHAPTER 7

### Conclusion and Future Scopes

The research presented in this thesis focuses on wide range of experimental work, which is conducted with the following objectives: synthesis and characterization of three 4'-aryl substituted 2,2': 6',2''-terpyridine (terpy) derivatives. Synthesis, photophysical, electrochemical and thermal behaviour of Zn(II) and Ru(III)-based 4'-aryl substituted terpy metal complexes investigated for OLED applications. Further, TCF has been prepared and characterised using synthesised AgNWs as replacement for conventional ITO electrode. Fabrication and comparison of fluorescent green OLEDs using Alq<sub>3</sub> based on PEDOT:PSS/AgNWs hybrid-composite anode and commercial ITO anode have also been done.

#### 7.1 Conclusion

*Chapter 1* summarizes the significance of organic semiconductors and its lighting applications and also provides a thorough review of the current literature. In addition, device structure, operating mechanism, materials selection and energy-level alignment of OLEDs have also been reviewed.

*Chapter 2* describes the thin-film fabrication technique used in this work including thermal evaporation and spin coating. Further, morphological analysis, such as atomic force microscopy, and field emission scanning electron microscope have been explored. Moreover, photophysical characterization methods used in this study, such as UV-Vis absorbance spectroscopy, photoluminescence, and time-resolved fluorescence spectroscopy have been discussed under material properties. In addition, the electrical and electroluminescent behaviours of OLEDs device have also been explored.

*Chapter 3* discusses the design, synthesis and characterization of three 4'-aryl substituted terpy derivatives (C-1–C-3) in a single pot reaction. They have good thermal stability, significant emission in the blue region (380–440 nm) and fast fluorescence lifetimes such as 0.35, 1.55 and 0.29 ns for C-1, C-2 and C-3, respectively. The 3, 4, 5-trimethoxy-phenyl-substituted terpyridine derivative showed a high red shift with respect to 4-methylphenyl and 2-furyl substituted terpy

derivatives. This could be due to a smaller reorganization energy associated with the charge transfer transition of trimethoxyphenyl. The calculated HOMO and LUMO values suggest that the synthesised terpy derivatives favour the electron-transporting and fluorescent emitter to design the blue fluorescent OLEDs.

*Chapter 4* addresses the synthesis, photophysical, thermal and electrochemical properties of three novel blue-to-green fluorescent Zn(II)-based terpy complexes (**Zn(L<sub>1</sub>-L<sub>3</sub>)**). The charge transition is investigated as the potential charge transfer to the  $n-\pi^*$  and  $\pi-\pi^*$  states of the ILCT in the complexes are efficient. The geometry optimization and electronic structure of these complexes were assessed by density functional theory (DFT). These complexes show a sky-to-deep blue fluorescence in DMSO and a deep blue-to-green luminescence in the crystalline states. The **Zn(L<sub>2</sub>)** complex has a broadened emission spectrum ca. 365–600 nm in DMSO. These observations show that substituting suitable functional groups onto terpyridine ligands can lead band engineering to offer a required colour. **Zn(L<sub>1</sub>)** complex exhibits a deep blue emission, while **Zn(L<sub>2</sub>)** complex emits deep green colour. These results suggest that appropriately substituted ligands on Zn(II) ions, the result of Zn(II)-based terpy complexes, can generate long-lived fluorescence at room temperature, which is quite rare for Zinc ions. Such molecules are of fundamental interest, yet are poised for potential application in optoelectronics and luminescence-based technologies.

*Chapter 5* explores another interesting and noteworthy class of organometallic complexes as a series of three novel 4'-aryl substituted orange-fluorescent Ru(III)-based terpy complexes. Spectral analysis exhibits that the luminescence originated from electronic transition between SUMO and SOMO energy levels. All complexes exhibit orange emissions in DMSO with emission spectra ca. 591–620 nm, and the **Ru(L<sub>2</sub>)** complex shows broad orange emission. Electronic excitation occurs due to MLCT and ILCT processes of these complexes. The bands centered at 591 and 620 nm demonstrate that these emissions originated from the transition of SUMO to SOMO energy levels, that is, from radiative decay from the doublet exciton. Due to the heavy metal effect of Ru(III) ions the photophysical behaviour depends on MLCT rather than on ILCT process. Since all three **Ru(L<sub>1</sub>-L<sub>3</sub>)** complexes are the orange emission, it can be

concluded that substituting the functional groups onto terpy ligands of Ru(III) complex does not stand much chance in optical band gap.

The first part of *Chapter 6* describes the synthesis of silver nanowires of around 20  $\mu\text{m}$  length and 200 nm diameters by adjusting the polyol-process and studied their performances. The optimized concentration of AgNWs is 0.5 mg in 1 ml of PEDOT:PSS and was used to fabricate PEDOT:PSS/AgNWs hybrid-composite TCF electrode on Corning microscope slide by spin-coating process, resulting in reduced sheet resistance as 30  $\Omega/\text{sq}$  with high transparent (88%) thin film. The second part of the chapter describes the fabrication of fluorescent green OLEDs based on PEDOT:PSS/AgNWs hybrid-composite anode and ITO anode and the comparison of their performance. The OLED fabricated on PEDOT:PSS/AgNWs hybrid-composite-based TCF has more current density than one made with ITO anode. The measured current densities were 370 and 293  $\text{mA}/\text{cm}^2$  for OLEDs fabricated on PEDOT:PSS/AgNWs hybrid-composite TCF-based anode and ITO anode, respectively. The observed maximum luminous intensities were 1610 and 1260  $\text{counts}\cdot\text{s}^{-1}$  for OLEDs fabricated on PEDOT:PSS/AgNWs hybrid-composite TCF and ITO anode, respectively, at 530 nm. The current density together with the brightness of OLED fabricated on PEDOT:PSS/AgNWs hybrid-composite TCF is significantly improved; it could be due to the enhancement of WF of PEDOT:PSS/AgNWs hybrid-composite.

## 7.2 Future scopes

Solid-state lighting devices, such as OLEDs, will soon replace conventional illumination sources because of their advantages like low power consumption, high brightness, and environmental friendliness. WOLED is of particular importance as lighting source for developing efficient solid-state lighting, and the key challenges to WOLED technology are general illumination applications including white light with high colour rendering index (CRI), low cost, low operational potential, and long lifetime. A key point in WOLED development for application in full-colour display could be in two ways; one is a set of a red, green and blue emitter with high efficiency, colour purity, and stability, while the other method is mixing of yellow emitter with blue emitter in an equal ratio. However, the mixing of two ideally complementary-emitting compounds opens the door for efficient WOLEDs. In future, this approach should be

investigated in more detail, especially how to conserve the white emission by balancing the charge carriers in the consecutive layers of WOLEDs.

Synthesis and characterization of thermally activated delayed fluorescence (TADF) materials exhibit delayed fluorescence at room temperature, which enables the derivative to possess long-lived luminescence. As its lifetime is of the order of some microseconds to even milliseconds, the derivative will be very useful in time-resolved fluorescence imaging and OLEDs. These particular properties including a long luminescence lifetime and large stoke shift make this derivative the potential candidate to replace conventional luminescent complexes such as lanthanide and transition metals.

Preparation and performance of highly conductive TCF is based on conductive PEDOT:PSS with CNTs or metal nanowires hybrid-composite on the flexible polymeric substrate for the fabrication of ITO-free optoelectronic devices. Of the total cost of the optoelectronic device, 60% went towards the TCF electrode. Hence, our TCF results show the cost-effectiveness of the preparation of optoelectronic devices in the preparation of roll-to-roll TCF anode on flexible substrate.

## APPENDIX A

### Spectral characterization of C<sub>1</sub>-C<sub>3</sub> complexes

---

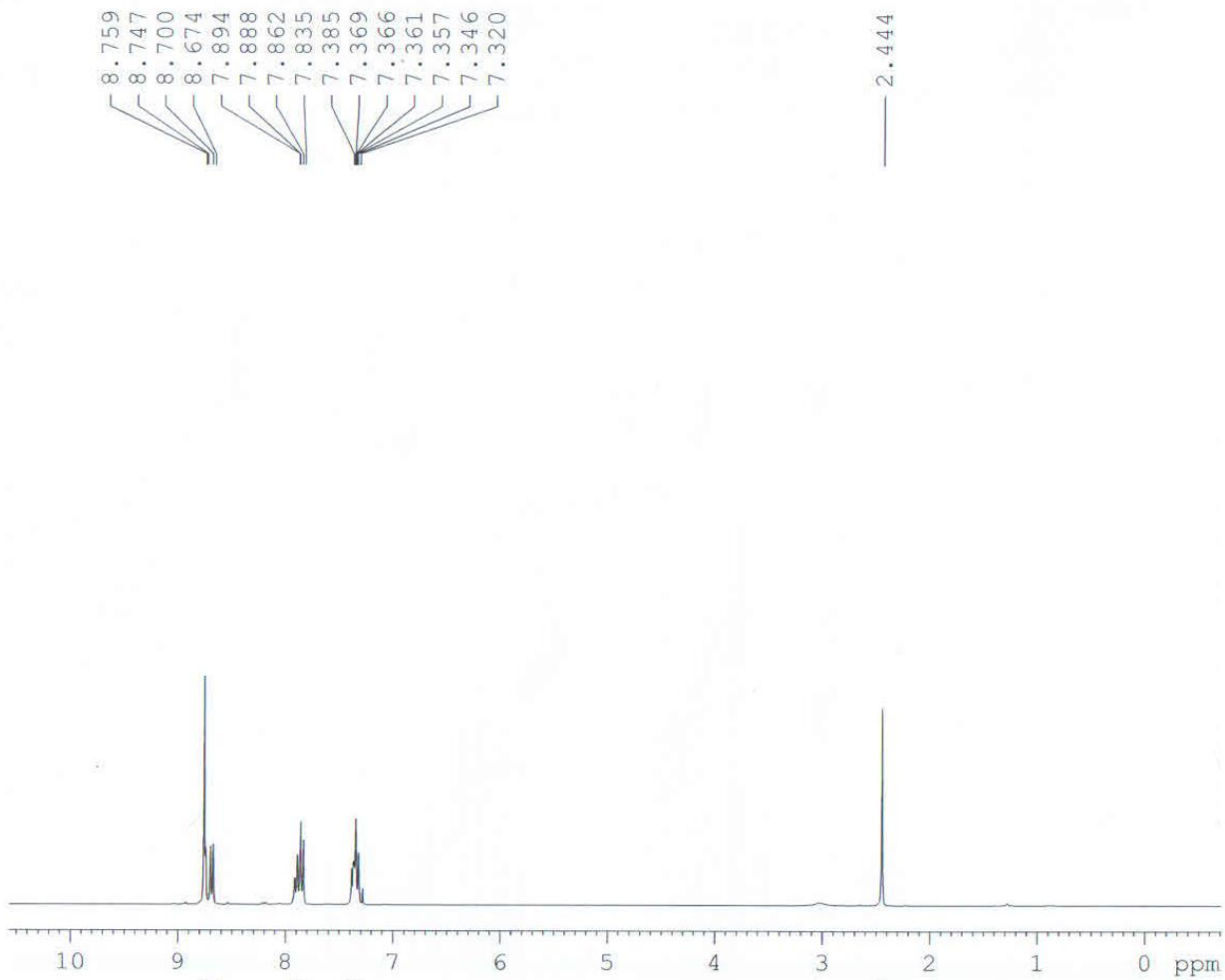


Figure A1.1: <sup>1</sup>H-NMR spectrum of C-1

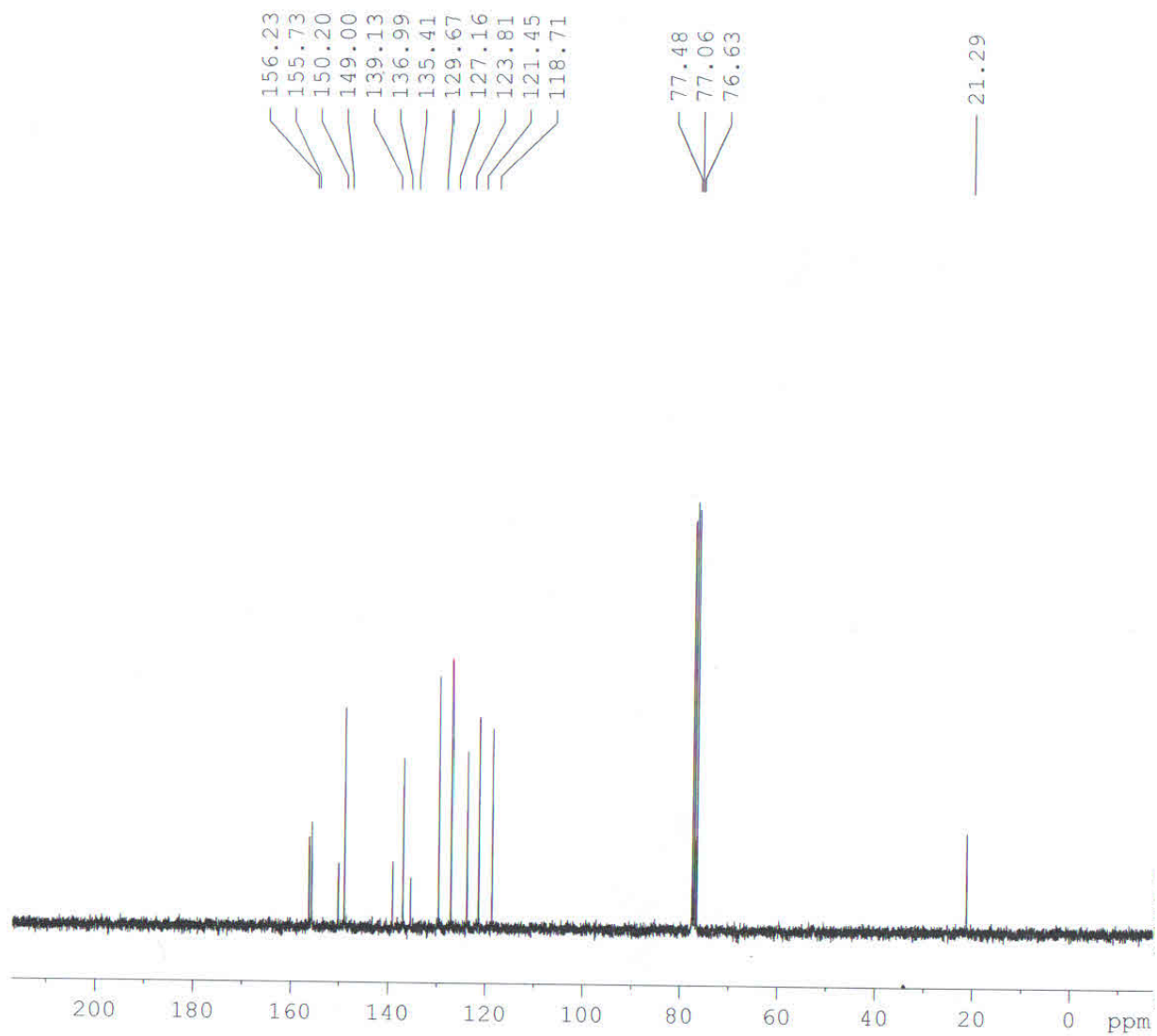


Figure A1.2:  $^{13}\text{C}$ -NMR spectrum of C-1

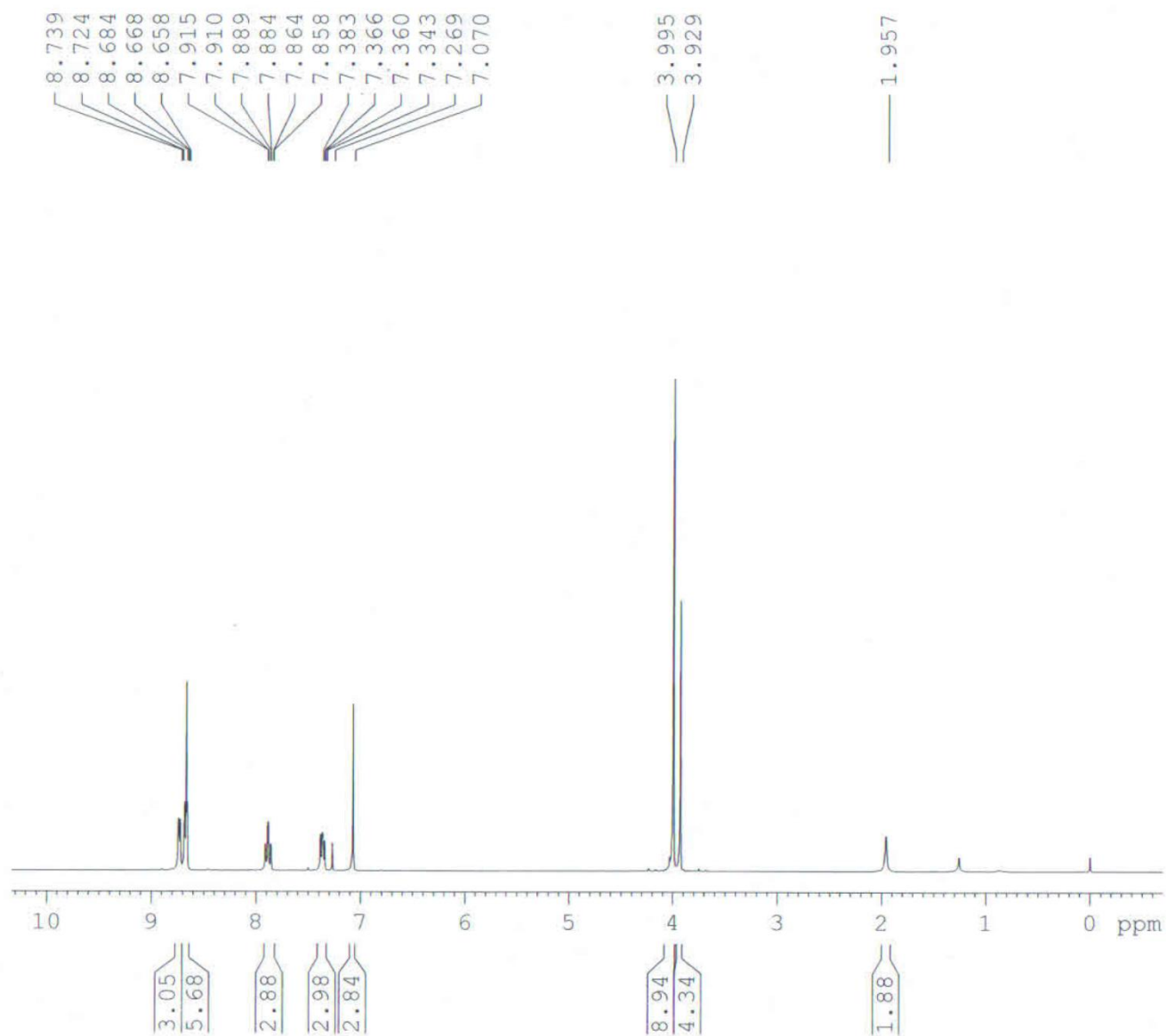


Figure A1.3: <sup>1</sup>H-NMR spectrum of C-2



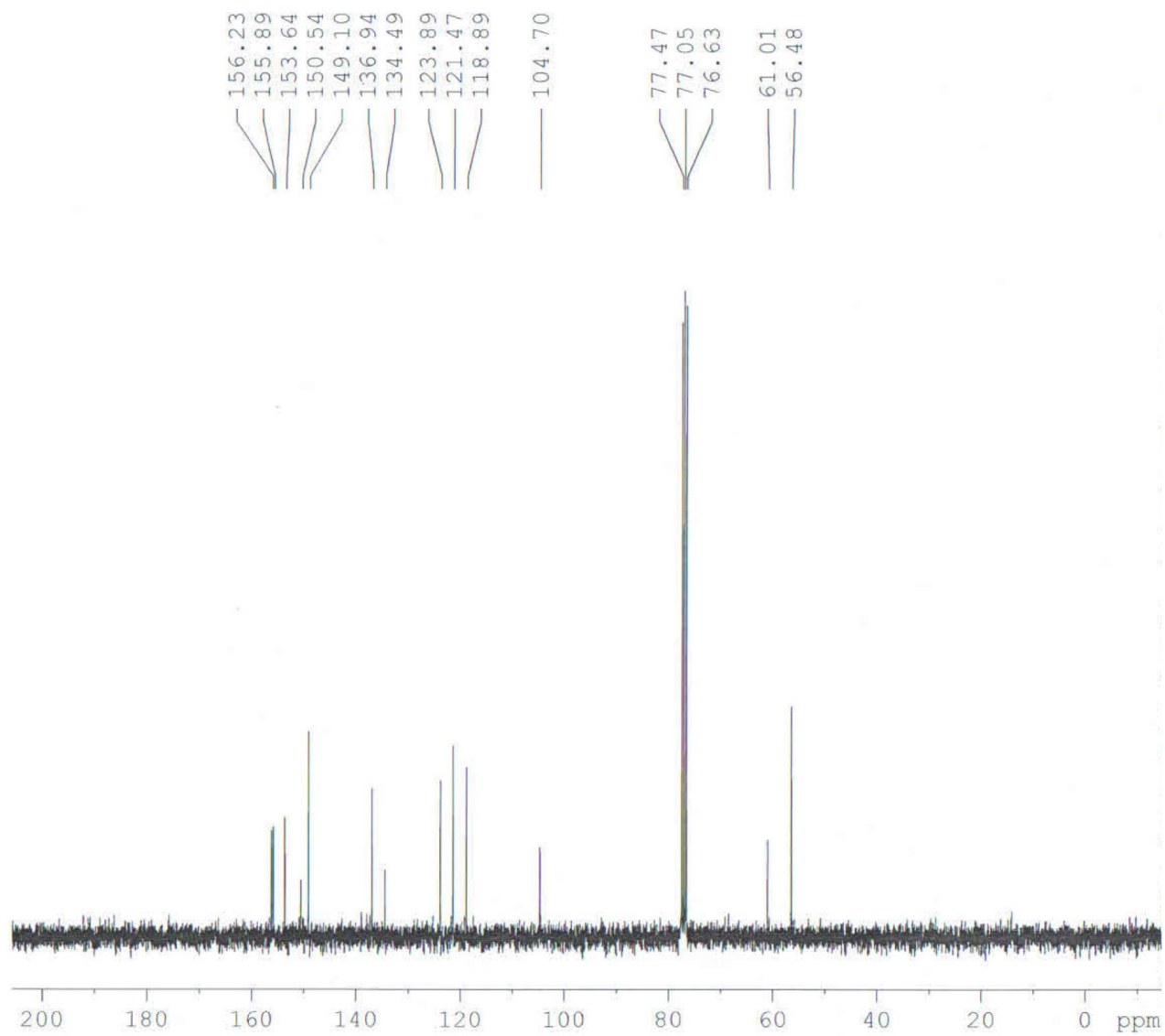


Figure A1.4:  $^{13}\text{C}$ -NMR spectrum of C-2

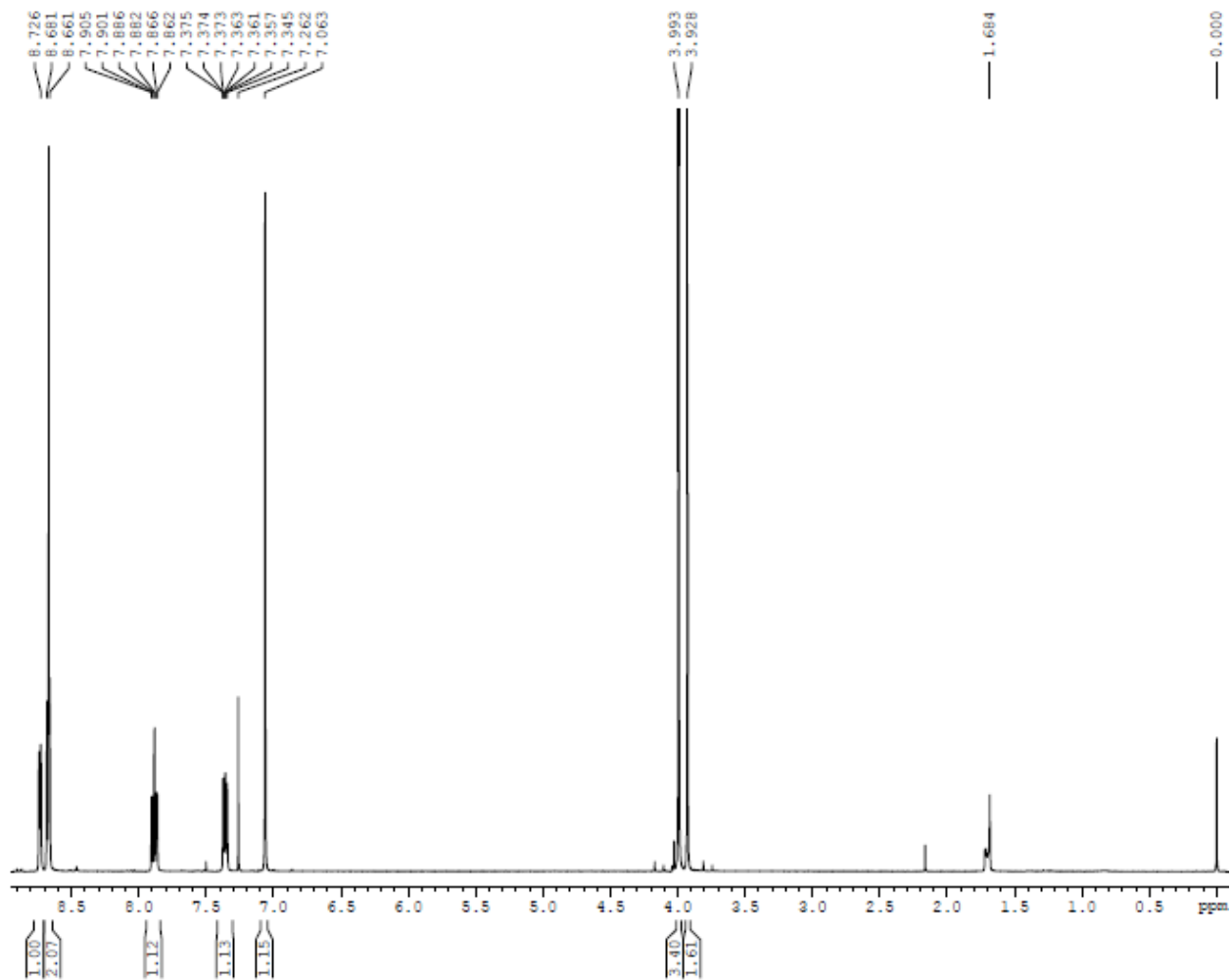


Figure A1.5: <sup>1</sup>H-NMR spectrum of C-3

TERPY-TRYM

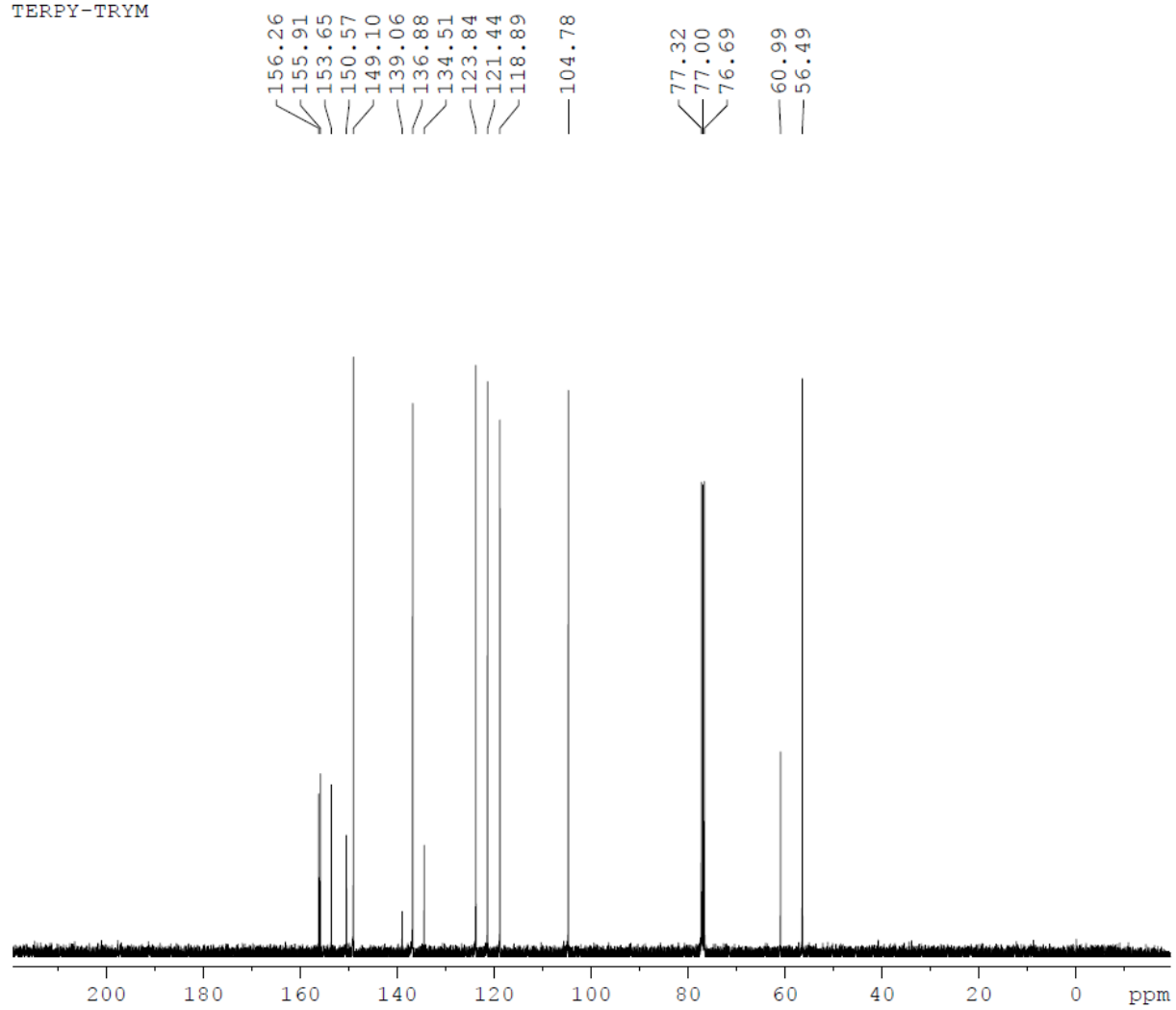


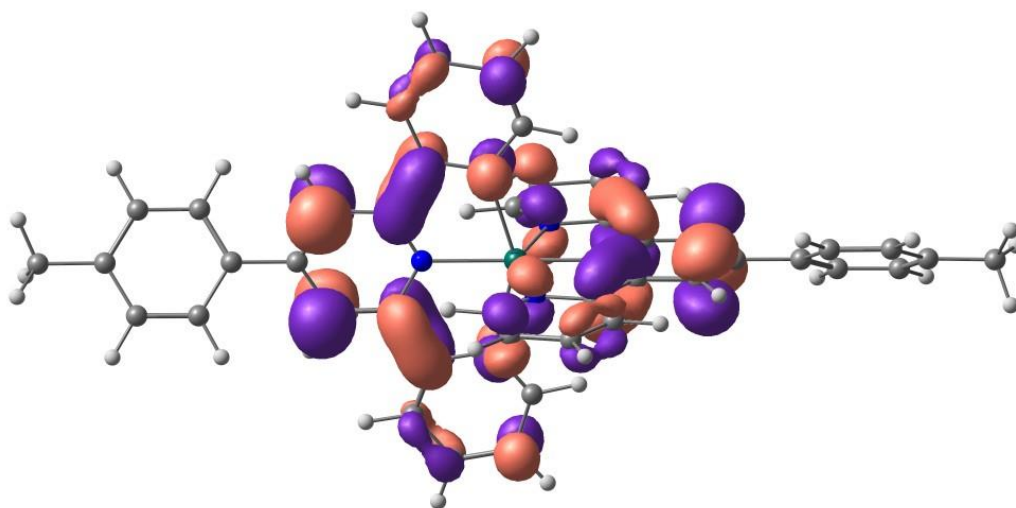
Figure A1.6:  $^{13}\text{C}$ -NMR spectrum of C-3

## APPENDIX B

### HOMO and LUMO orbital levels, photophysical properties and fluorescence images of Zn(L<sub>1</sub>-L<sub>3</sub>) complexes

LUMO+1

Zn(L<sub>1</sub>)



HOMO-1

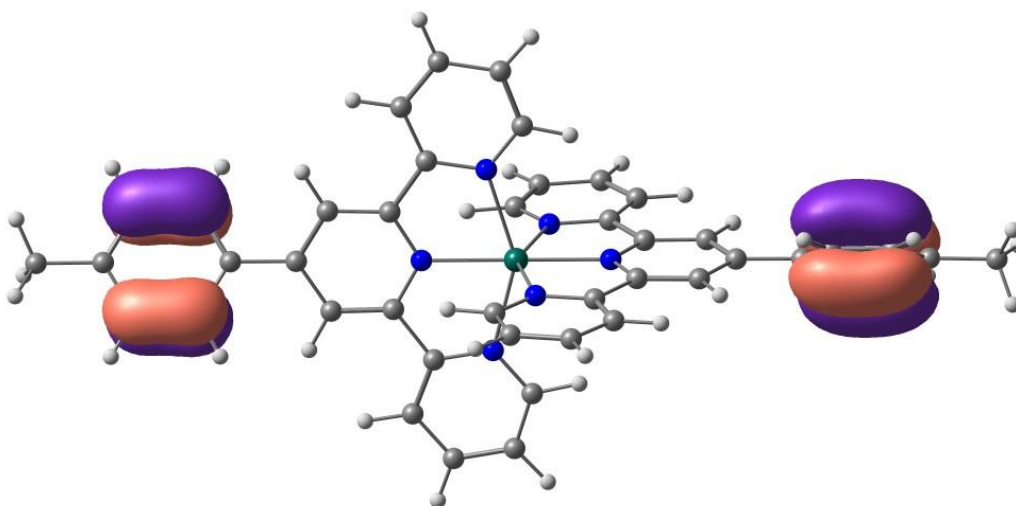
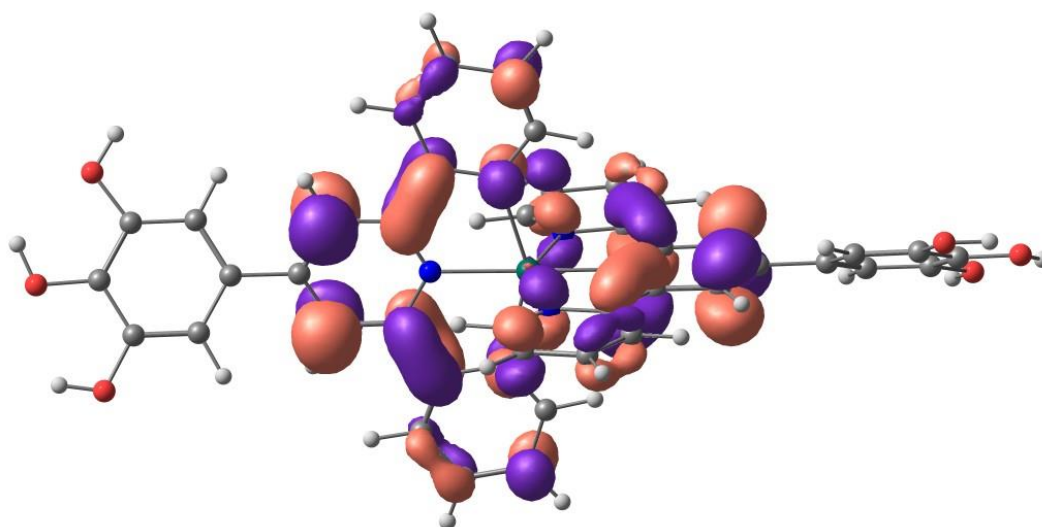


Figure B2.1: The LUMO+1 and HOMO-1 orbitals of complex Zn(L<sub>1</sub>) complex.

LUMO+1

Zn(L<sub>2</sub>)



HOMO-1

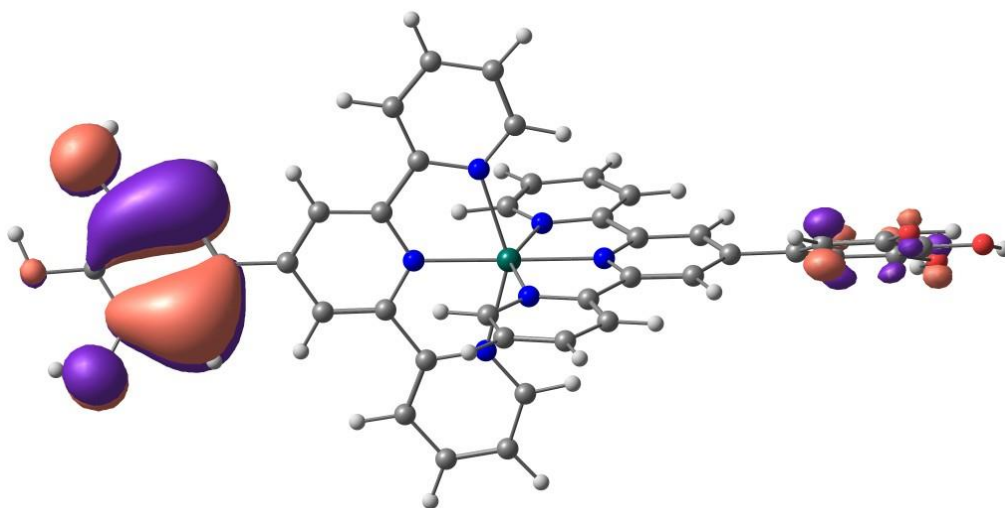
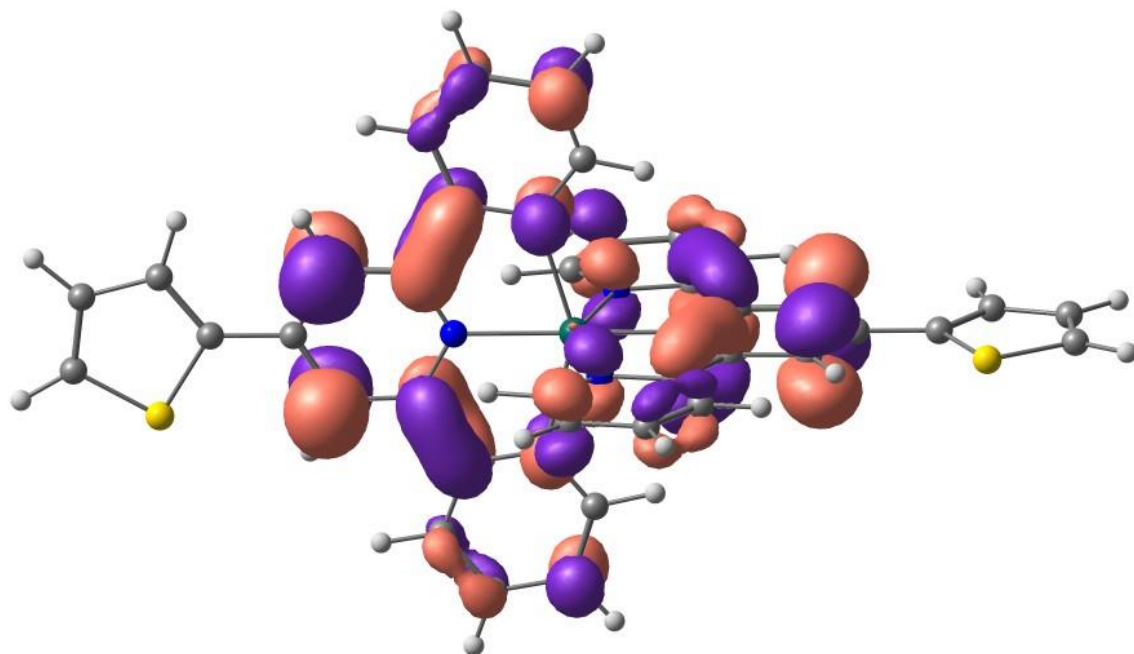


Figure B2.2: The LUMO+1 and HOMO-1 orbitals of complex Zn(L<sub>2</sub>) complex.

LUMO+1

Zn(L<sub>3</sub>)



HOMO-1

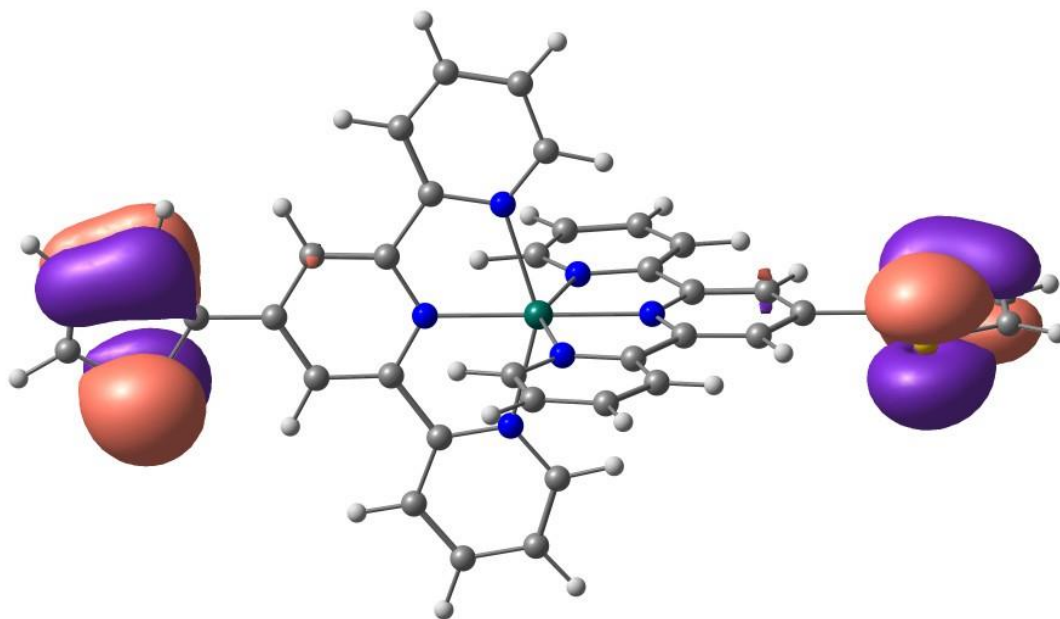


Figure B2.3: The LUMO+1 and HOMO-1 orbitals of complex Zn(L<sub>3</sub>) complex

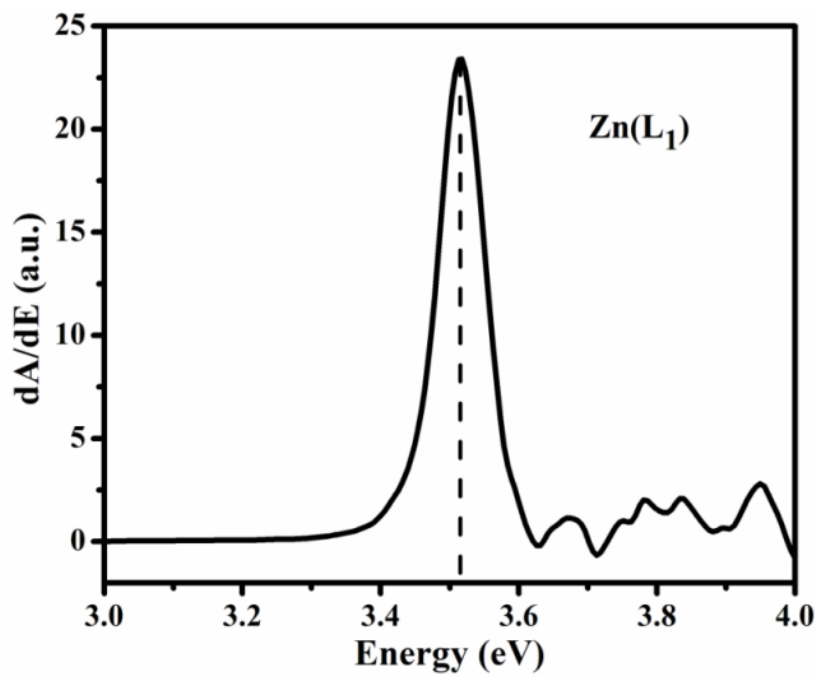


Figure B2.4: Variation of the first derivative of optical absorption intensity with respect to the illuminated photon energy of Zn(L<sub>1</sub>) complex

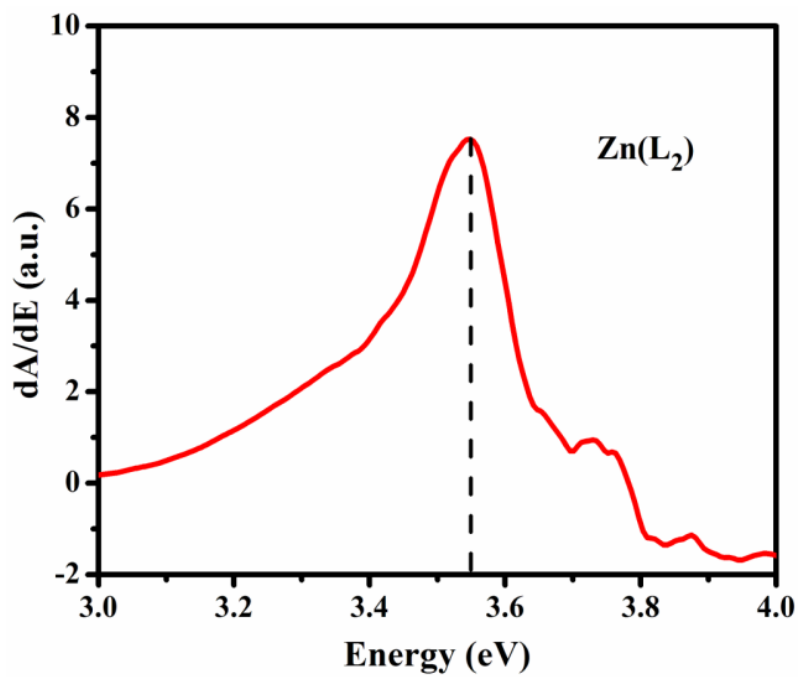


Figure B2.5: Variation of the first derivative of optical absorption intensity with respect to the illuminated photon energy of the Zn(L<sub>2</sub>) complex



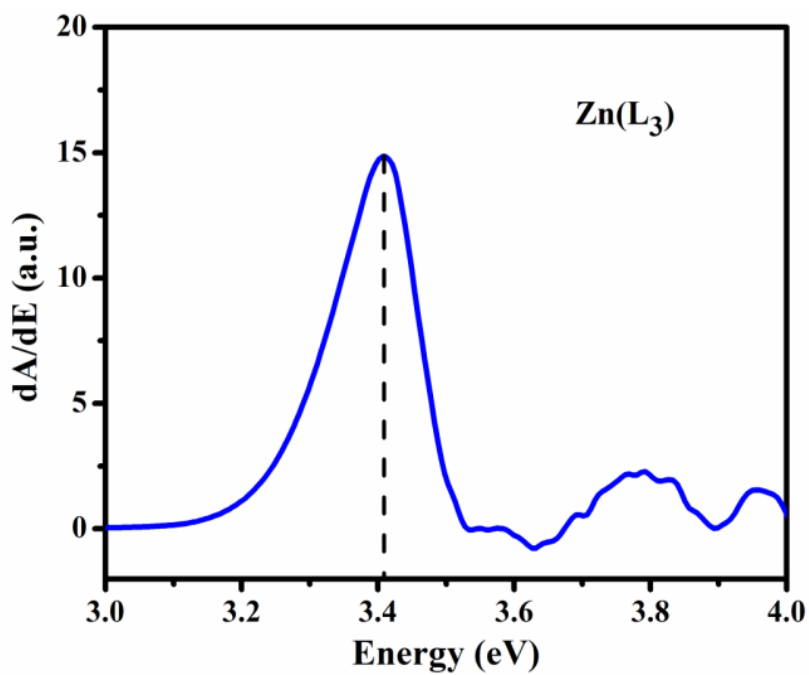


Figure B2.6: Variation of the first derivative of optical absorption intensity with respect to the illuminated photon energy of the Zn(L<sub>3</sub>) complex.

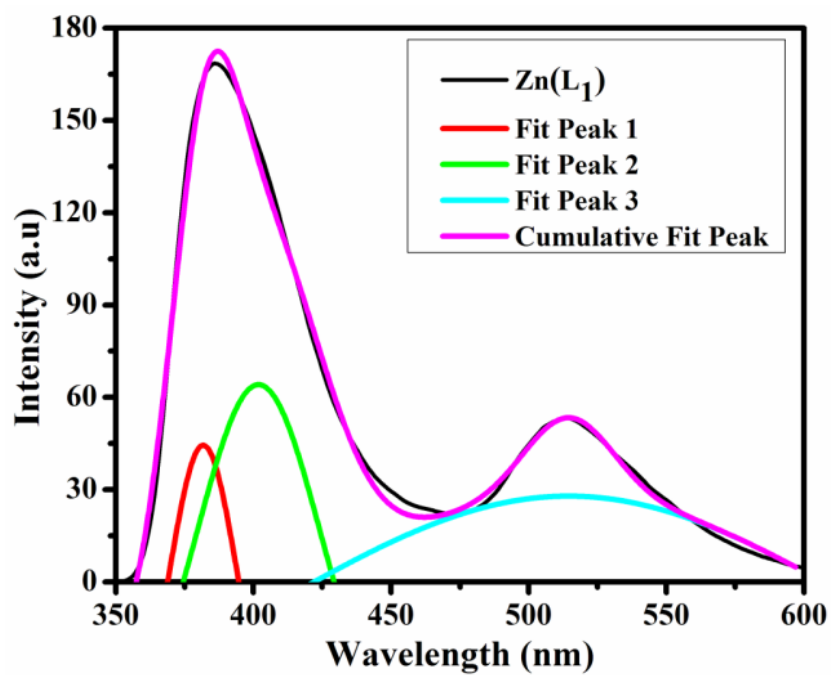


Figure B2.7: Fine fitting plots of PL spectra of Zn(L<sub>1</sub>) complex.

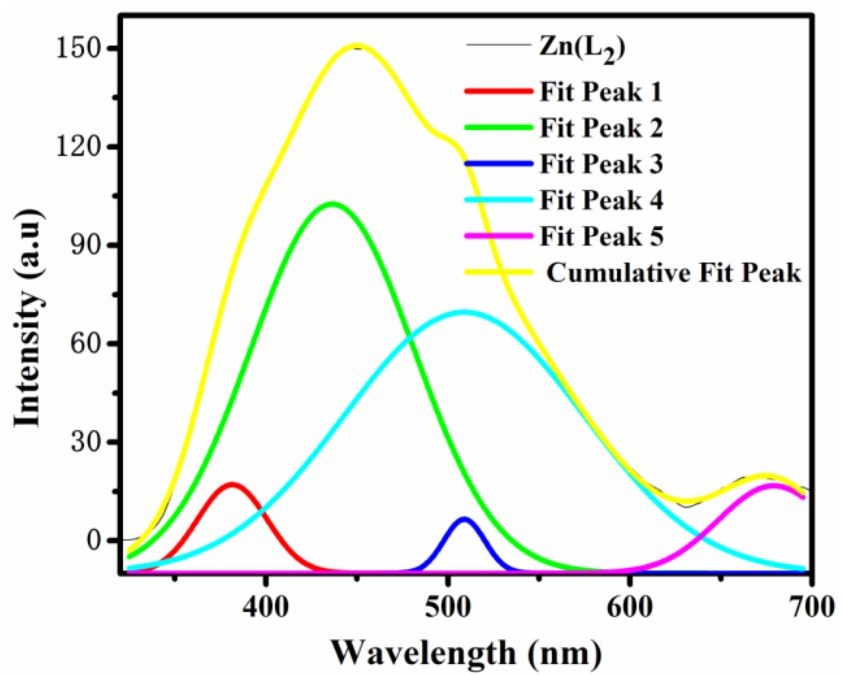


Figure B2.8: Fine fitting plots of PL spectra of Zn(L<sub>2</sub>) complex

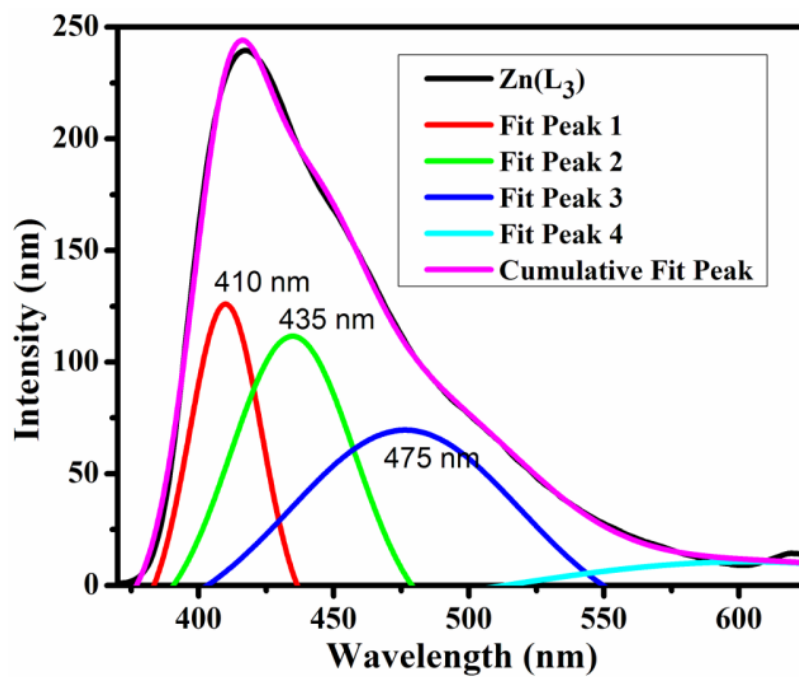


Figure B2.9: Fine fitting plots of PL spectra of Zn(L<sub>3</sub>) complex

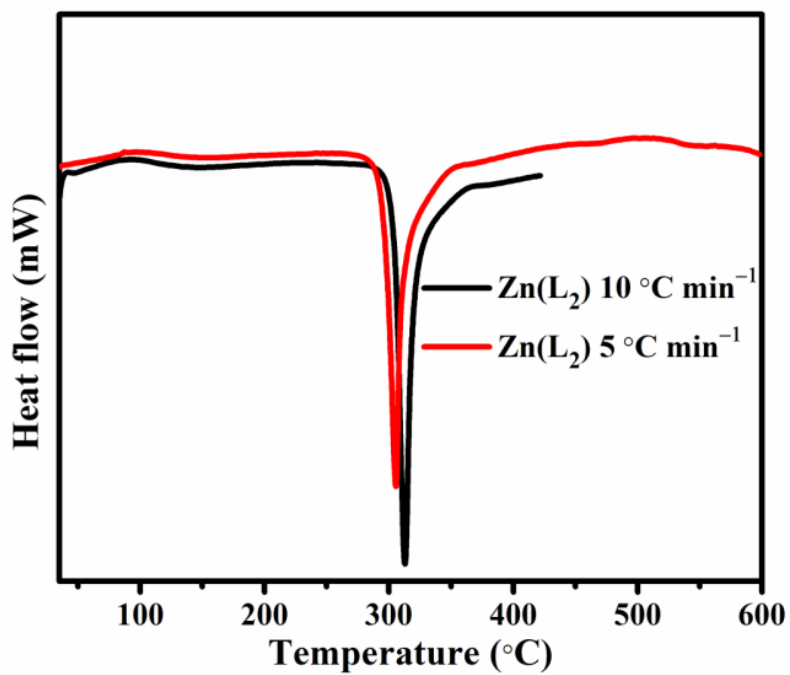
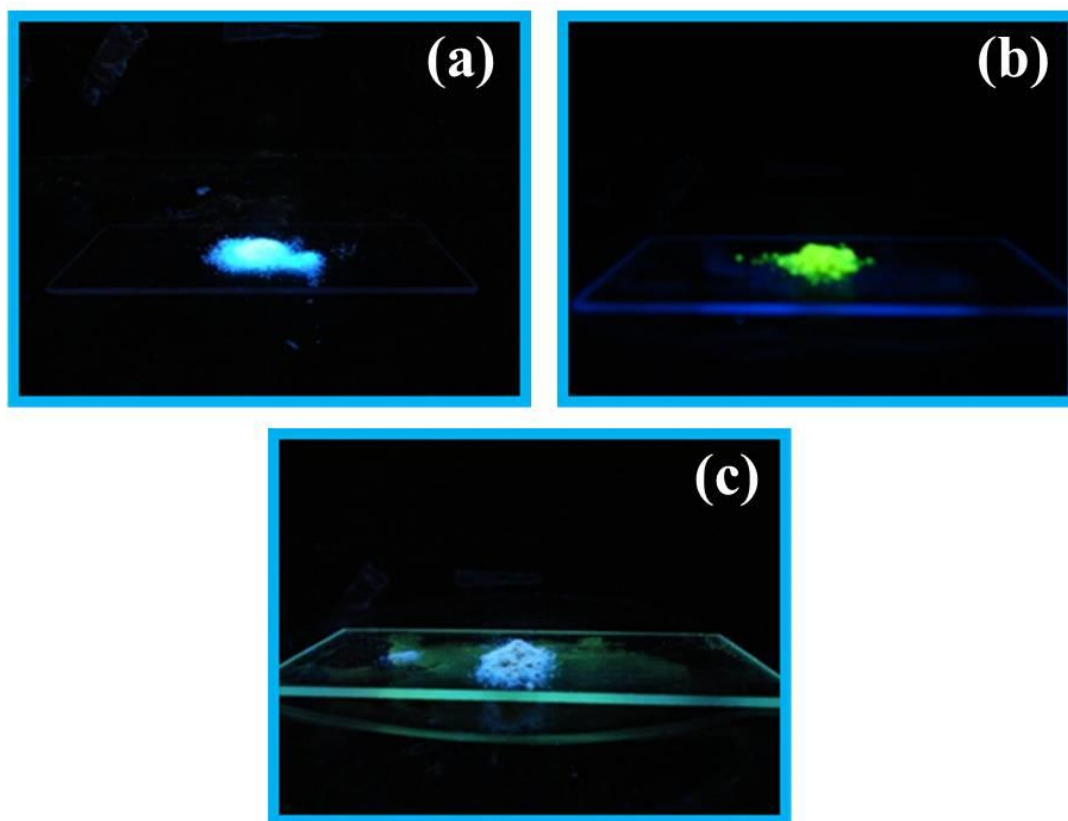


Figure B2.10: DSC plots of Zn(L<sub>2</sub>) complex with the scanning rates of 5 °C min<sup>-1</sup> (red-line) and 10 °C min<sup>-1</sup> (black-line) under the nitrogen atmosphere.



**Figure B2.11: Fluorescence images of Zn(L<sub>1</sub>-L<sub>3</sub>) complexes in solid state under the UV radiation.**

## APPENDIX C

### Electroluminescence spectrum at various bias voltages

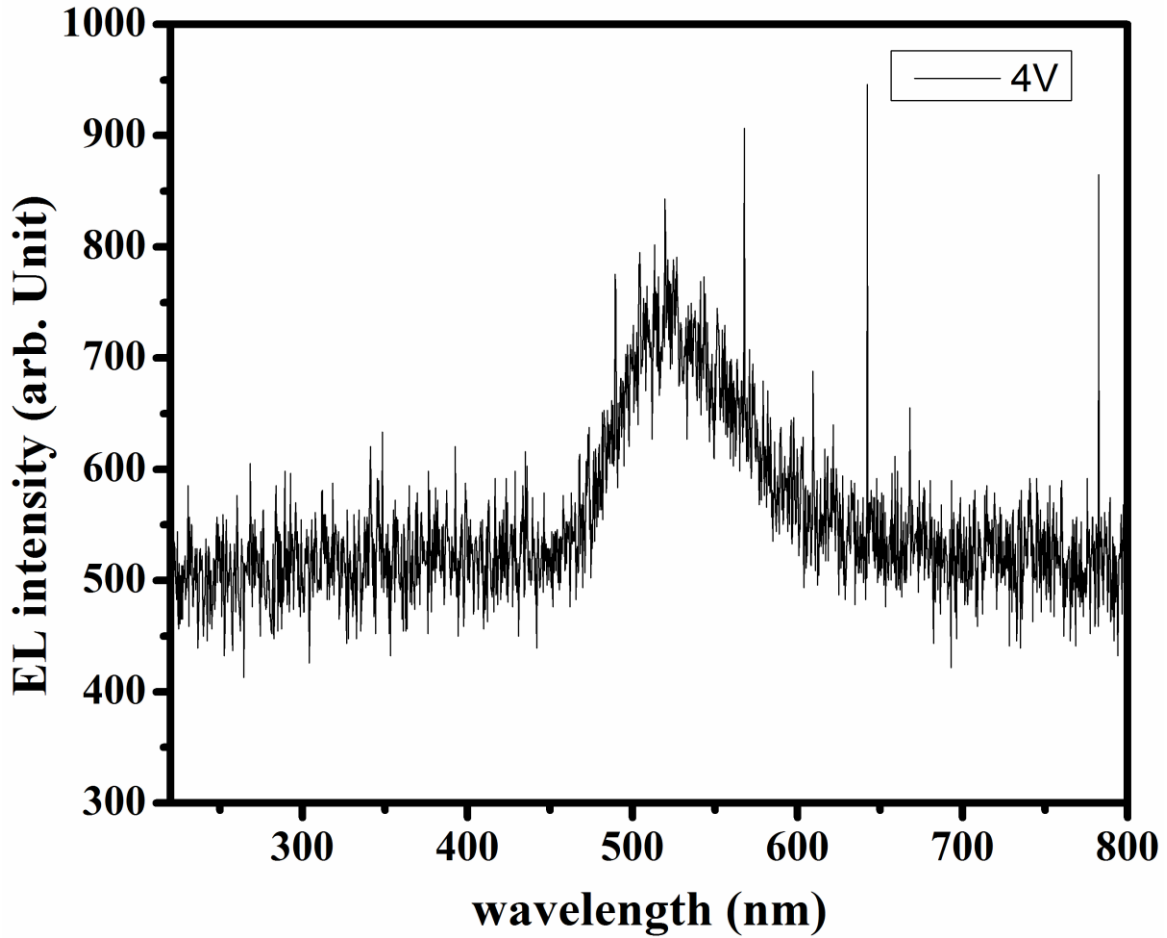


Figure C3.1: Electroluminescence spectrum for 4 V bias.

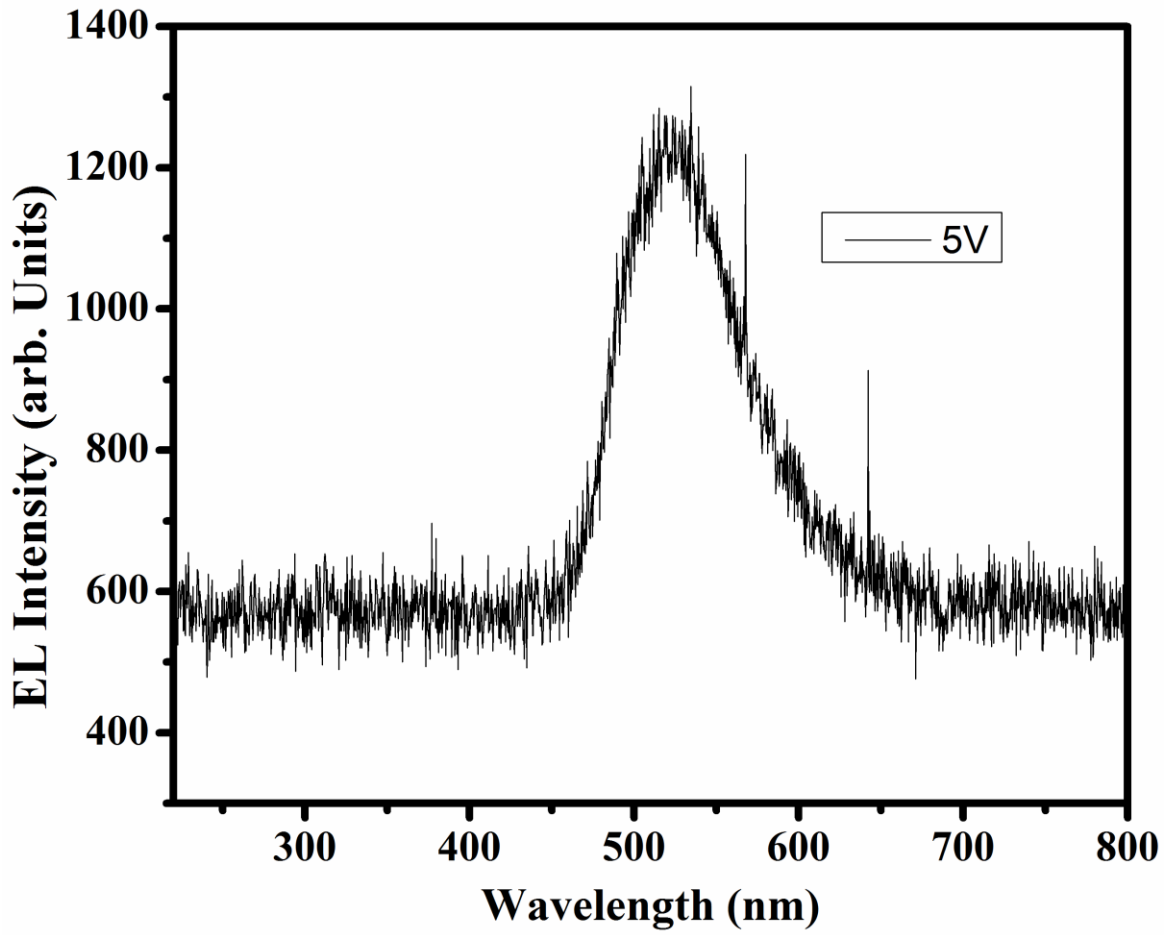


Figure C3.2: Electroluminescence spectrum for 5 V bias.



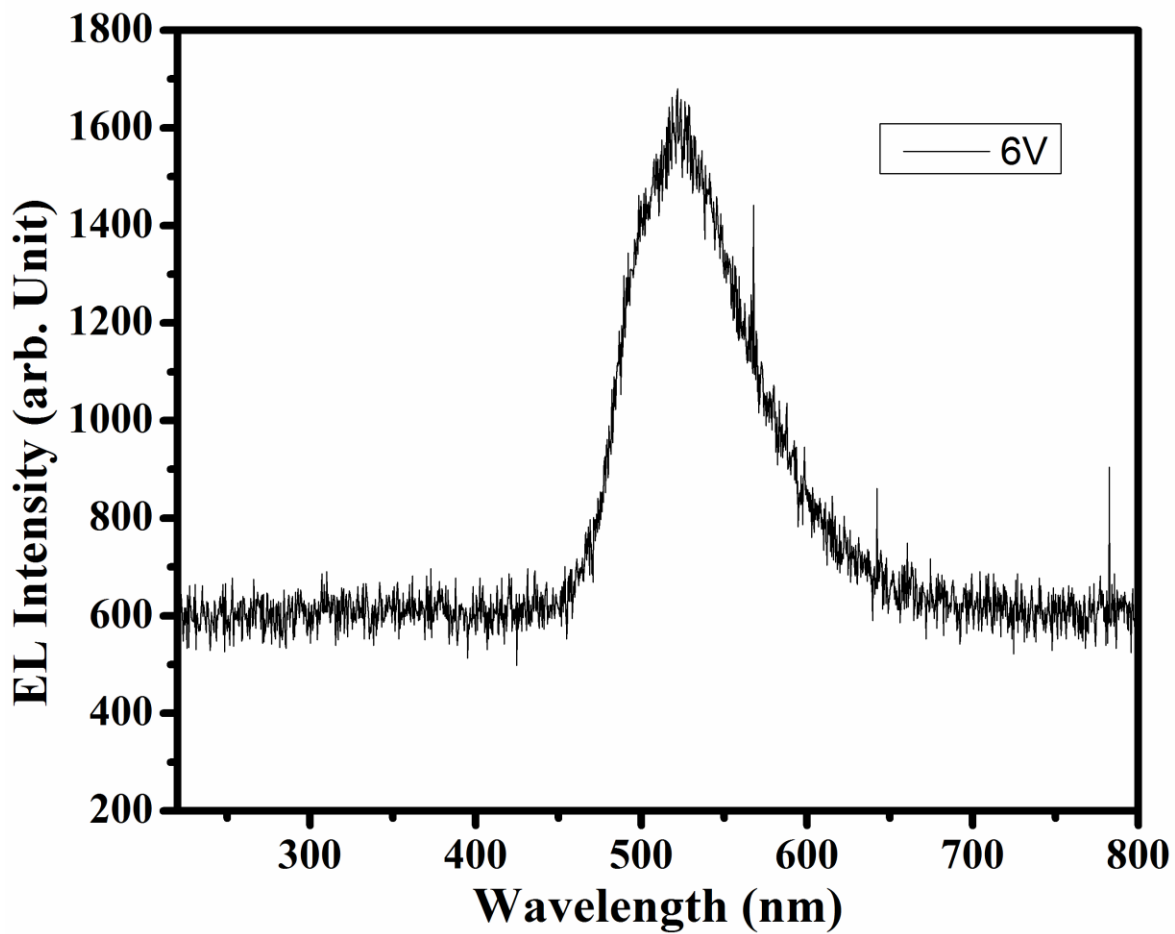


Figure C3.3: Electroluminescence spectrum for 6 V bias

## List of publications in international journals

---

1. **Raja L.**, Raja P.P., Shivaprakash N. C., Sindhu S. “Specroelectrochemical, Switching Kinetics, and Chronoamperometric Studies of Dibenzyl Derivative of Poly(3,4-propylenedioxythiophene) Thin-Film-Based Electrochromic Device” *J. Appl. Polym. Sci.* 131, 2014: 40717.
2. Siju C.R., **Raja L.**, Shivaprakash N.C., Sindhu S., “Grey to Transmissive Electrochromic Switching Using Electropolymerized Poly (3,4-ethylenedioxythiophene)-Ionic Liquid Functionalized Graphene Films” *J. Solid State Electrochem*, 2015, 19: 1393–1402.
3. **Raja L.**, Shivaprakash N.C., Sindhu S. “Spectral characterizations and photophysical properties of one-step synthesised blue fluorescent 4'-aryl substituted 2,2':6',2''-terpyridine for OLEDs application” *J. Lumin.*, 2015, 168: 145–150.
4. **Raja L.**, Raja P.P., Shivaprakash N.C., Sindhu S., “Fabrication of fast switching electrochromic window based on poly(3,4-(2, 2-dimethylpropylenedioxy) thiophene) thin film” *J. Mater Science: Mater Electron.*, 2016, 27: 6035–6042.
5. **Raja L.**, N.C. Shivaprakash, S. Sindhu, “Switching from sky blue to deep green fluorescent Zn(II) complexes for OLEDs applications” *J. Lumin.*, 2018, 196, 136-145.
6. **Raja L.**, N.C. Shivaprakash., S. Sindhu, “Orange Fluorescent Ru(III) Complexes Based on 4'-Aryl Substituted 2,2':6',2''-Terpyridine for OLEDs Application” *J. Fluoresc.*, 2018, 28, 173-182.

## Papers presented in national and international conferences

---

1. **L. Raja**, P.P Raja, C.R. Siju, K. Narasimha Rao, S.Sindhu “Comparison of electrochemical properties of dimethyl and dibenzyl derivatives of PProDOT thin films for energy saving devices” (Poster) National conference in condensed matter physics, BITS, Pilani, Rajasthan, India, 2012.
2. **L. Raja**, C.R. Siju, P.P Raja, K. Narasimha Rao and S. Sindhu “Optical and morphological analysis of dibenzyl derivative of PProDOT thin film for the fabrication of optoelectronic devices” (Poster) 6<sup>th</sup> international symposium on Macro- and supramolecular Architectures and Materials, K.S.R. College of Engineering, Tamil Nadu, India, 2012.
3. **L. Raja**, P.P. Raja, N. C. Shivaprakash S. Sindhu “A study on spectroscopic, morphological and switching properties of dibenzyl derivative of Poly (3, 4-Propylenedioxythiophene) thin film based electrochromic device” (Poster), IUMRS-International Conference in Asia, Indian Institute of Science, Bangalore, India, 2013.
4. **L. Raja**, C.R. Siju, N. C. Shivaprakash, S. Sindhu “Spectral Characterization and Photophysical Properties of One-Step synthesized of 4'-Aryl Substituted 2,2':6',2''-Terpyridine for Fluorescent OLED Applications” (Oral presentation) First International Conference on Large Area & Flexible Microelectronics, R V College of Engineering, India, 2014.
5. **L. Raja.**, C.R. Siju, N. C. Shivaprakash, S. Sindhu “Fabrication and characterization of green light emitting diode based on synthesized tris-(8-hydroxyquinoline) aluminum” (Oral presentation), ICMAT & IUMRS-ICA2015, Suntec, Singapore, 2015
6. **L. Raja.**, N. C. Shivaprakash, S. Sindhu., “Synthesis and characterization of phenanthroline derivative as electron transport and electroluminescent material for OLED applications” (Oral presentation) International Workshop on Physics of Semiconductor Devices, Indian Institute of Science, India, 2015.

7. **Raja L.**, N. C. Shivaprakash, S. Sindhu “Photophysical, thermal and electrochemical properties of 4'-Aryl Substituted 2,2':6',2''-terpyridine derivatives for blue OLED Applications” (Oral presentation) International Workshop on Physics of Semiconductor Devices, Indian Institute of Science, India, 2015.
8. **Raja L.**, N. C. Shivaprakash, S. Sindhu “Improvement of hole transportation in organic light emitting devices (OLEDs) by Silver nanoparticles decorated PEDOT: PSS” (Oral presentation), ICAMPE-2015, Mahatma Gandhi University, Kerala, India 2015.
9. **Raja L.**, N. C. Shivaprakash and S. Sindhu “Graphene oxide and PEDOT: PSS nano composite for improve the hole transportation property in organic light emitting devices” (Poster), IUMRS-ICEM, Suntec, Singapore, 2016.
10. **Raja L.**, Shivaprakash N.C., Sindhu. S “Fabrication and characterization of electrochromic pixel display using Di-isopropylbenzyl Derivative of Poly (3,4-propylenedioxythiophene) (oral presentation), IUMRS-ICEM, Suntec, Singapore, 2016.
11. **Raja L.**, Shivaprakash N.C, Sindhu. S “Photophysical, electrochemical and thermal properties of Ru(III) based 4'-aryl substituted 2.2':6'2'' terpyridine derivatives for red light emitting OLEDs application” (oral presentation) ICYRAM-2016, Indian Institute of Science, India.
12. Sindhu. S., **Raja L.**, Shivaprakash N.C., “Designing And Fabrication Of Electrochromic Pixels Displays Using Di-Isopropylbenzyl Derivative Of Poly (3,4-Propylenedioxythiophene)” ICMAT 2017, Suntec, Singapore, 2017.

## Brief Biography of the Supervisor

---

Prof. S. Sindhu is an experimental and theoretical condensed matter physicist. She has completed her Ph.D. from the Mahatma Gandhi University, Kerala, in 1998. She has later worked as a postdoctoral fellow at the Department of Electrical Engineering, University of Twente, Netherlands, between January 1999 and April 2000. She has also worked as a postdoctoral research fellow at the Department of Physics, Martin-Luther Universitat, Halle, Germany, for more than two years (Feb. 2002–May 2004) after which she joined as a Research Associate at the Dept. of Instrumentation, Indian Institute of Science, Bangalore, India, and worked there till year 2007. Later, she joined as an Assistant Professor in the Department of Physics, BITS Pilani. At present, she is an Associate Professor with the Department of Physics and Associate Dean in Practice School Division, Bangalore Off-campus Center, BITS-Pilani. Her major research interests are both experimental and theoretical analysis of condensed matter physics, especially fabrication of molecular electronic devices, which include electrochromic devices and organic light-emitting diodes (OLEDs) for energy-saving systems. She has wide range of research experience in surface and material science, lattice dynamics and magnetism. She is the author and corresponding-author of more than 20 articles published in reputed international journals. She serves as an editorial member, and reviewer for several journals. Currently, she is a principal investigator for several ongoing projects funded by DST and CSIR, India.

## Brief Biography of the Candidate

---

L. Raja was born in Salem, Tamil Nadu, India. He received his Bachelor of Science and Master of Science degrees in Physics from Periyar University in 2006 and 2008, respectively. He pursued his Master of Technology in Nanoscience and Technology from Anna University, Tiruchirappalli, Tamil Nadu in 2010. Currently, he is a full-time research scholar at the Department of Physics, Birla Institute of Technology and Science, Pilani, Rajasthan, India. His field of research is synthesis of organometallic complexes, such as Zn(II) and Ru(III)-based 2,2':6',2''-terpyridine derivatives, development of transparent conducting thin films and fabrication of organic light-emitting diodes (OLEDs). His research work has appeared in several international journals and has also presented it in over 10 international/national conferences held across India and overseas.

### **Awards while continuing research**

- Awarded DST travel grant for attending conference (IUMRS – 2016, Singapore)
- Awarded CICS, Chennai travel grant for attending conference (IUMRS – 2016, Singapore)